Robust and Fast Quantitative MRI for Clinical Deployment

Daniel Papp

A dissertation submitted in partial fulfilment
of the requirements for the degree of
Doctor of Philosophy
granted by
University College London

Institute Of Neurology
University College London
2018

Declaration of independent work

I, Daniel Papp confirm that the work presented in this thesis is my own. Where information has been derived from other sources, I confirm that this has been indicated in the thesis.

_____ _____

Signature Date

Abstract

Within this thesis, my work carried out in order to prepare an existing quantitative imaging method, multi-parameter mapping, for clinical use, is summarized.

My tasks were to improve the motion-robustness of the acquisitions used in this protocol, and to reduce the scan time of the protocol to a clinically viable level.

In order to reduce acquisition times, I investigated the use of higher parallel imaging acceleration factors, compared to those used in the protocol to date. I found that increasing the acceleration factor from 2 to 2-by-2 is a viable approach to decrease scan time, as is elliptical k-space coverage.

In order to improve the robustness versus inter-scan motion, I investigated the effect of inter-scan motion on the quantitative maps derived from the protocol. I found that, while rigid-body motion correction is not sufficient in cases where a map is calculated from more than one scan, as the changes in the receive field are unaccounted for. I introduced a correction method, based on measuring the receive field for each structural scan, and showed that it improves image quality in the presence of inter-scan motion.

Motion robustness was also improved by selecting a relatively motion-insensitive acquisition trajectory, from a set of clinically available trajectories.

To further address the issue of intra-scan motion, I developed a novel navigator technique, based on acquiring data concurrent with gradient spoiling. Crucially, the acquisition of this navigator did not require additional scan time. I found that this navigator is sufficiently sensitive to motion, such that outlier rejection can be used to identify motion-corrupted data points. I implemented a data re-acquisition approach, based on the outlier rejection, and showed that image quality can be improved by this method.

Acknowledgements

I would like to thank, first and foremost, my two internal PhD supervisors, Prof. Nikolaus Weiskopf and Dr. Martina Callaghan. I am grateful for the opportunity of having been their student, and without their help, guidance and support, as well as their endless patience during the write-up period, this thesis would not exist.

I am indebted to my colleagues at the FIL Physics group for their advice both professional and personal, be it delivered next to a scanner, a computer, a good thai meal, or a pint, during my three and a bit years as a PhD student.

Dr. Indran Davagnanam was gracious enough to let me shadow his work, allowing me to gain some insight into how differently a neuro-radiologist looks at scans, compared to my own view as a physicist.

Dr. Uri Hertz was kind enough to share laboriously collected motion trajectories with me. Without that input, I am unsure if anything past Chapter III would have come to pass.

I greatly enjoyed my time as an intern researcher at the Siemens factory in Erlangen. For showing me the ropes, as well as some good local beer, I thank my external supervisors, Dr. Craig Buckley and Dr. Heiko Meyer.

Dr. Iulius Dragonu, likewise of Siemens, has shown great patience towards me as I fumbled my way through ICE code.

I would like to thank my social support group, both local in London, and scattered by the winds, for helping me through the dark times of this PhD, and enjoying the good times with me.

Table of contents

List of tables

List of figures

Chapter I: Introduction

Magnetic resonance imaging (MRI) is an important clinical imaging modality, with an average of fifty MRI examinations (scans) per thousand inhabitants in the European Union (1,2). In the United Kingdom, close to three million MRI scans are performed annually (2). Both within the EU and the UK, MRI is the fastest growing imaging modality, with annual growth rates in excess of 12% (3). Due to the prevalence of MRI, it is important that the latest findings from research and development are translated into clinical practice. In this thesis, I present the work done to prepare a quantitative MRI (qMRI) method for clinical deployment. This work was focused on accelerating the acquisition of MRI scans acquired for the protocol, and on making the scans more robust against motion that occurs between, and during acquisitions, with the aim of delivering a fast and robust protocol.

The majority of clinical MRI scans are evaluated in a qualitative framework, where the diagnostic outcome is determined by the contrast of greyscale images, e.g. is a region relatively hyper- or hypo-intense consistent with the suspected pathology? While the importance of this approach cannot be understated, it is subjective, which additionally means that longitudinal, and cross-site comparisons are made difficult by intra-, and inter-observer variability (4,5). On a greyscale image, the same contrast changes can be the result of different pathologies and may manifest via changes in one or more underlying tissue parameters that contribute to the overall signal intensity on an MR image, reducing the pathological specificity of qualitative MRI (6).

qMRI methods can address these issues by presenting data as quantitative maps that reflect specific MRI properties of the tissue, such as the longitudinal relaxation rate improving reproducibility and specificity (7,8). In spite of the advantages they present, qMRI methods are rarely used in neuroimaging clinical practice. To date, only the use of T2 mapping of the hippocampus has seen clinical uptake, where it performs equal or better compared to qualitative imaging in hippocampal sclerosis (9,10). Outside the field of neuroimaging, qMRI methods are seeing clinical interest in cardiac imaging (11,12) and cartilage imaging (13–15).

Several reasons contribute to the lack of widespread clinical adoption. Quantitative maps are estimated from scans with relatively long scan times, or by combining data from several scans, at the cost of additional scan time. This long scan time renders qMRI scans sensitive to patient motion, which is the primary cause of poor image quality in clinical practice (16). In addition, high quality, reproducible quantification typically requires tailored acquisition methods and standardised operating procedures, reducing their flexibility in a clinical setting. Quantitative data is typically derived from imaging data after extensive post-processing, which further limits clinical availability and utility. Quantitative imaging, like qualitative imaging, is also sensitive to changes and inhomogeneities in the static magnetic field as well as the transmit, and receive fields of the MRI scanner. For qMRI methods to become widespread in clinical, diagnostic use, it is crucial that these issues are addressed.

During this PhD project, several steps were undertaken to enable the more widespread clinical use of multi-parameter mapping (MPM) (17–19), a qMRI method recently developed for research. The MPM method provides a multi-contrast view, sensitive to brain microstructure, that has been utilised in a variety of studies, from brain development during adolescence (20) and healthy aging (21,22), obesity-related changes (23), myelin mapping (24–26), and measurement of the g-ratio, which quantifies the degree of myelination of fibre pathways (27).

These steps were undertaken with three goals in mind: the reduction of protocol acquisition time to a level comparable with clinical scanning, the improvement of motion robustness, and the translation of acquisition and post-processing steps into a clinical setting.

The goal of scan time reduction was based on the hypothesis that the original total acquisition time of 25 minutes can be reduced while maintaining adequate quantitative precision. This was achieved by utilizing parallel imaging, and a reduction in k-space coverage, for a protocol acquisition time of approximately 17 minutes, without a significant loss in data quality.

Motion between scans was addressed based on the hypothesis that this type of motion affects quantitative parameters chiefly through the change in the receive field the multi-channel coils despite the application of image registration. This field was measured, and corrected for, using short, low resolution scans, improving robustness against motion between scans.

Based on the hypothesis that different acquisition k-space trajectories are not equally sensitive to motion, several trajectories were evaluated for their motion sensitivity, and the least motion sensitive was chosen to make the acquisitions more robust to motion during acquisitions.

A novel method for detecting, and correcting for the effect of motion during scanning was developed, based on the hypothesis that data acquired concurrent with gradient spoiling is sensitive to motion in the type of sequence used to acquire quantitative data in the protocol. Crucially, this technique did not require additional scan time, in accordance with the goal of reduced scan time.

To aid future clinical deployment, several post-processing steps were implemented in a Siemens prototyping environment, and the acquisition parameters of the sequence used in the MPM protocol were partially implemented in a clinically available sequence.

Thesis outline

In Chapter II, I present the theoretical background of topics relevant to the thesis. Basic concepts of MRI physics, such as excitation, relaxation, image formation, and parallel imaging are reviewed. Quantitative approaches to analysing MRI data are introduced, and the theoretical background and modelling approaches of the MPM protocol are described. The theoretical basis for the motion sensitivity of MRI acquisitions is described, together with existing motion correction techniques. The concept of general linear models, used to refine the navigator technique developed during the project, is introduced.

In Chapter III, the effect of inter-scan motion, or motion between scans, on quantitative parameter estimation in the MPM method is evaluated. The theoretical background for the sensitivity of estimated quantitative values to changes in the receive field due to inter-scan motion is explained, and the novel correction method, based on measuring and correcting for these changes, is introduced and validated in an in vivo study. The feasibility of using existing methods for measuring the receive field is investigated, and a recommendation is given for best practice.

In Chapter IV, I present the results of decreasing scan time by increasing parallel imaging factors, and by skipping the acquisition of low k-space energy points. I evaluated the impact of this speedup on quantitative values in a phantom study and in vivo, and I give a recommendation for the parallel imaging factor based on the prevalence of image artefacts. I measured the impact of motion during scanning on images acquired with the MPM protocol for several clinically available acquisition trajectories in a phantom study, and select the trajectory used in the remainder of this thesis.

In Chapter V, the development of a novel motion detection technique is presented, based on navigator data that are acquired concurrently with gradient spoiling, thereby resulting in no extra scan time. I show that despite the markedly low signal-to-noise ratio of these navigator data, they are sensitive to motion. The outlier rejection technique I developed to capitalise on this sensitivity is described and proof-of-principle capability is demonstrated in vivo. The viability of a general linear model approach in improving the sensitivity and specificity of outlier rejection, is shown. A motion correction technique, based on re-acquiring data classified as having been affected by motion, is introduced, and evaluated in vivo.

In Chapter VI, the results of two research-industrial collaboration internships with Siemens Healthcare are shown.

Chapter VII offers a summary of the work accomplished during the PhD project, and highlight potential avenues for future development.

Chapter II: Theory

In this Chapter, the theoretical background of this thesis is reviewed. Basic MRI concepts, such as the origin and spatial encoding of the MRI signal are explained. The concepts of k-space and accelerated imaging are detailed to lay the theoretical foundation for the concepts explored in this thesis. The topics of motion sensitivity and basic quantitative MRI measures, as well as commonly used measurement methods are introduced. Lastly, general linear models, as used in the fifth Chapter, are detailed.

II.1: Origin of the MRI signal

Magnetic resonance imaging is based on the phenomenon of nuclear magnetic resonance (NMR), with the addition of image encoding (28,29). The NMR phenomenon arises from the interaction of a fundamental property of matter, the interaction of the magnetic moment of a nucleus with an external magnetic field $\mathbf{B_0}$. The magnetic moment of a nucleus is described by (30):

$$\boldsymbol{\mu} = \mathbf{I}\gamma \qquad \text{[II.1]}$$

where $\boldsymbol{\mu}$ and $\mathbf{I}$ are the magnetic moment and the nuclear angular momentum, or spin, and γ is the gyromagnetic ratio. Spin is a quantum mechanical property, and can only take specific values along a given axis:

$$\mathrm{I}_z = \mathrm{m}_I \hbar \qquad \text{[II.2]}$$

where I_z is the magnitude of the spin along the axis z, and m_I is the magnetic quantum number.

For a given nucleus with a spin quantum number of I, the values of m_I range from –I to I in steps of one. Thus, there are 2I+1 states the magnitude of the spin can take along a given axis. For a nucleus to be detectable through NMR, the number of different states has to be at least two. The most biologically abundant nucleus of the human body detectable through NMR is hydrogen (^{1}H), bound in water, which contributes approximately 63% of total body mass of an adult human. The hydrogen nucleus is composed of a single proton, and thus the quantum spin number is $I_H = 1/2$. For this reason, the terms “spin”, “proton”, and “water molecule” are often used semi-interchangeably, though imprecisely in the MRI literature.

For a hydrogen nucleus, the possible values of I_z are $+1/2\hbar$ and $-1/2\hbar$. The energy associated with these states is:

$$E = -\boldsymbol{\mu}\mathbf{B} \qquad \text{[II.3]}$$

In the absence of an external field, these states are degenerate, i.e. have the same energy. To generate an NMR signal, and enable MRI imaging, this degeneracy has to be lifted.

If an external magnetic field, $\mathbf{B_0}$=(0,0,B_0) is applied, the direction of this external field determines the z axis of Equation II.2. Thus, the spin can either be aligned parallel to the

external field (the "spin-up", $I_z = 1/2\hbar$ state), or anti-parallel to the external field ($I_z = -1/2\hbar$, "spin-down").The energy difference between the "spin-up" and "spin-down" states, ΔE is:

$$\Delta E = E_+ - E_- = 2\mu B_0 \quad \text{[II.4]}$$

Combining Equations II.1, II.2 and II.4, the energy required to transition between the "spin-up" and "spin down" states can be formulated as:

$$\Delta E = \gamma \hbar B_0 \quad \text{[II.5]}$$

Transition between the two states can occur if a photon of a certain frequency is absorbed. In other words, resonance absorption occurs for a specific frequency, the Larmor frequency, or resonance frequency (ω_0), given as an angular frequency by (31):

$$\hbar\omega_0 = \gamma \hbar B_0 \quad \text{[II.6a]}$$

$$\omega_0 = \gamma B_0 \quad \text{[II.6b]}$$

Commonly, the resonance frequency is expressed in units of Hz. For the hydrogen nucleus, $\gamma = 2.68 * 10^8\ rads^{-1}T^{-1}$,may be expressed as ${}^{\gamma}/_{2\pi} = 42.6\ {}^{MHz}/_{T}$. For the results presented in this thesis, B_0≈3T, i.e. the resonance frequency, ${}^{\omega_0}/_{2\pi}$ is ≈127 MHz.

In MRI, matter is imaged on a macroscopic scale. A typical MRI voxel has a volume of 1mm^3, containing approximately 3.3*10^{22} water molecules. Thus, a semi-classical, rather than quantum mechanical description is used to describe the behavior of the protons within the voxel.

Using Ehrenfest's theorem (32), it can be shown that, in the presence of an external magnetic field, the motion equation for the expected value of the magnetic moment is a torque equation, and thus can be described using classical electrodynamics:

$$\frac{d}{dt}\langle \boldsymbol{\mu} \rangle = \gamma \langle \boldsymbol{\mu} \rangle \times \boldsymbol{B_0} \quad \text{[II.7]}$$

Ehrenfest's theorem can be used, because the Hamiltonian function describing a spin in an external magnetic field does not have off-diagonal elements:

$$H = \begin{pmatrix} -{}^{1}/_{2}\,\hbar\omega_0 & 0 \\ 0 & {}^{1}/_{2}\,\hbar\omega_0 \end{pmatrix} \quad \text{[II.8]}$$

The voxel can be described by the sum of the magnetic moments, the net magnetization vector, **M**:

$$\boldsymbol{M} = \frac{1}{V}\sum_{i=1}^{N} \boldsymbol{\mu_i} \quad \text{[II.9]}$$

where $\boldsymbol{\mu_i}$ is the magnetic moment of spin i, N is the number of spins in voxel volume V.

In the presence of an external magnetic field, the equilibrium net magnetisation of a voxel can be derived from the population difference of the "spin-up" and the "spin-down" states:

$$\boldsymbol{M_0} = \Delta \mathrm{N}\boldsymbol{\mu} = (N_+ - N_-)\boldsymbol{\mu} \quad \text{[II.10]}$$

where $\mathbf{M_0}$ is the net magnetisation vector of the voxel at equilibrium, N_- and N_+ are the population of the "spin-down" and "spin-up" states, respectively, given by the Boltzman distribution:

$$\mathrm{N}_+/_{N_-} = e^{-\Delta E/_{kT}} \quad \text{[II.11]}$$

where k is the Boltzmann constant, T of the voxel, and ΔE is the energy difference between these two states, defined in Equation II.4.

For human body temperature, T≈310K, the exponential term in Equation II.11 can be approximated using a Taylor approximation:

$$e^{-\Delta E/_{kT}} \approx 1 - \Delta E/_{kT}. \quad \text{[II.12]}$$

Thus, the net magnetization vector of a given voxel is:

$$\boldsymbol{M_0} = \mathbf{B_0}\frac{N\hbar^2\gamma^2}{4kT} \quad \text{[II.13]}$$

Equation II.13 can be rewritten, by introducing the spin density of the voxel, ρ, defined as the number of spins in the voxel, divided by its unit volume (such that V≡1).

$$\rho = \frac{\mathrm{N}}{V} \quad \text{[II.14]}$$

$$\boldsymbol{M_0} = \boldsymbol{B_0}\rho\frac{\hbar^2\gamma^2}{4kT} \quad \text{[II.15]}$$

The behavior of the net magnetization vector in the presence of an external magnetic field can be described by a torque equation:

$$\frac{d}{dt}\boldsymbol{M} = \gamma\,\mathbf{M} \times \boldsymbol{B_0} \quad \text{[II.16]}$$

II.2: Excitation, relaxation and detection

This system may be moved from the thermal equilibrium via the application of an additional magnetic field, $\mathbf{B_1}$., a circularly polarized field, perpendicular to $\mathbf{B_0}$. In the laboratory reference frame, $\mathbf{B_1}$ rotates in the x-y plane perpendicular to $\mathbf{B_0}$ with a frequency of ω, such that $\mathbf{B_1}(t)=(B_1\cos(\omega t), B_1\sin(\omega t), 0)$. The motion equation of the net magnetization vector in the presence of this additional field becomes:

$$\frac{d}{dt}\boldsymbol{M} = \gamma\,\mathbf{M} \times \begin{pmatrix} B_1\cos(\omega t) \\ B_1\sin(\omega t) \\ B_0 \end{pmatrix} \quad \text{[II.17]}$$

Equation II.17 can be simplified by introducing a new reference frame, the rotating reference frame, that is, a reference frame that rotates around the z axis, as determined by $\mathbf{B_0}$, with the

frequency of ω. In this reference frame, prior to the excitation, $\mathbf{M_0}$ is aligned with $\mathbf{B_0}$, such that $\mathbf{M_0}$=(0,0,M_0). For ease, all further descriptions are made in the rotating reference frame, unless otherwise noted. In the rotating reference frame, assuming that $\mathbf{B_1}$ is aligned with the x axis of the rotating frame, Equation II.17 becomes:

$$\frac{d}{dt}\boldsymbol{M} = \gamma\,\mathbf{M} \times \begin{pmatrix} B_1 \\ 0 \\ B_0 - {\omega}/{\gamma} \end{pmatrix} \qquad \text{[II.18]}$$

In MRI, the frequency of ω is typically matched to the resonance frequency, ω= ω_0, in order to achieve on-resonance excitation. Thus, the frequency of the $\mathbf{B_1}$ field lies in the radio-frequency range, and is referred to as a radiofrequency, or RF field. Under this condition, **M** is rotated around the y axis of the rotating frame of reference, as described by Equation II.18.. This rotation induces transverse components in **M**. The ratio of transverse to longitudinal components is determined by the flip angle, α:

$$\alpha = \arcsin\left({M_{xy}}/{M_0}\right) \qquad \text{[II.19]}$$

where M_{xy} is the magnitude of the transverse components of magnetization induced by $\mathbf{B_1}$. The flip angle is proportional to the time integral of the RF field:

$$\boldsymbol{\alpha} = \gamma \int_o^{t'} \mathrm{B1}(t)dt \qquad \text{[II.20]}$$

After this excitation, the system will return to the equilibrium through a process called relaxation. The relaxation process is governed by the Bloch equations (28):

$$\frac{d}{dt}\begin{bmatrix} M_x \\ M_y \\ M_z \end{bmatrix} = \begin{bmatrix} -{1}/{T2} & \gamma B_0 - \omega & 0 \\ -\gamma B_0 + \omega & -{1}/{T2} & 0 \\ 0 & 0 & -{1}/{T1} \end{bmatrix}\begin{bmatrix} M_x \\ M_y \\ M_z \end{bmatrix} + \begin{bmatrix} 0 \\ 0 \\ {M_0}/{T1} \end{bmatrix} \qquad \text{[II.21]}$$

where M_z is the component of the magnetization vector in the z direction, the longitudinal magnetization, M_x and M_y are the transverse components of the magnetization vector, in the x and y direction, respectively, and T1 and T2 are the of longitudinal and transverse relaxation time, respectively. Assuming that, immediately after the application of $\mathbf{B_1}$, the longitudinal component is zero, and all magnetization has been flipped into the x-y plane, the solution to the Bloch equations can be described as:

$$\mathrm{M}_z(\mathrm{t}) = \mathrm{M}_0\left(1 - e^{-{t}/{T_1}}\right) \qquad \text{[II.22a]}$$

$$\mathrm{M}_{xy}(\mathrm{t}) = \mathrm{M}_0 e^{-{t}/{T2}} \qquad \text{[III.22b]}$$

The relaxations are facilitated through interactions with the surrounding environment. T1 relaxation, or spin-lattice relaxation, can be explained by considering the local magnetic field fluctuations induced by the molecular tumbling. The surrounding molecules, the lattice in which the spins that give rise to **M** are embedded, may be treated as dipoles that, due to their

thermal motion, induce small, local magnetic fields that perturb the net magnetization. The motion can be characterized by the correlation time of τ_c, defined as the time needed for a rotation of one radian. How well the lattice facilitates relaxation is determined by the ratio of the correlation time to the resonance frequency. If $\tau_c\omega_0 \sim 1$, the lattice facilitates relaxation well, and T1 is short. The tissue-dependent difference in τ_c is the main source of T1 contrast in MRI.

The relaxation of the transverse component, T2, or spin-spin relaxation, occurs through a loss of phase coherence. Immediately following excitation, all the spins in the excited volume are aligned with $\mathbf{B_1}$. However, due to fluctuations in the local field, a phase is imposed on the spins:

$$\phi(t) = \gamma \int_0^t \Delta B(\tau) d\tau \qquad \text{[II.23]}$$

where $\phi(t)$ is the phase imposed upon the spin by the varying magnetic field of ΔB over time. This varying phase evolution leads to a decrease of net magnetization.

$$\mathrm{M}_{xy}(\mathrm{t}) = \int_V M_0 e^{i\phi_j(t)} dV \qquad \text{[II.24]}$$

As both T1 and T2 depend on the speed at which the local field fluctuates, they can both be expressed in terms of the correlation time (33):

$$\frac{1}{T1} = \mathrm{K}\left(\frac{\tau_c}{1+{\tau_c}^2\omega_0^2} + \frac{4\tau_c}{1+4{\tau_c}^2\omega_0^2}\right) \qquad \text{[II.25a]}$$

$$\frac{1}{T2} = {}^{\mathrm{K}}\!/_{2}\left(3\tau_c + \frac{5\tau_c}{1+{\tau_c}^2\omega_0^2} + \frac{2\tau_c}{1+4{\tau_c}^2\omega_0^2}\right) \qquad \text{[III.25b]}$$

$$K = \frac{3\mu_0^2\hbar^2\gamma^6}{160\pi^2 r^6} \qquad \text{[III.25c]}$$

where the constant K is defined here for proton nuclei, and r is the distance between two nuclei. For tissues routinely imaged in MRI, the correlation time, at body temperature, is on the order of nanoseconds, thus T1 and T2 can be separated, as shown in Figure II.1.

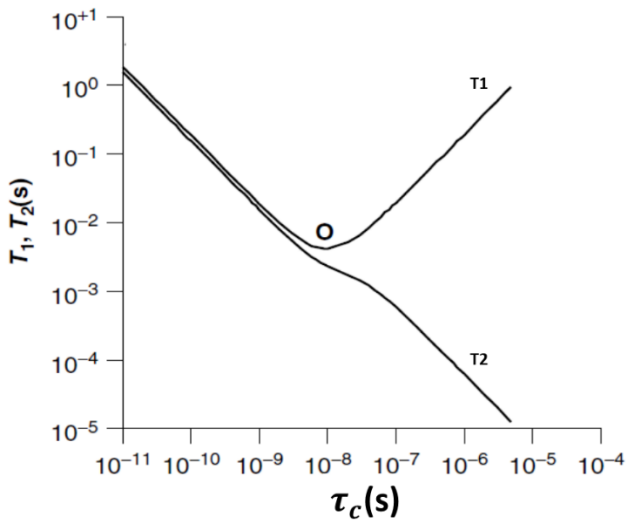

Figure II.1: The relationship between correlation time and relaxation times. O indicates the condition where $\tau_c\omega_0 \sim 1$. Adapted from (7)

An additional term has to be considered for transverse relaxation. Equation II.22b only describes the behavior due to local field fluctuations in the immediate environment of the spin, and assumes a homogeneous lattice. When field changes caused by inhomogeneities in the lattice are taken into account, the transverse relaxation can be described by:

$$\mathrm{M}_{xy}(\mathrm{t}) = \mathrm{M}_0 e^{-t/T2^*} \qquad \text{[II.26a]}$$

$$1/T2^* = 1/T2 + 1/T2' \qquad \text{[II.26b]}$$

where T2' is the time constant of the decay due to non-local inhomogeneites of the magnetic field.

As the magnetization relaxes to the equilibrium, it can be detected by coil loops, or simply "coils", arranged around the sample. The presence of magnetization results in an electromotive force, given by (34):

$$\mathrm{emf}(\mathrm{t}) = -\frac{d}{dt}\int_{volume} \boldsymbol{M}(r,t)\boldsymbol{B_{rec}^1}(r)dr^3 \qquad \text{[II.27]}$$

where emf(t) is the electromotive force at time t, **M**(r,t) is the magnetization at time t, and $\boldsymbol{B_{rec}^1}$ is the receive field of the coil. The detected signal is proportional to this electromotive force, and thus depends on the proton density of the volume (through $\mathbf{M_0}$), the flip angle (through **M**(r,t)), and the characteristics of the receive coil, referred to as the sensitivity field.

III.3: Image encoding in MRI

In sections II.1 and II.2, a bulk signal was observed from the whole of the excited volume. Such a procedure would result only in a spatially nonspecific NMR signal. To create an image, a spatial dependence is imposed on the signal. In MRI, this is achieved by making the resonance frequency spatially dependent by using additional magnetic field gradients. Assuming an explicit dependence on time and spatial location, the detected signal described in Equation II.27 can be rewritten as:

$$\mathrm{S(t)} = \int_{volume} \widehat{\rho(r)} e^{(i\phi(r,t))}\, dr \qquad \text{[II.28]}$$

where $\widehat{\rho(r)}$ is the effective spin density, containing all the constants from Equations II.15 and II.27, assuming a uniform receive field, and where relaxation effects have been ignored. The phase term is the phase difference accumulated over time t, as imposed by the spatially varying resonance frequency:

$$\phi(\mathrm{r,t}) = -\int_0^t \omega(r,t')dt' \qquad \text{[II.29]}$$

The resonance frequency can be manipulated by changing the local magnetic field, by applying a gradient in a specific direction. For example, if a time-dependent, but spatially constant gradient is applied in the x direction:

$$\omega(\mathrm{x,t}) = \gamma(\mathrm{B}_0 + xG(t)) = \omega_0 + \gamma x G(t) \qquad \text{[II.30]}$$

where $\omega(\mathrm{x,t})$ is the resonance frequency at time t along the x axis, and G(t) is the constant rate of change of the magnetic field along the x axis. The time integral of the gradient is defined as:

$$\mathrm{k(t)} = \gamma \int_0^t G(t')dt' \qquad \text{[II.31]}$$

where k(t) is the spatial frequency along the direction of the gradient, acquired at time t. Combining Equations II.29 through II.31, and extending the formalism to three dimensions, the signal can be described as dependent on the spatial frequency:

$$\mathrm{s}(\mathbf{k}) = \int_{volume} \widehat{\rho(\boldsymbol{r})} e^{-i2\pi \boldsymbol{kr}} d\boldsymbol{r} \qquad \text{[II.32]}$$

The values of k are represented in a 3D space called k-space. Thus, Equation II.32 describes the signal intensity in k-space as the Fourier-transform of the effective spin density in real space. From a fully sampled k-space, the image can be reconstructed by means of

inverse Fourier transformation. This relationship between the image and its k-space is illustrated in Figure II.2:

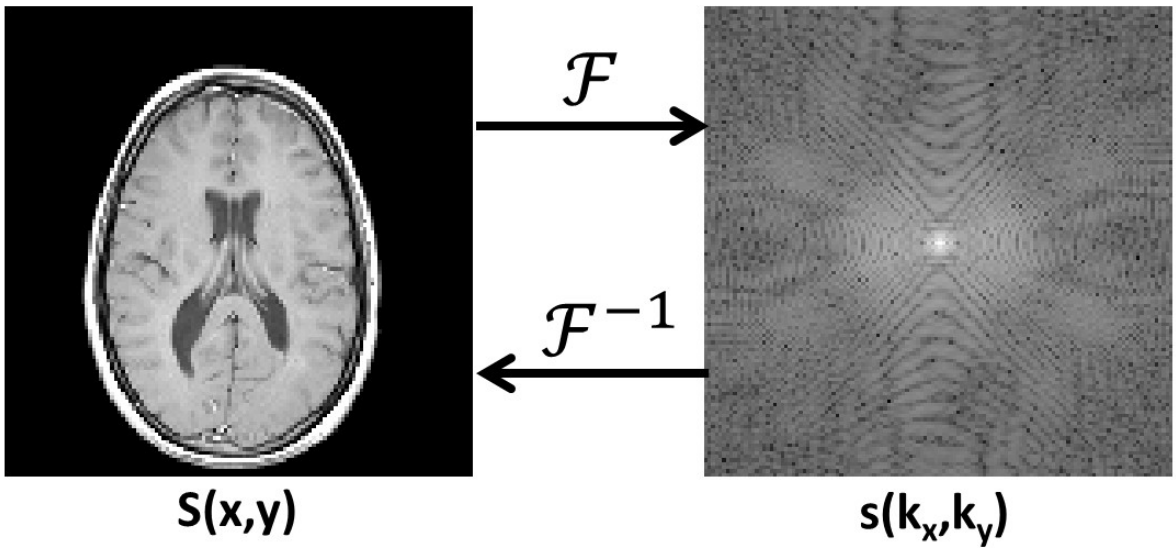

Figure II.2: The relationship between image space (left) and k-space (right). The image on the left, S(x,y), composed of signal intensities associated with a pixel, has been transformed into k-space, where each k-space point carries information about the whole image. Note the bright central portion of k-space, as well as its conjugate symmetry. To increase visibility, the logarithm of the magnitude of (k_x,k_y) is shown.

As k-space encodes the image not on a voxel-by-voxel basis, but by spatial frequency, the center, where the low spatial frequencies are encoded, is bright, while the outer edges of k-space carry considerably less energy. This is due to the nature of imaged object, in this case, a human brain. Within the same tissue type, the signal intensity is relatively homogeneous, thus the spatial frequency is low, while there are relatively few transitions between one tissue type to another, which are encoded in the edges of k-space. This uneven distribution of information, as well as the conjugate symmetry of k-space are exploited in Chapter IV.

Theoretically, k-space can both be sampled and traversed in an arbitrary fashion. However, k-space is typically sampled in an ordered fashion. To acquire an image with isotropic resolution along an axis, k-space along that axis has to be sampled evenly. The desired resolution in image space, as well as the size of the field of view dictate the extent of k-space and the step size in k-space, respectively:

$$\Delta x = {}^{1}/_{2}\, k_{xmax} \qquad \text{[II.33a]}$$

$$\Delta k_x = \frac{1}{FoV_x} \qquad \text{[II.33b]}$$

where Δx is the desired resolution in the x direction, k_{xmax} is the highest spatial frequency sampled in the x direction, Δk_x is the step size in the x direction in k-space, and FoV_x is the field of view in the x direction. Typically, k-space is traversed in a sequential manner. In the case of 3D imaging, on one axis, the gradient is applied such that that the whole of k-space is traversed on said axis (the readout direction), while on the other two axes, only a step of Δk is made (phase encoded axes).

It must be noted that transmit and receive fields are assumed to be homogeneous in this example. Signal localization via localized RF transmit fields alone requires multiple transmit coils, and may lead to adverse effects, thus there has been little clinical uptake in neuroimaging to date (35). In in-vivo NMR spectroscopy, signal localization via the receive coils may be used (36), but it is generally not suitable for hydrogen MRI imaging, due to the high number of coils necessary (37,38).

II.4: The FLASH sequence

MRI images are acquired by sampling k-space, and performing an inverse Fourier transformation. In order to fully sample k-space, typically many instances of excitation, signal encoding, and signal acquisition have to be performed, typically in sequential order, by varying the phase encoding gradients, but keeping excitation and acquisition unchanged through the scan. For the experiments detailed in this thesis, the majority of data was acquired using a Fast Low Angle Shot (FLASH) sequence (39,40), a type of gradient recalled echo (GRE) sequence.

Data collection in gradient echo sequences relies on the sequential dephasing and rephasing of magnetization, accentuating the effect of T2* decay. Prior to data collection, a dephasing gradient is applied along the readout axis while the other two directions are phase encoded, and a re-phasing gradient is used to traverse all of k-space in the readout direction, generating a gradient echo. Multiple echoes can be collected by traversing k-space in the positive, then negative k-space direction, sequentially.

The FLASH sequence used for the MPM protocol is a gradient and RF spoiled steady state gradient echo sequence. After an excitation, if the system has not yet relaxed back to the equilibrium, there is both longitudinal and transverse magnetization present. A subsequent excitation would therefore not result in the same signal intensity, as not all of the longitudinal magnetization has recovered. For human brain tissue, T1 values are of the order of 1000 ms at 3T (41). For M_0 to fully recover, such that the same signal intensity can be detected, several seconds would have to pass, increasing scan times beyond the clinically feasible. However, it is possible to drive the system to a steady state, where the same amount of magnetization is

recovered between excitations as is excited during an excitation, while the transverse magnetization is effectively spoiled (ideally, reduced to zero).

In this steady state, the signal amplitude can be described by the Ernst equation (42):

$$S = \rho \frac{sin\alpha \left(1 - e^{-TR/T1}\right) e^{-TE/T2^*}}{1 - cos\alpha \left(e^{-TR/T1}\right)} \quad \text{[II.34]}$$

where TR is the repetition time, the time between subsequent excitations, and TE is the echo time, or the time between an excitation, and the center of the subsequent readout gradient lobe collection. To ensure that no transverse components are present prior to excitation, additional spoiling, or crusher gradients are applied after all echoes have been collected (43).

RF spoiling is applied (44) by systematically incrementing the phase of the B1 field from excitation to excitation. Thus, any improperly crushed transverse magnetization is out of phase with that of subsequent excitations. In the 3D implementation of the FLASH sequence used in this thesis, gradient spoiling is applied on the readout axis, while the phase encoded gradients are rewound. Gradient and RF spoiling characteristics are optimized based on recommendations in the literature (45,46).

A single TR of a 3D FLASH sequence, as used in this thesis is shown in Figure II.3.

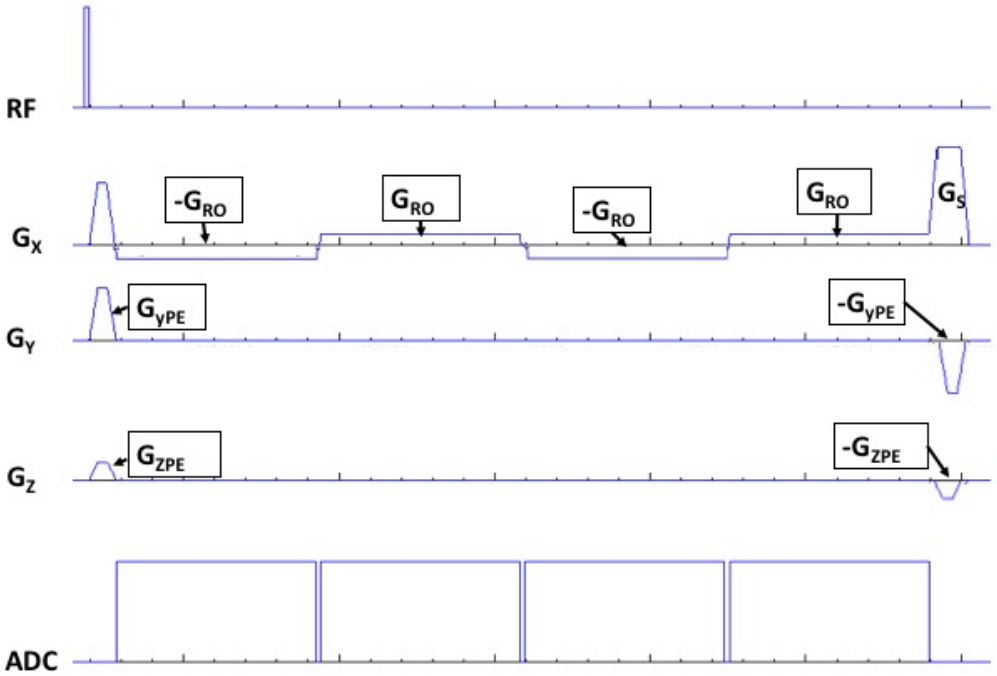

Figure II.3: A pulse sequence diagram showing one TR of a FLASH sequence with four echoes acquired consecutively, using a bi-polar readout gradient. The axes show the radiofrequency pulse, the three gradient directions, and the operation of the analogue-to-digital converter for data acquisition. Axes y and z are the phase encoded axes, and x is the frequency encoded, or readout gradient direction. By convention, gradients that traverse k-space in a positive direction are denoted as positive. On the phase encoded axes, gradients (G_{YPE} and G_{ZPE}) are played out to designate the k_y and k_z coordinates of this encoding step, referred to as pre-winding. On the x axis, a gradient is played out to move the system to k_{xmax}, and a readout gradient ($-G_{RO}$) is played out to traverse k-space in the x direction for k_{xmax} to $-k_{xmax}$, forming the first echo. An equal and opposite gradient (G_{RO}) is played out to traverse k-space in the positive x direction, forming the second echo. The process is repeated for the third and fourth echoes. After the fourth echo has been acquired, an additional spoiling gradient (G_S) is played out on the x axis, while on the phase encoded axes, re-winding gradients are played out ($-G_{YPE}$, $-G_{ZPE}$), setting the k_z and k_y coordinates to 0. To traverse the whole of k-space, the magnitude and direction of the phase encoding gradients is changed. Radiofrequency spoiling is achieved by changing the phase angle of the RF pulse from TR to TR. Note that during the thesis, typically 6 or 8 echoes were acquired.

II.5: Qualitative MRI

The majority of clinical scans are evaluated in a qualitative framework, where the diagnostic information is derived from image contrast. To appreciate the topic of this thesis, quantitative MRI, qualitative MRI has to be presented first.

The MRI-visible parameters of tissues, such as their spin density or relaxation times, are not identical (41,47–49), and may change due to healthy aging (50–53) or pathology (54,55). By carefully selecting the acquisition parameters, such as TR, TE and flip angle, the effect of one, or more of these differences in relaxation times, spin density, or other MR parameters, can be attenuated, which translates to a change in the contrast between tissues. This type of MR imaging is referred to as weighted imaging, and the resulting images as weighted images (in contrast to the quantitative maps discussed in this thesis). For simplicity, only the contrasts relevant to this thesis are discussed in detail.

A generalized signal equation for a system in the steady state, where the effect of flip angle has been discounted can be formulated as:

$$S = \rho\left(1 - e^{-TR/T1}\right)e^{-TE/T2^*} \qquad \text{[II.35]}$$

If echo times are chosen such that TE<<T2*, the contribution of the second exponential term is negligible, and the contrast between two tissues is primarily weighted by T1. Conversely, if TR>>T1, the contrast is weighted towards T2*. If both conditions are true, then the contrast is weighted primarily by spin density, illustrated in Figure II.4.

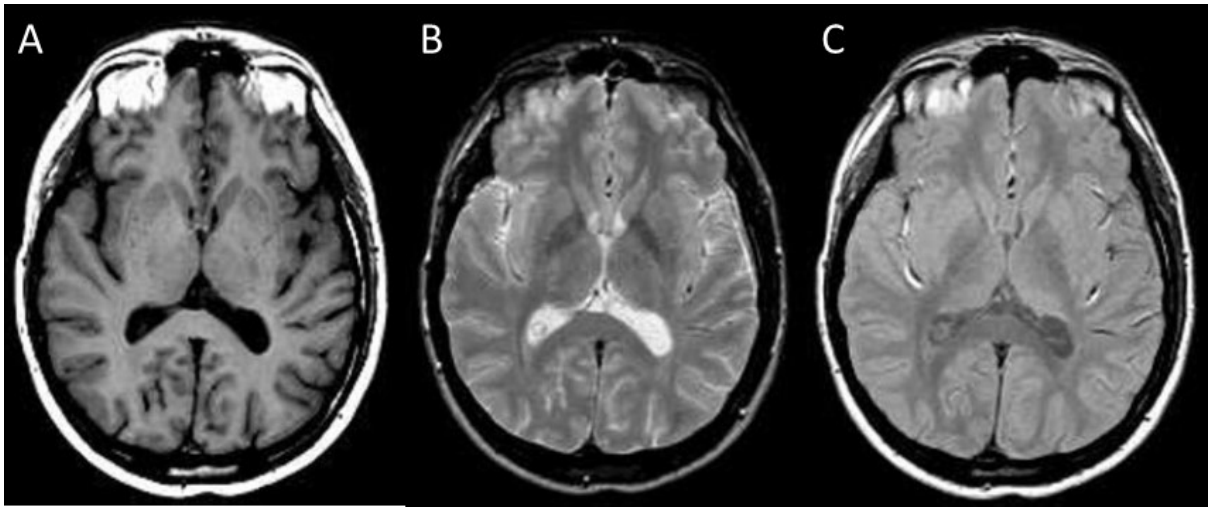

Figure II.4: The same anatomy, imaged with a T1-weighted (A), a T2-weighted (B), and a proton density weighted (C) sequence. Reproduced from (34)**.**

For the FLASH sequence, as used in the MPM protocol, the image contrast is manipulated by changing the flip angle for PD and T1 quantification (relaxometry), and by the application of an off-resonance saturation pre-pulse for magnetization transfer weighting. This is discussed in greater detail in sections II.7 and II.8.

II.6: Parallel imaging

As discussed in section II.3, all of k-space has to be sampled in order to reconstruct an image. For high-resolution images of the whole brain, this can result in very long scan times even for acquisitions with a short TR. As an example, if a standard 3D FLASH sequence, as used in the MPM protocol, with 1 mm resolution and whole brain coverage, were to be reconstructed from a fully sampled k-space, the total acquisition time would be:

$$\mathrm{T}_{acq} = \mathrm{N}_{PE1}\mathrm{N}_{PE2}\mathrm{TR}_{acq} = 240 \cdot 176 \cdot 25\, ms \approx 17.5\, min \qquad \text{[II.36]}$$

where N_{PE1} and N_{PE2} are the number of phase-encoding steps in the first and second phase encoded direction, respectively, and TR_{acq} is the TR of the sequence. T_{acq} is approximately 17.5 minutes, reducing clinical viability. Thus, the scanning procedure has to be accelerated.

This can be achieved by not acquiring certain k-space points, and exploiting redundancies and prior information to synthetize the missing data. Because the number and spacing of k-space points is inherently linked to the resolution and field of view of the final image, undersampling k-space, while maintaining the resolution results in an aliased image, as shown in Figure II.5.

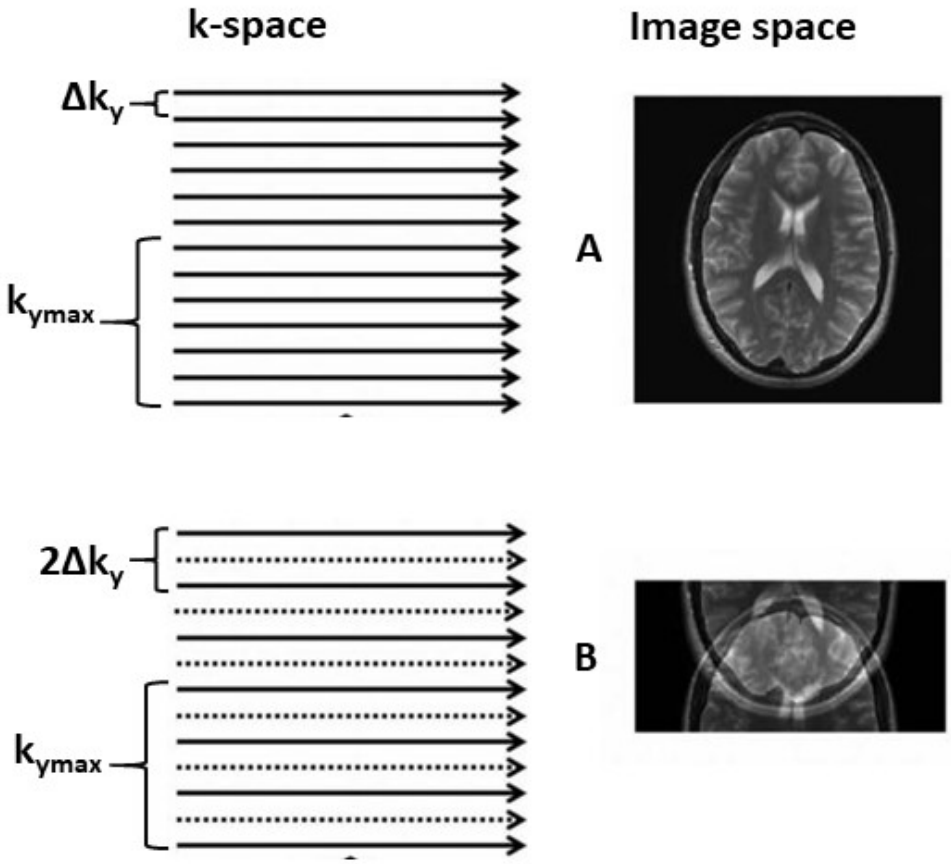

Figure II.5: K-space and image space for fully sampled (A) and undersampled (by a factor of 2) k-space. Keeping the image space resolution constant, the undersampling increases Δk, thus decreasing FoV, which results in a fold-over in image space. Adapted from (56)

This aliased image can be unfolded by exploiting the redundancies in MRI data acquired with multiple coils. If more than one coil is arranged around the imaged volume, then the detected signal intensity is the sum of the individual coil images (56–58):

$$S_i = \sum_j^{Nc} S_{i,j} = \sum_j^{Nc} C_{i,j}\rho_i \qquad \text{[II.37]}$$

where S_i is the combined detected signal coming from voxel i, $S_{i,j}$ is the signal coming from voxel I, as detected by coil j, $C_{i,j}$ is the receive sensitivity of coil j at voxel i, and ρ_i is the effective spin density of voxel i. In the k-space formalism, this multiplication is replaced by a convolution:

$$s_k = \sum_j^{Nc} c_{k,j} * \rho_k \qquad \text{[II.38]}$$

where s_k is the k-th k-space point, and c_{kj} is the Fourier-transform of C_{ij}

In the case of sub-sampled k-space, the signal of the aliased image is the signal of the un-aliased image, folded on top of itself, as illustrated in Figure II.6:

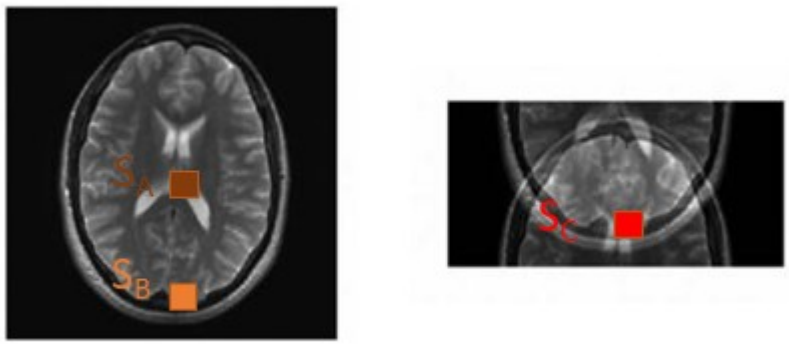

Figure II.6: The signal in the aliased voxel C, S_C is the sum of the signal at the un-aliased locations A and B, S_A and S_B

Exploiting the redundancy described in Equations II.37 and II.38 the signal can be unfolded, and a full image can be reconstructed. The two main methods to acquire and reconstruct accelerated images are Sensitivity Encoding (SENSE) (59) and Generalized auto calibrating partially parallel acquisition (GRAPPA) (60). In brief, SENSE unfolds the data in image space, while GRAPPA unfolds it in k-space.

In SENSE, the coil sensitivities are explicitly used in the unfolding algorithm:

$$\rho = (C^H \Psi^{-1} C)^{-1} C^H \Psi^{-1} \hat{S} \qquad \text{[II.39]}$$

where $(C^H C)^{-1} C^H$ is the pseudoinverse of the coil sensitivities, and $\hat{S}$ is the aliased image, and Ψ is the receiver noise matrix, estimated from noise data acquired in the absence of MRI signal. To obtain the coil sensitivities of C, low-resolution, full-FOV images are acquired with each individual coil, and a reference coil, typically the body receive coil of the scanner, as it can be assumed that its sensitivity profile is flat compared to the receive profiles of the local coils.

In this thesis, the acquired data were reconstructed using the GRAPPA formalism. In a k-space formalism, the effect of a non-uniform receive sensitivity is to smear out the original k-space information, such that the value of a k-space point can be estimated from that of its neighbors. If this pattern is known, then the k-space points that have not been acquired can be populated (60):

$$s_j(\mathrm{k}_y - \mathrm{m}\Delta\mathrm{k}_y) = \sum_{l=1}^{L} \sum_{0}^{N_b - 1} n(j, b, l, m) S_j(k_y - bR\Delta k_y) \qquad \text{[II.40]}$$

where $s_j(k_y\text{-}m\Delta k_y)$ is the k-space of coil j at locations $k_y\text{-}m\Delta k_y$, index l indexes the L coils, and index b counts through the blocks, or segmented areas, of k-space where the missing signal is synthetized. The weights of n(j,b,l,m) are calculated with the help of fully sampled autocalibration signal (ACS) lines. In this thesis, ACS lines are referred to as “reference lines”. A schematic is offered in Figure II.7.

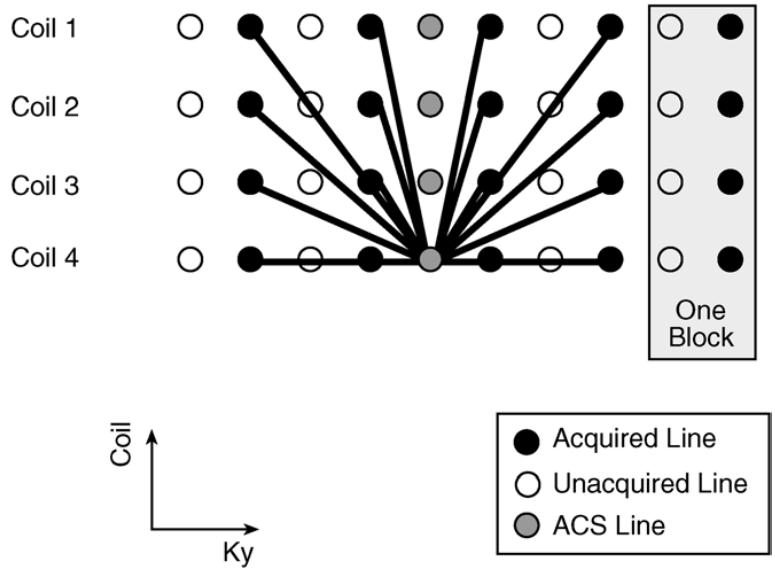

Figure II.7: A schematic representation of the GRAPPA reconstruction algorithm. For each ACS line (grey), for each coil, the weights corresponding to the acquired lines (black) are calculated. These weights are then applied to synthetize the skipped data in a blockwise fashion. Reproduced from (60)**.**

If parallel imaging is applied, the signal-to-noise ratio (SNR) of the resulting image is reduced, as less data is acquired. The resulting loss of SNR is $\sqrt{R}$, where R is the undersampling, or acceleration factor. However, additional SNR reduction can be observed:

$$SNR_R = \frac{SNR}{\sqrt{R}g} \qquad \text{[II.41]}$$

where SNR_R is the signal to noise ratio of the accelerated image, SNR is the signal to noise ratio of the unaccelerated image, and g is the g-factor, which describes the noise amplification depending on how well the inverse problems in Equation II.39 and II.40 are conditioned. This conditioning is dependent of the coil geometry, hence the name g, or geometry factor (61,62).

II.7: Quantitative MRI

In Section II.5, I presented the qualitative approach to interpreting MRI data. Here, the concept of quantitative MRI (qMRI), and the qMRI parameters mapped in this thesis are

introduced, along with several single-parameter and multi-parameter qMRI techniques, as well as their research and clinical use.

While qualitative MRI derives information based on contrast, quantitative MRI seeks to quantify the underlying physical properties, such as relaxation times or spin density, that produce the observed contrast (7,63). qMRI offers improvements upon qualitative imaging by providing data that is reproducible, and thus comparable across timescales, scanner types, and patients, while being sensitive to underlying changes in microstructure (such as the changes that influence relaxation times), and specific to these underlying changes. With the help of qMRI approaches, tissue-specific quantitative parameters can be used as biomarkers for the integrity and pathology of said tissue, providing valuable clinical insights (64).

Relaxation parameters can be quantified, or mapped, by sampling the signal intensity at various time points during relaxation. The gold standard for mapping the longitudinal relaxation time is inversion recovery (IR), in which an inversion RF pulse of 180° is used to flip the magnetization antiparallel with the B_0 field. After the inversion time (TI), a 90° pulse is played out to generate the MRI signal (65–67). Assuming TR>>T1:

$$S(TI) = S_0\left(1 - 2e^{-TI/T1}\right) \qquad \text{[II.42]}$$

By repeating this acquisition with different inversion times, T1 can be mapped. The IR method of T1 mapping is a time-consuming acquisition, as the measurement time is fundamentally dependent on the relaxation time, due to the assumption of TR>>T1, and T1 is typically several hundred milliseconds long. To overcome this limitation, multi-slice fast spin echo techniques are often used to image more than one slice for each inversion time. The value of T1 may also be mapped by measuring the signal intensity of the recovery described by Equation II.42 at different time points. This forms the basis of the Look-Locker approach to T1 mapping (65,68,69). Images acquired with different inversion times may also be combined to form quantitative maps of T1. One example of this approach is the magnetization-prepared gradient echo (MP2RAGE) method (70). If, instead of an inversion pulse of 180°, a saturation pulse of 90° is played out, T1 can be mapped using saturation recovery (71). In this thesis, T1 is mapped by an approach that is not based on signal recovery. The variable flip angle (VFA) method if T1 mapping is described in detail in Chapter II.8 (72).

The quantitative value of T1 (often expressed as a rate constant, R1=1/T1) is related to the macromolecular content of the tissue, the water content of the tissue, the presence of strongly paramagnetic materials, and other factors that chiefly influence the correlation time introduced in section II.2. Most commonly, quantitative T1 values are associated with the presence of macromolecules. For neurological applications, the most abundant macromolecule in the human brain is myelin, therefore the quantitative value of T1 has been used as a surrogate marker for myelination (25,73,74). In studies of pathology, this association

between T1 and myelin has been exploited in studies of multiple sclerosis (75,76), temporal lobe epilepsy (77), Alzheimer's disease (78), and schizophrenia (79). Outside neurological applications, several derivatives of the Look-Locker method have been used in cardiac imaging (80,81), to map the changes in the T1 value of the myocardium due to fibrosis (82), and cardiomyopathy (83).

The relaxation parameters of T2 or T2* can be mapped by acquiring a series of images where the difference in image intensity is governed by T2 or T2*. In practice, a set of images with different T2 or T2*-weighing are acquired using either a gradient echo or a spin echo sequence (84–86). In the method used during this PhD project, the rate constant of R2*=1/T2* was mapped, using a series of gradient echoes (19). T2* relaxation is influenced by the inhomogeneities in the magnetic field within a voxel, which are in turn related to the magnetic susceptibility of the local tissue. In neuroimaging, R2* has been used as a surrogate biomarker for iron content (87,88), due to the large magnetic susceptibility for iron, or for myelin (89,90), due to the susceptibility of the lipid bilayers. In patient studies, R2* has been used as a biomarker for brain iron content in neurodegenerative diseases such as Huntington's (91) and multiple sclerosis (92), and in healthy aging (50). However, R2* quantification may be confounded by an orientation dependence relative to the B_0 field (93), and by susceptibility artefacts (94). R2 quantification has seen widespread use in the assessment of the hippocampus in multiple sclerosis (9,10,86,95), in Alzheimer's disease (96,97), epilepsy (98,99), and stroke (100). R2 mapping has also been used to monitor intervertebral disk degeneration (101,102), and in spinal cord imaging (103). Outside neurological applications, T2 or T2* relaxation parameters have been used knee imaging to assess cartilage damage an osteoarthritis (104,105), and measure iron load in the liver (106–108) the kidneys (109), and the heart (108,110), and in clinical cardiac imaging studies (111,112) and practice (113).

As described by Equation II.16, the signal intensity of an MRI image is inherently linked to the proton density (PD) of the tissue, which can in turn be quantified (114–117). However, unlike relaxation rate mapping, the absolute signal intensity of the signal has to be taken into account. As this intensity is influenced by the receiver profile (Equation II.27) this additional weighting has to be taken into account either by modeling or measuring the receive field, or by providing an external signal intensity reference in the form of a pure water sample (94,118–120).In the method used in thesis, the contributions of the receive field are taken into account via modeling (121). As the signal intensity is linked to the density of NMR-visible hydrogen atoms, PD can be used as a biomarker for free water (122). In neurological clinical applications, proton density and brain water content has been used to characterize the effect of multiple sclerosis (123–126), ischemia (127), encephalopathy (128), brain tumors (118), and cervical myelopathy (129).

Not all protons in the tissue are found in free water. A separate, bound pool of protons can be found in the hydrate shells surrounding the macromolecular content of the tissue. This pool is generally not detectable using MRI, as the T2 of this pool is on the order of microseconds. However, a continuous exchange occurs between these two pools, through dipole-dipole interactions (130), or chemical exchange (131). By exploiting this exchange, the bound pool can be interrogated. For a given pool, T2 governs the spectral line width, the spread of frequencies around the resonance frequency of ω_0 where absorption occurs. The line width is proportional to 1/T2, thus, for the bound pool, spectral width is in the kHz range, as illustrated by Figure II.8. Using a tailored excitation pulse, that is played out not at ω_0, but with frequency offset, , this bound pool can be exclusively excited, and due to the exchange mechanisms, the strength of this magnetization transfer (MT) mechanism can be mapped (132–136).

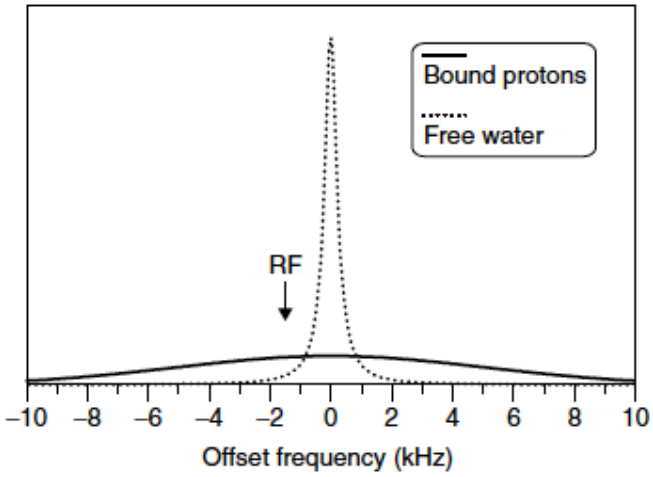

Figure II.8: The resonance frequency distribution around ω_0 for the two pools of an MT experiment. The RF pulse is applied off-resonance, exciting the bound pool, but not exciting the free pool. Reproduced from (7).

Several methods are available to characterize the MT mechanism, and quantify the size and exchange rates between the two pools (137–139). The quantification method used in this thesis is introduced in section II.8.

As magnetization transfer is related to the macromolecular content of the tissue, MT can be used as another surrogate biomarker for myelin content (140,141). This relation between the MT effect and myelin content is used to evaluate multiple sclerosis lesions (142,143), response to therapy in glioblastoma patients (144,145), and measure the integrity of the spinal cord in demyelinating diseases (146,147).

In this thesis, the four quantitative markers (R1, R2*, PD, MT) are used. However, these are by means a comprehensive list. Without further discussion, it must be noted that quantitative markers can be derived from diffusion weighted imaging (148), susceptibility weighted imaging (149), arterial spin labeling (150), or spectroscopic imaging (151).

Quantitative imaging sequences may be used to map a single quantitative parameter, using the techniques described above. However, using a careful selection of imaging parameters, several quantitative parameters may be mapped during a single imaging session. In this approach, several scans are acquired, and then combined to yield multiple maps, exploiting the synergies between the acquired scans. While an in-depth description and comparison of these methods is beyond the scope of the thesis, several approaches are briefly summarized below.

In the DESPOT technique (152,153), the relaxation parameters of R1 and R2 are quantified. Longitudinal relaxation is mapped using a VFA approach, using spoiled gradient echo scans acquired with different flip angles, while transverse relaxation parameter is calculated from the signal intensity of steady-state free precession scans acquired with different flip angles, and the R1 parameters calculated using the VFA approach. The relaxation parameters of multiple tissue compartments, such as the free and bound water pool, are mapped in an extension of the original technique, multi-compartment DESPOT (154,155). The DESPOT technique has been used in temporal lobe epilepsy (156,157), and to quantify infant brain myelination (158).

In the QRAPTEST (119) approach R1, R2*, and PD are mapped in a single sequence. A dual-echo gradient echo saturation recovery scan is performed. R1 is calculated from the saturation recovery signal, while R2* is derived from the signal intensity of the first and second echoes, and proton density is calculated from the signal intensity after correction for T1 and T2* decay, as well as the receiver profile. In a modified version of the approach, QRAPMASTER (159), a spin echo sequence is used instead of a gradient echo sequence. This method, in which R1, R2, and PD are mapped, is aimed at clinical usage, where it has been shown to improve tissue segmentation in patients with multiple sclerosis and Alzheimer's disease (160,161).

The properties of the steady-state signal are exploited in the dual-echo steady-state relaxometry, DESS (162), and triple-echo steady state relaxometry, TESS (163) methods of quantitative imaging. In the DESS approach, R1, R2 and proton density are mapped, while in the TESS approach, R1 and R2 are mapped. Both methods rely on a careful selection of imaging parameters, such that consecutive echoes are weighted differently with regards to R1 and R2, and the relaxation parameters can be calculated by combining these echoes. TESS has been applied to map R2 in healthy brains (164), and in pathologic knee joints (165).

A multi-echo MP2RAGE sequence is used in a recently published method to map the relaxation parameters of R1 and R2*, as well as magnetic susceptibility (166).

In the magnetic resonance fingerprinting (MRF) approach, TR and flip angle are adjusted on a TR-by-TR basis, unlike in other qMRI techniques, and k-space is covered in a highly under sampled, non-Cartesian fashion (167). While the signal intensity of each voxel

varies greatly between TRs, this evolution is determined by the underlying tissue parameters. The signal can be simulated, based on the Bloch equations, for a wide range of tissue parameters, and the measured signal evolution can be matched, like a fingerprint, to a specific set parameters using a dictionary approach. Relaxation parameters, as well as proton density, are mapped during MRF. MRF techniques have undergone significant development (168,169), and have been deployed in tumor imaging (170), cerebral vascular imaging (171), and to measure age-rated changes in the brain (172).

The qMRI method used to acquire data presented in this thesis is detailed in the next section.

II.8: The multi-parameter mapping protocol

During the PhD project, data were acquired using the qMRI method called multi-parametric mapping (MPM) protocol. As the name implies, the MPM protocol aims to acquire not only a single parametric map, but a series of maps. The MPM protocol has been shown to produce robust and reliable data (19) and has been used in multiple clinical (173,174) and neuroscientific studies, e.g. in aging studies (21,22), morphometric studies (175,176), and studies of myeloarchitecture (24,25).

For the MPM protocol, three 3D FLASH (39) scans are acquired consecutively. The signal of these FLASH scans can be described using the Ernst equation (42), and the quantitative maps are derived by a rational approximation (17,18) :

$$S = \rho \sin\alpha \frac{\left(1 - e^{-TR/T1}\right)}{\left(1 - e^{-TR/T1} \cdot cos\alpha\right)} \quad \text{[II.43]}$$

where S is the detected signal, ρ is the effective spin density, and α and TR are the flip angle and the repetition time, respectively.

For the short TR regime, that is for TR<<T1, the exponential terms can be approximated:

$$e^{-TR/T1} \cong \left(1 - {}^{TR}/_{T1}\right) \quad \text{[II.44a]}$$

$$S \cong \rho \sin\alpha \frac{TR/T1}{1 - cos\alpha(1 - TR/T1)} \quad \text{[II.44b]}$$

The signal equation can be transformed from a trigonometric function of α into a rational function of the substitute variable, τ,

$$S \cong \rho 2\tau \frac{TR/T1}{\frac{(1-t^2)TR}{T1} + 2t^2} \quad \text{[II.45]}$$

Using the substitution of:

$$\tau = \tan\left({}^{\alpha}/_{2}\right) \qquad \text{[II.46]}$$

For small flip angles, $\tan\alpha \approx \alpha$, thus the expression can be further simplified:

$$S \cong \mathrm{p}\alpha \frac{TR/T1}{\frac{\left(1-{}^{\alpha^2}/_{4}\right)TR}{T1} + {}^{\alpha^2}/_{2}} = \mathrm{p}\alpha \frac{TR/T1}{\frac{TR}{T1} + {}^{\alpha^2}/_{2} - \frac{\alpha^2 TR}{4T1}} \qquad \text{[II.47]}$$

For small flip angles and short TR the third term in the denominator can be neglected, and the signal can be approximated by:

$$S \cong \mathrm{p}\alpha \frac{TR/T1}{\frac{TR}{T1} + {}^{\alpha^2}/_{2}} \qquad \text{[II.48]}$$

The two unknowns in Equation II.48 are the relaxation time T1, and the spin density, ρ. Using two acquisitions with different flip angles, the relaxation time and the spin density can both be calculated in a variable flip angle framework:

$$S_A \cong \rho\alpha_A \frac{TR/T1}{\frac{TR}{T1} + {}^{\alpha_A{}^2}/_{2}} \qquad \text{[II.49a]}$$

$$S_B \cong \rho\alpha_B \frac{TR/T1}{\frac{TR}{T1} + {}^{\alpha_B{}^2}/_{2}} \qquad \text{[II.49b]}$$

$$T1 \cong 2TR \frac{{}^{S_A}/_{\alpha_A} - {}^{S_B}/_{\alpha_B}}{S_B\alpha_B - S_A\alpha_A} \qquad \text{[II.50a]}$$

$$\rho \cong \frac{1}{TR_A} \frac{S_A\alpha_A}{S_B\alpha_B - S_A\alpha_A} \left({}^{\alpha_B}/_{\alpha_A} - {}^{\alpha_A}/_{\alpha_B}\right) \qquad \text{[II.50b]}$$

The effect of magnetization transfer can be characterized in the same framework by extending a dual excitation description:

$$S = \rho\sin\alpha_1 \frac{\frac{TR}{T1} - (1-cos\alpha_2)\frac{TR_1}{T1}}{1 - cos\alpha_1 cos\alpha_2\left(1 - \frac{TR}{T1}\right)} \qquad \text{[II.51]}$$

where α_1 and α_2 are the flip angles of the first and second consecutive excitation, respectively, TR_1 and TR_2 are the repetition times of the consecutive excitations, and $TR=TR_1+TR_2$. Short TR regime approximation has already been applied in Equation II.51.

Applying the substitution and small flip angle approximation described for the single-excitation case:

$$S = \rho\sin\alpha_1 \frac{\frac{TR}{T1}}{(1-cos\alpha_1) + {}^{\alpha_2^2}/_{2} + \frac{TR}{T1}} \qquad \text{[II.52a]}$$

$$S = \rho\alpha_1 \frac{\frac{TR}{T1}}{\alpha_1^2/_2 + \alpha_2^2/_2 + \frac{TR}{T1}} \quad \text{[II.52b]}$$

Equation II.52b describes the behavior of a system with saturation pulses. The effect of the saturation, the signal loss due to the second excitation, is encapsulated by the additional term of $\alpha_2^2/2$ in the denominator. The effect of magnetization transfer can be described similarly, by considering the exchange with the bound proton pool as a saturation step. In the MPM protocol, this magnetization transfer saturation, referred to as MT in the thesis, is quantified.

$$S_{MT} \cong \rho\alpha \frac{\frac{TR}{T1}}{\frac{TR}{T1} + \delta + \alpha^2/_2} \quad \text{[II.53]}$$

where S_{MT} is the detected signal for a FLASH scan, with flip angle α, with a magnetization transfer pre-pulse, and δ is the magnetisation transfer saturation. If T1 and ρ are known, based on Equations 50, then the δ can be calculated.

During the PhD project, multi-echo FLASH scans, in addition to scans mapping the B_0 and B_1 fields, were used to acquire the signals described in the Equations II.43-II.53. The typical acquisition and processing pipeline is detailed below. In order of acquisition, the B_0 and B_1 fields were mapped first.

The flip angles described in equations II.43 to II.53 are assumed to be spatially constant. In practice, this is not the case, as the B_1 transmit field is inhomogeneous, and it is necessary to map the transmit field (177).

In the MPM protocol, as used in this thesis, the B1 transmit field was mapped using a series of spin and stimulated echo EPI images. During the PhD project, the acquisition parameters of the 3D EPI sequence were: FoV=256x240x176 mm^3, 4mm isotropic resolution, echo time for spin echoes: 37.06 ms, echo time for stimulated echoes: 37.06 ms, mixing time: 31.2 ms, TR=500 ms. To maximise the precision of the estimation, eleven nominal flip angels were used, from 65° to 115°, in steps of 5°, and for each voxel, the five SE-STE pairs with the highest SE signal intensity were used. To account for the distortions in the B_0 field, additional B0 mapping was carried by a 2D dual-echo gradient echo sequence, acquired with the following parameters: FoV=192x192 mm^2, 64 slices of slice thickness 2 mm with a 1mm gap, in-plane resolution of 3 mm, echo times of 10/12.46 ms, TR of 1020 ms, and a nominal flip angle of 90°. The B1 mapping method is described in detail in (178). Total acquisition time of the B1 mapping method was approximately 5 minutes.

Following the mapping of the transmit field, three 3D FLASH scans are acquired. During the PhD project, unless otherwise noted, the common acquisition parameters for the three scan were FoV=256x240x176 mm^3, and an isotropic resolution of 1mm^3, TR=25 ms, TE

of the first echo=2.2 ms, echo spacing 2.3 ms. Differential contrast was achieved by varying the flip angle, and applying an off-resonance pre-pulse. Unless otherwise noted, during the PhD project, a primarily magnetization-transfer weighted sequence (MTw scan), using an off-resonance pulse of a Gaussian shape, 4ms duration, a nominal flip angle of 220°, and 2kHz off-resonance, and a relatively low flip angle (6 degrees, unless otherwise noted), was acquired first, followed by a proton density weighted sequence (PDw scan), acquired using a relatively low flip angle (6 degrees, unless otherwise noted), followed by a primarily T1 weighted sequence (T1w scan), acquired using a relatively high flip angle (21 degrees unless otherwise noted). Unless otherwise noted, 6 echoes were acquired for the MTw scan, and 8 for the PDw and T1w scans.

After the B_1 and B_0 maps, and the three weighted FLASH images were acquired, four quantitative maps were calculated in the following way (17–19).

From the relative signal intensities of the distortion-corrected stimulated and spin echo EPI images of the B_1 mapping sequence, the flip angle can be calculated by (179):

$$\alpha_{local} = \arccos\left(\frac{S_{STE}e^{TM/T1}}{S_{SE}}\right) \qquad \text{[II.54]}$$

where S_{STE} and S_{SE} are the signal intensities of the stimulated and spin echoes, respectively, and TM is the mixing time, the duration between RF pulses used to generate spin echoes and RF pulses used to generate stimulated echoes. To optimise the SNR of the resulting B1 map, the five spin echo- stimulated echo pairs corresponding to the highest spin echo signal intensity were summed in a sum of squares fashion to produce S_{STE} and S_{SE} for each voxel.

Maps of the effective transverse relaxation rate (R2*) was calculated from the eight echoes of the PDw scan, by log-linearization of the signal decay described by Equation II.55:

$$S_{PD}(TE) = S_{PD}(0)e^{-R2^*TE} \qquad \text{[II.55]}$$

where $S_{PD}(TE)$ is the signal intensity of PDw scan at echo time TE, and $S_{PD}(0)$ is the signal intensity of PDw scan at time 0. The log-linear fit aims to minimise the following error term:

$$\varepsilon = \sum_{nE=1}^{nE_{max}} \left[\left(\ln\left(S_{PD}\left(TE(nE)\right)\right)\right) - R2^*TE(nE) - \left(\ln\left(S_{PD}(0)\right)\right)\right]^2 \qquad \text{[II.56]}$$

where index nE counts through the number of echoes. An exemplary R2* map is shown in Figure II.9.

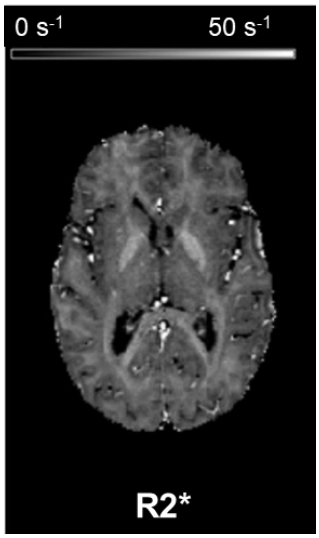

Figure II.9: An exemplary map of the effective transverse relaxation rate, R2*, calculated from PD FLASH echoes. Adapted from (19)

This approach can be extended to include not just the PDw scan, but all three contrasts, in the ESTATICS approach (180):

$$\varepsilon = \sum_{k=1}^{3} \sum_{nE=1}^{nE_{max}} \left[\left(\ln\left(S_k\left(TE(nE)\right)\right) - R2^{*} TE(nE) - \left(\ln\left(S_k(0)\right)\right) \right]^2 \qquad \text{[II.57]}$$

where index k counts through all three contrasts (T1w , PDw, MTw).

To increase the SNR of the quantitative maps (181), the arithmetic mean of the first six echoes for each contrast is used in the following calculations, denoted $\overline{S_{PD}}$, $\overline{S_{T1}}$ and $\overline{S_{MT}}$ for the PDw T1w, and MTw scans, respectively. As a result, these three mean images all have an effective echo time of approximately 8 ms, depending on the exact echo timing used. The mean images of $\overline{S_{T1}}$ and $\overline{S_{MT}}$ are co-registered (182) to $\overline{S_{PD}}$.

The longitudinal relaxation rate, as shown in Figure II.10, is calculated from $\overline{S_{T1}}$ and $\overline{S_{PD}}$:.

$$R1 = \frac{1}{2}\psi^2 \frac{\overline{S_{T1}}\alpha_{T1}/TR_{T1} - \overline{S_{PD}}\alpha_{PD}/TR_{PD}}{\overline{S_{PD}}/\alpha_{PD} - \overline{S_{T1}}/\alpha_{T1}} \qquad \text{[II.58]}$$

where ψ is the ratio of the local lip angle and the nominal flip angle, in other words, the scaled B1+ map.

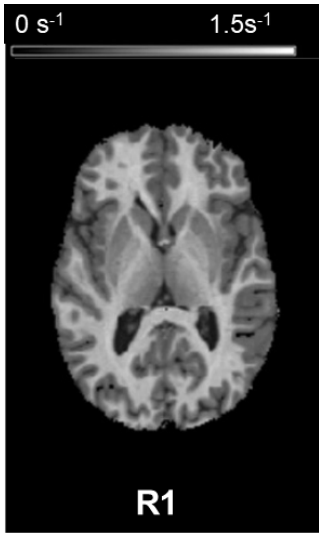

Figure II.10: An exemplary map of the longitudinal relaxation rate, R1. Adapted from (19)

An un-normalized proton density map is derived from the R1 map and the signal intensity of T1w scan:

$$\mathrm{P} = \frac{\overline{S_{T1}}\alpha_{T1}}{2\ R1TR_{T1}} + \frac{\overline{S_{T1}}}{\alpha_{T1}} \qquad \text{[II.59]}$$

The value of P in Equation II carries, as shown in II.7, receive field effects. These are removed from P by estimating the bias field (121,183), and re-scaling the values of P such that in white matter, the effective proton density, PD*, is 69p.u. relative to pure water in line with literature reports (7). The nomenclature and symbol of effective proton density, PD* are used to indicate that this value is calculated from data with a non-zero effective echo time, thus, a residual R2* weighing is imposed on the proton density values. An exemplary PD* map is shown in Figure II.11.

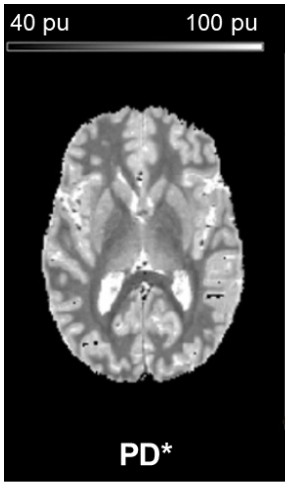

Figure II.11: An exemplary map of the effective proton density, PD*. Adapted from (19)

Magnetisation transfer saturation is calculated using the un-normalized proton density map (18,184):

$$\delta = \frac{\mathrm{P}\overline{S_{MT}}\alpha_{MT}}{\overline{S_{MT}}TR_{MT}/_{R1} - {\alpha_{MT}}^2/_2} \quad \text{[II.60]}$$

To take into account residual inhomogeneity effects of the transmit field, the saturation value is corrected by (185). An exemplary map of the corrected value is shown in Figure II.12:

$$\delta_{corr} = \frac{\delta(1-0.4)}{(1-0.4\psi)} \quad \text{[II.61]}$$

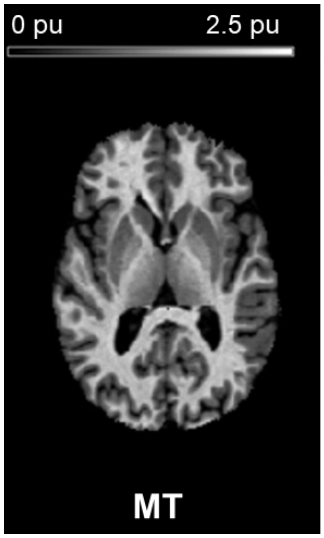

Figure II.12: An exemplary map magnetisation transfer saturation, MT. Adapted from (19)

II.9 Motion detection and correction in MRI

MRI is a non-instantaneous technique of image acquisition, and is therefore susceptible to motion during scanning. A full overview of all motion types and all detection and correction methods is outside the scope of this thesis. Here, I only summarize the effect of rigid bulk head motion, and the correction methods developed to address it (186–188).

The impact of rigid head motion can be understood by examining the relationship between motion in real space, and its manifestation in k-space. Image space and k-space form a Fourier pair, thus translations in real space result in a phase offset in k-space, and rotations in real space result in a rotation in k–space (Figure II.13):

$$F[\rho(x_0 + \Delta x, y_0 + \Delta y)] = \mathrm{s}(\mathrm{k}_x, \mathrm{k}_y)\mathrm{e}^{-i2\pi k_x \Delta x}\mathrm{e}^{-i2\pi k_y \Delta y}$$
$$= F[\rho(x_0, y_0)]\mathrm{e}^{-i\Delta\varphi} \quad \text{[II.62a]}$$

$$\Delta\varphi = 2\pi(k_x \Delta x + k_y \Delta y) \quad \text{[II.62b]}$$

where F denotes the Fourier transform, $\Delta x + \Delta y$ is the translation in real space, and $\Delta\varphi$ is the phase ramp in k-space imposed by this translation.

$$F[A\rho(x_0, y_0)] = \mathrm{As}(\mathrm{k}_x, \mathrm{k}_y) \quad \text{[II.63a]}$$

$$A = \begin{bmatrix} \cos\theta & -sin\theta \\ \sin\theta & \cos\theta \end{bmatrix} \quad \text{[II.63b]}$$

where A is the rotation matrix describing a counter-clockwise rotation by angle θ.

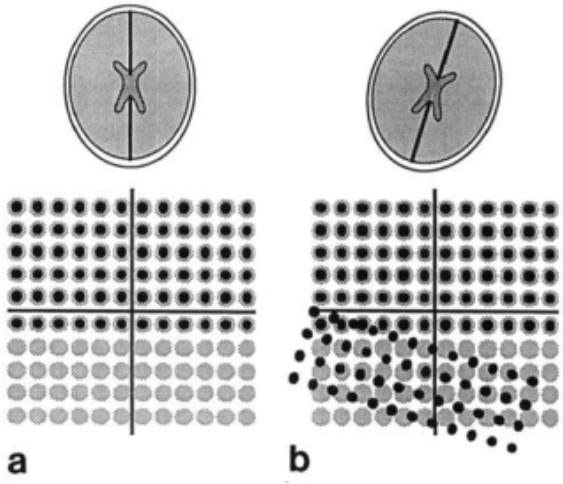

Figure II.13: A schematic representation of the effect of rotation in real space on k-space. A rotation during the acquisition results in some k-space frequencies that would have been sampled (grey in a) not being sampled at all (b), while their respective k-space energy is spuriously attributed to other frequencies (grey dots covered by black dots in b). Adapted from(189)

As a result of these properties, a motion in real space results in the mis-allocation of spatial frequency components in k-space. This mis-allocation can result in many types of image distortions, or artefacts, including blurring (due to a loss of high spatial frequency k-space points), or ringing (due to the overrepresentation of a spatial frequency). Motion artefacts can significantly hinder image analysis and processing (190–192), and may lead to repeat scanning, at a significant cost (16).

To be able to correct for motion in MRI, the extent of this motion must first be known. Motion detection methods applied in MRI can broadly be categorized as those that track the motion of tissue, and those that track some external marker attached to the tissue. This external marker may be tracked optically (193–198), or via the changes in the magnetic field, as is the case with NMR probes (199–201). While external tracking methods have a proven

track record, they suffer from two major drawbacks, the issue of marker fixation, as a loosely fitted marker results in a mismatch between the measured position and the position of the brain, and an extensive need for equipment.

Motion of the tissue may be inherently tracked using modifications of the sequence. In navigator techniques, small sections of the sequence are designed to provide positional information. Depending on the degrees of freedom measured by the navigator echo, motion can be detected along one dimension (for example the motion of the diaphragm due to motion (202)), two dimensions (203–206), or for all six degrees of freedom of a rigid body in three dimensions (207–211). A one dimensional navigator is shown in Figure II.14.

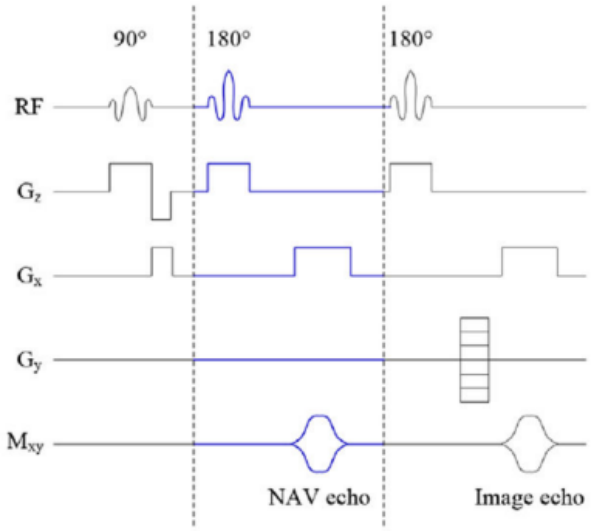

Figure II.14: A simple navigator using signal encoding (projection) along the x axis. Adapted from (188)

In the navigator techniques introduced above, the signal of the navigator echo is encoded along one or more spatial directions. In recent years, advanced navigator techniques have been developed that aim to detect motion without the need for spatial encoding, but based on the multi-channel detection of a FID signal (212), or in the changes of the coil characteristics (213,214).

If data is acquired as a series of images, then motion information can be derived from the images themselves, using the co-registration information (215,216). Such approaches are typically deployed in functional (217) or diffusion-weighted MRI, where a series of 2D or 3D EPI images are acquired in quick succession.

An ideal motion detection technique would be one that requires no extensive equipment, and one that requires no additional scan time. In Chapter V, work carried out towards such a navigator is presented.

Another way of classifying motion detection and correction methods is to divide them into prospective and retrospective motion correction methods. In prospective methods, motion information is used to adjust the imaging field of view during the acquisition, according to the detected motion (186,218–220), thus ensuring that the acquired signal is not mis-allocated. In retrospective approaches, the effect of motion on the raw data is compensated during reconstruction (221–223).

II.10 General linear models

In Chapter V, a novel navigator technique is introduced, and analysed in a general linear model (GLM) framework. Here, a short introduction to the GLM framework is given (224,225).

An interrogated linear system can be characterized by the measurable response, which can be expressed as the linear combination of known properties of the system, assuming a perfect measurement:

$$y = \sum_{i=1}^{N} \beta_i x_i \qquad \text{[II.64]}$$

where x_i are the N known properties of the system, β_i are the parameters of interest,. The measurement can be repeated many times, and the resulting linear system of equations can be expressed in matrix form:

$$X\beta = Y \qquad \text{[II.65]}$$

where Y is the column vector of K independent observations, X is a matrix of the K-by-N properties (one row for each measurement, and one column for each parameter), and β is a column vector of the N parameters. If the β matrix were known, the response of the system to any arbitrary excitation could be calculated, and the system could be characterised in full.

To obtain a generalized model of the system, an estimate for β, $\hat{\beta}$ must be found such that the following error term must be minimized:

$$\varepsilon = \sum_{k=1}^{K} \left(Y_k - x_{k1}\widehat{\beta_1} - \ldots - x_{kN}\widehat{\beta_N}\right)^2 \qquad \text{[II.66]}$$

where ε is a column vector with length K. The error term is minimal if its derivative with regards to any given $\widehat{\beta_\iota}$ is zero:

$$\partial\varepsilon / \partial\widehat{\beta_\iota} = 0 \qquad \text{[II.67a]}$$

$$\sum_{k=1}^{N} -x_{k,i}\left(Y_k - x_{k1}\widehat{\beta_1} - \ldots - x_{kN}\widehat{\beta_N}\right) = 0 \qquad \text{[II.67b]}$$

$$\sum_{k=1}^{N} x_{k,i} Y_k = \sum_{k=1}^{N} x_{k,i} \left(x_{k1}\widehat{\beta_1} + \ldots + x_{kN}\widehat{\beta_N} \right) \quad \text{[II.67c]}$$

As this holds true for any given i, Equation can be rewritten as:

$$\mathrm{X}^T\mathrm{Y} = (\mathrm{X}^T X)\hat{\beta} \quad \text{[II.68]}$$

Thus, the general model of the system, $\hat{\beta}$ can be obtained by solving the inverse problem of:

$$(\mathrm{X}^T X)^{-1}\mathrm{X}^T\mathrm{Y} = \hat{\beta} \quad \text{[II.69]}$$

In practice, the inverse problem is ill-posed, in other words, the condition number of X is high. For example, the data points are not measured perfectly, but with some noise:

$$\breve{Y} = Y + \breve{e} \quad \text{[II.70]}$$

where Y are the observations without error, and $\breve{e}$ is the error vector, indicating measurement noise. The estimate of β obtained using this noisy measurement is:

$$(\mathrm{X}^T X)^{-1}\mathrm{X}^T\breve{\mathrm{Y}} = (\mathrm{X}^T X)^{-1}\mathrm{X}^T(Y + \breve{e}) = \hat{\beta} + (\mathrm{X}^T X)^{-1}\mathrm{X}^T\breve{e} \quad \text{[II.71]}$$

This estimate is typically dominated by the propagated noise of $(\mathrm{X}^T X)^{-1}\mathrm{X}^T\breve{e}$, and is thus both unstable and not informative of β. Regularization methods can be used to address this problem. In regularization approaches, additional terms are introduced into the error term ε, in order to penalize large, and unstable solutions.

In this thesis, Tikhonov regularisation is used (226), in which an additional term is added into the least squares expression:

$$\varepsilon = \sum_{k=1}^{K} \left(Y_k - x_{k1}\widehat{\beta_1} - \ldots - x_{kN}\widehat{\beta_N} \right)^2 + \sum_{k=1}^{K} (\lambda x_k)^2 \quad \text{[II.72]}$$

where λ is the regularisation parameter. If λ is too large, the error term is dominated by it, and the estimated $\hat{\beta}$ will tend to zero. If λtoo small, the error term remains unregularised, and a large, unstable solution is not penalized. The optimal λ value can be determined by the L-curve approach, comparing the solution to the error term (226).

Chapter III: Correcting for inter-scan motion

III.1: Introduction:

The multi-parameter mapping (MPM) protocol differs from conventional, qualitative approaches in that multiple scans are acquired, and data are combined to produce quantitative maps. The MPM protocol is thus sensitive not only to motion occurring within a scan (intra-scan motion), as will be addressed in Chapters IV and V, but also motion occurring between scans (inter-scan motion). This Chapter investigates the impact of inter-scan motion on the quantitative values and develops correction methods to compensate for this type of motion.

As the vast majority of MRI applications, research or clinical, are single-scan approaches, inter-scan motion has not been addressed to the same depth as intra-scan motion. One common approach is to co-register sequentially acquired scans using 3D affine co-registration methods, to achieve spatial correspondence between the scans (227). This method is reviewed in more depth in the Theory section of this chapter (section III.2). As an alternative approach, a navigator method has been used to monitor for inter-scan motion in a clinical framework (228). One method involving inter-scan motion proposed to address intra-scan motion occurring during long acquisitions by splitting them into several shorter ones, thus transforming intra-scan motion into inter-scan motion, which was addressed via co-registration (229). It is important to note that all these methods were developed for conventional, contrast-weighted MRI acquisitions.

By contrast, several quantitative MRI methods combine data from multiple scans acquired in the same session. For example, in a variable flip angle framework (VFA) (230,231), which is used e.g. in the DESPOT1/2 (232) and MPM methods (17,19), the longitudinal relaxation rate (R1) is calculated from two scans, thus making it susceptible to inter-scan motion.

In the VFA approach the main mechanism by which inter-scan motion affects the calculated quantitative values relates to the receive field of multi-channel radio-frequency head coils. Data acquired with such coils shows an additional signal intensity modulation, corresponding to the receive sensitivity field of the head coil. As the head moves to a different position due to inter-scan motion, the modulation pattern changes, leading to a difference in estimated quantitative values. If this field could be estimated, its impact could be corrected for. This idea forms the basis for the study presented in this Chapter. The study is divided into two halves. First, efforts to evaluate and use pre-existing methods are presented, while in the second part of this Chapter, a novel correction method is described.

The main text and results of this Chapter are based on work published during the PhD project with Daniel Papp as first author (233).

III.2: Theory

III.2.1: The effect of inter-scan motion on the receive field and detected signal intensity

If a multi-channel RF coil is used to acquire MRI data, the detected signal will have a spatial variation in intensity imposed upon it, related to the sensitivity of the receive coil. This effect is best described in a coordinate system fixed to the brain:

$$S(r) = C(r) \cdot S_0(r) \quad [III.1]$$

where r is the spatial position in 3D space, S(r) is the detected signal intensity, C(r) is the magnitude of the combined receive sensitivity of the multi-channel head coil at position r, and $S_0(r)$ is the signal intensity at position r in the absence of modulation. $S_0(r)$ is driven by the anatomy, and the acquisition parameters.

In such a frame of reference, the impact of motion within the receive sensitivity field is easily apparent. Let scan A be the first of a series of two scans, scans A and B. The acquired signal intensity will be:

$$S_A(r) = C(r) \cdot S_{0,A}(r) \quad [III.2]$$

where $S_A(r)$ and $S_{0,A}(r)$ are the detected and unmodulated signal intensities of this scan, respectively. Let scan B be the second scan in the series, acquired after a movement of Δr, and with a different contrast than scan A. After scan B has been co-registered to scan A, the signal intensity of scan B will be:

$$S_{RB,B}(r, r') = C(r') \cdot S_{0,B}(r) \quad [III.3a]$$

$$r' = r + \Delta r \quad [III.3b]$$

$S_{RB,B}(r,r')$, the detected signal intensity of scan B after rigid body motion correction to scan A, and C(r') is the detected signal intensity of scan B after rigid body motion correction to scan A, Δr is the difference in position between the two scans, C(r') is the magnitude of the combined receive sensitivity of the multi-channel head coil at position r'. $S_{0,B}(r)$ is the unmodulated signal intensity of scan B, determined by anatomy and acquisition parameters, and crucially, not equivalent to $S_{0,A}(r)$.

In Equations III.2 and III.3a, the part of the detected signal that is driven by the anatomy and acquisition parameters, $S_{0,A}(r)$ and $S_{0,B}(r)$ are spatially matched, and, for example if the flip angle differed between the two, these could be used in a VFA framework to quantify R1.

However, $S_{RB,B}(r,r')$, the detected signal intensity of scan B, is differently modulated by the receive sensitivity than $S_A(r)$, as illustrated in Figure III.1a.

This illustrates that rigid body motion correction does not account for the difference in modulation by the receive sensitivity. However, if C(r) was known at each position, it could be corrected for via division. This correction is illustrated in Figure III.1, and detailed in the next section.

III.2.2: Correction for the effect of inter-scan motion

In addition to rigid body motion correction, the position, and thus inter-scan motion dependent contributions of the receive sensitivity field, have to be taken into account. This can be achieved by measuring C(r) prior to each scan. It can be assumed that, over the extent of the head (approximately 20 centimeters), the receive sensitivity of the body coil is constant (59). If the same anatomy is imaged, using the same acquisition parameters, by both the multi-channel head coil and the body coil, then, in the absence of inter-scan motion, the ratio of the two receive sensitivity fields can calculated:

$$S_{HC}(r) = C(r) \cdot S_0(r) \quad \text{[III.4a]}$$

$$S_{BC}(r) = C_{BC} \cdot S_0(r) \quad \text{[III.4b]}$$

$$\beta(r) = S_{HC}(r)/S_{BC}(r) = C(r)/C_{BC} \quad \text{[III.4c]}$$

where $S_{HC}(r)$ and $S_{BC}(r)$ are the signal detected by the multi-channel head coil and the body coil, respectively, C_{BC} is the magnitude of the receive sensitivity of the body coil, which is assumed to be constant, C(r) is the magnitude of the combined receive sensitivity of the head coil, and $S_0(r)$ is the signal dependent on the anatomy and acquisition parameters.

Since C_{BC} is constant, β(r) is the receive sensitivity of the head coil, divided by a constant. β(r) can be used to remove the receive sensitivity dependent modulation from Equation III.3a:

$$S_{RB+SC,B}(r,r') = \frac{C(r') \cdot S_{0,B}(r)}{\beta(r')} = \frac{C(r') \cdot S_{0,B}(r)}{\frac{C(r')}{C_{BC}}} \quad \text{[III.5a]}$$

$$S_{RB+SC,B}(r,r') = S_{0,B}(r) \cdot C_{BC} = S_{RB+SC,B}(r) \quad \text{[III.5b]}$$

where $S_{RB+SC,B}(r,r')$ is the detected signal intensity of scan B after both correction for receive sensitivity modulation and rigid body motion correction. After division, as seen in Equation III.5b, the modulation is corrected for, and the signal is no longer dependent on r'. This procedure is illustrated in Figure III.1b.

III.2.3: Estimation of MPM parameters in the case of inter-scan motion

In the MPM framework, quantitative parameters are derived from combining several scans. The effect of inter-scan motion is shown using the calculation of R1.

To calculate R1, two 3D FLASH scans are acquired; one predominantly proton density weighted (PDw), and one predominantly T1 weighted (T1w). The differential contrast weighting is achieved by changing the RF excitation flip angle, 6° for PDw, 21° for T1w. Based on the rational approximations of the Ernst equation (17,18), these two scans are combined after rigid body co-registration to calculate R1:

$$\mathrm{R1_{RB}(r)} = \frac{1}{2}\frac{\frac{\mathrm{C(r)S_{0,B}(r)}\alpha_B(r)}{\mathrm{TR_B}} - \frac{\mathrm{C(r)S_{0,A}(r)}\alpha_A(r)}{\mathrm{TR}_A}}{\frac{\mathrm{C(r)S_{0,A}(r)}}{\alpha_\mathrm{A}(r)} - \frac{\mathrm{C(r)S_{0,B}(r)}}{\alpha_B(r)}} \qquad \text{[III.6a]}$$

$$\mathrm{R1_{RB}(r)} = \frac{1}{2}\frac{\frac{\mathrm{S_{0,B}(r)}\alpha_B(r)}{\mathrm{TR_B}} - \frac{\mathrm{S_{0,A}(r)}\alpha_A(r)}{\mathrm{TR}_A}}{\frac{\mathrm{S_{0,A}(r)}}{\alpha_\mathrm{A}(r)} - \frac{\mathrm{S_{0,B}(r)}}{\alpha_B(r)}} \qquad \text{[III.6b]}$$

Here, the receive coil sensitivity, C(r), which is explicitly noted in Equation III.6a, cancels by division (Equation III.6b). $S_{0,A}$, TR_A and α_A are the unmodulated signal intensity, flip angle and repetition time of the PDw image, while $S_{0,B}$, TR_B and α_B are the unmodulated signal intensity, flip angle and repetition time of the T1w image. In practice, the contribution of locally varying flip angles, due to inhomogeneities in the transit field, are corrected using a map of the local RF transmit field map, i.e., α_A and α_B are the effective flip angles including RF transmit field inhomogeneities (178).

If motion occurs between the two weighted FLASH scans, the calculated R1 map is affected:

$$\mathrm{R1_{RB}(r,r')} = \frac{1}{2}\frac{\frac{\mathrm{C(r')S_{0,B}(r)}\alpha_B(r')}{\mathrm{TR_B}} - \frac{\mathrm{C(r)S_{0,A}(r)}\alpha_A(r)}{\mathrm{TR}_A}}{\frac{\mathrm{C(r)S_{0,A}(r)}}{\alpha_\mathrm{A}(r)} - \frac{\mathrm{C(r')S_{0,B}(r)}}{\alpha_B(r')}} \qquad \text{[III.7]}$$

where r and r' are analogous to Equation III.3. Unlike in Equation III.6b, the contributions of the receive field do not cancel by division, hence the mismatch between $R1_{RB}(r)$ and $R1_{RB}(r,r')$ despite the application of rigid body motion co-registration. It is assumed that, for the spatial scale in consideration, the transmit field does not vary, i.e., $\alpha(r')= \alpha(r)$.

If the receive field is estimated for both scans (Equations III.8a and III.8b), the mismatch can be corrected for by:

$$S_{RB+SC,A}(\mathrm{r}) = \frac{\mathrm{C}(\mathrm{r}) \cdot \mathrm{S}_{0,\mathrm{A}}(\mathrm{r})}{\frac{\mathrm{C}(\mathrm{r})}{C_{BC}}} = \mathrm{S}_{0,\mathrm{A}}(\mathrm{r}) \cdot C_{BC} \qquad \text{[III.8a]}$$

$$S_{RB+SC,B}(\mathrm{r}) = \frac{\mathrm{C}(\mathrm{r}') \cdot \mathrm{S}_{0,\mathrm{B}}(\mathrm{r})}{\frac{\mathrm{C}(\mathrm{r}')}{C_{BC}}} = \mathrm{S}_{0,\mathrm{B}}(\mathrm{r}) \cdot C_{BC} \qquad \text{[III.8b]}$$

$S_{RB+SC,A}(\mathrm{r})$ and $S_{RB+SC,B}(\mathrm{r})$ are the signal intensities of the PDw and T1w scans after correction for the contributions of the receive sensitivity field, and rigid body motion correction. These signal intensities are the unmodulated signal intensities, multiplied by a scaling factor. This scaling factor cancels by division, resulting in an R1 map free of inter-scan motion related bias:

$$\mathrm{R1}_{\mathrm{RB+SC}}(\mathrm{r}) = \frac{1}{2}\frac{\frac{\mathrm{S}_{0,\mathrm{B}}(\mathrm{r})\alpha_B(r)}{C_{BC}\mathrm{TR}_{\mathrm{B}}} - \frac{\mathrm{S}_{0,\mathrm{A}}(\mathrm{r})\alpha_A(r)}{C_{BC}\mathrm{TR}_A}}{\frac{\mathrm{S}_{0,\mathrm{A}}(\mathrm{r})}{C_{BC}\alpha_{\mathrm{A}}(r)} - \frac{\mathrm{S}_{0,\mathrm{B}}(\mathrm{r})}{C_{BC}\alpha_B(r)}} \qquad \text{[III.9a]}$$

$$\mathrm{R1}_{\mathrm{RB+SC}}(\mathrm{r}) = \frac{1}{2}\frac{\frac{\mathrm{S}_{0,\mathrm{B}}(\mathrm{r})\alpha_B(r)}{\mathrm{TR}_{\mathrm{B}}} - \frac{\mathrm{S}_{0,\mathrm{A}}(\mathrm{r})\alpha_A(r)}{\mathrm{TR}_A}}{\frac{\mathrm{S}_{0,\mathrm{A}}(\mathrm{r})}{\alpha_{\mathrm{A}}(r)} - \frac{\mathrm{S}_{0,\mathrm{B}}(\mathrm{r})}{\alpha_B(r)}} \qquad \text{[III.9b]}$$

This correction method is illustrated in Figure III.1b.

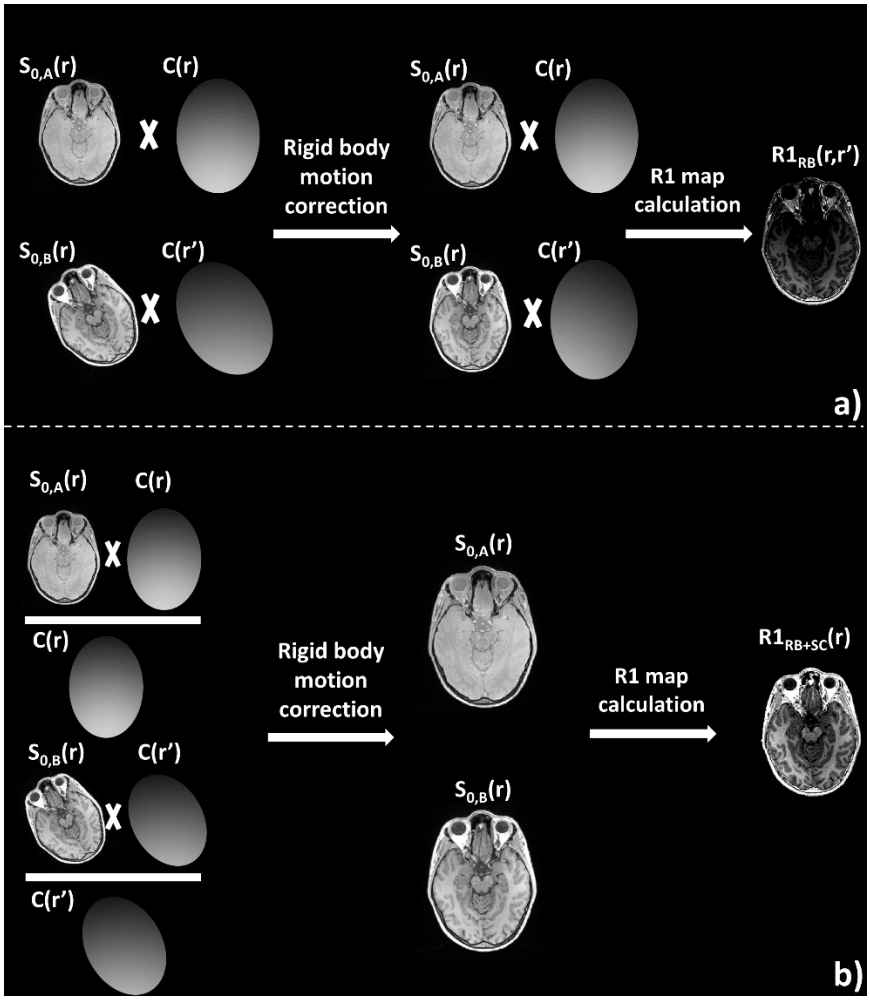

Figure III.1: The effect of inter-scan motion on R1 mapping (a), and the proposed receive sensitivity correction method (b). The bias visible in $R1_{RB}(r,r')$ is removed in $R1_{RB+SC}(r)$.

III.3: Evaluating existing receive sensitivity correction methods for the purpose of inter-scan motion correction

Image intensity variations caused by inhomogeneities in the RF receive field are well-known, and can affect diagnostic image quality and fMRI results (234,235). Accordingly, several correction methods have been developed (236,237), and deployed by MRI vendors.

One common approach is to estimate the RF receive field by acquiring a set of images on both the body coil, and the head coil. As shown in the Theory section of this Chapter, the ratio of such images is related to the relative RF receive field of the head coil.

In the following study, I evaluated a particular, vendor-specific implementation of this correction technique. On Siemens scanners, such as the ones used in this PhD project, the correction method is termed Prescan Normalize (PSN).

When Prescan Normalize (PSN) is enabled, two versions of the same scan may be stored on the scanner, one without PSN (without correcting for image intensity variations resulting from the receive field variations), and one with PSN (with a flattened image intensity profile). In a study, the viability of using PSN for inter-scan motion correction was investigated. It must be noted that it is possible to only store the version of the scan with PSN, this option was not used in the study.

As shown in Chapter II, parallel imaging in a SENSE framework requires the receive sensitivity field of the head coil. If the sensitivities are estimated relative to the body coil, then receive sensitivity is implicitly corrected for (59). In the following studies presented in this Chapter, this approach was not studied, as scans were acquired using the GRAPPA (60) parallel imaging technique. In addition, typical implementations of SENSE acquire the coil sensitivity profiles once per scanning session, thus the coil information is not updated in the case on motion between scans. SENSE also corrects for complex coil sensitivity effects, while for the correction method detailed in this Chapter, only magnitude effects have to be accounted for.

III.3.1: Methods

During the PSN procedure, a pre-scan acquisition is performed, during which data are acquired both on the multi-channel head coil and the body coil. This pre-scan is performed with: FoV=500x500x500 mm^3, TR=2.05 ms, FA=10^o, TE=1/2 ms, for acquisition on the head coil and body coil, respectively, using elliptical k-space coverage.

PSN is performed as part of the pre-scan adjustments, where parameters including shim currents, center frequency, transmit voltage, scaling factors, etc. are set. In the current

implementation, it is not possible to acquire the PSN scan before each acquisition separately, i.e., account for dynamic inter-scan effects, unless all the pre-scan adjustments are invalidated thereby triggering a repeat of the full calibration procedure. I refer to this as forced re-adjustment.

A homogeneous agar phantom (238), was scanned with the following version of the MPM protocol: FoV=256x240x176 mm, 1 mm^3 isotropic resolution, TE=2.2 ms, TR=23.7 /18.7ms (PDw/T1w scan), α=6°/21° (PDw/T1w scan), 6/8 echoes (T1w/PDw), GRAPPA acceleration factor 2, partial Fourier factor: 6/8. Vitamin E capsules were attached to the phantom, to aid the rigid body co-registration.

The RF transmit field was mapped in the first position (before inter-scan motion) using a B1+ mapping technique acquiring spin (SE) and stimulated (STE) echoes with a 3D EPI sequence (FOV=256x192x192 mm^3, 4 mm isotropic resolution, TR/TE/mixing time: 500/37.06/31.2 ms, flip angles from 65° to 115° in steps of 5°). The B0 field was mapped to correct for distortions in the EPI readout (178,239).

One PDw scan, and four T1w scans were acquired, consecutively. The first T1w scan was acquired in the same position, and with the same adjustment parameters. The second T1w scan was acquired in the same position, but after a forced re-adjustment. The third and fourth scans were acquired after the phantom was manually moved to a different position, and before and after a forced re-adjustment in this new position, respectively. The process is illustrated in Figure III.2.

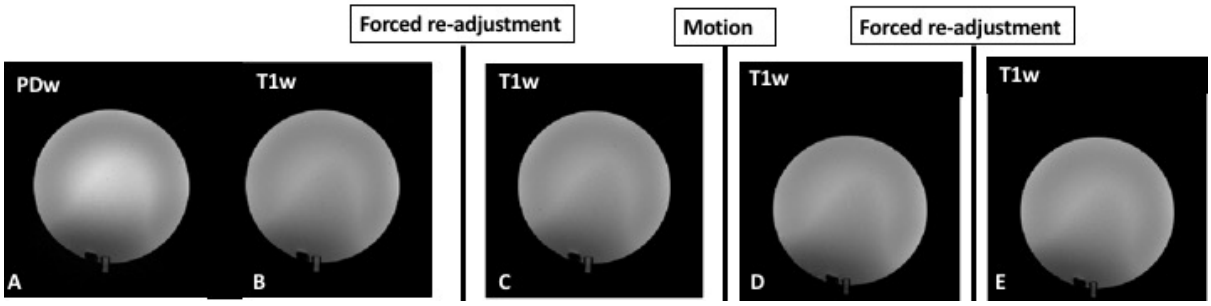

Figure II.2: A schematic of the acquisition procedure for motion and re-adjustment. A set of PDw and T1w scans (A and B) were acquired, after which the adjustment parameters were forcefully reset. A new T1w scan was acquired (C). The phantom was manually moved to a new position, and a T1w scan acquired (D), and after another forced reset of the adjustments, another T1w scan was acquired (E).

A total of eight R1 maps were calculated using the standard MPM post-processing pipeline detailed in Chapter II, four using uncorrected images, and four using the prescan normalized images. It was thus possible to compare the effect of forced re-adjustment, and of prescan normalisation both in the presence and absence of motion. A mask was derived from

the PDw scan using an intensity threshold to mask out the void outside the phantom. This mask was applied to all R1 maps, in order to compare the mean and standard deviation of R1 values within the phantom.

In vivo, a volunteer (37y, male) was scanned using the same sequence parameters and study design as those used for the agar phantom. Tissue probability maps were derived using the unified segmentation algorithm implemented in SPM12b (183), from the R1 map estimated without inter-scan motion, forced re-adjustment or PSN. Tissue-specific masks were generated by thresholding at 95% probability of grey and white matter. The conjunction of grey and white matter masks was used as a brain tissue mask. Mean and standard deviations for the tissue-specific R1 maps were calculated, and the distributions of R1 values inside the brain mask were plotted as histograms to investigate bias.

For both in vivo and phantom acquisitions, the extent of inter-scan motion was derived from the co-registration parameters.

III.3.2: Results

III.3.2.1: Inter-scan motion

Table III.1 shows the absolute translations and rotations between scans, both for the agar phantom and in the human volunteer.

	x [mm]	y [mm]	z [mm]	pitch [deg]	roll [deg]	yaw [deg]
Phantom	0.09	0.58	8.84	0.63	0.22	0.34
In vivo	1.44	1.67	18.4	2.01	1.22	0.21

Table III.1: Translation and rotation parameters for inter-scan motion.

III.3.2.2: Image intensity flattening

Image intensity variations were successfully corrected for by using PSN, as can be seen in Figure III.3. The high signal intensity regions at the edges of the phantom (Figure III.3A) were removed after prescan normalization (Figure III.3B). However, the signal intensity was not flat, but showed a domed profile, with the center of the phantom being brighter than its outer region. This may be due to the sensitivity profile of the body coil not being completely flat, or due to the inhomogeneity of the transmit field. In vivo, the higher signal intensities at the anterior and posterior portions of the brain (e.g. the areas closest to the receive coil) are readily apparent (Figure III.3C), and are corrected for using PSN (Figure III.3D).

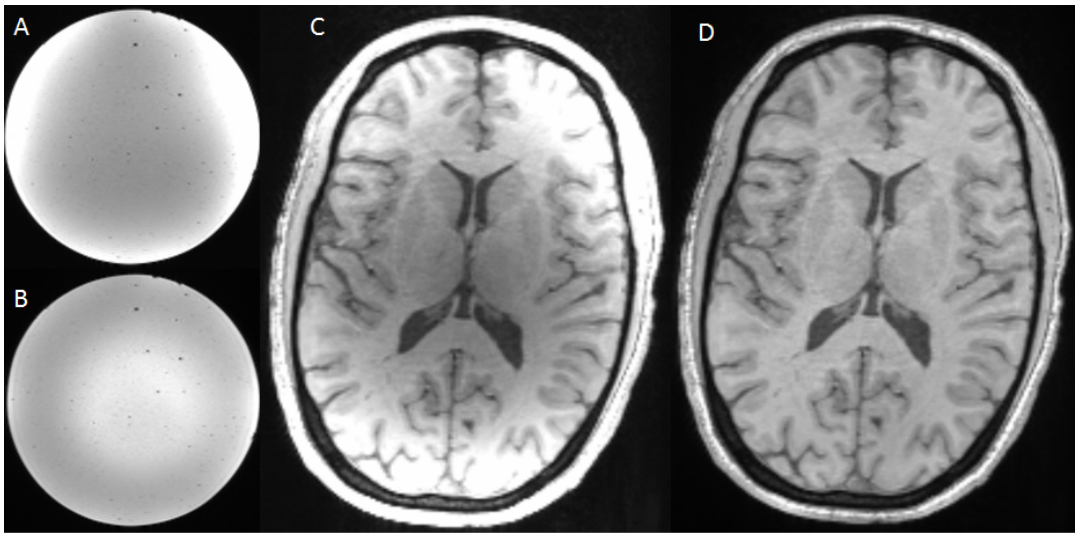

Figure III.3: Axial views of T1-weighted scans acquired on the agar phantom, without (A) and with (B) pre-scan normalisation. The image flattening effect is reproduced in the volunteer scan (C, D).

III.3.2.3: Estimated R1 values of the agar phantom

Table III.2 summarizes the estimated R1 values of the agar phantom (mean±standard deviation) for all eight cases. For all cases, PSN reduced the spread of R1 values, reflecting a flatter image intensity profile. In the absence of inter-scan motion, PSN did not induce an offset in estimated R1 values, even when adjustments were forcefully re-set. In the presence of inter-scan motion, an offset bias was observed in the R1 values estimated with and without PSN. For inter-scan motion and no forced re-adjustment, PSN reduced this bias, however, with re-measured adjustment values, the bias was not corrected for. Histograms of the R1 values are shown in Figure III.4.

	R1 value (mean±sd) [s^{-1}]	
	Without PSN	With PSN
No inter-scan motion, no re-adjustment	1.81±0.13	1.83±0.06
No inter-scan motion, forced re-adjustment	1.82±0.13	1.82±0.06
Inter-scan motion, no re-adjustment	1.63±0.19	1.74±0.16
Inter-scan motion, forced re-adjustment	1.62±0.18	1.64±0.13

Table III.2: Means and standard deviations of the eight R1 maps estimated from data with or without inter-scan motion, forced re-adjustment, or PSN.

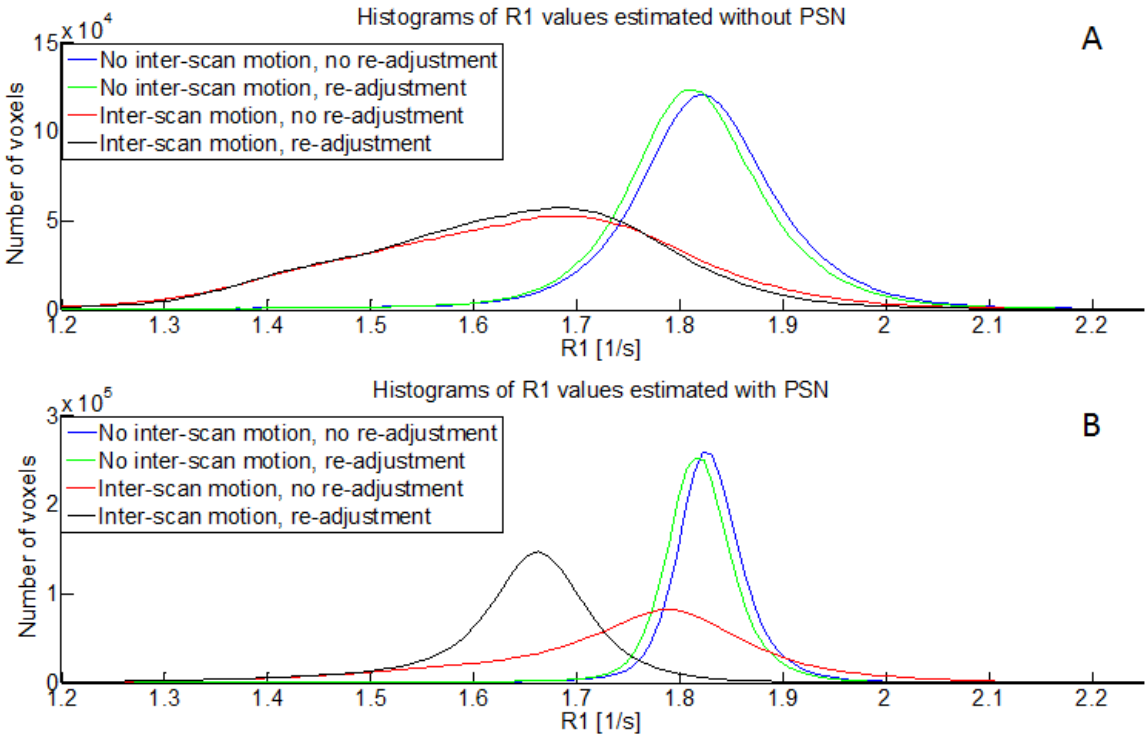

Figure III.4: Histograms of estimated R1 values for the agar phantom, without (A), or with (B) PSN.

III.3.2.4: R1 values estimated in vivo

R1 values for grey and white matter, estimated for all combinations of inter-scan motion and PSN corrections, are summarized in Table III.3. In the absence of inter-scan motion, PSN did not induce an offset bias in the estimated R1 values, even in the case of a forced re-adjustment. In the presence of inter-scan motion, mean R1 values calculated without PSN in both grey and white matter were comparable before and after forced re-adjustment. However, for R1 values calculated after inter-scan motion and after forced re-adjustment, PSN induced an appreciable offset bias. Histograms of the R1 values are shown in Figure III.5.

	R1 (mean±sd) [s^{-1}]			
	Grey matter		White matter	
	Without PSN	With PSN	Without PSN	With PSN
No inter-scan motion, no re-adjustment	0.626±0.108	0.623±0.106	0.994±0.088	0.987±0.088
No inter-scan motion, forced re-adjustment	0.637±0.109	0.644±0.114	1.005±0.084	1.009±0.085
Inter-scan motion, no re-adjustment	0.543±0.129	0.633±0.127	0.853±0.099	1.021±0.119
Inter-scan motion, forced re-adjustment	0.5301±0.126	0.535±0.102	0.834±0.104	0.848±0.079

Table III.3: Means and standard deviations of R1 estimated in grey and white matter in vivo, for all variations of inter-scan motion, forced re-adjustment and PSN.

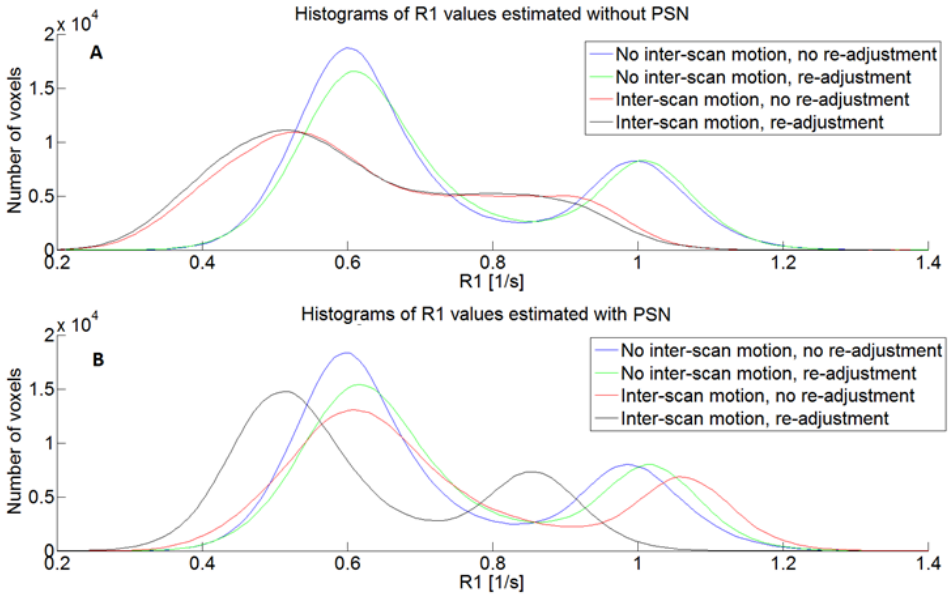

Figure III.5: Histograms of estimated R1 values in vivo, without (A), or with (B) PSN.

In the absence of PSN, the distribution of R1 was not strongly affected by forced re-adjustment, as seen in the near overlap of blue/green and red/black lines in Figure III.5A. However, while PSN corrected for the effect of inter-scan motion to a certain degree (compare the blue and red lines in Figure III.5B), a large bias was observed after forced re-adjustment (black line in Figure III.5B).

III.3.3: Discussion

Since the vendor-specific PSN implementation is part of the general scanner adjustment procedure, it was not possible to measure the relative sensitivity field for each acquisition without changing additional parameters. Thus, it was necessary to investigate the effect of re-measuring the additional adjustment parameters. The re-adjustment of these parameters did not introduce appreciable offsets in the estimated R1 value, neither in an agar phantom, nor in the volunteer scan, under the condition of no motion.

Inter-scan motion introduced an offset bias in estimated R1 values, both in in vivo and an agar phantom. This is in accordance with the assumptions outlined in the Theory section of this Chapter (III.2), particularly Equations III.7-III.9b.

If PSN was used, the contributions of the receive field were accounted for, but not in a consistent manner. If a scan was acquired after inter-scan motion, but before a forced re-adjustment, the bias introduced by inter-scan motion was partially corrected for. This can be seen by comparing the before inter-scan motion, before re-adjustment (blue), and after inter-scan motion, before re-adjustment (red) histograms in Figures III.4B/5B. In such a case, the sensitivity map from the initial position was used to correct for the contributions of the sensitivity field:

$$S_{RB+PSN,B}(r, r') = \frac{C(r') \cdot S_{0,B}(r)}{\frac{C(r)}{C_{BC}}} = S_{0,B}(r) \cdot C_{BC} \cdot \frac{C(r')}{C(r)} \qquad [III.10]$$

where $S_{RB+PSN,B}(r)$ is the signal intensity after rigid body motion correction and PSN. The modulation by C(r')/C(r) partially corrects for the variation in the receive sensitivity field, due to C(r')/C(r) being a smoothly varying field as compared to C(r), but the dependence on r' was not removed.

If both PSN and a forced re-adjustment were used, an offset bias could be observed in the estimated R1 values. This bias is attributed to the PSN procedure given that in the absence of PSN, the R1 values estimated before and after forced re-adjustment (after motion) were comparable. Thus, I hypothesized that a scaling factor was introduced by PSN after forced re-adjustment. This indicates that the sensitivity maps estimated by PSN were not reproducible under inter-scan motion conditions, as it was not possible to accurately correct for receive sensitivity contributions for each scan before and after motion. Thus, PSN could not be used as an inter-scan motion correction procedure.

III.4: Development of a novel correction method based on estimating and correcting for receive sensitivities, and evaluation on a phantom

III.4.1: Introduction

As detailed in section III.3, PSN was not found to be adequate for inter-scan motion correction, as it was not possible to robustly measure the sensitivity maps when inter-scan motion occurred. A novel method was thus developed, and compared with the PSN approach in a pilot phantom study. The validation of the method in a group of volunteers is described in section III.5.

The novel method was designed to measure the receive sensitivity field for each scan, based on acquiring two short, low-resolution calibration scans before each high-resolution scan, without the need for a forced re-adjustment of scanner parameters. This approach was compared to the PSN method on a set of weighted acquisitions. I hypothesized, based on the findings of section III.3, that the offset bias observed in PSN images after inter-scan motion and forced re-adjustment would be present in the signal intensities of weighted images, and that this bias could be eliminated by accurately measuring the contributions of the receive field, using the proposed method.

In the remained or this Chapter, the method based on the two short calibration scans will be referred to as “sensitivity correction”.

III.4.2: Methods

Four T1 weighted scans were acquired on the agar phantom, using the version of the 3D FLASH sequence described in section III.3. The second T1w scan was acquired in the same position as the first, but after forced re-adjustment. The third and fourth scans were acquired after the phantom was manually moved to a different position, and before and after a forced re-adjustment in this new position, respectively.

Before every high-resolution scan apart from the first, two short (~15 s for each), low-resolution calibration scans were acquired with the following parameters: FoV=256x240x220 mm^3, resolution=4x4x5 mm^3, FA=20^o, TR/TE=6/2.05 ms. One was acquired receiving on the 32-channel RF receive head coil, the other receiving on the RF body coil.

Modulation of the signal intensity by the receive sensitivity of the array coil was corrected for in the following way: the two low-resolution calibration scans were co-registered to the corresponding high-resolution scan (182), and re-sampled to a matching 1mm isotropic

resolution. These up-sampled to higher-resolution calibration images were smoothed with a Gaussian smoothing kernel with a full width half maximum of 12 mm. This kernel width was selected to correct for artefacts arising from the resampling and co-registration processes, while preserving the spatial details of the combined coil sensitivity. After smoothing, the smoothed, up-sampled to higher-resolution calibration image acquired with the 32 channel head coil was divided voxel-wise by the image acquired with the RF body coil (as described in Equation III.4). This net modulation was removed from the T1 weighted echoes by voxel-wise division.

For each condition (before or after motion, with or without PSN, and with or without sensitivity correction), the arithmetic mean of the acquired echoes was taken to produce a T1 signal intensity image, in line with the R1 calculation pipeline used in the MPM protocol. All T1 signal intensity images were co-registered to the T1 signal intensity image derived from the T1w scan acquired in the first position, without PSN or sensitivity correction. An image intensity mask, derived from the same scan, was used to mask out the void outside the phantom. Mean and standard deviation of the estimated T1 signal intensity values were calculated from within this mask.

To investigate the offset bias observed in section III.3, maps of the signal modulation by the receive sensitivity were compared before and after forced re-adjustment. For the PSN framework, these maps were not provided by the scanner, and thus had to be calculated from the acquired data. These “PSN sensitivity” maps were re-created by, for a given scan, dividing the signal intensity of the first echo acquired with PSN in a voxel-wise fashion by the signal intensity first echo acquired without PSN. These “PSN sensitivity” maps were calculated for the third and fourth T1w scan (after motion and before and after forced re-adjustment, respectively), and their ratio was calculated by voxel-wise division.

For the proposed sensitivity correction method, the maps of the signal modulation by the receive sensitivity explicitly calculated from the low-resolution calibration images acquired with the body and head coils. As for the “PSN sensitivity” maps, their ratio for the third and fourth scan was calculated.

The two ratio maps were masked with an intensity mask derived from the T1w scan acquired after inter-scan motion, before forced re-adjustment. The two ratios were compared to assess the presence and extent of offset bias.

The extent of inter-scan motion was derived from the co-registration parameters.

III.4.3: Results

III.4.3.1: Inter-scan motion

Table III.4 shows the absolute translations and rotations of inter-scan motion. A large displacement was chosen to highlight the effect of inter-scan motion.

x [mm]	y [mm]	z [mm]	pitch [deg]	roll [deg]	yaw [deg]
0.21	1.28	14.6	2.05	0.14	0.82

Table III.4: Translation and rotation parameters for inter-scan motion.

III.4.3.2: T1 signal intensity values

Table III.5 shows the means and standard deviations for the T1 signal intensity values for all conditions. As expected based on the results of section III.3, after inter-scan motion, and after forced re-adjustment, PSN induced an appreciable offset in the signal intensity values. The proposed sensitivity correction method corrected for this bias, but a large baseline offset bias was induced. The offset bias induced by PSN, and the baseline offset induced by the proposed method are apparent on the histograms shown in Figure III.6.

	T1 signal intensity values (mean±sd) [au]		
	Without PSN	With PSN	With sensitivity correction
No inter-scan motion, no re-adjustment	1001±399	1000±178	
No inter-scan motion, forced re-adjustment	1003±398	1001±178	1464±206
Inter-scan motion, no re-adjustment	914±373	968±200	1445±218
Inter-scan motion, forced re-adjustment	912±372	919±178	1445±215

Table III.5: Means and standard deviations of the T1 signal intensities estimated from data with or without inter-scan motion, forced re-adjustment, or PSN, and sensitivity correction.

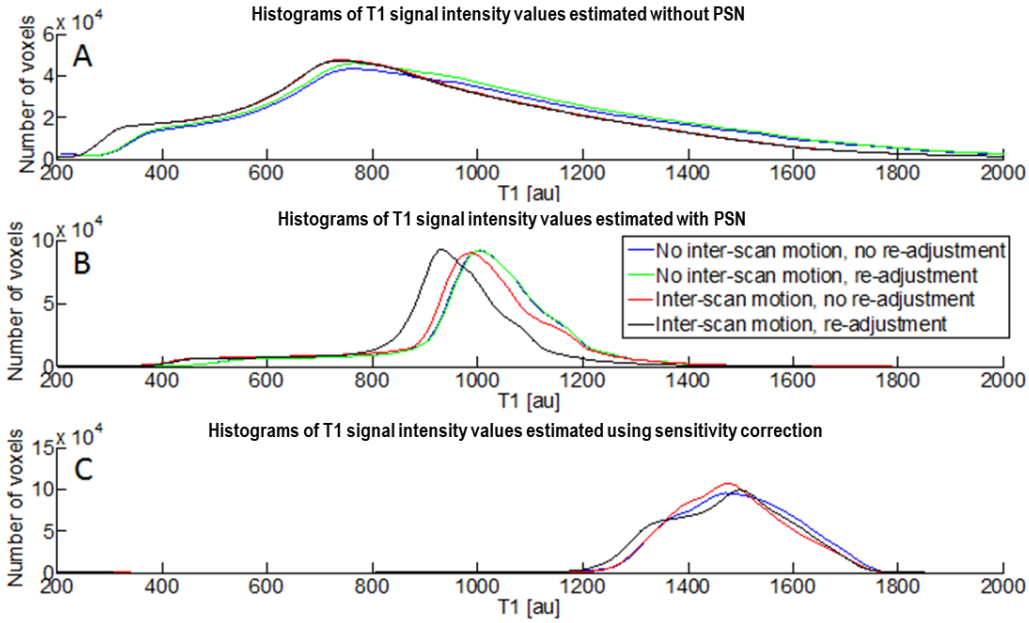

Figure III.6: Histograms of estimated T1 signal intensity values for the agar phantom, without PSN (A), with PSN (B) or with sensitivity correction (C).

III.4.3.3: Comparison of sensitivity maps used in PSN and in the proposed method

For the re-created "PSN sensitivity" maps, the ratio of the sensitivity maps for the third and fourth scan was 0.957±0.128 (mean±standard deviation across all voxels). For the maps used in the proposed correction method, this ratio was 1±0.063.

III.4.4: Discussion

A method was developed to reliably and reproducibly measure the contributions of receive sensitivity to the detected signal, termed sensitivity correction.

T1 signal intensity values calculated using the sensitivity correction after inter-scan motion compared well with those calculated before inter-scan motion, and forced re-adjustment did not induce an appreciable offset after motion, while this offset was observed when PSN was used.

Compared to re-created sensitivity maps used in the PSN method, the sensitivity maps used during the proposed sensitivity correction method were found to be both more accurate, as the ratio of two maps measured in the same position, before and after forced re-adjustment was found to be 1, while this was not the case for the PSN maps, indicating an offset bias between the map acquired before and after re-adjustment, and more precise, indicated by the

lower dispersion of the ratio of the sensitivity maps measured in the same position using the proposed method, compared to the dispersion of the PSN maps. Forced re-adjustment thus rendered the PSN maps unsuitable for inter-scan motion correction.

While the proposed sensitivity correction method did induce a large baseline offset in the measured signal intensities, this applied equally to all cases, and would manifest as a constant in Equations III.5-III.9, cancelling by division in quantitative MPM maps calculated from weighted scans acquired with this correction method.

The proposed method was thus found to be applicable for inter-scan motion correction, and will be evaluated in an in-vivo study, detailed in the following section, III.5.

III.5: Validation of a novel inter-scan motion correction method based estimating and correcting for receive sensitivities

III.5.1: Introduction

As detailed in the previous sections of this Chapter (III.2 and III.3), I have shown that inter-scan motion affects the quantitative parameter or R1 estimated in the MPM framework, due to the differential signal intensity modulation by the receive sensitivity field of the receive head coil.

If this modulation can be measured accurately and reliably, then the effect of inter-scan motion may be corrected for. A study was conducted to validate a novel inter-scan motion correction method, based on maps of the magnitude of the receive sensitivity field, derived from low-resolution calibration FLASH scans, in addition to rigid-body motion correction.

The core text of this section is taken from a previously published article which details the findings of the study with regards to the estimation of R1 (233). In this section, the results are reproduced, and expanded to include the effect of inter-scan motion, and the correction for inter-scan motion, by means of both PSN and by sensitivity correction.

III.5.2: Methods

III.5.2.1: FLASH-based sensitivity maps

In this study, the scans used to map the receive sensitivity field (as detailed in Chapter III.4) were further refined. An isotropic resolution was chosen so as to avoid anisotropic mapping of the sensitivity field, which could potentially result in unequal correction for inter-scan motion effects depending on the direction of inter-scan motion. To minimize scan time, the readout bandwidth was increased to 1015 Hz/pixel, and the TR was reduced. To minimize contributions from the innate tissue contrast, a lower flip angle was chosen. The acquisition parameters of the low-resolution calibration scans were: FoV=256x240x176 mm^3, 4 mm^3 isotropic resolution, TR/TE/α=4.64 ms/2 ms/6°, readout bandwidth=1015 Hz/pixel, acquisition time approximately 12 s.

III.5.2.2: Volunteers

Five volunteers (2 males, 37±4 years) were recruited and scanned in accordance with local Ethics guidelines after obtaining written informed consent.

III.5.2.3: Study design

Individual MRI sessions were structured in the following way. The local RF transmit field was mapped first, as described in section II.8 (178). Then, a full set of MPM acquisitions, consisting of three FLASH scans (one predominantly weighted by magnetization transfer, MTw, one predominantly proton density weighted, PDw, and one predominantly T1 weighted, T1w) were acquired in the first head position. The volunteers were then asked to perform large inter-scan motion, by moving between 10 to 20 mm in one continuous motion in the direction out of the bore, moving towards their feet. The volunteers were also asked to perform a nod, such that the second position included both a translational and rotational offset as compared with the first position. Two FLASH scans were then acquired in the second position, one PDw and one T1w. Before each high-resolution FLASH scan, two low-resolution calibration scans used for sensitivity correction were acquired.

The instruction for inter-scan motion were chosen such that the resulting offset would be at the higher end of the range reported in patients (240), and previous studies regarding inter-scan motion (205,241), in order to robustly assess the method. The extent of inter-scan motion, both between the two positions, and within positions, was estimated retrospectively using rigid-body co-registration as implemented in SPM12b. Mean and standard deviation (sd) of the amplitudes of inter-scan motion within and between positions were calculated across all volunteers.

III.5.2.4: Image acquisition

In this study, an improved version of the MPM protocol was used compared to the one used in section III.4. A crucial difference compared to the parameters of the FLASH scans used in section III.4 is the approximate matching of transmit voltage between all three scans to the transmit voltage of the 3D EPI scans used for mapping the RF transmit field, so as to avoid any artefacts arising from the non-linearity of the RF amplifier (242). Additionally, acquisition parameters such as TR were matched across the three FLASH scans, where possible.

All data were acquired on a Siemens TIM Trio 3T MRI system, running software version VB17. For transmission, the RF body coil was used. For high-resolution FLASH scans, the 32-channel receive-only head coil was used. Low-resolution scans used for sensitivity correction were acquired on the head coil and body coil.

Acquisition parameters shared by the high-resolution FLASH scans were FoV=256x240x176 mm^3, 1 mm^3 isotropic resolution, TR=25 ms, GRAPPA acceleration

factor=2, 40 reference lines. GRAPPA acceleration was used in both phase-encoding directions, in conjunction with elliptical k-space coverage, for an acquisition time of 4 minutes and 5 seconds per high-resolution scan. PSN was used in the high-resolution acquisitions, and the resulting images with and without signal intensity flattening were saved.

PDw and T1w scans were acquired with TE/echo spacing/echoes=2.34 ms/2.3 ms/8, and a flip angle of 6^{o} (PDw scans) or 21^{o} (T1w scans), respectively. MTw scans were acquired with an off-resonance pulse of Gaussian shape, 4 ms duration, 2 kHz off-resonance frequency, and 220^{o} nominal flip angle, followed by the acquisition of 6 echoes with TE/echo spacing =2.34 ms/2.3 ms.

The RF transmit field was mapped in the first position using spin and stimulated echoes acquired with a 3D EPI sequence of FoV=256x192x192 mm3, 4 mm^{3} isotropic resolution, TR/TE/mixing time of 500/37.06/31.2 ms, using eleven nominal flip angles ranging from 65^{o}-115^{o} in increments of 5^{o}. A GRE-based B0 field map was acquired to correct for EPI readout distortions and off-resonance effects (178,239).

III.5.2.5: Image processing

All data were processed using SPM12 and custom-made scripts in a MATLAB 8.3 environment. Three of the four quantitative parameters of the MPM protocol (R1, MT, PD*) were calculated. Although R2* is typically calculated as part of the MPM protocol, the effect of inter-scan motion on this metric was not investigated since R2* was not typically calculated from multiple scans at the time of this study.

Data were combined according to four scenarios: in scenario A, all scans acquired before inter-scan motion were used. In scenario B, the MTw scan before, and the PDw and T1w scans after inter-scan motion were used. In scenario C, the MTw and PDw scans acquired in the first, and the T1w scan acquired in the second position were used. Lastly, in scenario D, MTw and T1w scans acquired in the first, and PDw scan acquired in the second position were used (see Figure III.7).

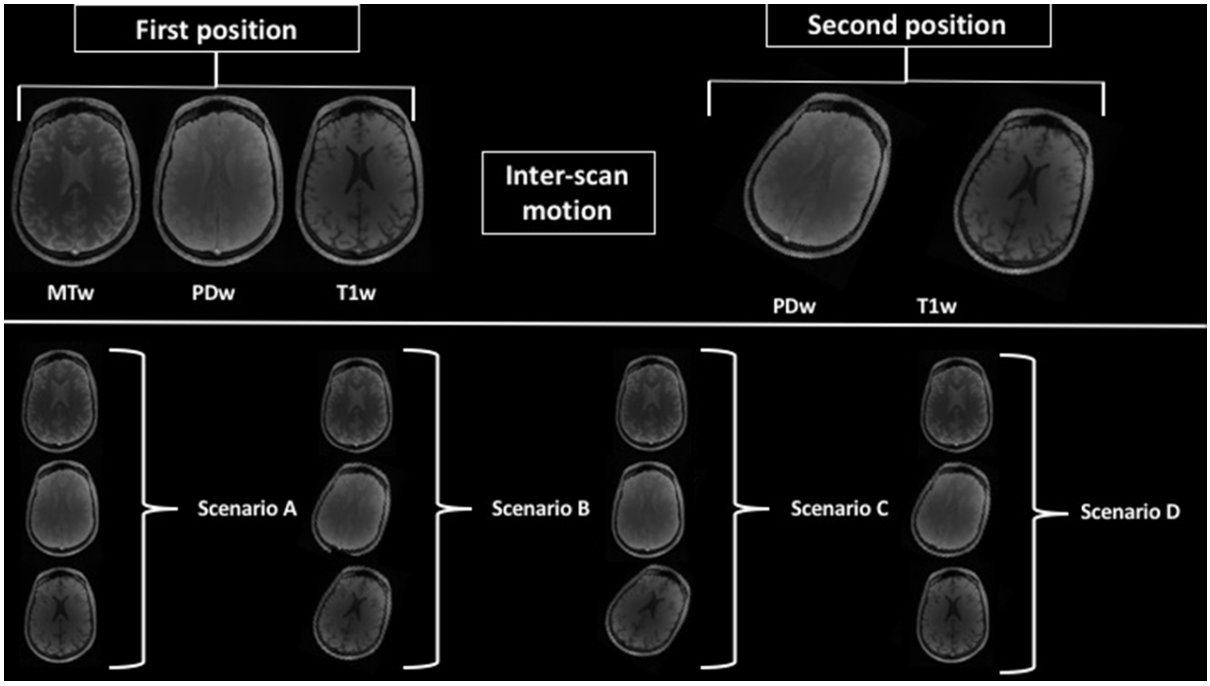

Figure III.7: A schematic of the acquisition of five weighted FLASH scans (top) acquired before and after inter-scan motion, represented here as a rotation, and the four data combination scenarios (bottom).

For every scenario, three versions of the maps were estimated. In the rigid-body (indexed as RB) motion correction case, the scans without PSN were used, and inter-scan motion was corrected for by rigid-body co-registration. In the PSN and rigid body (indexed as RB+PSN) motion correction case, the scans with PSN were used, and inter-scan motion was corrected for by rigid-body co-registration. In the sensitivity correction and rigid-body (indexed as RB+SC) case, the contributions of the receive sensitivity field were removed with the method detailed below, and rigid-body co-registration was used. Thus, a total of 12 maps were estimated per volunteer and quantitative parameter.

Inter-scan motion artefacts due to the changes in the receive coil sensitivity were corrected for in the following way. The two low-resolution calibration scans, acquired before each high-resolution scan, to map the receive sensitivity field were co-registered to the high-resolution scan to correct for any motion between the three scans (182). In the same step, the low-resolution calibration scans were resampled to 1 mm isotropic resolution. The resampled calibration images were then smoothed in order to correct for image processing artefacts. A Gaussian smoothing kernel with a full width at half maximum of 12 mm was chosen to preserve the spatial details of the combined coil sensitivity. After smoothing, a map of the combined spatial receive sensitivity field was estimated by dividing the smoothed calibration image acquired with the 32 channel receive coil by the image acquired by the RF body coil on

a voxel-by-voxel basis. The signal intensity modulations due to this field were removed from all echoes of the T1w, PDw, and MTw scans by voxel-wise division.

Quantitative maps were estimated according to the methods described in Chapter II. Accordingly, the different data combination scenarios introduced different sensitivity to inter-scan motion for the three quantitative maps. R1 and PD* are calculated from two FLASH scans, T1w and PDw. Thus, there maps were calculated in the absence of inter-scan motion in scenarios A and B, and affected by inter-scan motion for C and D. MT is calculated using all three scans, thus, only scenario A was not affected by inter-scan motion.

III.5.2.6: Characterizing the effect of inter-scan motion

All 12 R1 maps estimated for a given volunteer were co-registered to the $R1_{RB}$ map calculated in scenario A, and the transformation was applied to all other quantitative maps, bringing all 48 quantitative maps per volunteer into the same coordinate system. Tissue probability maps were derived from the $R1_{RB}$ and $R1_{RB+SC}$ maps estimated in scenario A, using the unified segmentation algorithm of SPM12b (183). The resulting probability maps were thresholded at 95% probability for grey or white matter, respectively, used to create a grey matter white matter mask. The conjunction of the grey and white matter mask was used to create a brain mask. Probability maps were estimated from the RB and RB+SC cases to avoid biasing the analysis towards corrected or uncorrected data. These tissue masks were applied to all quantitative maps.

The homogeneity of the estimated quantitative values was assessed by calculating the coefficient of variation (CoV), defined as the standard deviation over the mean, for both grey and white matter masks and all quantitative values and estimation scenarios. The tissue masks covered rather homogeneous tissue, thus an increase in CoV was interpreted as a loss of homogeneity, and a negative effect of inter-scan motion.

The different estimation scenarios were also evaluated by taking the normalized root mean square error (NRMSE) of a given quantitative value estimated with a given scenario, as compared to the quantitative map estimated in scenario A using the RB method, for all voxels within the brain mask:

$$NRMSE_{q,s} = \sqrt{\frac{1}{N}\sum_{j=1}^{N}\left(\frac{M_{q,s}(j) - M_{q,1}(j)}{M_{q,1}(j)}\right)^2} \qquad \text{[III.11]}$$

where $NRMSE_{q,s}$ is the normalized root mean square error of quantitative map q estimated in scenario s, $M_{q,1}(j)$ is the j-th voxel of quantitative map q estimated in scenario A with rigid-body

motion correction only, index s runs across all combinations of inter-scan motion cases and correction methods, and j runs across all N nonzero voxels within the brain mask.

Histograms of the four quantitative values within the brain mask were plotted in order to visualize offset biases.

A conjunction of all probability maps (both grey matter and both white matter probability maps), with a probability threshold of >35% was used to mask the quantitative maps for visual inspection, and to generate voxel-wise difference maps.

III.5.3: Results

III.5.3.1: Inter-scan motion

All volunteers executed the head motion as instructed. The magnitude of instructed inter-scan motion between the two positions was approximately an order of a magnitude larger than undesired inter-scan motion within the two acquisition positions. Figure III.8 shows magnitudes of translation and rotation parameters across all volunteers.

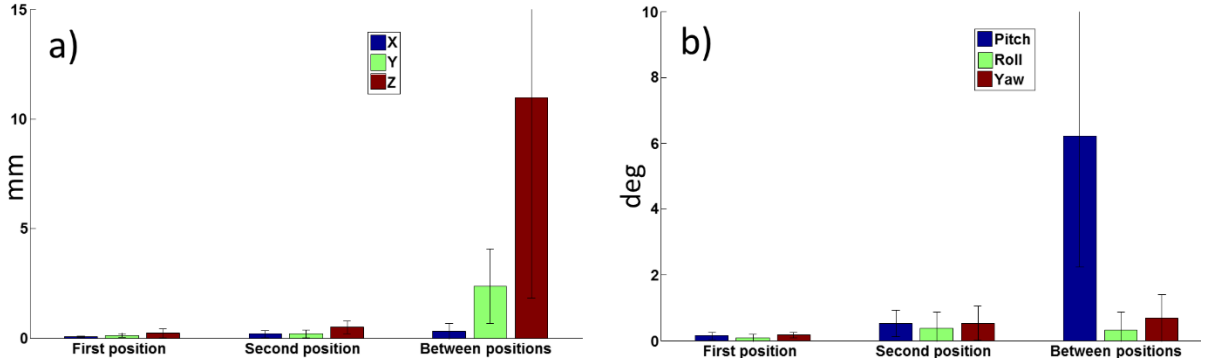

Figure III.8: Translation (a) and rotation (b) parameters (mean±sd across all volunteers) for within (undesired) and between (instructed) position motion.

III.5.3.2: Receive sensitivity maps

An exemplar of the sensitivity maps calculated in the RB+SC correction method is shown in Figure III.9. The sensitivity maps were calculated on the PDw scans of volunteer 2, and co-registered for better visual comparison.

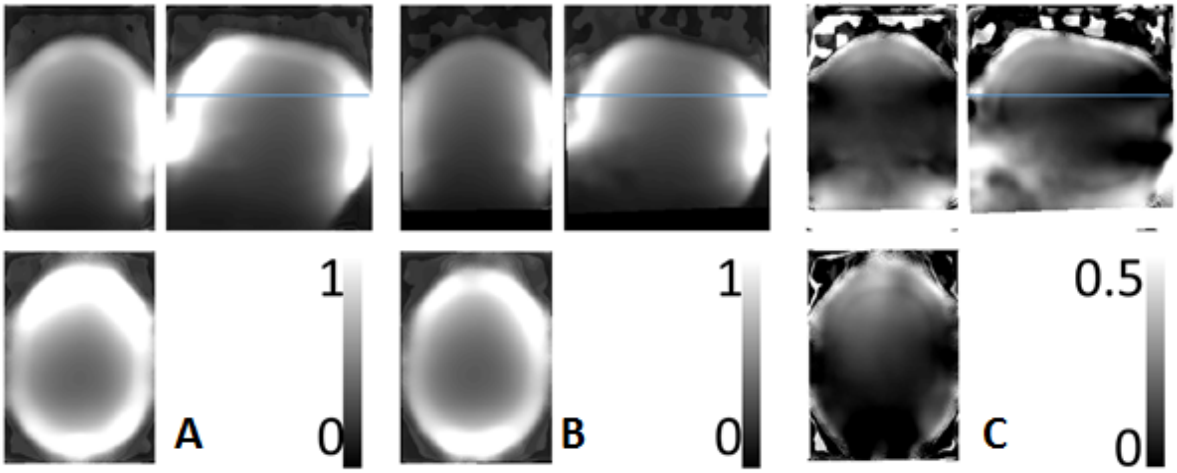

Figure III.9: Maps of the magnitude of the net RF receive sensitivity field for the PDw acquisition of volunteer 2, in the first position (A), in the second position (B), and the difference of the co-registered maps (C). Sensitivity was high along the periphery, where the head was close to the receive coil, and dropped off towards the centre of the brain. The difference map (C) reflects these characteristics, with the largest difference being in the periphery of the brain. The blue line indicates the position of the two difference maps shown in Figure III. 10.

III.5.3.3: Visual comparison of quantitative maps

Inter-scan motion affected image quality of R1 and MT maps, but not PD* maps, as is shown in Figures III.10-12.

For R1 maps, if only RB correction was used, inter-scan motion resulted in an anterior-posterior image intensity gradient (Figure III.10b). Difference maps (Figure III.10e,g) show this effect more clearly. Accounting for the effect of receive sensitivity reduced this artefact to a negligible level (Figure III.10 f and h).

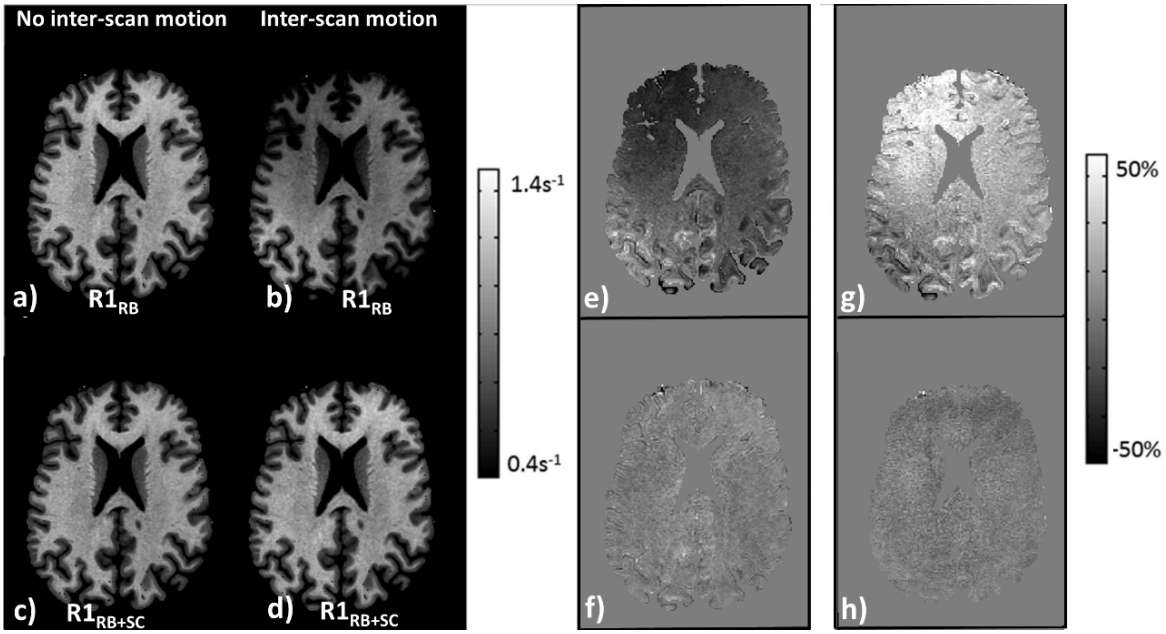

Figure III.10: R1 maps for participant 2 corrected with rigid body motion correction (RB) or rigid body motion correction and additional receive sensitivity correction (RB+SC). a) $R1_{RB}$ map for scenario A; b) $R1_{RB}$ map for scenario C; c) $R1_{RB+SC}$ map for scenario A; d) $R1_{RB+SC}$ map for scenario C. e) difference between (a) and (b); f) difference between (c) and (d); compared to (a) and (c), respectively. The bias introduced by inter-scan motion is mainly apparent as an anterior-posterior gradient (e) that was removed by the sensitivity correction (f). Difference maps for scenario D are also shown: g) difference map for $R1_{RB}$ maps; h) difference map for the $R1_{RB+SC}$ maps.

For MT maps, if only RB correction was used, inter-scan motion resulted in a slight intensity gradient, and an overall brightening in the chosen slice, as seen in Figure III.11b. Additional receive sensitivity correction did not introduce an appreciable bias in the absence of inter-scan motion (Figure III.11c), and reduced the effect of inter-scan motion (Figure III.11f and h).

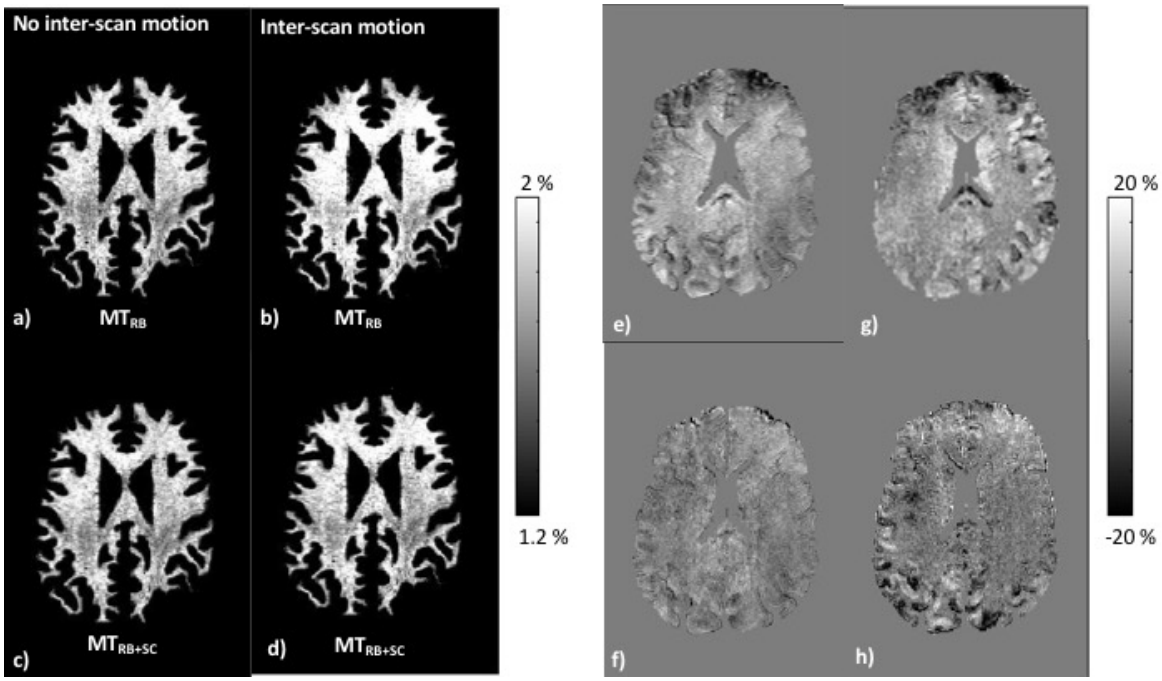

Figure III.11: MT maps for participant 2 corrected with rigid body motion correction (RB) or rigid body motion correction and additional receive sensitivity correction (RB+SC). a) MT_{RB} map for scenario A; b) MT_{RB} map for scenario C; c) MT_{RB+SC} map for scenario A; d) MT_{RB+SC} map for scenario C. e) difference between (a) and (b); f) difference between (c) and (d). Difference maps for inter-scan motion scenario D are also shown: g) difference map for MT_{RB} maps; h) difference map for the MT_{RB+SC} maps.

For PD* maps, shown in Figure III.12, due to the inherent correction for receive effect present in the estimation of PD*, inter-scan motion did not result in appreciable changes in image intensity. Additional receive correction did not degrade image quality.

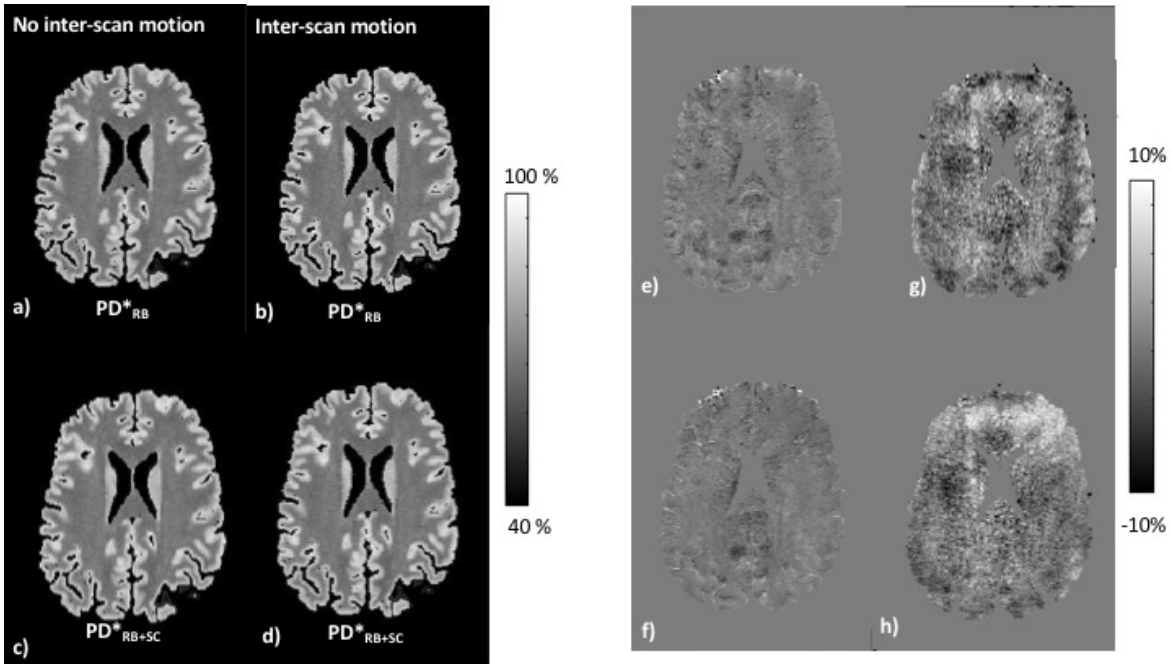

Figure III.12: PD* maps for participant 2 corrected with rigid body motion correction (RB) or rigid body motion correction and additional receive sensitivity correction (RB+SC),). a) PD^*_{RB} map for scenario A; b) PD^*_{RB} map for scenario C; c) PD^*_{RB+SC} map for scenario A; d) PD^*_{RB+SC} map for scenario C. e) difference between (a) and (b); f) difference between (c) and (d). Difference maps for scenario D are also shown: g) difference map for PD^*_{RB} maps; h) difference map for the PD^*_{RB+SC} maps.

III.5.3.4: Inter-scan motion effects on R1

Inter-scan motion had an appreciable effect on the homogeneity of the estimated R1 values. For both data combination scenarios affected by inter-scan motion (scenarios C and D), CoV for RB correction was increased compared to the CoV for both combination scenarios not affected by inter-scan motion (scenarios A and B). This loss of homogeneity was reduced by RB+PSN, while RB+SC resulted in a CoV comparable to that calculated in the absence of inter-scan motion, as shown in Table III.6.

Data combination scenario	Tissue mask	Correction method		
		RB	RB+PSN	RB+SC
Scenario A (no inter-scan motion)	Grey matter	0.1222±0.0056	0.1229±0.0047	0.1236±0.0045
	White matter	0.0834±0.0092	0.0834±0.0092	0.0839±0.0092
Scenario B (no inter-scan motion)	Grey matter	0.1443±0.0178	0.1414±0.0136	0.1371±0.0176
	White matter	0.0878±0.0128	0.0862±0.0103	0.0836±0.0112
Scenario C (inter-scan motion)	Grey matter	0.2057±0.0353	0.1518±0.0219	0.1362±0.0098
	White matter	0.1301±0.0273	0.1044±0.0229	0.0896±0.0099
Scenario D (inter-scan motion)	Grey matter	0.1950±0.0365	0.1665±0.0383	0.1340±0.0111
	White matter	0.1404±0.0259	0.1009±0.0246	0.0839±0.0099

Table III.6: Coefficient of variation for R1 maps estimated in the four scenarios (mean±sd across all volunteers), using rigid-body motion correction (RB), rigid-body motion correction and PSN (RB+PSN), or using rigid body motion correction and sensitivity correction (RB+SC). Inter-scan motion greatly increased CoV, if only rigid-body motion correction was used. RB+PSN reduced CoV, while RB+SC resulted in CoV comparable to that of scenario A.

The scan-rescan variability, as captured by the NRMSE of the R1 map estimated in scenario B using the RB correction method, was approximately 10%. The NRMSE due to inter-scan motion was approximately twice that, and was corrected to the level of scan-rescan variability using the RB+PSN correction method, and below the level scan-rescan variability using the RB+SC correction method, for both inter-scan motion scenarios (C and D), as shown in Table III.7.

Data combination scenario	Correction method		
	RB	RB+PSN	RB+SC
Scenario A (no inter-scan motion)		2.76±1.19%	2.53±0.68%
Scenario B (no inter-scan motion)	10.05±2.06%	10.47±1.29%	9.72±2.06%
Scenario C (inter-scan motion)	17.79±5.47%	10.03±2.14%	7.49±1.27%
Scenario D (inter-scan motion)	22.27±11.64%	12.52±4.12%	8.33±0.92%

Table III.7: NRMSE for R1 maps estimated with all motion conditions and correction methods, compared to the R1 map estimated in the first identical position case, using the RB correction method.

Inter-scan motion had a great effect on the accuracy and precision with which R1 was estimated. This is shown clearly in Figure III.13. Compared to the two cases where R1 was estimated from data acquired in the same position (Figure III.13A and B), inter-scan motion results both in a bias towards lower values, and a loss of precision, reflected in the broadening of the histograms (Figure III.13C and D), which was not corrected for using only rigid-body motion correction. RB+PSN corrected for the loss of precision, resulting in comparable histogram shapes, but the values were estimated with a bias towards higher values (compare the peaks on Figures III.13. A/B and C/D). The RB+SC correction method restored both accuracy, and precision.

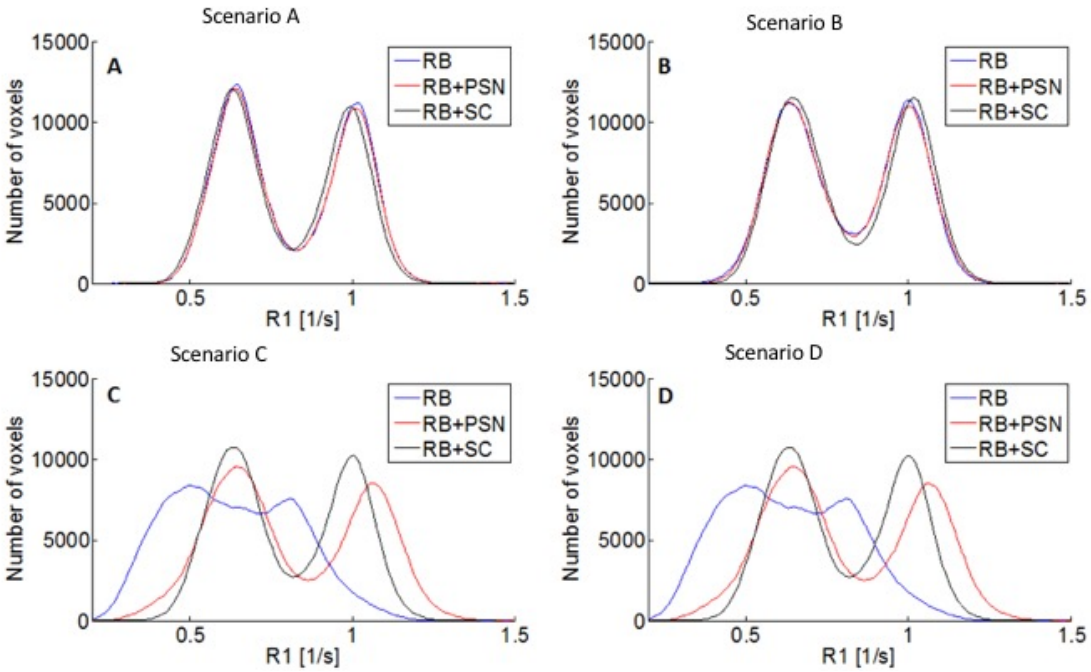

Figure III.13: Histograms of R1 estimated in the four scenarios (A,B,C,D) using all three correction methods for volunteer 2. Inter-scan motion introduces large effects (C,D). RB+PSN reduces the loss in precision, but introduces a bias for higher values. RB+SC corrects for both the loss of precision, and the offset bias.

III.5.3.5: Inter-scan motion effects on PD*

There was little appreciable effect on the homogeneity of PD* due to inter-scan motion. For white matter, the increase in mean CoV across the group due to inter-scan motion did not exceed the sd across the group for no inter-scan motion cases. For scenario B, RB+PSN and RB+SC resulted in a slight increase in the CoV of grey matter, while white matter was unaffected. These results are shown in Table III.8.

Data combination scenario	Tissue mask	Correction method		
		RB	RB+PSN	RB+SC
Scenario A (no inter-scan motion)	Grey matter	0.0637±0.0029	0.0643±0.0029	0.0648±0.0028
	White matter	0.0441±0.0029	0.0447±0.0026	0.0448±0.0027
Scenario B (no inter-scan motion)	Grey matter	0.0685±0.0065	0.0731±0.0054	0.0727±0.0098
	White matter	0.0463±0.0054	0.0489±0.0047	0.0462±0.0039
Scenario C (inter-scan motion)	Grey matter	0.0719±0.0057	0.0715±0.0021	0.0691±0.0025
	White matter	0.0464±0.0029	0.0469±0.0023	0.0456±0.0028
Scenario D (inter-scan motion)	Grey matter	0.0663±0.0073	0.0758±0.0074	0.0692±0.0049
	White matter	0.0459±0.0053	0.0508±0.0057	0.0459±0.0049

Table III.8: Coefficient of variation for PD* maps estimated in the four motion cases (mean±sd across all volunteers), using rigid-body motion correction (RB), rigid-body motion correction and PSN (RB+PSN), or using rigid body motion correction and sensitivity correction (RB+SC).

Scan-rescan variability, as captured by the NRMSE of the PD* map estimated in scenario B using the RB correction method, was approximately 5%. Inter-scan motion effects were comparable. RB+PSN and RB+SC did not alter the NRMSE values of these motion cases in an appreciable manner. These results are shown in Table III.9.

Data combination scenario	Correction method		
	RB	RB+PSN	RB+SC
Scenario A (no inter-scan motion)		0.78±0.14%	0.94±0.25%
Scenario B (no inter-scan motion)	5.14±1.07%	5.71±0.96%	5.42±1.03%
Scenario C (inter-scan motion)	2.45±0.79%	3.50±1.02%	2.31±0.37%
Scenario D (inter-scan motion)	5.25±1.13%	5.99±1.28%	5.09±0.84%

Table III.9: NRMSE for PD* maps estimated with all motion conditions and correction methods, compared to the PD* map estimated in scenario A, using the RB correction method.

The only appreciable effect of inter-scan motion on PD* was an offset in the PD* of grey matter (Figure III.14 C/D) in the case where only rigid body co-registration is used. For all other motion cases and correction methods, there is no appreciable effect.

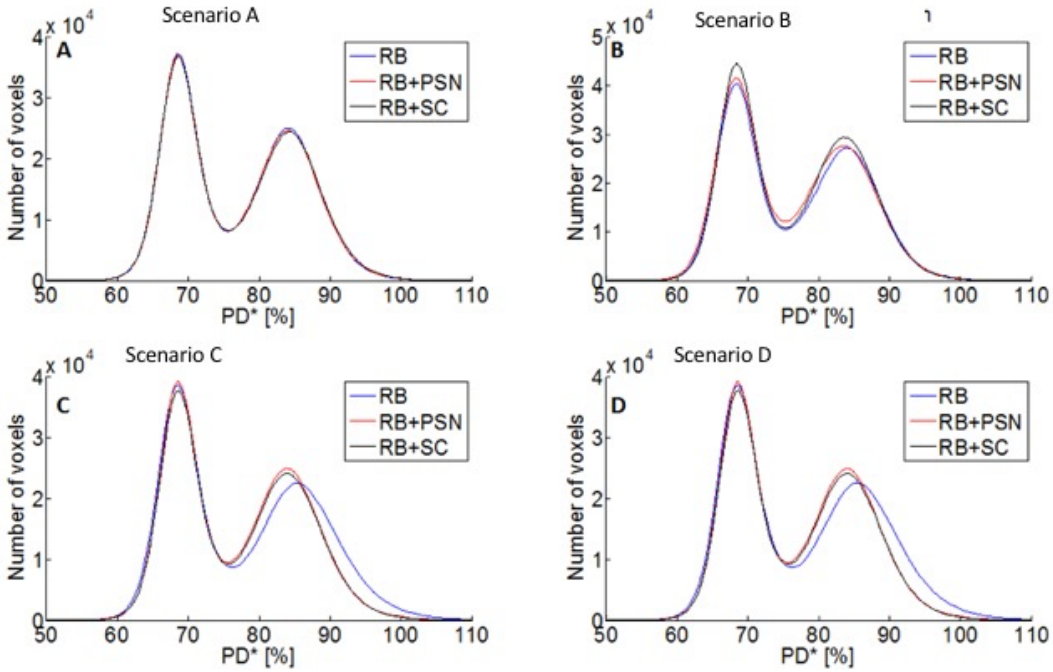

Figure III.14: Histograms of PD* estimated in the four motion scenarios (A,B,C,D) using all three correction methods for volunteer 2.

III.5.3.6: Inter-scan motion effects on MT

Inter-scan motion had an appreciable effect on the estimated MT values. For all three scenarios (B, C and D) affected by inter-scan motion, CoV for the RB correction was increased compared to scenario A. This loss of homogeneity was reduced by RB+PSN, while RB+SC resulted in a CoV comparable to that of scenario A, as shown in Table III.10.

Data combination scenario	Tissue mask	Correction method		
		RB	RB+PSN	RB+SC
Scenario A (no inter-scan motion)	Grey matter	0.1703±0.0097	0.1721±0.0095	0.1716±0.0089
	White matter	0.1032±0.0113	0.1035±0.0110	0.1034±0.0112
Scenario B (inter-scan motion)	Grey matter	0.3962±0.1407	0.2498±0.0596	0.2064±0.0198
	White matter	0.1970±0.0558	0.1375±0.0341	0.1133±0.0116
Scenario C (inter-scan motion)	Grey matter	0.2396±0.0258	0.1920±0.0178	0.1765±0.0107
	White matter	0.1334±0.0137	0.1163±0.0143	0.1059±0.0103
Scenario D (inter-scan motion)	Grey matter	0.3598±0.1410	0.2362±0.0471	0.1972±0.0154
	White matter	0.1483±0.0312	0.1208±0.0172	0.1067±0.0093

Table III.10: Coefficient of variation for MT maps estimated in the four motion cases (mean±sd across all volunteers), using rigid-body motion correction (RB), rigid-body motion correction and PSN (RB+PSN), or using rigid body motion correction and sensitivity correction (RB+SC).

Within the confines of this study, only one MTw scan was acquired. Thus, a scan-rescan variability could not be determined for MT, as three of the four data combination scenarios were affected by inter-scan motion. For scenario B, two of the three scans used in the calculation of MT were affected by inter-scan motion (PDw and T1w), while for scenario C and D, only the T1w scan and PDw scan were affected, respectively. Accordingly, NRMSE for

RB correction was highest in scenario B. For all data combination scenarios, NRMSE was reduced more with RB+SC than with RB+PSN. These results are summarized in Table III.11.

Data combination scenario	Correction method		
	RB	RB+PSN	RB+SC
Scenario A (no inter-scan motion)		4.43±1.34%	4.47±1.44%
Scenario B (inter-scan motion)	30.62±10.97%	17.16±4.55%	11.95±1.25%
Scenario C (inter-scan motion)	16.79±3.94%	9.63±2.08%	6.48±0.86%
Scenario D (inter-scan motion)	25.08±10.23%	15.29±3.15%	10.44±0.84%

Table III.11: NRMSE for MT maps estimated with all motion conditions and correction methods, compared to the MT map estimated in scenario A, using the RB correction method.

The inter-scan motion effect observed for R1 can be, in part, observed for the histograms of MT shown in Figure III.15. However, the greatest offset bias and loss of precision could be observed in scenario B, where both the PDw and T1w scan were affected by inter-scan motion. For all motion cases, RB+PSN and RB+SC restored the histogram shape, however, RB+PSN correction introduced a bias towards higher values, in line with the effect observed in R1.

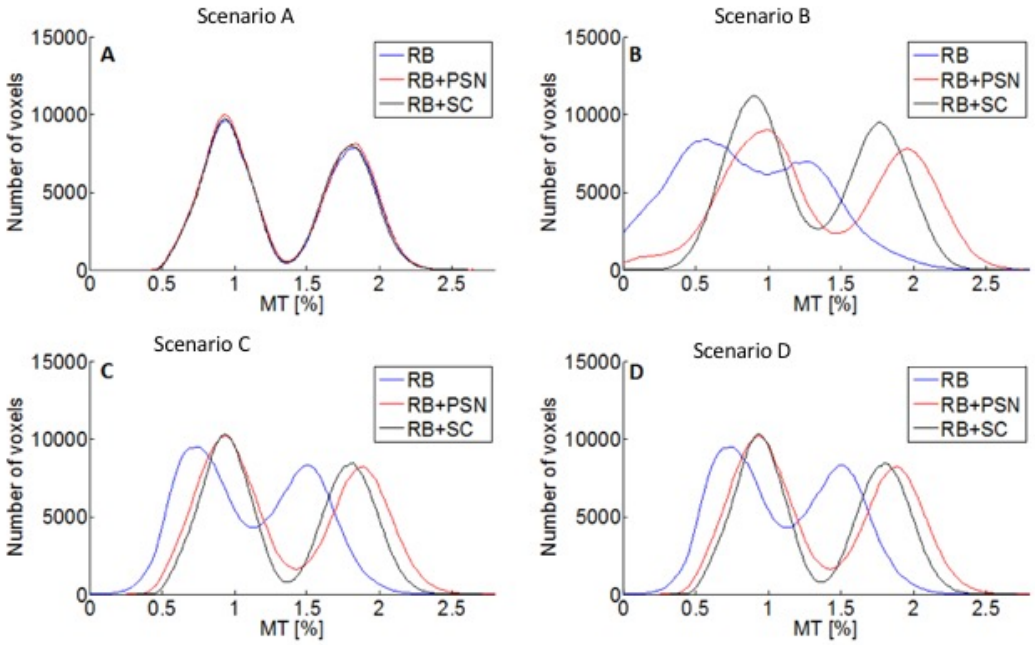

Figure III.15: Histograms of MT estimated in the four motion scenarios (A,B,C,D) using all three correction methods for volunteer 2. Inter-scan motion introduces large effects (C,D). RB+PSN reduces the loss in precision, but introduces a bias for higher values. RB+SC corrects for both the loss of precision, and the offset bias.

III.5.4: Discussion

Inter-scan motion between different scans used in quantitative mapping can introduce prominent artefacts in the estimated maps, if inter-scan motion is addressed only by rigid body co-registration, and the changes in the effective receive sensitivity are not accounted for in a dynamic, scan-to-scan manner. A method was introduced that additionally accounts and corrects for said changes, and compared to a vendor provided method of image intensity flattening, which did not account for dynamic changes.

III.5.4.1: Inter-scan motion effects and their correction in R1 mapping

In R1 mapping, inter-scan motion introduced a bias that was greater than scan-rescan variability. NRMSE was doubled compared to the scan-rescan experiment, from ~10% to ~20%. If PSN was used in conjunction with rigid body co-registration (thus, as per Equation III.10, the receive sensitivity estimated in the first position is used to correct in the second position), RMSE was reduced to ~11%, a level comparable to scan-rescan variability. If the sensitivity maps estimated in the matching position were used to dynamically correct for inter-scan related sensitivity effects, as in the RB+SC method, NRMSE was reduced below scan-

rescan variability, to an average of ~8% across the two inter-scan motion scenarios. In terms of RMSE, the two correction methods in which receive sensitivity is taken into account introduced a bias that was significantly lower (~2.5%) than the standard scan-rescan variability. In all motion cases, additional sensitivity correction outperformed PSN.

The inhomogeneity of estimated R1 values was greatly increased by inter-scan motion in the absence of sensitivity correction, marked by an increase in CoV of ~64% in gray and ~62% in white matter, respectively. PSN reduced this increase by half, to ~30% and ~23%, while sensitivity correction reduced this increase to a level comparable with that in scan-rescan experiments, ~10% and ~6% respectively.

Visual image quality was also greatly affected by inter-scan motion, due to the change in the RF receive sensitivity field. The superficial cortical areas, where the sensitivity gradient was steep (e.g. the frontal cortex, as seen in Figures III.9C and III.10), showed the greatest bias, but significant biases were observable throughout the brain. Due to the rapidly varying nature of the receive sensitivity, even small motion could lead to appreciable signal changes, particularly in areas close to the head coil, like superficial grey matter. Additional receive sensitivity correction did not alter visual quality of R1 maps estimated in an inter-scan motion scenario (Figure III10a and c), while the apparent bias due to inter-scan motion was successfully corrected for (Figure III.10b, and d).

III.5.4.2: Inter-scan motion effects and correction in MT mapping

Given the chosen study design (necessitated by how long participants could spend in the scanner), scan-rescan variability in the absence of motion was not measured for MT maps. Under all but one data combination scenario (scenario A), MT was affected by inter-scan motion. Highest NRMSE was observed when both the PDw and T1w scan were in a different position from the MTw scan. This NRMSE was reduced to approximately half by PSN, and to a third by additional receive sensitivity correction. If only the T1w or PDw scan were in a different position, NRMSE was accordingly lower, however the trend of sensitivity correction reducing the NRMSE more than PSN was also observed here. In the absence of inter-scan motion the NRMSE introduced by the proposed sensitivity correction method was comparable to that of PSN.

The inhomogeneity of estimated MT values was greatly increased by inter-scan motion, with an increase in CoV of ~76% in grey and ~36% in white matter, respectively for the scenario most affected by inter-scan motion, with respect to the no inter-scan motion case. This effect was reduced to ~26% and 15% in grey and white matter, respectively, when PSN was used, and to ~10% and 3% if additional sensitivity correction was performed.

Visually, the same trend could be observed on the MT maps as described for the R1 maps. Additional sensitivity correction did not introduce appreciable image quality degradation in the absence of inter-scan motion, and lessened the impact in the presence of inter-scan motion.

III.5.4.3: Inter-scan motion effects and correction in PD* mapping

In the estimation process for PD*, the receive sensitivity is estimated and corrected for based on the UNICORT approach (121), and PD* values are re-scaled, such that the mean PD* value for white matter is 69% (19). Inter-scan motion effects are thus lessened even if only rigid-body motion correction is used, as offsets in the PD* value of white matter are corrected for via this re-scaling. An appreciable offset in the PD* estimated in grey matter was detected for the two inter-scan motion cases and rigid-body motion correction, which was corrected for by additional receive sensitivity correction.

III.5.4.4: Additional considerations

The potential inter-scan motion between the two short calibration scans used for receive sensitivity estimation and the subsequent high-resolution scan, was not accounted for in terms of receive sensitivity contributions. Due to the short acquisition time of the receive sensitivity calibration scans and the sequential nature of these scans, it can be assumed that, compared to the magnitude of instructed inter-scan motion, no inter-scan motion took place. Due to their short duration, it can be assumed that the calibration scans are less sensitive to intra-scan motion than the high-resolution scans. Ideally, the two low-resolution calibration scans would be combined with the high-resolution scan, translating inter-scan motion into intra-scan motion.

The method described in this Chapter does not correct for intra-scan motion. Thus, some effects in NRMSE and CoV that were ascribed to inter-scan motion may be due to intra-scan motion. However, as experienced volunteers were imaged in this study with an express instruction to stay still, it can be assumed that even if intra-scan motion affected the estimated quantitative maps, there was no differential effect of intra-scan motion across the four motion cases, thus the overall impact on inter-scan motion remains unchanged, and dwarfed by the impact of inter-scan motion.

The receive sensitivity field is estimated in the proposed sensitivity correction method based on the assumption that the receive sensitivity of the body coil has a flat profile. Deviations from this assumption will lead to residual errors that are not corrected by the

method. However, as the receive sensitivity field of the body coil can always be assumed to be flatter than the head coil, the proposed correction method will always lead to an improvement.

The proposed method does not address the effect of inter-scan motion on the transmit field. This issue is addressed further in the next section.

III.6: Inter-scan motion related changes in the transmit field

III.6.1: Introduction

In this Chapter, the assumption has been made that inter-scan motion does not affect the transmit field. In Equations III.6-III.9, this is explicitly stated by $\alpha(r') = \alpha(r)$. To validate this assumption, during the study described in section III.5, the effect of inter-scan motion on the transmit field was investigated on three of the five participants.

III.6.2: Methods

For three of the five participants of the study, the transmit field was mapped in the second position, after inter-scan motion and the acquisition of T1w and PDw scans, with the method described in the previous section III.5. The EPI images used in the calculation of the transmit field in the second position were co-registered to those used in the calculation of the transmit field in the first position, and the same was done for the B_0 maps, such that the resulting B1+ maps were in the same space for each participant. The B1+ maps were masked using the tissue probability maps described in section III.5.2.

The difference between the first and second position B1+ maps were compared to the difference maps for R1. For this comparison, the B1+ were masked with the same conjunction of all probability maps, with a probability threshold of 35%, as was applied to the quantitative maps in section III.5. To compare the NRMSE of the B1+ maps to that of the quantitative maps, the same probability map was applied, using a treshold of 95%, and the NRMSE of the second position B1+ map, compared to the first position B1+ map, was calculated.

III.6.3: Results

NRMSE of the masked B1+ map acquired in the second position, as compared to the masked B1+ acquired in the first position was 0.69±0.27 % (mean±sd over the three participants).

Compared to the difference map in R1 values estimated in volunteer 2 between the first identical position case and the first inter-scan motion case, the difference map between the B1+ map acquired in the first and second positions is flat, as shown in Figure III.16.

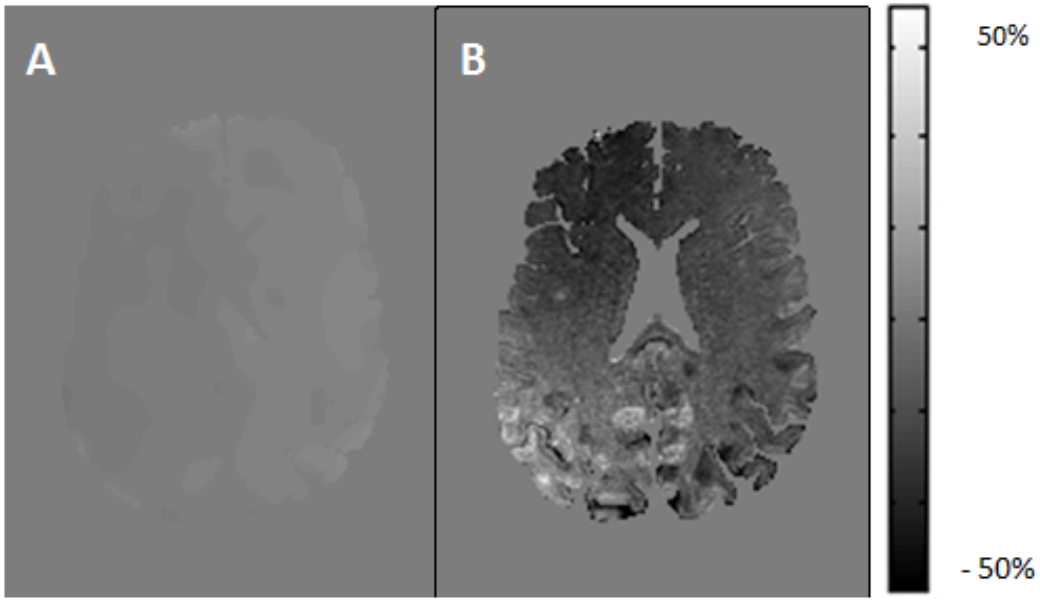

Figure III.16: Differences between first position and second position B1+ maps (A) and R1 maps estimated in the first identical position case and first inter-scan motion case (B), for volunteer 2. The same windowing is used for both maps.

III.6.4: Discussion

Errors in the estimation of the B1+ field propagate through to the map of R1 in a quadratic manner (17). As the NRMSE due to inter-scan motion was an order of a magnitude higher than the NRMSE observed in the B1+ map, the changes in the RF transmit field cannot be the main source of inter-scan motion artefacts in R1.

Additionally, the differences in the B1+ maps appear almost flat on the same scale as differences in R1 map, further highlighting that the transmit field is not significantly affected by inter-scan motion, when compared to the receive field effects on R1.

Thus, on the spatial scale of inter-scan motion investigated in this Chapter, the assumption that $\alpha(r')=\alpha(r)$ can be considered reasonable.

III.7: Conclusion and recommendation

This Chapter assessed the effects of inter-scan motion on quantitative parameters estimated as part of the MPM protocol. Inter-scan motion affects the signal intensity modulations arising from the receive sensitivity field of multi-channel head coils, as detailed in the Theory section.

This leads to errors in the estimation of quantitative MR parameters, if more than one scan is used in the estimation process, such as when quantifying R1.

Vendor-specific methods are available to correct for the image intensity variation due to the variations in the receive field. In this thesis, the Siemens-specific correction method, termed pre-scan normalize (PSN), was investigated for use in inter-scan motion correction. Due to the particulars of its implementation, this was not found to be feasible with the precision required by the MPM protocol. The receive sensitivity is mapped as part of the general adjustment procedure at the start of the scan, but not updated during the session. Inter-scan motion effects are thus not taken into account. It is not possible to re-measure the receive field alone, only as part of a general re-adjustment. Thus, the sensitivity maps are either reproducible, or dynamically updated, but not both.

A method was thus developed to map, and correct for the contributions of the receive sensitivity field to the quantitative maps estimated in the MPM framework.

This method was validated in-vivo, and performed better than pre-scan normalization in reducing bias due to inter-scan motion. Of the maps estimated in the MPM framework, R1 and MT were the most affected by inter-scan motion, and for both quantitative map types, additional correction for receive sensitivity reduced the errors. Within session scan-rescan variability was measured for R1, and the proposed correction method reduced the effect of inter-scan motion to a level comparable to scan-rescan variability. Without correction, the changes in these quantitative values due to inter-scan motion were comparable, or in excess to those measured in pathology (76–78), and thus clinically unviable, while with inter-scan motion correction, they were below those observed in healthy aging (21,176,243).

The effect of inter-scan motion on the transmit field was also investigated, and the contributions of it to the accuracy and precision of R1 maps was found to be an order of magnitude lower than that of the receive field. It must be noted, however, that for higher field strengths, inter-scan motion effects on the transmit field may have bigger contributions, due to the lower transmit field homogeneity, compared to transmit field at 3T (244,245).

The limitations of the proposed technique include the increased scan time (by approximately 30 seconds per high-resolution FLASH scan, not including the calibration steps of the scanner), the need to acquire the two short scans used for inter-scan motion correction

separately each high-resolution FLASH scan, and the susceptibility of the sensitivity mapping to motion during scanning.

As discussed preciously in this Chapter, receive sensitivity information is used in the SENSE framework of parallel imaging. In common applications, the receive field is mapped only once per session. While this approach was not investigated in this study, it may be possible to combine a dynamically updated SENSE reconstruction framework with the proposed method, by deriving the magnitude of the receive field from the complex sensitivities estimated in the SENSE framework.

For best practice, I recommend that, in quantitative MRI studies, the transmit field be mapped only once, provided the study is carried out at a field strength of 3T, and that the receive field be mapped in a way similar to that described in this study. However, if the receive field can only be mapped once, the effects of inter-scan motion would still be reduced by incorporating this into the estimation of R1, MT and PD* parameters. Thus, it is recommended that quantitative data be acquired with the image intensity flattening technique available on SIEMENS scanners. I have not investigated the solutions provided by other vendors, but a short phantom study, such as the one outlined in III.3 may be used to evaluate their utility in inter-scan motion correction.

Chapter IV: Reducing motion sensitivity

IV.1: Introduction

One of the goals of the PhD project was to prepare the MPM protocol for clinical deployment. This necessitated addressing two key issues: motion sensitivity, and scan time. In the first part of this Chapter, a study is presented, aimed at finding the least motion-sensitivity k-space trajectory from a set of existing trajectories that can be reconstructed on the scanner without additional modification. In the second part, a study is presented, aimed at investigating the effect of various acceleration methods on image quality, quantitative values, and clinical utility.

IV.1.1: The interaction of motion trajectories and k-space trajectories

High-resolution, 3D structural MRI scans, such as the ones used in this PhD project, are acquired on a timescale of minutes. This results in motion being a significant source of artefacts (187), as the images are not acquired instantaneously. However, acquisition time is not the only factor determining the sensitivity of a given acquisition to motion. The order in which k-space is filled is another important factor.

In conventional MRI acquisition methods for structural scans, k-space is traversed in an ordered fashion, with data points in the frequency-encoded direction acquired on the timescale of milliseconds, which, relative to the timescale of the phase-encoded directions, may be treated as being acquired instantaneously (222). The phase-encoded direction(s) are acquired on a timescale orders of magnitudes higher. For example, in the 3D FLASH acquisitions used in the MPM protocol, k-space is filled sequentially, with all the k-space points in the first phase encoded direction acquired before the next point is acquired in the second phase encoded direction. The distance between two k-space points acquired in the first phase encoded direction is one TR, 25 ms, while, in the absence of acceleration, the distance between two points in the second phase encoded direction is ~200 TRs, or five seconds. In addition, not all k-space points contribute equally to the final image, and as such, the same type of motion might result in very different artefact levels, depending on when the motion took place.

The interplay of motion trajectories enacted by the participant, the k-space trajectories used to traverse k-space, and the differential weighing of k-space points results in a theoretically infinite problem space. To restrict the problem space of the study, realistic trajectories, derived from participants of another study carried out at the Birkbeck-UCL Centre for Neuroimaging were used in conjunction with a set of k-space trajectories already implemented within the FLASH sequence.

IV.1.2: Speedup methods for MRI acquisitions

MRI acquisition times can be reduced by sampling only a part of k-space. In this Chapter, three such methods are employed: parallel imaging, partial Fourier imaging, and elliptical coverage. The underlying concepts and implementations are discussed in Chapter II. Thus, only a short review is offered in this Chapter.

Parallel imaging relies on the inherent redundancy of multi-channel coils, in order to reconstruct missing lines in k-space. To reconstruct a full field of view (FoV) of the imaged object from a single coil, all k-space data has to be acquired. If, for example, every second line of k-space is skipped in a sequential manner, the resultant image is an aliased image of size FoV/2 (Figure IV.1):

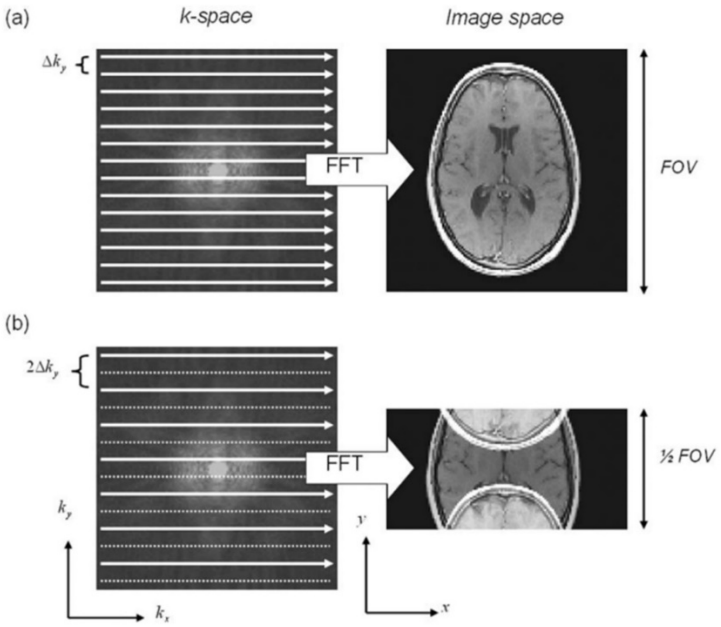

Figure IV.1: Anatomy reconstructed from a fully sampled k-space (a), and from a k-space acquired with an acceleration factor of 2 (b). Dashed lines of k-space are skipped, leading to the folded appearance of the anatomy in image space. Image reproduced from (58)**.**

If multiple different, aliased views of the original object are acquired using a multi-channel coil, the missing data can be estimated with the help of coil sensitivity data, and a full FoV image can be reconstructed. In this Chapter, the GRAPPA reconstruction method (60) is used, in which a weighing kernel, representing the contributions of the different coil sensitivities to the k-space data, is derived from a fully sampled central portion of k-space, and the missing data points are estimated on a channel-by-channel basis in k-space.

Partial Fourier imaging exploits the symmetry of k-space (34). In theory, the objects imaged in MRI are real valued, and thus the corresponding k-space is conjugate symmetric.

Given this theoretical conjugate symmetry, only half of k-space would need to be acquired, with the missing half reconstructed via complex conjugation, thus halving scan time.

Unfortunately, several sources, such as motion, flow effects and variations in local susceptibility violate the assumption that the detected signal is real valued. Thus, it is necessary to correct the phase inconsistencies in order to avoid image artefacts. As a result it is typical to acquire more than half of k-space, e.g. 6/8 or 7/8 and use these data to estimate the phase in a manner consistent with the acquired data. In practice, for ease of computation, the missing data are often simply left as zeros.

High-frequency k-space points, located at the outer rim of k-space, are of low k-space energy, that is, these points contribute weakly to the contrast of the final image. Scan time may be reduced by not acquiring the k-space points located outside an ellipsoid, hence the name of this method: elliptical k-space coverage (Figure IV.2).

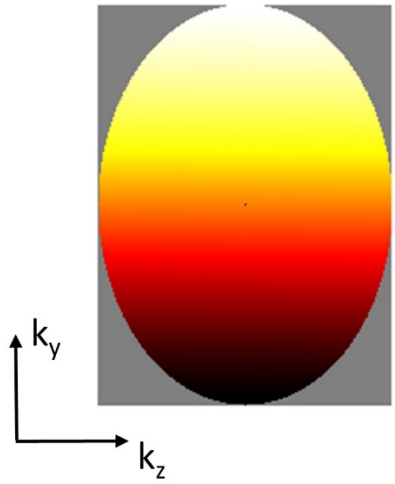

Figure IV.2: Elliptical coverage of k-space. Data is acquired sequentially (red to white). K-space lines in grey are skipped.

All three acceleration methods have an impact on image quality. Fundamental to all is a loss of SNR due to the relative loss of acquired data, as compared to a fully sampled image.

For parallel imaging, this effect is compounded by the g-factor, or geometry factor, dependant on the correlation of the detected signal across coils (and thus, the coil's geometry). The SNR of an image acquired with an acceleration factor r, is:

$$SNR_r = \frac{SNR_1}{g\sqrt{r}} \qquad \text{[IV.1]}$$

Where SNR_r is the SNR of the image acquired with parallel imaging, and SNR_1 is the SNR of the image acquired in the absence of parallel imaging.

With high-frequency points in k-space being skipped, both partial Fourier and elliptical coverage may suffer from blurring in image space, with additional ringing for partial Fourier acquisitions due to truncation of comparatively high k-space energy data points.

These drawbacks place a limitation on how far scan times can be reduced. In addition, reconstruction of undersampled data is computationally expensive, placing an additional limitation on clinical viability, and forcing a trade-off between reconstruction speed and quality. Ultimately, these limitations meant that a relatively modest acceleration factor of 4 was chosen for the scans acquired during the PhD project.

IV.2: Finding the least motion sensitive k-space trajectory available

IV.2.1: Introduction

One method of reducing the sensitivity of a given MRI scan to motion is to find the least motion-sensitive acquisition trajectory, that is, the traversal of k-space that results in the least amount of image artefacts for a given type of motion (motion trajectory). Ideally, the k-space trajectory would be updated on a TR to TR basis, thus being individually tailored to each patient and scan, to account for the effect of motion (246). For clinical purposes, such an arrangement is unsuitable, due to the need to both monitor motion, and the limitations of the acquisition and reconstruction algorithms employed by clinical scanners.

A study was performed to find the optimal k-space trajectory from a pre-existing set of trajectories that can be acquired and reconstructed on clinical scanners. Realistic motion trajectories were derived from data acquired at a partner site, and were used to synthetize motion-corrupted data using a previously published method (247). The impact of this simulated motion was evaluated using image quality metrics in order to find the least motion-sensitive k-space trajectory.

IV.2.2: Methods

IV.2.2.1: Motion trajectory acquisition and processing

Motion trajectories used in this study were acquired by Dr. Uri Hertz at the Birkbeck-UCL Centre for Neuroimaging (BUCNI) during a study consisting of both functional EPI and structural 3D MDEFT scans (248). During this study, a total of 69 scanning sessions were acquired on a pool of untrained, but compliant volunteers (age range: 18-24; mean age 19; 49f, 20m). These motion trajectories can thus be used to simulate typical participant motion during scanning. The dataset will be referred to as the BUCNI dataset in the remainder of this Chapter.

The trajectories were acquired using a system (Metria Innovation, WI, USA) , in which a high-speed camera (Kineticor, HI, USA), installed in the scanner bore, tracked a Moire phase marker fixed to the forehead of the participants at a frame rate of 80 Hz (198). The position of the marker can be tracked with a precision of tens of microns and hundredths of degrees. The position, logged as millimetres for translations and quaternions for rotations, was saved into log files on the host PC of the camera system. The system was designed to prospectively correct for head motion by dynamically changing the acquisition parameters in accordance

with the movement of the marker. However, in the case of the study conducted by Dr. Uri Hertz the system was used only to track, but not correct for, participant motion. A similar camera system has been used in conjunction with the MPM protocol to correct for participant motion (197).

As the log files of the BUCNI dataset were saved in the frame of reference of the camera, and with the default framerate of the system, several processing steps were necessary before they could be used to synthetize motion. First, the log files were transformed into a MATLAB compatible format. All further processing was performed in a MATLAB environment. The motion trajectories were then transformed from the camera's frame of reference into the frame of reference of the scanner, using a calibration file stored on the host PC of the camera system. In the next processing step, the rotation parameters were transformed from quaternions to Euler angles, using a processing script provided by Metria Innovation. During this processing step, several log files failed to process. This issue was traced to a set of logs acquired close in time, all of which were characterised by un-normalised rotation quaternions, and unrealistic motion trajectories, including sudden translations of several centimetres, or flat, unchanged trajectories for several minutes (Figure IV.3). These logs were eliminated from further processing leaving 36 unique datasets. Finally, all successfully transformed logs were down-sampled to the TR of the FLASH acquisition (25 ms), corresponding to a sampling frequency of 40 Hz.

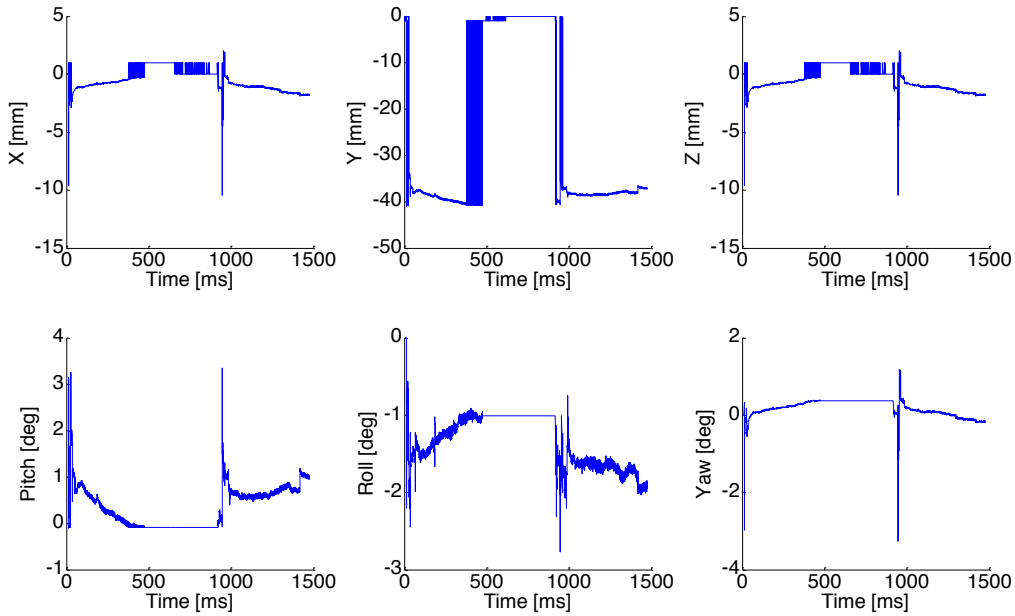

Figure IV.3: An exemplar of the unrealistic, rejected trajectories. Note the jumps in the Y and Z traces, as well as the flat, unchanged trajectory in the middle.

The transformed logs were sorted according to a mean distance metric, $\overline{D}$, defined as:

$$D(t) = \sqrt{(x(t) - x_0)^2 + (y(t) - y_0)^2 + (z(t) - z_0)^2} \quad \text{[IV.2a]}$$

$$\overline{D} = \sum_{t=1}^{N-1} D(t) \quad \text{[IV.2b]}$$

where x(t),y (t),z (t) are the values of the appropriate motion trace at time point t, and x_0,y_0,z_0 is the initial position, and N is the number of TRs in the acquisition. Based on this sorting, the logs were further divided into quartiles. For each quartile, the log with the median $\overline{D}$ value of said quartile was chosen as a representative motion trajectory, which was then further split into the first and second five minutes. For the simulations, the first five minutes were used as a surrogate for motion during the beginning of a scanning session, while the second five minutes were used as a surrogate for motion during the middle of a scanning session.. Thus, eight motion trajectories were created in total, named e.g. Q1 1st or Q4 2nd etc., where Q denotes the quartile of which the trajectory is representative, and 1st or 2nd denotes the first or second five minutes of the trajectory. Lastly, the log files were transformed into difference logs with regards to the first logged position, in compliance with the format of the motion trajectories as logged on the scanner, in order to prepare them for use in synthetizing motion.

IV.2.2.2: Image acquisition

A Siemens structural phantom (SIEMENS Multipurpose Phantom E) was used in this study. This plastic phantom had a complex internal structure, and was filled with a solution of 1.25g $NiSO_{4,aq}$ and 5g NaCl per 1000 ml, providing excellent image contrast, and was thus well suited for the study.

The phantom was imaged using the T1-weighted scan of the MPM protocol, using three different k-space trajectories. The common imaging parameters were: Field of view=256 (frequency encoded, head-foot) x 240 (phase-encoded, anterior-posterior, “lines” direction) x 176 (phase encoded, left-right, “partitions” direction) mm, flip angle=21°, PPI acceleration factor: 2x2, with 40 reference lines in each direction, TR=25 ms, T_{acq}=5 min. The difference k-space trajectories were: “Partitions inside lines”, where k-space is filled in the left-right direction first, “lines inside partitions”, where k-space is filled in the anterior-posterior direction first, and “square spiral”, where the central portion of k-space is acquired first, as shown in Figure IV.4.

The phantom was imaged both in the absence and presence of simulated motion, for a total of nine scans per simulated k-space trajectory.

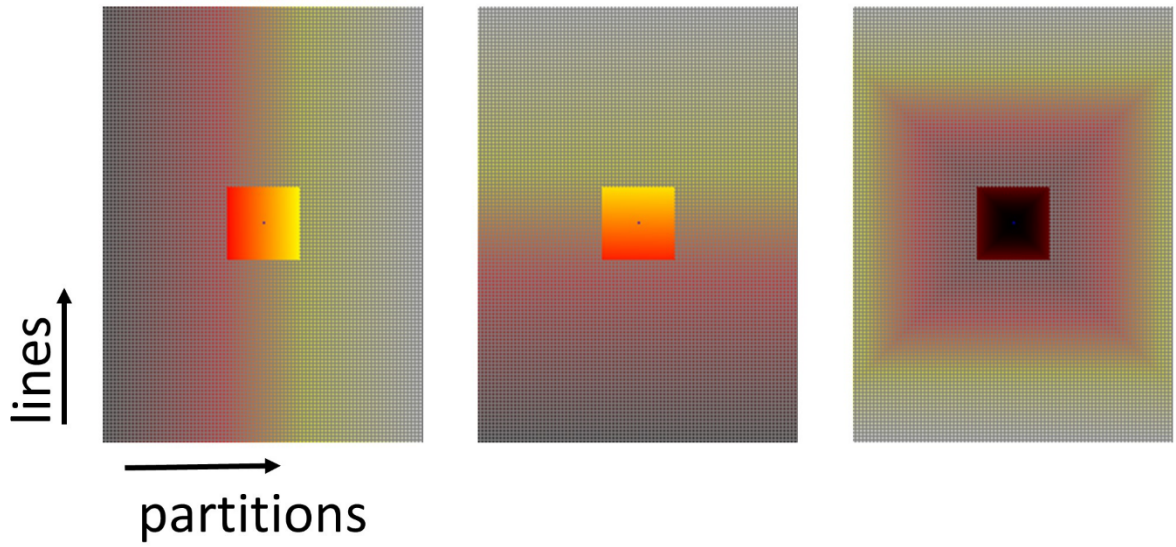

Figure IV.4 The three k-space acquisition trajectories: lines inside partitions (left), partitions inside lines (centre), square spiral (right). Acquisition times are colour coded, from dark (earlier) to bright (later), black points are skipped. The frequency-encoded dimension is perpendicular to the plane.

IV.2.2.3: Simulating motion

If the PMC system is used in conjunction with a bespoke version of the sequence that incorporates communication between the scanner and the camera system, the motion is logged on the scanner as well. The feedback functionality can be used to change sequence parameters such as gradient amplitudes and RF phase even in the absence of actual motion, thereby simulating motion (247). In this study, the representative motion trajectories generated from the BUCNI dataset were used to generate motion-corrupted acquisitions. It must be noted that this is not a full simulation of the effects of motion, as the receive sensitivity is constant over the acquisition, while in the case of real motion, the movement of the head in the receive coil would induce signal intensity changes related to the change in the relative receive sensitivity. Motion-related changes in the shim field are likewise not accounted for.

IV.2.2.4: Image quality metrics

The impact of synthetic motion was evaluated both qualitatively and quantitatively. Qualitatively, the images were investigated for the ringing artefacts characteristic of motion. Quantitatively, two image quality metrics were used to characterise the artefact level: image entropy and average edge strength.

Image entropy (222) is defined as:

$$E = \sum_{p=1}^{n_p} \frac{I_p}{I_{total}} ln\left(\frac{I_p}{I_{total}}\right) \quad [IV.3]$$

where index p denotes image pixel, n_p is the total number of pixels, and I_p is the image intensity, and I_{total} is the total image energy, given by

$$I_{total} = \sqrt{\sum_{p=1}^{n_p} {I_p}^2} \quad [IV.4]$$

Average edge strength (AES) (241) is defined as:

$$AES(z) = \frac{\sqrt{\sum_p E\left(I_p^z\right)\left\{\left[G_x\left(I_p^z\right)\right]^2 + \left[G_y\left(I_p^z\right)\right]^2\right\}}}{\sum_p E\left(I_p^z\right)} \quad [IV.5]$$

where I_p^z is the image intensity at pixel p and slice z, and G_x and G_y are the convolutions with x and y edge detection kernels, and $E\left(I_p^z\right)$ is a binary image consisting of the edges in image I at slice z. In order to maximize sensitivity to motion artefacts, average edge strength was calculated along the frequency-encoded head-foot direction, thus x and y in Eq. IV.5 are the two phase-encoded directions, left-right and anterior-posterior.

The mean (mAES) and standard deviation (sdAES) of AES along the chosen slice direction were used as the image quality metrics.

To properly evaluate the utility of these image quality metrics for characterising the impact of motion on image quality, image entropy and mAES were calculated on a subset of images, in order to find the metric with the greater dynamic range.

IV.2.2.5: Image processing

The difference in the acquisition time of the k-space centre between the different trajectories resulted in an apparent change in position for the images acquired with square-spiral sampling, compared to the other two trajectories. To address this issue, all images were co-registered to the image acquired with no simulated motion, and using a partitions inside lines k-space trajectory.

The image quality metrics were calculated on images with three levels of masking, each with different sensitivity to image artefacts. At the first level, no masking was applied ("unmasked image"). In this case, the image quality metrics measured not only the decrease in image quality in the volume of the phantom, but also the change in artefact level outside the phantom. At the second level, a simple intensity thresholded mask was created on the scan acquired in the absence of simulated motion and with a partitions in lines trajectory ("masked image"). This mask covered the MR visible parts of the phantom, but did not include

the internal voids, and was thus was not sensitive to signal mis-allocation into the voids. The third mask was derived from the second mask by iteratively filling the internal voids until all of the volume of the phantom was masked in ("masked and filled image"), thus being sensitive to all increase in artefact level over the volume of the phantom.

IV.2.3: Results

IV.2.3.1: Visual image quality

The simulated motion had a clear and apparent impact on the acquired images. In line with expectations, the different trajectories were differently sensitive to motion (Figure IV.5), with the characteristic ringing pattern appearing in the slow phase-encoded direction for partitions inside lines, or lines inside partitions trajectories.

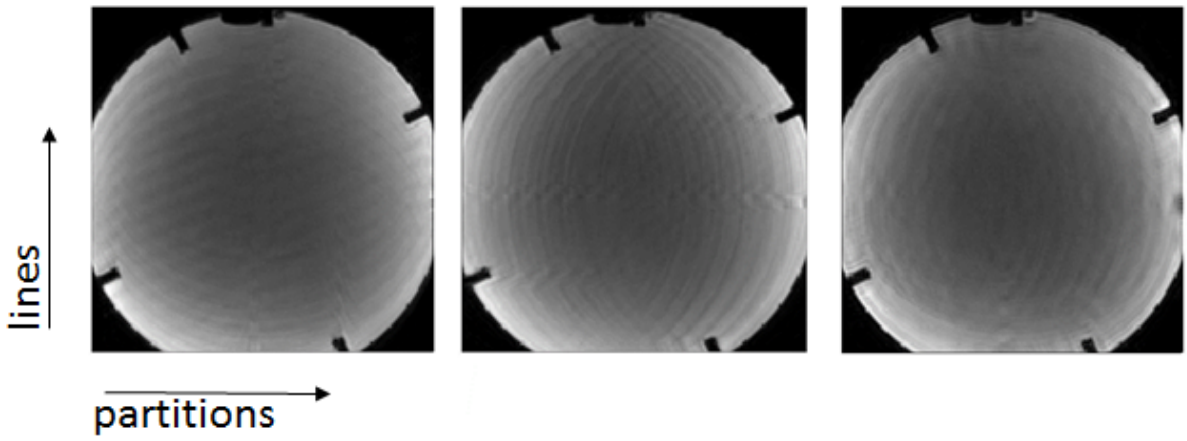

Figure IV.5: A sagittal view of the same phantom, with the same synthetic motion, images using partitions inside lines (left), lines inside partitions (centre), and square spiral (right) trajectories. Note the change in the direction of the characteristic ringing artefact, as the slow and fast encoding directions flip. The ringing artefact for the square-spiral trajectory appears as an interference pattern of the previous two artefacts, in line with expectations.

IV.2.3.2: Dynamic range of image quality metrics:

The dynamic range of an image quality metric, defined as the difference between the lowest and highest measure, divided by the mean measure, was calculated for both metrics on unmasked images acquired with the "partitions inside lines" k-space trajectory and the first five minutes of each representative motion trajectory, summarized in Table IV.1.

The dynamic range for image entropy was found to be 6% in this specific subset of images, while the dynamic range of mAES was 76%. Thus, only mAES was used as the image quality metric in further processing steps.

Motion trajectory	Image entropy	mAES
Q1 1st	11648	32.7
Q2 1st	11883	27.7
Q3 1st	11438	38.6
Q4 1st	11574	41.7
No motion	11185	57.9

Table IV.1: Image quality metrics for partitions inside lines k-space trajectory, and for motion trajectories.

IV.2.3.3: Quantitative impact of motion

The image quality metrics of mAES±sdAES were calculated for all combinations of motion and k-space trajectories and masking cases, and are presented on Figures IV.6-IV.8. In the absence of motion, all three k-space trajectories produced images with comparable mAES values. In the presence of motion, the images acquired with the partitions inside lines trajectories showed the highest mAES values in most motion cases, indicating the least amount of quantifiable image artefact. In most cases, the square spiral trajectory showed the lowest mAES values, indicating that this k-space trajectory is the most sensitive to motion.

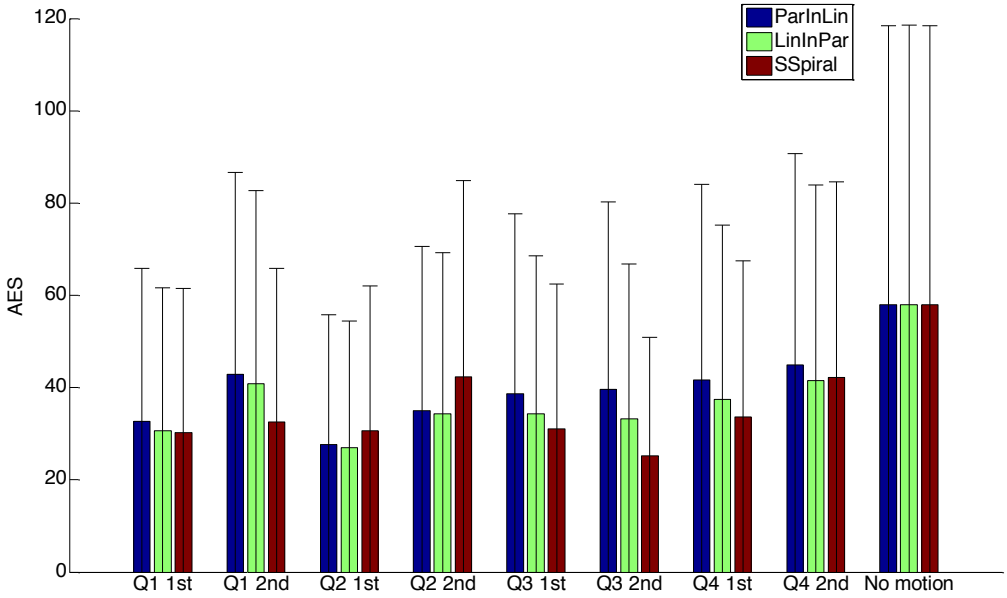

Figure IV.6: mAES±sdAES values for the unmasked images.

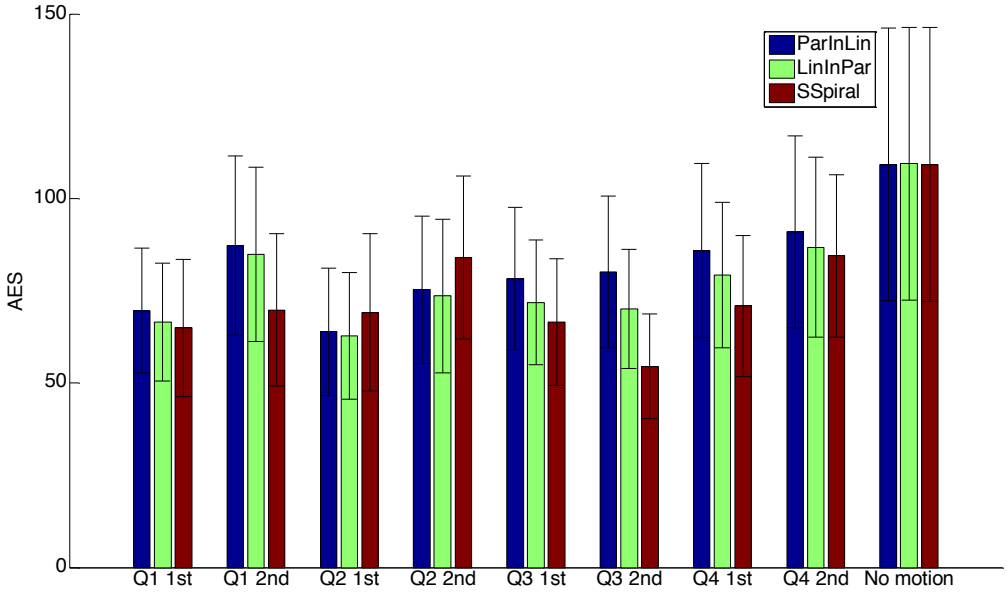

Figure IV.7: mAES±sdAES values for masked images.

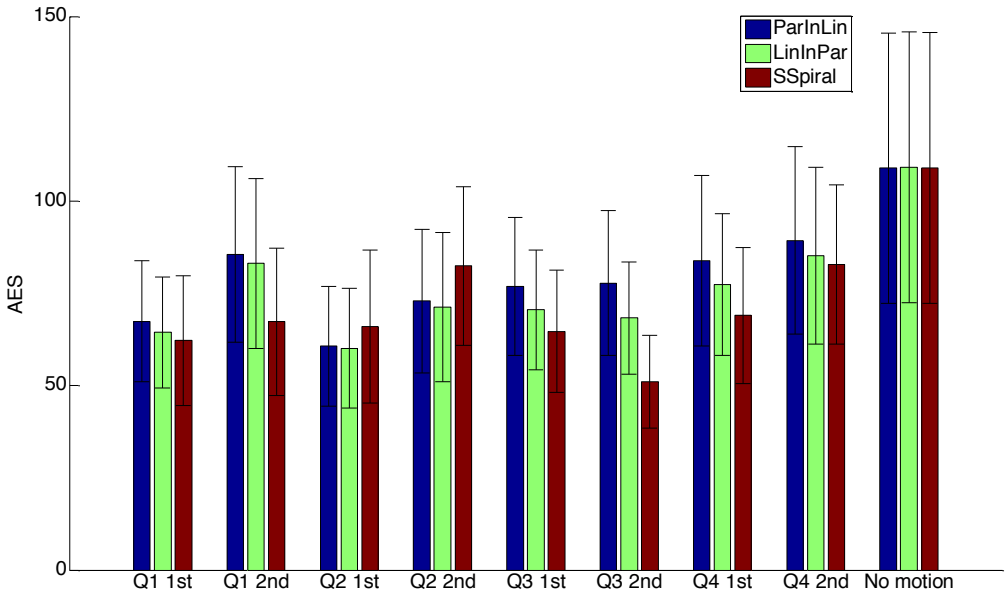

Figure IV.8: mAES±sdAES values for masked and filled images.

IV.2.4: Discussion

The motion trajectories used in this study were acquired in the absence of motion instructions, and thus describe participant motion when directed to stay still. Despite this, the motion trajectories, as characterised by their net displacement, cover a wide range, which is reflected in image quality when reproduced in a structural phantom. Thus, even when directly instructed to stand still, the natural motion of volunteers may result in significant image artefacts. It must be noted that this pool of volunteers is healthy, and younger than the average clinical population, thus the extent of clinical motion is likely to be in excess of that investigated in this study. The mode of motion observed in these volunteers was dominated by slow drifts, similar to previously reported motion trajectories of healthy volunteers (249). The motion of clinical patient groups may take different forms, and may be dependent on pathology (188,250). Thus, results presented in this chapter are not readily generalizable to clinical populations.

Average edge strength was, for all three levels of masking, highest for the no motion cases, and was decreased by motion, in line with expectations. Masking increased AES across all cases, as the artefacts pushed into the noise region were excluded from the calculation.

In the absence of simulated motion, all three acquisition schemes performed equally well. This indicates that there is no inherent difference in image quality, thus the subsequent results are not biased by unequal reconstruction performance. However, it was necessary to

co-register all images to a baseline image. The choice of this baseline image as the one acquired using a partitions inside lines k-space trajectory may have been a source of bias.

For all three levels of masking, the partitions inside lines k-space trajectory outperformed the other two k-space trajectories for six motion trajectories out of eight. Thus, during the PhD project, scans were acquired using a partitions inside lines k-space trajectory.

During this chapter, the field of view of the acquisitions was not rotated. Scans were acquired using a true axial orientation, with the phase and frequency encoded directions parallel to the principal axes of the scanner. In addition, the motion trajectories used to simulate the effect of motion were acquired in a head first, supine position. The results presented in this chapter are only valid for such an arrangement. If the field of view is rotated, the encoding axes are rotated as well, compared to the main modes and directions of head motion, influencing the relative motion sensitivity of different k-space trajectories, and a different k-space traversal scheme may be found to be the least motion sensitive. During this PhD project, all scans were acquired using a true axial field of view, thus for the studies presented in this thesis, the conclusions of this chapter are valid. For other orientations of the field of view, of for other patient positions, a similar study would have to be performed to find the best performing k-space trajectory out of those readily available on the scanner.

It must be noted that for all levels of masking, the trend in AES values did not follow the ranking of the motion trajectories, despite expectations to the contrary (for example, AES values for the acquisitions with the simulated motion trajectories of "Q2 1st" and "Q2 2nd" were lower than the AES values of the acquisitions with the simulated motion trajectories "Q1 1st" and Q1 2nd"). Thus, using the $\overline{D}$ metric to rank motion trajectories is not sufficient. This issue was investigated further in the next section.

IV.3: Motion trajectories and k-space energy

IV.3.1: Introduction

In Chapter IV.2, the least motion-sensitive k-space trajectory (out of the set of readily available trajectories) was found. However, the rankings of the BUCNI motion trajectories were not reflected in the image quality metrics of the scans acquired with said simulated motion trajectories. Further analysis was performed to better characterise the motion traces, as well as the interaction between the k-space trajectories, the motion trajectories, and image quality.

IV.3.2: Methods

In the acquisitions where synthetic motion was induced, the simulated motion traces were also logged by the system. These logs reflect the synthetic motion as experienced by the phantom. Thus, any potential experimental errors are present, and may account for the discrepancy between the ranking of the motion traces and the image quality metrics.

The logs were analysed by calculating two measures, an extended version of the distance metric:

$$D_{ext}(t) = \sqrt{(x(t))^2 + (y(t))^2 + (z(t))^2 + (pitch(t))^2 + (roll(t))^2 + (yaw(t))^2} \quad \text{[IV.6]}$$

And a speed metric:

$$\mathrm{S(t)} = \sqrt{\left(\frac{dx}{dt}\right)^2 + \left(\frac{dy}{dt}\right)^2 + \left(\frac{dz}{dt}\right)^2 + \left(\frac{dPitch}{dt}\right)^2 + \left(\frac{dRoll}{dt}\right)^2 + \left(\frac{dYaw}{dt}\right)^2} \quad \text{[IV.7]}$$

where translations are measured in millimetres and rotations are measured in degrees. The equal weighing of translations and rotations is equivalent to assuming the rotation takes place on a sphere of 57 mm radius, which is comparable with the size of a human head (196).

Mean and maximum of $D_{ext}(t)$ and S(t) values were calculated for all eight simulated motion trajectories.

It must be noted here that there was a discrepancy between the length of the image acquisition, and the length of the motion trajectories used to synthetize motion. There are 200 dummy cycles at the beginning of the acquisition, which were not taken into account. As a result, the last 200 k-space points were acquired in the absence of simulated motion, and the system reset the field of view to its original position.

While this did introduce a large, one-time motion, these data points are low energy k-space points, and are unlikely to significantly impact final image quality. The first 200 points on the logs were not taken into account in the further analysis, and the coordinates were

transformed into differences with regards to the 201st point (the first point during which MRI image data was acquired).

Two metrics were calculated to account for the different k-space energy of individual k-space points:

$$D_K = \sum_{t=0}^{N-1} D_{ext}(t) \cdot E_k(t) \quad \text{[IV.8a]}$$

$$S_K = \sum_{t=0}^{N-1} S(t) \cdot E_k(t) \quad \text{[IV.8b]}$$

where D_k distance-weighted k-space energy of the acquisition, S_k is the speed-weighted k-space energy of the acquisition, Dext(t) and S(t) are the extended distance and speed measures for time point t, and N is the number of TRs. $E_k(t)$ is the k-space energy for the t-th TR, defined as:

$$E_k(t) = \frac{M(t)}{\sum_{i=0}^{N-1} M(t)} \quad \text{[IV.9]}$$

where M(t) is the magnitude of the first echo of the t-th TR.

IV.3.3: Results

IV.3.3.1: K-space energy distribution

Figure IV.9 shows the k-space energy per TR of the “partitions inside lines”, and the “square spiral” acquisition trajectories. The edges of the central, fully sampled portion of k-space are highlighted. The ratio of k-space energy contained in the central, fully sampled portion is approximately twice the k-space energy contained in the outer, undersampled portion of k-space. The oscillatory nature of k-space energy per TR, best seen in Figure IV.9A reflects the ordered traversal of k-space, as the individual spikes reflect the central point of the k-space plane being traversed.

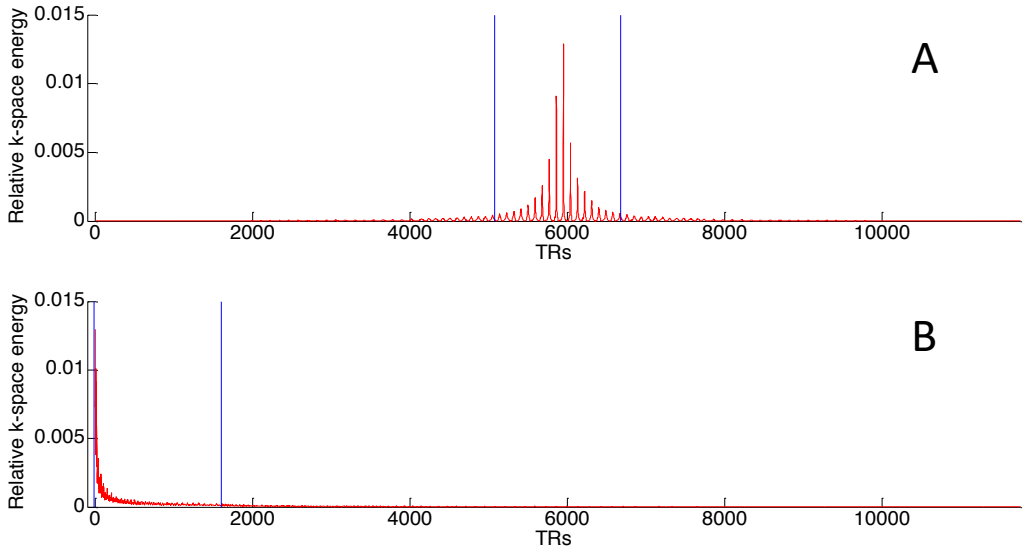

Figure IV.9: The relative k-space energy per TR for "partitions inside lines" (A) and "square spiral" (B) acquisition trajectories, with the central portion of k-space denoted between blue lines.

IV.3.2.2: Distance and speed rating of motion trajectories

Mean and maximum of the extended distance and speed measures, denoted as $\overline{D_{ext}}$, $D_{ext,max}$ and $\bar{S}$, S_{max}, respectively, for the eight motion trajectories are summarized in Table IV.2. The order of motion trajectories according to $\overline{D_{ext}}$ matches the original rating according to the simpler mean distance metric, $\bar{D}$. However, the order according to the other three measures does not match the original order.

Motion trajectory	$\overline{D_{ext}}$	$D_{ext,max}$	$\bar{S}$	S_{max}
Q1 1st	3.41	6.18	2.46	101.89
Q1 2nd	3.37	5.83	1.74	12.2
Q2 1st	2.67	4.61	3.17	101.71
Q2 2nd	1.16	4.23	2.18	20.38
Q3 1st	1.23	3.26	1.78	40.91
Q3 2nd	1.25	6.61	2.53	52.97
Q4 1st	0.68	2.21	2.14	71.03
Q4 2nd	0.55	1.50	1.66	16.42

Table IV.2: Mean and maximum speed and distance measures for the eight motion trajectories used in section IV.2.

IV.3.2.3: Ranking k-space energy weighted motion trajectory measures

The k-space weighted measures described in Equations IV.8a and IV.8b were calculated for all three trajectories, and compared with the mean average edge strength based ranking (from most corrupted to least corrupted), as calculated on the thresholded and void filled mask, as summarized in Tables IV.3-5. Pearson's correlation coefficient was calculated to compare these rankings with each other (Table IV.6).

Motion trajectory	D_K	Rank according to D_K	S_K	Rank according to S_K	mAES	Rank according to mAES
Q1 1st	4.358	1	2.046	5	67.4	2
Q1 2nd	3.996	2	1.831	6	85.5	7
Q2 1st	2.796	3	2.969	1	60.7	1
Q2 2nd	1.549	4	2.068	4	72.9	3
Q3 1st	1.199	6	1.778	8	76.9	4
Q3 2nd	1.252	5	2.677	2	77.8	5
Q4 1st	0.679	8	2.228	3	83.8	6
Q4 2nd	0.689	7	1.810	7	89.3	8

Table IV.3: K-space weighted speed and distance metrics, as well as mAES values for the "partitions inside lines" trajectory.

Motion trajectory	D_K	Rank according to D_K	S_K	Rank according to S_K	mAES	Rank according to mAES
Q1 1st	4.358	1	2.047	5	64.4	2
Q1 2nd	3.996	2	1.831	6	83.1	7
Q2 1st	2.797	3	2.969	1	60.1	1
Q2 2nd	1.549	4	2.068	4	71.2	5
Q3 1st	1.199	6	1.777	8	70.5	4
Q3 2nd	1.252	5	2.678	2	68.3	3
Q4 1st	0.679	8	2.226	3	77.3	6
Q4 2nd	0.689	7	1.807	7	85.2	8

Table IV.4: K-space weighted speed and distance metrics, as well as mAES values for the "lines inside partitions" trajectory.

Motion trajectory	D_K	Rank according to D_K	S_K	Rank according to S_K	mAES	Rank according to mAES
Q1 1st	1.581	1	2.932	2	62.2	2
Q1 2nd	1.118	3	1.725	6	67.3	5
Q2 1st	1.5	2	3.539	1	66	4
Q2 2nd	0.443	5	2.139	3	82.4	7
Q3 1st	0.435	6	1.623	7	64.7	3
Q3 2nd	0.544	4	2.116	4	51.1	1
Q4 1st	0.321	7	1.928	5	69	6
Q4 2nd	0.204	8	1.587	8	82.8	8

Table IV.5: K-space weighted speed and distance metrics, as well as mAES values for the "square spiral" trajectory.

Trajectory	Rank according to DK	Rank according to SK
Lines inside partitions	0.48	0.55
Partitions inside lines	0.48	0.55
Square spiral	0.62	0.38

Table IV.6: Pearson's correlation coefficient between rank according to k-space energy weighted distance and speed, and rank according to mAES.

IV.3.4: Discussion

To better characterize the impact of motion on an MRI acquisition, it is important to take several factors into account. The timing of motion influences the k-space energy corrupted by said motion, as can be seen when the rank according to D_K or S_K of the same motion trajectory is compared for motion trajectories where high k-space energy points are in the middle of the acquisition ("partitions inside lines" or "lines inside partitions"), or in the beginning of the acquisition ("square spiral").

The overall displacement ($\overline{D_{ext}}$) during a motion trajectory is likewise not enough to characterise a motion trajectory, as can be seen when the ranking according to overall displacement is compared with the ranking according to overall speed ($\bar{S}$).

Compared to the ranking according to image quality, S_K correlated better than D_K for the two trajectories with central portions of k-space acquired in the middle of the acquisition. However, even k-space weighted speed was not a perfect predictor of image quality as measured via mAES. This is likely due to the scans used in this study being under-sampled scans, where non-acquired data is synthetized from acquired data. Thus, the final image quality depends not only on the motion and k-space trajectories, but also on the reconstruction algorithm used.

To better characterise the interplay between motion and acquisition trajectories, both distance, speed, and k-space energy were taken into account in Chapter V.

IV.4: Faster imaging

IV.4.1: Introduction

Scan duration is another important determinant of the motion sensitivity of a given acquisition, as for longer scans, patients and volunteers are tasked with staying still for extended periods of time. This increases the likelihood of movement, thus the likelihood of obtaining a scan with degraded image quality (251). Thus, reducing scan time would serve both to make the MPM protocol clinically viable in terms of overall time spent in the scanner, but also in making the acquisition more robust versus motion.

A study was performed comparing three versions of the MPM protocol, each with a different acceleration factor, thus a different scan time. Data was acquired both on a phantom and in vivo. Results were compared both across the three protocols and with previously published values, in order to find the ideal acceleration factor that did not significantly impact precision or image quality. In vivo results were additionally evaluated by a consultant neuro-radiologist.

IV.4.2: Methods

IV.4.2.1: Imaging protocols

Three different versions of the MPM protocol were used in the study, termed “GRAPPA 2”, “GRAPPA 4” and “GRAPPA 4+elliptical”. Common imaging parameters across the protocols were: Field of view=256 x 240 x 176 mm, flip angle=6°/6°/21° (PDw/MTw/T1w), 1mm isotropic resolution, first echo time TE=2.34 ms, echo spacing: 2.3 ms, 6/8 echoes (MTw/PDw and T1w). For the MTw scans, an off-resonance pre-pulse of 2kHz frequency offset, 220° flip angle and 4 ms duration was applied prior to the excitation pulse. The acceleration factors and acquisition time per scan for the three protocols is summarized on Table IV.7:

Protocol name	GRAPPA 2	GRAPPA 4	GRAPPA 4+elliptical
Acceleration factor (A-P)	2	2	2
Reference lines (A-P)	18	40	40
Acceleration factor (R-L)	Not used	2	2
Reference lines (R-L)	Not used	40	40
Partial Fourier factor (R-L direction)	6/8	Not used	Not used
Elliptical coverage	Not used	Not used	Used
Acquisition time [min:sec]	7:12	5:00	4:03

Table IV.7: Summary of acquisition parameters used in the three different protocols. R-L: right-left, A-P: anterior-posterior. Partial Fourier: partial coverage of k-space, exploiting the theoretical phase symmetry of k-space. . Elliptical coverage: only part of k-space within an ellipse is acquired. Acquisition time is measured for one FLASH scan.

IV.4.2.2: Image acquisition:

For the phantom study, an agar phantom (238) designed to have T1 and T2 values comparable to grey matter was imaged using all three versions of the protocol. For in vivo validation, a volunteer (38, male) was scanned using the GRAPPA 4 and GRAPPA 4+elliptical protocols in the same session.

IV.4.2.3: Image analysis:

Quantitative measures were extracted from the scans acquired on the agar phantom. A simple intensity thresholded mask was derived from the mean signal intensity of the proton density weighted echoes of the GRAPPA 2 protocol, tresholded to exclude voxels outside the volume of the phantom.

The mean and standard deviation of the quantitative metrics was extracted from the masked maps, and compared across the three protocols. The quantitative values were plotted as histograms, and the centre point of these distributions was found using a Lorentizan function:

$$L(x) = \frac{1}{\pi} \frac{\frac{1}{2}\Gamma}{(x - x_o)^2 + \left(\frac{1}{2}\Gamma\right)^2} \quad \text{[IV.10]}$$

where Γ controls the width of the fitted function, and x_0 is the centre point. The centre point was used to assess any bias between the protocols.

The normalized root means square error (NRMSE) of the two protocols with higher acceleration factor was also calculated, with respect to the GRAPPA 2 protocol:

$$\mathrm{NRMSE}_{G2\_4} = \sqrt{\frac{1}{N}\sum_{=1}^{N}\left(\frac{G2_{i,j} - G4_{i,j}}{G2_{i,j}}\right)^2} * 100 \quad \text{[IV.11a]}$$

$$\mathrm{NRMSE}_{G2\_4ellip} = \sqrt{\frac{1}{N}\sum_{j=1}^{N}\left(\frac{G2_{i,j} - G4ellip_{i,j}}{G2_{i,j}}\right)^2} * 100 \quad \text{[IV.11b]}$$

where $G2_{i,j}$, $G4_{i,j}$ and $G4_{ellip,i,j}$ are the image intensity for the contrast or quantitative map indexed by i, at voxel j, acquired using the GRAPPA 2, GRAPPA 4 or GRAPPA 4+elliptical acquisition, respectively, and N is the number of voxels in the masked maps.

IV.4.2.4: Processing of in vivo data

In vivo data was analysed using the standard post-processing pipeline described in Chapter II and III. Tissue-specific quantitative maps were derived by thresholding grey and white matter probability maps, generated using the unified segmentation algorithm (183), of the GRAPPA 4 acquisition at 90% probability. The means and standard deviations of the quantitative values within these masked maps were calculated, and compared to values reported in a previous study (19), which used a variant of the GRAPPA 2 protocol.

IV.4.2.5: Neuro-radiological evaluation

The quantitative maps derived from the GRAPPA 4+eliiptical protocol were further evaluated by Dr. Indran Davagnanam, a consultant neuro-radiologist with seven years of experience. The quantitative maps, originally in a NIfTI format, were converted into DICOM images and displayed using an Agfa Impax 6.5 PACS system with high-resolution monochrome monitors. The maps were evaluated specifically for their viability in clinical

diagnosis, considering factors such as grey and white matter contrast, homogeneous intensity within tissue classes, apparent resolution and image distortions and artefacts.

IV.4.3: Results

IV.4.3.1: Phantom study

In the phantom study, the signal intensities of the mean across echoes for the weighted acquisitions, as well as the quantitative values estimated from their combination, were comparable across all three versions of the protocol. The differences between the mean values of the different protocols were within one standard deviation. For both the GRAPPA 4, and GRAPPA 4+elliptical protocol, the standard deviation of the estimated quantitative values increased, compared to the GRAPPA 2 protocol, indicating a loss of precision in the estimation, due to a decrease in SNR. The RMSE of the two protocols with higher acceleration did not exceed 5%, with respect to the GRAPPA 2 protocol.

Scan/map	Mean±sd, GRAPPA 2	Mean±sd, GRAPPA 4	Mean±sd, GRAPPA 4+elliptical	$NRMSE_{G2\_4}$ [%]	$NRMSE_{G2\_4ellip}$ [%]
T1w [au]	1043±401	1028±403	1037±406	3.6	3.7
PDw [au]	617±223	605±223	611±225	4.1	4.3
MTw [au]	598±216	593±219	585±217	4.2	4.5
R1 [s^{-1}]	1.87±0.04	1.89±0.07	1.88±0.08	4.6	4.7
R2* [s^{-1}]	21.1±3.9	21.3±4.4	21.1±4.4	4.7	4.9
PD* [%]	69.5±5.1	69±5.7	69±5.4	4.4	3.9
MT [%]	0.176±0.064	0.179±0.116	0.190±0.097	4.5	4.6

Table IV.8: Means and standard deviations of the mean weighted scan signal intensities and quantitative maps.

In the agar phantom, histograms of the estimated quantitative values derived from the GRAPPA 4 and GRAPPA 4+elliptical protocols did not show a significant offset with respect to the GRAPPA 2 protocol, as illustrated in Figure IV.10. The broadening of histograms corresponds to the increase in standard deviation, when compared to the GRAPPA 2 protocol.

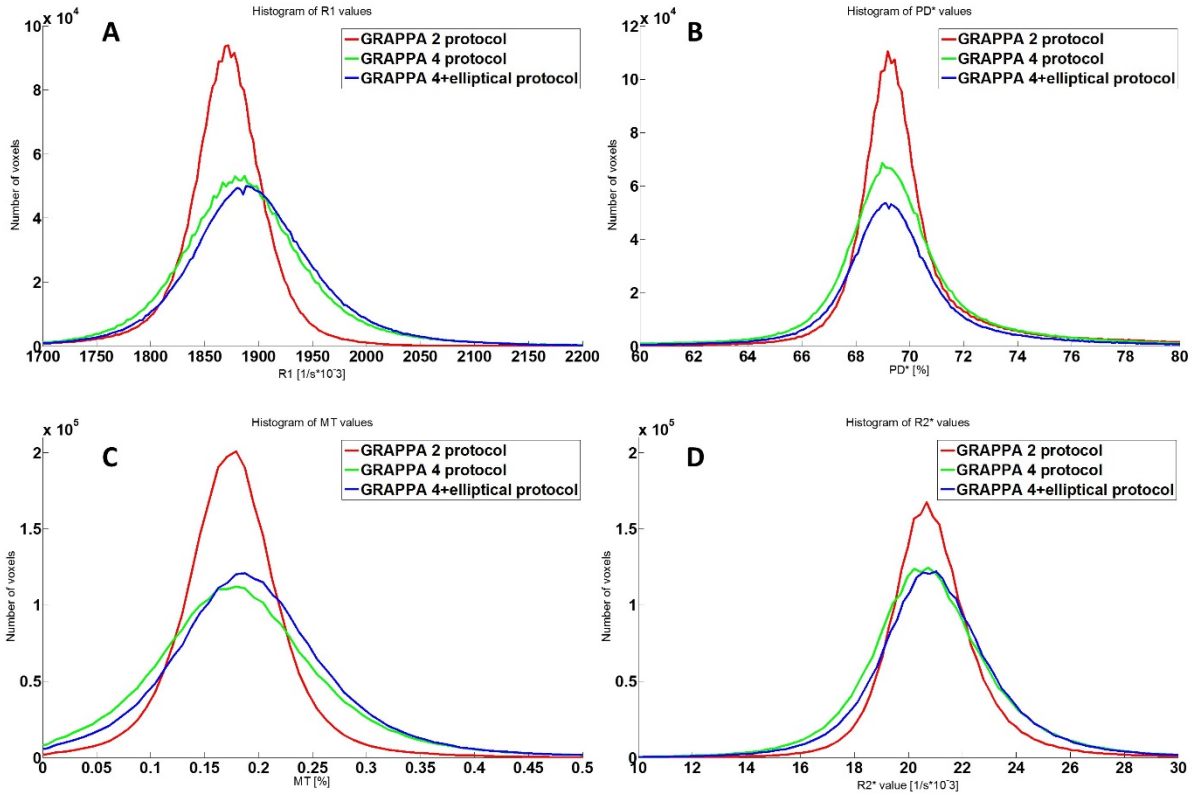

Figure IV.10: Histogram comparisons of the three protocols. A: Estimated R1 values; B: Estimated PD* values; C: estimated MT values; D: estimated R2* values. Red: GRAPPA 2 protocol, green: GRAPPA 4 protocol, blue: GRAPPA 4+elliptical protocol.

Centre points of the fitted Lorentzian functions were also compared, as seen in Table IV.9.

Map	GRAPPA 2 protocol	GRAPPA 4 protocol	GRAPPA 4+elliptical protocol
R1 [s^{-1}]	1.87	1.88	1.89
R2* [s^{-1}]	20.7	20.6	20.6
PD* [%]	69.2	69.2	69.2
MT [%]	0.17	0.18	0.18

Table IV.9: Centre points of the Lorentzian functions fitted to the histograms depicted in Figure 4.

Centre points were not strongly impacted by the choice of protocol. The greatest relative difference in centre points of 6% was seen in the MT maps.

IV.4.3.2: In vivo results

Quantitative values estimated using the accelerated versions of the protocol were compared with values previously reported (19), with the exception of R2* and MT values in grey matter. The difference between the mean R1 values in grey matter is less than 4% between the previously reported value and the GRAPPA 4+elliptical protocol. The R2* and MT values estimated in grey matter show a greater difference of 27% and 16.5%, respectively, while in white matter, this difference is within 3.5%.

However, it should be noted that the quantitative values reported in the previous literature were estimated from data acquired with a different version of the FLASH sequence used in the MPM protocol. It is not clear how much of this discrepancy may be due to these protocol differences. Standard deviations are likewise not directly comparable, as the study reported the standard deviation across a group of five subjects.

	Grey matter		
	Mean±sd, GRAPPA 4	Mean±sd, GRAPPA 4+elliptical	Mean, previously reported
R1 [s^{-1}]	0.631±0.098	0.633±0.125	0.609±0.008
R2* [s^{-1}]	18.3±0.9	19.1±1.3	15.2±0.4
PD* [%]	82.92±7.26	82.17±9.28	84.44±1.87
MT [%]	0.916±0.178	0.924±0.293	0.794±0.014
	White matter		
R1 [s^{-1}]	0.958±0.113	0.944±0.125	1.033±0.036
R2* [s^{-1}]	21±0.6	21±0.8	21±0.8
PD* [%]	67.92±4.71	68.94±5.19	68.35±0.06
MT [%]	1.768±0.209	1.709±0.336	1.764±0.066

Table IV.10: In vivo comparison of accelerated protocols to previously reported values(19)**.**

IV.4.3.3: Neuro-radiological evaluation

The neuro-radiological evaluation judged the quantitative maps to be suitable for diagnoses that require high-quality, high-resolution images, e.g., the diagnosis of epilepsy seeking to identify small cortical lesions. All maps were rated as having good tissue contrast

and intra-tissue homogeneity. In terms of visual quality, the R1 and R2* maps were ranked above maps of MT and PD*.

IV.4.3.4: Intermittent image artefact

Intermittently, a structured image artefact was observed in both in the GRAPPA 4 and GRAPPA 4+elliptical protocols, as shown by the blue arrows in Figure IV.11. This foldover artefact was observed in participants with larger heads. In addition, the image reconstruction algorithm of the scanner was optimised for processing speed. These two factors may have given rise to this artefact.

Figure IV.11: Image artefact observed on a proton-density weighted scan acquired with the GRAPPA 4+elliptical protocol. The foldover artefact of the scalp is visible, indicated by blue arrows. Note that the image has been windowed to better show the artefact.

IV.5: Discussion and conclusion

To deploy the MPM protocol more broadly in the clinical environment, acquisition times should be shortened, and motion sensitivity needs to be reduced. In this study, I evaluated the impact of the choice of k-space traversal trajectory, based on motion trajectory information derived from healthy volunteers, and measured the impact of partially parallel imaging with higher acceleration factors on the image quality and the estimated quantitative maps acquired in the MPM protocol.

For the acquisition protocol used throughout this thesis, where the field of view of the acquisition was not rotated away from an axial orientation, the partitions inside lines k-space trajectory was found to be the least motion sensitive. Thus, during the PhD project, this acquisition scheme was used for all MPM scans. However, this result is not readily generalizable to patient populations with different motion trajectories, or acquisitions in which the field of view is rotated.

Two versions of the protocol, acquired with higher overall acceleration factor (GRAPPA 4 protocol), and additionally reduced k-space coverage (GRAPPA 4+elliptical protocol) were evaluated on an agar phantom and in vivo.

In the agar phantom, the accelerated protocols were compared to a less accelerated version of the same scans (GRAPPA 2 protocol), acquired in the same session. The difference between the mean signal intensities and the estimated quantitative parameters of the different protocols is well within one standard deviation. RMSE was calculated for the GRAPPA 4 and GRAPPA 4+elliptical versions of the protocol, with respect to the GRAPPA 2 version. For all quantitative maps and mean signal intensities, RMSE was below 5%.

Histograms of the estimated quantitative parameters were visually compared and no significant offset was observed. Lorentzian functions were fitted to the histograms in order to quantify any offset. The differences between the centre points of the fitted functions were within 6%. Given this minimal degradation, the accelerated protocols were subsequently evaluated in vivo.

In vivo, quantitative values estimated within grey and white matter compared well to previously published results acquired using an acceleration equivalent to that of the GRAPPA 2 protocol, but with a previous version of the FLASH sequences. Differences between the mean values of the higher accelerated protocols and the previously reported values were low, in the 4-6% range, with the exception of R2* and MT estimated in grey matter. These changes are less than the group average differences that have been observed in healthy aging populations using the MPM protocol (21,176), indicating that higher acceleration factors are viable for acquiring relevant clinical information.

The GRAPPA 4+elliptical protocol was judged favourably in a neuro-radiological evaluation for feasibility in clinical diagnosis.

Due to underperforming image reconstruction, an artefact was observed intermittently in the GRAPPA 4, and more frequently in the GRAPPA 4+elliptical protocol. Thus, higher acceleration factors higher than 4 were not evaluated or used during the PhD project.

Chapter V: Development of a novel navigator technique

V.1: Introduction

Motion during scans is one of the leading causes of image artefacts, which can turn acquired scans clinically useless, necessitating re-acquisition at a cost in both scan time and money (16). Accordingly, motion correction methods have been developed since the start of MRI as an imaging modality. These methods are introduced in Chapter II.

An important feature of motion correction methods is the ability to acquire motion information. Motion information may be derived from the acquired data without explicit tracking of motion, such as in autofocusing approaches (252–255), by explicitly tracking motion, or by combining both approaches. Motion may be tracked by modifications to the MRI sequence (210–212,256,257), or via external means (197). Typically, sequence modifications entail dedicating a period of the scan to acquiring motion data, while external tracking is realised via a camera system tracking facial features (258) or a marker attached to the head (186).

The aim of the PhD project was to prepare the MPM protocol for clinical deployment. In this context, existing motion detection approaches are not suitable, as they either take additional scan time, which is contrary to the aim of fast imaging, or require extensive, expensive, and often intrusive instrumentation, which renders them ill-suited for clinical populations.

In this Chapter, I demonstrate a novel motion detection method, based on acquiring data during gradient spoiling. I demonstrate the sensitivity of this data to motion, and propose outlier rejection methods to correct for motion based on this navigator measure. The viability of an accept-reject-reacquire approach is assessed in vivo, and suggestions for further refinement and implementation in other scans with similar gradient spoiling are made.

V.2: Implementation and sensitivity of a novel navigator technique

One characteristic of the FLASH scans used in the MPM framework is the minimization of “dead time”, i.e. time during which there is no signal encoding, or signal acquisition. As such, an insertion of a conventional navigator would require any increase in TR, to accommodate the time taken to acquire the navigator. This increase in TR would in turn increase scan time, counter to the stated aims of this project. Thus, a novel navigator technique had to be developed, one that would acquire motion information without increasing the TR.

In FLASH, the signal encoding is rewound on the phase encoded axes, and a spoiling gradient is played out. In the FLASH sequence used in the MPM protocol, the spoiling gradient is played out in the readout direction. The spoiling gradients on the readout axis are played out identically during each TR with only the phase-encoding gradients changing. Therefore, if the timing of the sequence is such that the rewinding gradients are kept at a fixed duration that is exceeded by the spoiling gradient (Figure V.1), then, for every TR, the same trajectory is traversed through k-space. This trajectory will be at k=0 in each phase-encoded direction and extending from low to high k values along the readout direction. Although the MR signal at these high k values can be expected to be low in amplitude, proof of principle studies have recently shown that noise measurements can be sensitive to coupling across coil elements (259–261). Therefore, the hypothesis was that the data collected during these spoiling periods could be used as a motion navigator. I hypothesized that these data would be consistent in the absence of motion, but would be sensitive to motion, due to the inconsistencies introduced by variations in the participant’s position.

To evaluate the performance of the navigator approach, several proof-of-principle studies were taken. In this section, the first study is described, aimed at establishing if the data acquired concurrently with gradient spoiling is sensitive to motion. In subsequent sections, the normalisation of the navigator measure, the derivation of an independent gold standard, and the implementation of a general linear model framework are described. The end of this Chapter introduces an in-vivo proof-of-principle study. All scanning, was carried out on a Siemens 3T TIM Trio system.

V.2.1: Implementation of the navigator echo

An additional readout (navigator echo) was inserted into the FLASH scans after the phased-encoding was rewound on the phase-encoded axes. Concurrent with the re-winding gradients, a spoiler gradient of 26 mT/m is applied on the readout axis. The duration of the

spoiler gradient is set to impart 6π of dephasing across each voxel. At a resolution of 1mm, with an amplitude of 26 mT/m this amounts to a duration of 2.91 ms. The rewinding gradients were 0.83 ms in duration such that during each TR, the final 2.08 ms of the spoiler gradient traversed the same k-space trajectory. The sequence was modified, as shown in Figure V.1, to insert the navigator echo during this period. The data acquired during this echo is a one dimensional projection along the frequency encoding direction, encoded at higher k-space values, thus for higher spatial frequency along the z direction, than the data acquired during the echoes used for imaging.

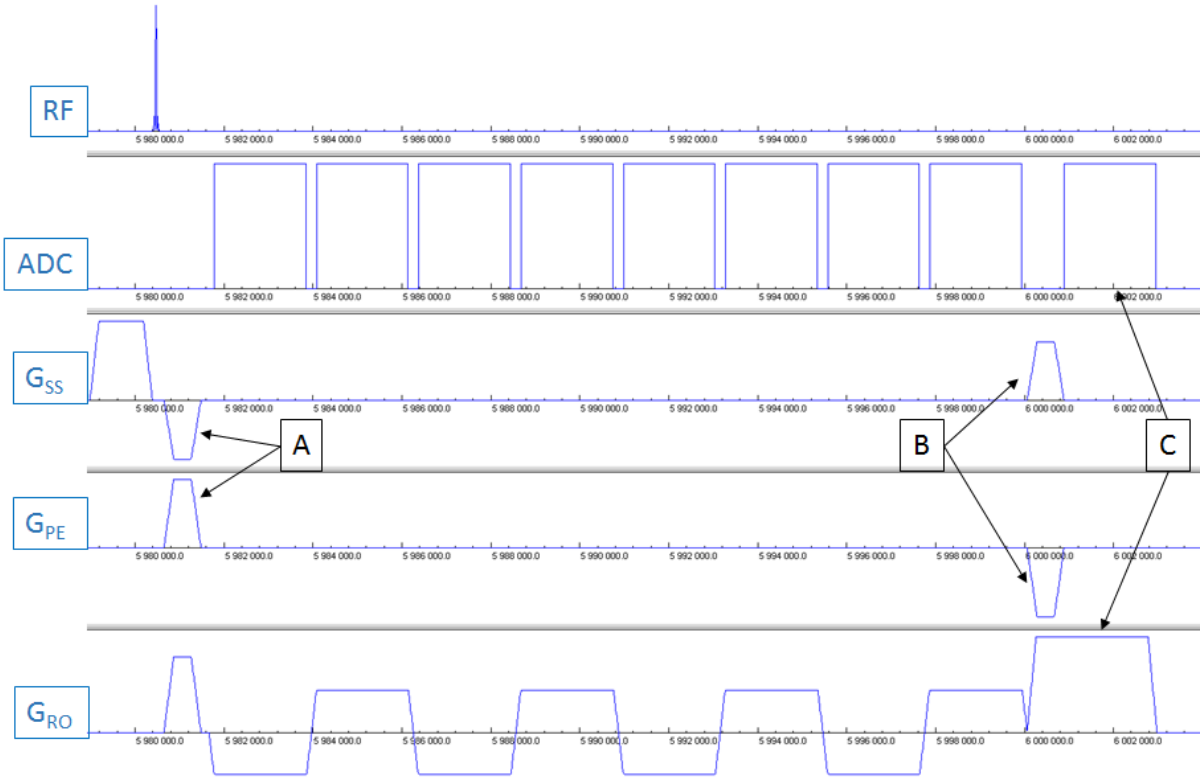

Figure V.1: Sequence diagram for the FLASH sequence used in the MPM protocol, with additional navigator echo. The arrows indicate the phase encoding gradients (A), the re-winding gradients (B), and the spoiler gradients and concurrent navigator echo (C). Note that the navigator echo starts immediately after rewinding, and lasts until the end of the spoiling gradient.

V.2.2: Data acquisition

A volunteer (34 years, female) was scanned under different motion conditions. First, a scan was acquired in a “no motion” condition, where the volunteer was instructed to stay as still as possible. Second, a scan was acquired under a “motion” condition, where the volunteer was instructed to perform large head motions, on the order of approximately one to three centimetres in translation and approximately one to ten degrees in rotation, during the scan.

Third, another “no motion” scan was acquired. To help the volunteer with the extent of head motion to be performed during scanning, they were asked to perform head motions while lying on the patient table outside of the scanner, with their head in the 32 channel head coil, and advised to adjust the frequency and extent of their motion if necessary.

The volunteer was scanned using the following sequence parameters: FoV=256x240x176mm^3, 1mm^3 isotropic resolution, TR=25ms, 8 echoes, TE/echo spacing=2.34/2.3ms, flip angle of 6 degrees, GRAPPA acceleration factor 2 in both phase encoded directions, with 40 reference lines integrated in each direction. At end of each TR, a navigator echo was acquired. For the remainder of this Chapter, this sequence is referred to as the basic navigator sequence, and only the T1w or PDw nature of the acquisitions is mentioned explicitly.

V.2.3: Navigator data processing

The raw k-space data of the navigator echo was analysed in Matlab using custom-made scripts. Raw k-space data, for each TR, consisted of one complex value for each of the 512 (an oversampling factor of 2 was applied in the frequency-encoded direction) frequency-encoded sample points, for each of the 32 channels of the receiver array. Thus, for each TR, 32768 navigator data points were acquired. The high dimensionality of this data was reduced to produce a single data point per TR. It was hypothesized that head motion in a 32 channel coil would result in the head moving closer, or further away from the sensitive volume of a channel, thus increasing or decreasing the detected navigator signal for in different channels, leading to a change in the signal variance across channels. Thus, for each of the 32 channels, and for each TR, the following data processing steps were taken:

1. Magnitude information was extracted from the complex data for each of the 512 sample points, by multiplying the data with its complex conjugate, and taking the square root, resulting in 512 data points per channel.
2. The mean of this magnitude across the 512 sample points was taken, resulting in a total of 32 data points, one per channel, representing the magnitude of the navigator data for that channel and TR.
3. The standard deviation across the 32 coil elements was calculated, resulting in one data point per TR, the navigator measure.

It was hypothesized that any real head motion would occur on a timescale significantly longer than a single TR. Thus, in order to supress the TR-to-TR temporal fluctuations of the navigator measure, and in turn increase its relative sensitivity to motion-related changes, a low-pass filter was applied to the navigator measure. This filtering was achieved by applying

a moving average filter with a width of 20 TRs, corresponding to 500 ms. This processing was applied to the navigator data from each of the three motion experiments described in V.2.2. The evolution of these time series were compared and they were further summarised by the mean and standard deviation over the whole of the scan time.

V.2.4: Results

The means and standard deviations across TRs of the navigator measures are shown in Table V.1. Motion during scanning increased the standard deviation of the navigator measure by a factor of four, compared to the standard deviation of the navigator measure acquired in the no motion conditions.

Motion condition	Mean±sd of navigator value [au]
No motion	1.192±0.009
Motion	1.213±0.036
No motion, rescan	1.210±0.009

Table V.1: Comparison of the navigator values across the three scans.

Figure V.2 shows the evolution over time of the three navigator signals. The two navigators acquired under no motion conditions showed similar levels of temporal fluctuation over time, on the order of 0.02 a.u., but there was an appreciable offset between the means of the two measures, in excess of their standard deviations over time. Motion affected the navigator signal, resulting in both higher and lower values compared to the no motion cases, with a difference between minimum and maximum values on the order of 0.14 a.u.

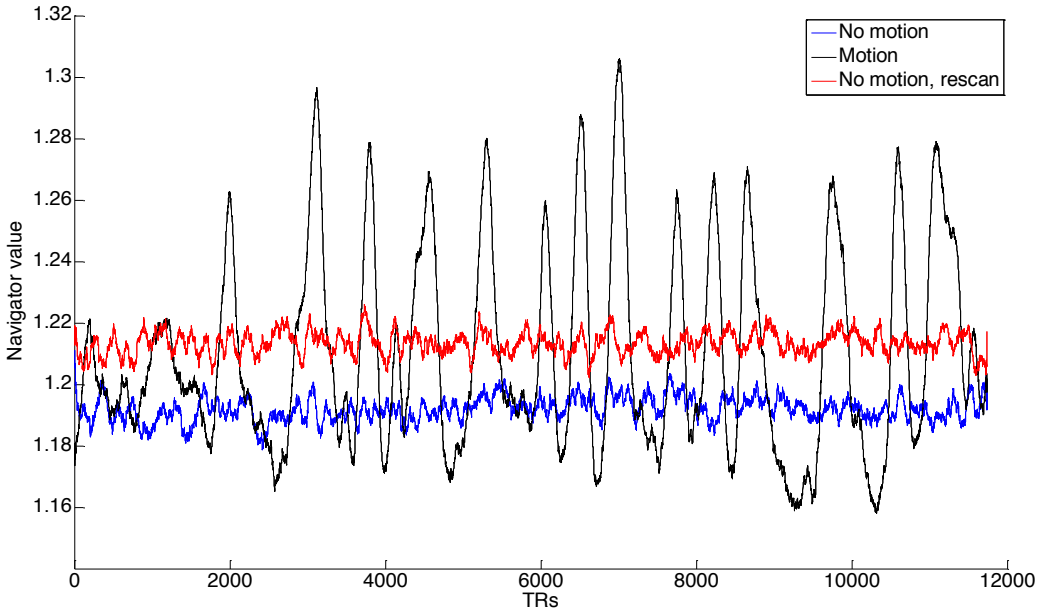

Figure V.2: Navigator values over TRs for the three acquisitions. The similar temporal behaviour of the two no motion cases, as well as the offset between their navigator values, is visible. In the case of motion, both an increase and a decrease of navigator values were observed. Note

that for better visualisation, a stronger low-pass filter of a moving average width of 100TRs was applied.

V.2.5: Conclusion

I have shown that the data acquired with this novel navigator technique were sensitive to motion. Changes in the navigator values acquired under motion conditions were approximately seven times the changes in navigator values observed under a no motion condition. During the motion condition, navigator values were both lower than and higher than the values acquired under a no motion condition. Based on this proof-of-principle result, the next aim of the project was to develop an outlier rejection method to discard data affected by motion. Due to the offset observed in this study between the navigators of the two no motion cases, a normalisation step was necessary before an outlier rejection threshold could be defined. This work is detailed in the next section.

V.3: Development of an outlier rejection method

As shown in the previous section, motion resulted in a navigator measure that was both greater than, and lower than, the navigator measure for a no motion case. Thus, it was hypothesized that an outlier rejection method could be developed, in which a TR would be identified as being affected by motion if its navigator value lies outside the typical range of navigator values measured in the absence of motion. To ascertain that such an outlier rejection approach is viable, it was first necessary to determine the range of navigator values for no motion cases, and investigate if a common outlier threshold could be defined. A short study was carried out to compare the reproducibility of navigator values in a no motion condition across volunteers, scanning sessions, and imaging contrasts.

The navigator value is calculated from raw k-space data, which can have different weighting factors (e.g. receiver gain, coil sensitivity) that vary across scans and more notably scanning sessions. To correct for this variable scaling, a normalisation factor had to be used that accounted for these weighing factors. It was hypothesised that such a factor could be derived from the acquired data, as it inherently carries these weighing factors. Two normalisation factors were investigated, one derived from noise calibration data acquired at the beginning of the scan, and one derived by taking the mean of all navigator values over the entire acquisition. A normalisation approach was accepted if for two datasets acquired under different conditions (different subject, or a different session of the same subject), the means of the normalised navigator values taken over the whole acquisition were within one standard deviation of each other, in order to minimize false positives in the absence of motion.

V.3.1: Methods

Four volunteers (2 males, age range: 34-43 years) were scanned using the navigator sequence, under a no motion condition. For all volunteers, a PDw scan was acquired, to investigate the variability of the navigator value across volunteers. For two of the volunteers, T1w scans were also acquired by increasing the flip angle to 21 degrees. Repeat acquisitions of PDw scans were performed on the same two volunteers, to measure the scan-rescan variability of the navigator values. The volunteer scanned in section V.2 was re-scanned, indicated as volunteer 1, and the two no motion scans acquired in section V.2 were included in this study, indicated as the first scanning session of volunteer 1.

The navigator value was calculated according to the process described in the previous section. Additional normalisation was carried out in two ways.

For the “noise adjust normalisation”, the 100 noise calibration data acquired at the outset of the acquisition (without excitation or encoding to facilitate pre-whitening) were used to normalise the navigator data, by taking the following steps:

1. Magnitude information was extracted from the complex data for each of the 512 sample points, by multiplying the data with its complex conjugate, and taking the square root, resulting in 512 data points per channel.
2. The mean of this magnitude across the 512 sample points was taken, resulting in a total of 32 data points, one per channel, representing the magnitude of the navigator data for that channel and noise calibration point.
3. The standard deviation across the 32 coil elements was calculated, resulting in one data point per noise calibration point.
4. A moving average filter with a width of 20 data points was applied to the results of step 3.
5. The normalisation factor was calculated by taking the mean of the results of step 4 across all 100 noise calibration data points.
6. The navigator value for every TR was divided by this normalisation factor.

For “normalisation by the mean”, the mean of the navigator value across all TRs was calculated. The navigator value for each TR was then normalised by this factor via division.

The means and standard deviations (sd) across the acquisition for the un-normalized, and normalized navigator values were compared across volunteers, sessions, and contrasts.

V.3.2: Results

V.3.2.1: Scan-rescan variability of the navigator measure

Figure V.3 shows the scan-rescan variability for the un-normalised navigator value, for PDw scans acquired on volunteer 1. The difference between the means of the two navigator values (across all TRs of their respective acquisitions) was an order of magnitude higher than the standard deviation of navigator values (across all TRs of their respective acquisitions), showing the need for normalisation. Additional smoothing was applied, by increasing the width of the moving average filter to 100 TRs, for better visualisation.

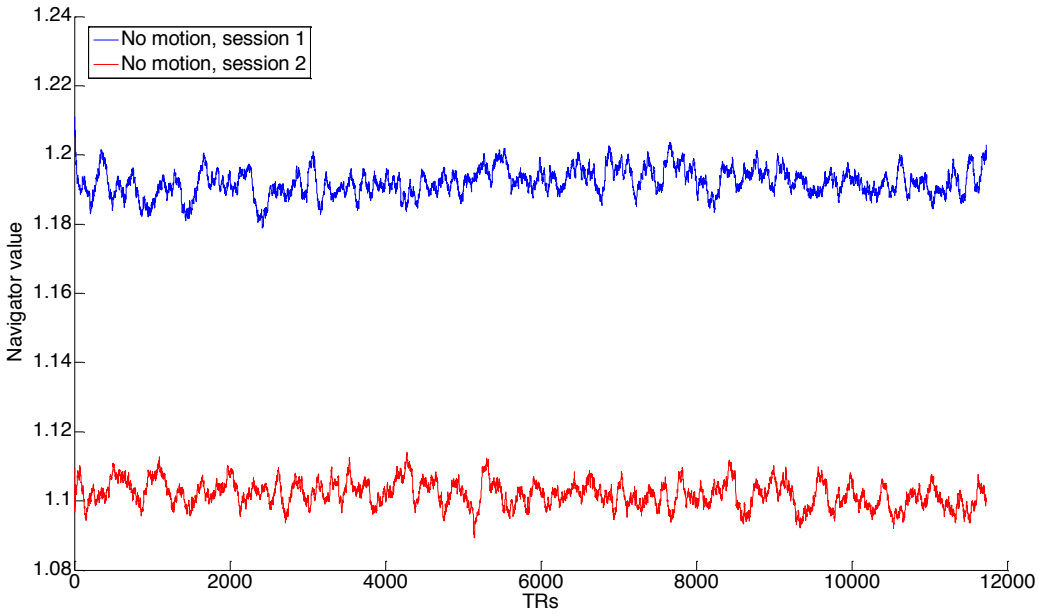

Figure V.3: Between-session scan-rescan variability of the navigator values for PDw scans acquired on Volunteer 1 under no motion conditions. While the two navigators were stable, as compared to the navigator acquired in the motion case of Volunteer 1 in section V.2, a significant offset could be observed between sessions.

V.3.2.2: The effect of normalisation on the navigator measure

Without normalisation, the means of the navigator measures differed by as much as ~20%, as seen in Table V.2, while the standard deviations remained comparable. This indicated that the variability of the navigator value was stable across volunteers and contrasts in the absence of motion, thus showing the possibility of outlier rejection based on a common threshold.

Volunteer number	Scanning session	Contrast	Mean±sd of unnormalized navigator value
1	First	PD	1.192±0.009
		PD	1.215±0.008
	Second	PD	1.102±0.009
		T1	1.102±0.009
2	First	PD	1.305±0.010
	First	T1	1.315±0.009
	Second	PD	1.226±0.009
3	First	PD	1.143±0.009
4	First	PD	1.139±0.009

Table V.2: Means and standard deviations for unnormalized navigator values.

For the “noise adjust normalized” navigator values, the means across all TRs of their respective scans were not stable, with the greatest difference between the means (0.06) exceeding the standard deviation across the means (0.017) by a factor of four.

Volunteer number	Scanning session	Contrast	Mean±sd of noise-adjust normalized navigator value
1	First	PD	1.956±0.015
		PD	1.962±0.014
	Second	PD	1.936±0.015
		T1	1.946±0.016
2	First	PD	1.969±0.014
	First	T1	1.994±0.014
	Second	PD	1.964±0.014
3	First	PD	1.980±0.015
4	First	PD	1.956±0.015

Table V.3: Means and standard deviations for navigator values normalized with noise adjust data.

Normalisation by the mean, by definition results in a stable mean value of exactly 1 across TRs, and the standard deviations of the navigator values normalized by the mean are comparable across volunteers, scan sessions and contrasts.

Volunteer number	Scanning session	Contrast	Mean±sd of mean-normalized navigator value
1	First	PD	1±0.007
		PD	1±0.007
	Second	PD	1±0.008
		T1	1±0.008
2	First	PD	1±0.007
	First	T1	1±0.007
	Second	PD	1±0.007
3	First	PD	1±0.008
4	First	PD	1±0.008

Table V.4: Means and standard deviations for navigator values normalized by its mean across TRs.

V.3.3: Discussion

Normalisation was found to be necessary in order to have comparable navigator measures across scanning sessions, volunteers and contrasts, and therefore to develop an outlier rejection method for motion detection. Two normalisation methods were compared.

Normalising by noise adjust data was found to be insufficient because the difference in the means of the normalised navigator values exceeded the standard deviation of these means across the acquisitions by a factor of four. Thus, an outlier rejection method defined on the mean of one dataset could result in some, or all, of the TRs of another session being falsely identified as motion-corrupted. For example, with an outlier rejection threshold defined on the mean and standard deviation of the navigator values of the PDw scan of the second session of volunteer (1.936±0.015) would result in more than 95% of the TRs for the PDw scan on the third volunteer (navigator values of 1.980±0.015) being falsely identified as motion corrupted.

Normalisation by the mean was found to be adequate for outlier rejection, as the means of the normalized navigator values were by definition 1, and the standard deviations were comparable. The decision was made to use this normalisation approach for the reminder of the project.

While normalisation by the mean was found to be the suitable approach, all relevant data has to be acquired first. In practice, the normalisation could only be performed at the end of a scan. This imposed a fundamental limitation on the use of this approach for motion

correction: rather than detecting, and correcting for motion in a prospective manner and online, the method could only be applied retrospectively.

V.4: Outlier rejection based on normalised navigator values

A suitable normalisation procedure was found in the previous section. Based on this normalised navigator value (referred to in this section as “normalised navigator”), an outlier rejection threshold could be defined. To find an appropriate rejection threshold, volunteer 2 of the previous section was scanned under motion conditions, and the sensitivity and specificity of the outlier rejection method was investigated. Sensitivity and specificity were compared to a gold standard, derived from motion information acquired with a camera system, as described in Chapter IV.

V.4.1: Methods

Volunteer 2 of the previous study (43 years, male) was scanned under motion conditions as well during the sessions presented in the previous section. For the motion conditions of the first session, one PDw and one T1w scan were acquired. For the motion conditions of the second session, two PDw scans were acquired. The volunteer was instructed during scanning to perform large and rapid head movements in all directions for sustained periods of at least 20 second during the motion conditions of the scanning sessions.

For volunteer 2, head motion was independently tracked, but not corrected for, using a high-speed optical motion tracking camera system, like the one described in Chapter IV (198). This camera system tracked a marker attached to a bite bar affixed to the upper front teeth, and therefore, the skull. Based on this fixation, it was assumed that the motion identified was equivalent to the motion of the brain. Using dedicated software libraries developed to integrate the camera’s motion tracking data into the imaging environment, the six degrees of freedom for the motion of the head was logged in the scanners’ frame of reference for each TR (198,247). These logs were saved and used for further processing in order to have a gold standard defining whether or not motion had occurred. The performance of the navigator-based motion detection scheme was evaluated with respect to these data. Note that for the other volunteers and sessions described in the previous sections, motion was not tracked independently using the camera system, due to difficulties with the experimental setup.

An outlier detection threshold was defined based on the normalised navigator data shown in Table V.4. Specifically, a particular TR was identified as motion-corrupted if it exceeded the normalised value of 1.0 by N times the mean standard deviation under no motion conditions. N was calibrated such that the navigator-based classification had a false positive rate no greater than 5%. The sensitivity and specificity of this classification of motion was compared to the gold standard classification based on the motion tracking position logs.

V.4.1.1: Gold standard classification and detection of motion based on camera data

The envisioned use case for the navigator approach was one of rapid movements, rather than slow, continuous drifts in head position. Accordingly, the gold standard classification was derived from the position logs of the camera system in such a way as to be insensitive to slow changes in the mean position over the scan, while being sensitive to periods of rapid head motion. Based on the results of Chapter IV, the speed measure, S(t), defined in Equation IV.7 was used to classify motion-corrupted TRs. A stringent classification threshold was derived from the values of S(t), acquired during the no motion scans of volunteer 2, such that less than 1% of all TRs acquired in a no motion case were to be classified as being affected by motion. The motion classification based on the camera data was regarded as the gold standard for further tests.

V.4.2: Results

V.4.2.1: Calibration of the gold standard classification threshold

A classification threshold of S(t)>3 was found to be sufficient for a false positive rate below 1% in the absence of motion. The S(t) values for the scan acquired under motion in the second session are shown in Figure V.3. The two periods of motion are clearly distinguishable, based on their high S(t) measures compared to the periods of no motion. During the no motion periods, no TR has an S(t) measure in excess of the threshold.

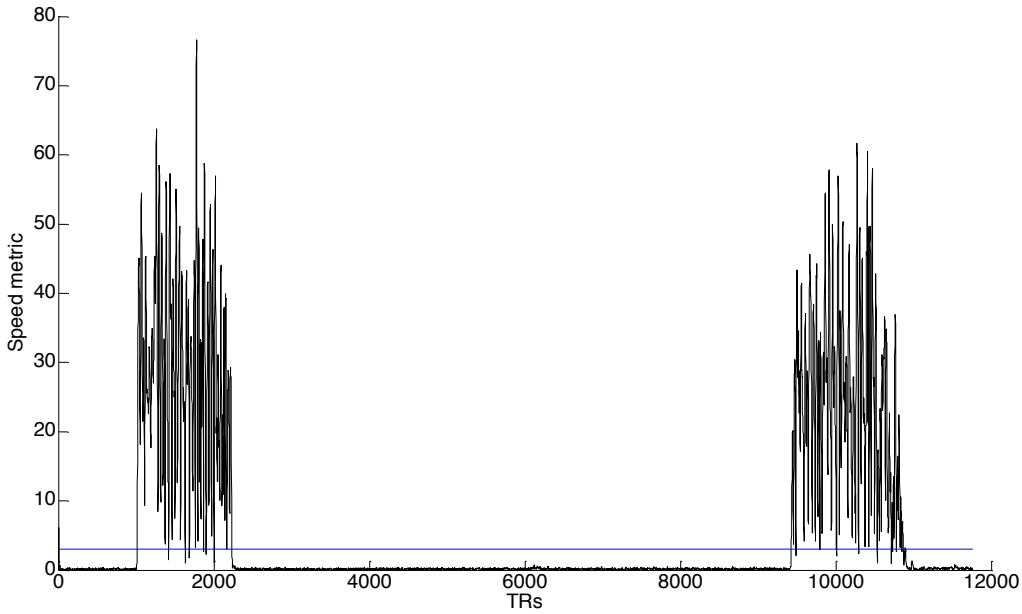

Figure V.4: Comparison of the speed measure for a motion case with the classification threshold. The S measure for the motion case of the second session (black), along with the classification threshold of S(t)=3 (blue). Note the two periods of motion around TRs ~1500 and ~10000, and the period of no motion between TRs ~2200 and ~9000. In this period, no TR is falsely classified as being affected by motion.

V.4.2.2: Motion classification and detection based on the normalised navigator values

Based on the normalized navigator values, a TR was classified as motion-corrupted if its navigator value was greater than, or lower than a threshold, defined as $1 \pm \mathrm{N} * \overline{SD}$, where $\overline{SD}$ was the mean of the standard deviations shown in Table V.4, 0.0075. Three values of N were investigated to calibrate the false positive rate, defined as the ratio of TRs falsely identified as motion corrupted based on their navigator measure, compared to the gold standard of the camera data, relative to the total number of TRs in a scan, which for the imaging protocol used in this section was 11760. The three values of N were N=2, N=2.5 and N=3. A value of N was accepted if the false positive rate was below 5%.

V.4.2.3: Calibration of the navigator-based rejection threshold

The three values of N were applied to the no motion scans of volunteer 2. The results are summarized in Table V.5. For all three outlier rejection thresholds, the false positive rate

was below 5%, regardless of scan session or imaging contrast. Thus, all three values were used during the evaluation of sensitivity and specificity of the navigator measure.

Scanning session	Contrast	N	False positive rate
First	PD	2	4.0%
		2.5	1.1%
		3	0.2%
	T1	2	3.5%
		2.5	0.7%
		3	0.1%
Second	PD	2	3.6%
		2.5	0.9%
		3	0.2%

Table V.5: False positive rates for the different outlier rejection thresholds for no motion cases

V.4.2.4: Sensitivity and specificity of the navigator-based rejection

The navigator-based outlier rejection was applied to the scans acquired under motion conditions for volunteer 2. For all three outlier rejection thresholds, sensitivity and specificity were compared to the gold standard derived from camera data. The ratio of TRs affected by motion, defined as the number of TRs with a gold standard S(t) value higher than 3 to the total number of TRs, was also calculated. Results are summarised in Table V.6, below.

Scanning session	Contrast	Ratio of motion-affected TRs	N	Sensitivity	Specificity
First	PD	67%	2	0.46	0.64
			2.5	0.38	0.76
			3	0.31	0.84
	T1	58%	2	0.56	0.50
			2.5	0.47	0.63
			3	0.39	0.72
Second	PD	39%	2	0.52	0.89
			2.5	0.43	0.96
			3	0.35	0.99
	PD, rescan	22%	2	0.49	0.92
			2.5	0.39	0.97
			3	0.32	0.99

Table V.6: Sensitivity and specificity of the navigator-based classification, compared to the gold standard

The four motion cases showed large differences in the extent of motion-corrupted data, from two-thirds of the scan being affected, to only one quarter (rescan of the PDw scan in the second session, S(t) values shown in Figure V.4). However, no strong effect on sensitivity or specificity could be discerned.

For all three values of N, the sensitivity of navigator-based classification was never below 0.3, and for all values of N, and for all motion cases, the classification was above chance.

V.4.3: Discussion

In this proof-of-principle evaluation, I have shown that based on the navigator values, an outlier rejection method can be developed to classify whether or not a particular TR is affected by motion, compared to a gold standard based on camera data and the speed of head movement.

The choice of the threshold, defined as $1 \pm \mathrm{N} * \overline{SD}$, dictated the false positive rate, which increased as N was reduced, reflecting the inherent variability of the navigator measure. The classification threshold of N also determined the specificity (or true negative rate), which increased with higher values of N, and the sensitivity (or true positive rate), which decreased

with higher values of N. Thus, with a reduced threshold, more data was classified as motion-corrupted, at the cost of an increased false positive rate.

The choice of N was determined by the intended implementation of the navigator technique. Due to the need for normalisation by the mean of all navigator values, as described in section V.3, data identified as motion corrupted would be re-acquired retrospectively. In the presence of motion, a method with low sensitivity would not reacquire data that had in fact been motion-corrupted thereby limiting the improvement afforded by the method. On the other hand, a method with low specificity, would falsely identify points as being motion-corrupted, unnecessarily triggering their reacquisition thereby increasing the scan time. Given that these two scenarios are traded against each other based on the threshold defining motion-corrupted navigator values, high sensitivity (translating to improved image quality) was deemed more important than high specificity (which would have limited the increase in scan duration).

For this reason, the classification threshold of N=2 was chosen, maximising sensitivity at the cost of specificity. In the absence of motion, this threshold would, based on the results of this section, not increase scan time by more than 5%. While this would go against the stated goal of not increasing scan time, 5% was considered to be acceptable.

Based on this, and the previous sections, it was possible to define a rejection threshold, such that any TR with a navigator value outside this threshold would be re-acquired. TRs rejected by this threshold correspond to a period of high speed motion, which can be used as a surrogate for coughs, head shaking, and tremors, modes of motion that affect clinical data quality (16,218,219,250,262). However, as the classification threshold was derived from healthy volunteer data, the choice of threshold may not be readily translatable to a clinical environment.

Re-acquisition of data itself, even in the absence of overt motion, may result in a decreased image quality, as even when participants are instructed to stay still, some intra-scan motion still occurs, as was shown in section IV.2. In the next section, I simulated the effect of retrospective data re-acquisition on image quality, in order to determine if the approach was viable.

V.5: The effect of retrospective data re-acquisition

In the previous sections, I introduced a navigator technique, and have shown that it can be used to detect motion. To correct for motion, the motion corrupted data has to be reacquired. As the navigator has to be normalized by its mean across TRs, such re-acquisition cannot take place immediately after motion occurs, but only at the end of the scan, after all of the imaging data have been acquired. The work presented in this section aimed to verify that data could be reacquired (and replaced) at the end of the acquisition without introducing artefacts that degrade image quality. The re-acquisition of data was simulated by taking data from identical scans acquired in the same session, under a no motion condition.

V.5.1: Methods

V.5.1.1: Data acquisition

A volunteer (36 years, male, described as volunteer 4 in section V.3) was imaged with the navigator sequence under no motion conditions. Four PDw scans were acquired sequentially, and the volunteer was instructed to stay as still as possible during the session. Motion was independently tracked using the camera system, and motion was identified according to the method described in section V.4.2.

V.5.1.2: Simulation of re-acquisition

Raw k-space data was saved for all four scans, and reconstructed offline in a SENSE framework, using custom-made scripts in a MATLAB environment. All reconstructed scans, both from mixed and unmixed data, were co-registered using rigid body co-registration to the first scan.

Re-acquisition was simulated by choosing a k-space data point of one scan (acting as the original data), and replacing it with the corresponding k-space data point from a different scan or scans (acting as the re-acquisition data). The resulting mixed dataset was reconstructed in the SENSE framework used to reconstruct the unmixed datasets. Variable amounts of re-acquisition were simulated, with a maximum of 50% of phase-encoded k-space data points being replaced. The position of the k-space data points to be replaced was determined by applying a binary mask to the acquired k-space data that randomly selected 10%, 30%, or 50% of data points. For the scan acting as the original data, these points were masked out, while the inverse of this binary mask was applied to the scan acting as the re-

acquisition data, and the masked datasets were then combined. When more than one dataset acted as re-acquisition data, the binary mask was further divided at random into an appropriate number of sub-masks, before being applied to the re-acquisition data. Thus, when more than one dataset acted as re-acquisition data, a given k-space point in the original scan was replaced with data from only one scan out of the replacement scans.

Several re-acquisition scenarios were examined. For scan-to-scan re-acquisitions (simulating a scenario where the time between acquisition and re-acquisition of a k-space point was the duration of a scan, approximately five minutes) were simulated by taking data from the first, second, and third scan, and replacing it with data from the second, third, and fourth scan, respectively. Two scenarios with more complex mixing patterns, in which data from the first scan was replaced with data taken from the second and third, or all three following scans, were also investigated in order to probe the robustness of this approach.

For all scenarios, data from the first echo was used. The acquisition scheme used in this sequence included integrated reference data for unfolding the outer under-sampled regions, derived from the first echo. No restriction was placed on the location of the reacquired k-space data points, in order to also simulate the potential re-acquisition of these reference lines.

All reconstructed mixed datasets were co-registered to the first scan as a template. The template image was segmented to obtain grey and white matter tissue probability masks. A brain mask was subsequently defined as those voxels that had a grey or white matter probability exceeding 50%. This brain mask was applied to all other images. A low probability was chosen in order to cover most of the volume of the brain.

Image quality was quantified by the normalised root mean square error, with respect to a reference image. For the scan-to-scan re-acquisition scenarios, the reference image was the scan acting as the source of the original data (the first, second, and third scan, respectively). For the complex re-acquisition scenarios, the reference scan was always the first scan.

Normalised root mean square error was calculated according to the formula below:

$$NRMSE_{k,n} = \sqrt{\frac{1}{N}\sum_{j=1}^{N}\left(\frac{I_n(j) - I_k(j)}{I_{ref}(j)}\right)^2} \qquad [V.1]$$

where $I_n(j)$ is the image intensity of scan n's first echo at voxel j, Sk(j) is the image intensity of scan k's first echo at voxel j, and index j sweeps across all nonzero voxels within the brain mask, and I_{ref} is the reference image.

A visual comparison was also performed to assess image quality.

V.5.2: Results

As characterised by the S(t) measure defined in Chapter IV, no TRs were identified as being affected by motion during scanning. Inter-scan motion, as measured by the parameters of rigid-body co-registration was less than 0.4 mm for translation and 0.2 degrees for rotation. This was judged to be sufficiently small such that the results could be interpreted within the context of no motion.

The pattern used to replace k-space points is shown in Figure V.5. K-space points were chosen at random, irrespective of their k-space energy, or if they were in the fully sampled central portion of k-space, used to generate sensitivity maps for the SENSE reconstruction algorithm.

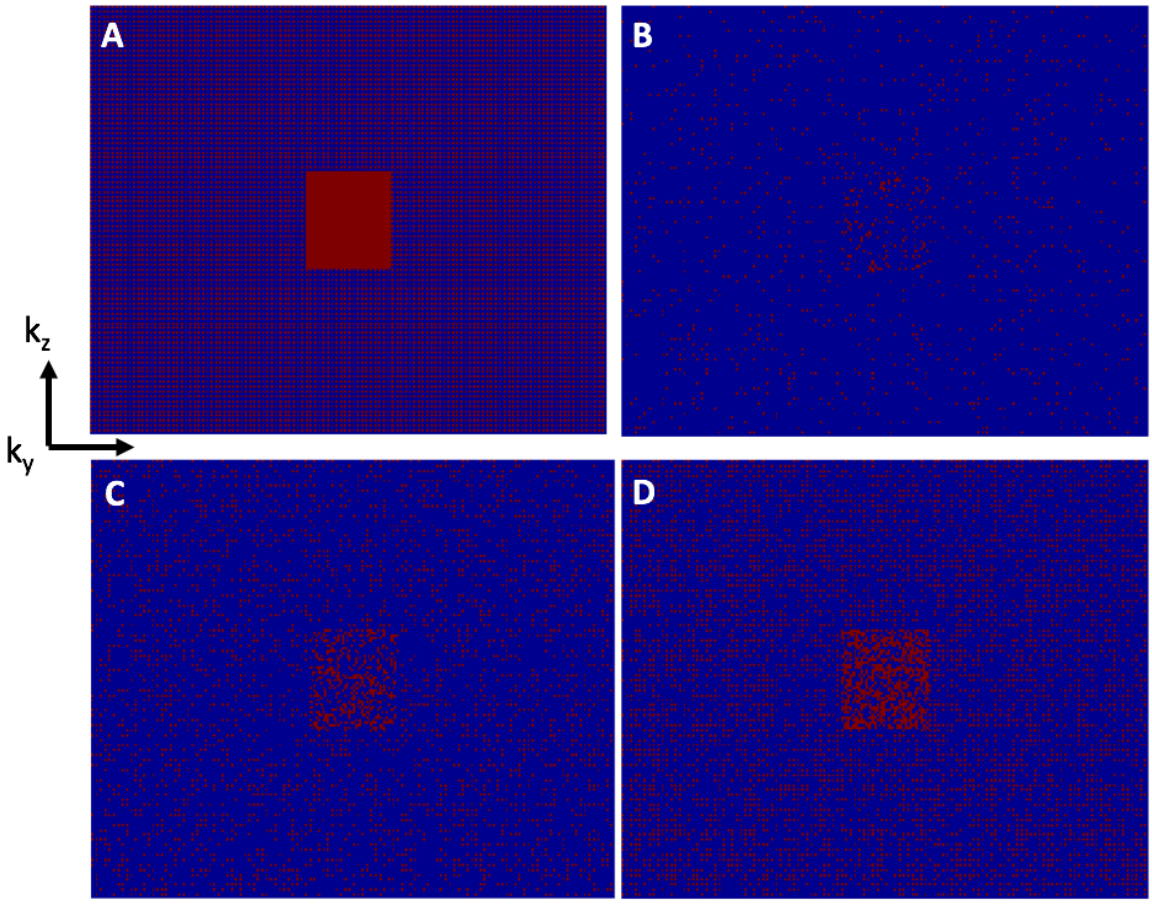

Figure V.5: Random k-space sampling patterns used in this section. Fully sampled k-space is shown on A, with the k-space points shown in red in Figures V.B, C and D indicating the location of the replaced k-space points for the scenarios with 10%, 30%, and 50% of all points replaced by data from another scan, respectively, for a given random sampling. Figures show the phase-encoded directions of k_y and k_z, with the readout direction, k_x, going through the plane.

Visually, only the scenario where 50% of k-space data is replaced with data from three other scans showed image quality degradation. In all other cases, no overt visual impact was observed.

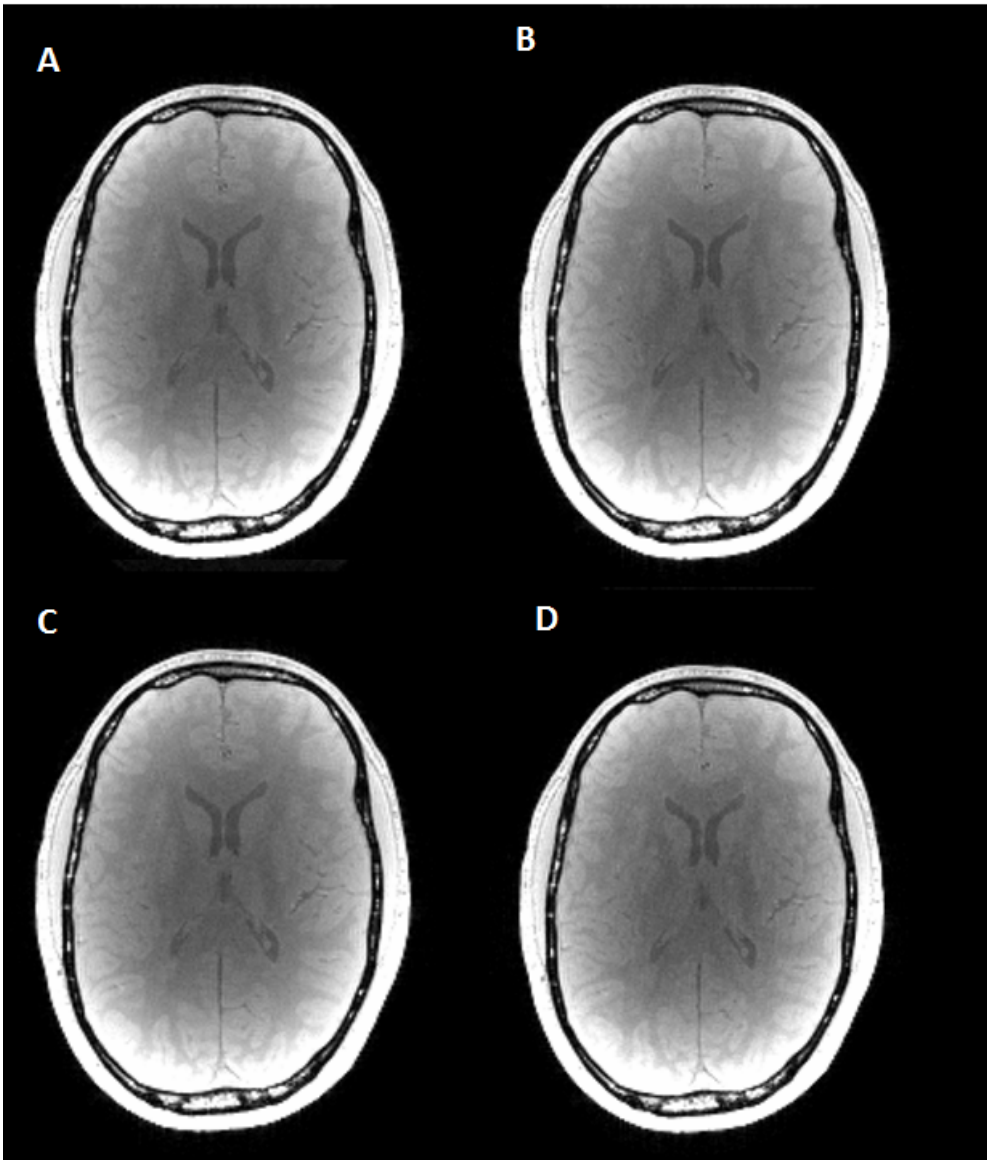

Figure V.6: Visual image quality for the first scan (A), the last scan (B), and the scenario where data from all four scans is used, for a replacement level of 10% (C) and 50% (D).

Scan-rescan variability, as characterised by the NRMSE comparing the two subsequent scans, was approximately ~5.3%, as seen in Table V.7.

	NRMSE for scan pair
Scan 1 - Scan 2	5.3%
Scan 2 - Scan 3	5.4%
Scan 3- Scan 4	5.2%

Table V.7 Scan-rescan NRMSE in the absence of k-space data replacement

NRMSE for all replacement scenarios are shown in Table V.8. For all but one scenario, where 50% of all k-space data for the first scan was randomly replaced by data taken from all following scans, NRMSE remained below average of scan-rescan variability, 5.3%.

Original scan	Source of replacement data	Level of replacement	NRMSE
Scan 1	Scan 2	10%	2.2%
		30%	3.6%
		50%	4.4%
Scan 2	Scan 3	10%	2.2%
		30%	3.6%
		50%	4.4%
Scan 3	Scan 4	10%	1.9%
		30%	3.1%
		50%	3.8%
Scan 1	Scans 2&3	10%	3.1%
		30%	4.8%
		50%	5.4%
Scan 1	Scans 2&3&4	10%	3.8%
		30%	5.2%
		50%	5.6%

Table V.8 NRMSE for the various replacement scenarios

V.5.3: Discussion

During acquisitions presented in this section, the extent of intra-scan motion was low enough that no TRs were identified as being affected by motion. Inter-scan motion was less than 0.4 mm and 0.2 degrees, thus the results presented in this section were a suitable surrogate to evaluate the effect of re-acquiring data that has been falsely classified as motion affected in a no motion case. K-space points were replaced in a random fashion, including simulating the effect of replacing data points used to drive the image reconstruction algorithm.

NRSME of images reconstructed from pooled data, with respect to their reference (the image that had parts of its k-space replaced) only exceeded scan-rescan variability in the scenario where data from four different scans were combined, with a replacement rate of 50%. The target false positive rate for the technique is 5%, an order of a magnitude lower.

Thus, I concluded that re-acquiring data retrospectively does not negatively impact image quality in the absence of intra-scan motion. Therefore, a retrospective correction method may be developed, based on classifying data points as either motion corrupted or not, replacing motion-corrupted data points with data re-acquired in the absence of intra-scan motion. This approach is similar to that of a recent study, in which data acquisition is suspended during periods on motion, and resumed once the head is at rest. While not directly comparable, the results presented in said study support the assumption that re-acquiring motion-corrupted data improves image quality at a reasonable increase in scan time (263).

The classification was previously done in a fashion where data from multiple coils was collapsed into one data point per TR. In the following sections of the thesis, I present the improvements to the sensitivity and specificity of the classification that can be achieved if the individual coils are treated as separate sources of navigator data. Combined with independently derived motion information, a general linear model could be designed, and the classification threshold can be defined on the prediction derived from this model.

V.6: Modelling head motion based on navigator values

During the studies described in previous sections of this Chapter, navigator data was treated as a single, descriptive value for a given TR. The navigator data acquired for all channels of a head coil (in the studies presented in this Chapter, 32 channels) were collapsed by looking at the variation of the navigator measure across coils. This approach greatly reduced the richness of the navigator data.

If each coil is treated as a separate source of data, 32 data points are collected for each TR. The 32 coils are arranged in a way to maximise head coverage. As has been shown in the FID navigator approach (212), this arrangement can be exploited to localise the detected signal, and derive 3D motion information. In this section, I detail the approach used during the PhD project to derive 3D motion information from the navigator proposed in the beginning of this Chapter. A general linear model is formulated, relating to the head position, as measured independently using the camera system, and the individual navigator values measured by each coil.

V.6.1: Methods

V.6.1.1: A general linear model framework

In the proposed navigator technique, an array coil with 32 channels is used to acquire the navigator data. Head motion, assuming rigid body motion, is described by up to six degrees of freedom that describe translation along x, y and z and rotation about each of these axes. It is hypothesised that such motion could differentially affect the navigator in each of the 32 channels and that this dependence could be modelled using a general linear model framework. An ideal model would estimate the six degrees of freedom of the head motion from the 32 degrees of freedom of the coils without any residual errors. A matrix formulation of this estimation is described below:

$$X = \beta \cdot N \qquad [V.2]$$

where vector X contains the six coordinates of head position in space, and vector N contains the 32 navigator values, one per channel. β is a 6-by-32 matrix describing the model that relates navigator values to head position. Note that X and N are measured for each TR, while the model is time-independent. This time dependence is not noted in the following sections, unless otherwise stated. In essence, the model relates the changes in head position over the whole of the acquisition to changes in the navigator values over the whole of the acquisition.

From the measured data of X and N, an estimate of the model parameters of β, $\hat{\beta}$ can be derived:

$$\hat{\beta} = N^{+} \cdot X \quad [V.3]$$

where N^{+} is the pseudoinverse of matrix N.

Using this model, the head position may be estimated from navigator values:

$$\hat{X} = \hat{\beta} \cdot N \quad [V.4]$$

where $\hat{X}$ is the model-based estimate of the head position, X.

The difference between the model-based estimate, $\hat{X}$ and the measured head position, X, is the residual of the model formulation, ε:

$$\varepsilon = \hat{X} - X = \hat{\beta} \cdot N - X \quad [V.5]$$

The inverse problem described in V.3 is ill-posed. During the acquisitions described in this Chapter, the condition number of N was found to be high, typically in the range of 350-750. Regularisation has to be applied to overcome the ill-conditioned nature of the system. In the implementation presented in this Chapter, Tikhonov regularisation was applied, and $\hat{\beta}$ was therefore estimated in a regularised least squares framework, minimizing the following term:

$$[\![\hat{\beta} \cdot N - X]\!]^2 + \|\lambda I \cdot N\| \quad [V.6]$$

Where λ is the regularisation parameter, and I is the identity matrix.

To evaluate the feasibility of using this predicted head position, $\hat{X}$ as the basis for tracking the head during scanning, this general linear model framework was applied to several previously used datasets, as well as new data.

V.6.1.2: Training datasets for the general linear model

Four pairs of head position and navigator data, X and N, acquired under motion conditions, were used in the estimation of the linear model. Motion datasets 1 through 3 were acquired on volunteer 2, concurrent with the acquisitions described in section V.4, using the PDw navigator sequence. Motion dataset 4 was acquired on an additional volunteer, described previously as volunteer 4 (36 years, male), using the PDw navigator sequence, where the volunteer was instructed to perform large and rapid head movements, in excess of millimetres and degrees, for several seconds at instructed times.

No motion datasets were also acquired. Two no motion pairs of head position and navigator data were acquired on volunteer 2, as described in section V.4, and one dataset was acquired on volunteer 4, in the same session as the motion dataset described above.

V.6.1.3: Data processing

Raw k-space data collected by the navigator echo was processed in the following way:

1. The square of the magnitude of the complex data was taken for each of the 512 sample points for each coil element and each TR. It was hypothesised, based on previous results, that taking the square magnitude would result in a measure more sensitive to large movements, the envisioned use case of the method.
2. For each TR and each coil element, the mean of the square magnitude across the 512 sample points was calculated.
3. A moving average filter was applied across TRs, as described in section V.2. The width of the moving average filter was treated as a parameter to be optimised, thus several filter widths were applied, as described in the next section.
4. For each coil element, the mean of this filtered measure was calculated across all TRs.
5. Normalisation was applied for each coil element and TR, by dividing the filtered measure, calculated in step 3, by the mean over all TRs, calculated in step 4.

Position logs from the camera system were processed by applying the same moving average filter as was applied to the navigator echo data. Position logs were used as input for the general linear model framework both with and without mean-centring. Mean-centring was applied to the position logs, by calculating, for each parameter, the mean over all TRs, and subtracting it from the position data of for all TRs.

V.6.1.4: Model comparison and analysis

For any given pair of X and N, two parameters had to be optimised in order to find the $\hat{\beta}$ that maximises the estimated position information of $\hat{X}$ while minimising the residual ε. These two parameters were the regularisation parameter of λ, and the width of the moving average filter (i.e. the number of TRs over which the averaging was performed). In addition, the models were estimated using position information, X, with and without mean-centring. 12 values of λ, λ=[0, 0.05, 0.1, 0.15, 0.2, 0.25, 0.5, 0.75, 1, 1.5, 2, 5], and 8 values of filter width (1, 5, 10, 15, 20, 25, 35, 50) were used in model estimation for each dataset. This large pool of potential models was analysed by the following hierarchical selection, based on the inflection point methods (264).

The effect of filter width was investigated in the first selection step. It was hypothesised that, for a given level of regularisation, an optimal filter width could be found. A filter width higher than this optimum would lead to an over-smoothed model, reducing the estimated position (as changes in position are smoothed out), while a filter width lower than this optimum

would result in a model sensitive to TR-to-TR fluctuations in the navigator measure, rather than motion-induced changes, increasing the residuals.

For a given dataset, and for a given model type (with or without mean-centring position log data), the residuals ε and the estimated position $\hat{X}$ were both transformed from matrices into vectors, and their L2 norm was taken. The logarithm of the norm (log-norm) was calculated. For a given regularisation parameter of λ, the log-norm of the residuals was plotted against the log-norm of the estimated position. These data points were found to fit onto an inverted parabolic curve. A parabolic function was fitted to the data points, and the inflection point of this parabola was determined. The data point closest to this inflection point was chosen as the optimal width of the moving average filter for the given regularisation parameter of λ. This selection process was repeated for all values of λ, giving one chosen filter width per regularisation parameter and model type.

The selected λ-filter width pairs were taken to the next level of selection In an l-curve approach, the log-norm of the solution estimated with a given combination of λ and filter width, chosen from the previous step, was plotted against the log-norm of the residuals for the same combination of λ and filter width, and the λ value corresponding to the maximum curvature was selected as the ideal regularisation parameter for a given dataset and taken to the next level of analysis. Thus, both the filter width and the regularisation parameter were fixed at the end of this selection step.

The selection process was repeated for both model types, resulting in two models, that is two estimated $\hat{\beta}$ matrices and two pairs of estimated position, $\hat{X}$ and residuals, ε, for each original pair on N and X. The model type, with and without mean-centring of X, with the lower residuals was taken to the next level, generalisation.

Selection criteria for a model type, applicable to all datasets, were: the ideal values of λ and filter width had to be close to each other across the four datasets, and only allowed to vary by one step (for example, if the ideal pair for dataset 1 was 1-20, and for dataset 4 0.75-25, the model would be accepted, but if the ideal pair for dataset 4 was 0.5-10, the model would be rejected). The $\hat{\beta}$ matrices for the ideal model on all four datasets were visualised to compare their structure.

If the same model, with comparable λ and filter width pairs was found to be the optimal for all datasets, a general model was created by taking the mean of the four $\hat{\beta}$ matrices estimated for the four datasets. If different model types (with or without mean-centring position log data) were to be found to be optimal for different datasets, then no general model could be established.

In the last evaluation step, all five $\hat{\beta}$ matrices (the four $\hat{\beta}$ matrices estimated on individual datasets, and the mean $\bar{\beta}$ matrix) were applied to all four datasets. If the mean

model, described by the mean $\bar{\beta}$ matrix was consistently the model with the second lowest residuals, the mean model was selected as the ideal model for modelling head position from navigator data. It was expected that the mean model would not outperform the model corresponding to a pair of X and N, but would outperform the models corresponding to other datasets. For example, on the first motion dataset, the model (the $\hat{\beta}$ matrix) derived from the position and navigator data of the first dataset was expected to perform best (give the lowest residuals), the mean model was expected to perform second best, and the models derived from the other three motion data sets were expected to perform worse.

The mean model was evaluated both on motion and no motion datasets, to assess the performance both in the presence and in the absence of motion. Ideally, the mean model would be such that in the absence of motion, no motion is predicted by it, and that in the presence of motion, periods of motion and no motion are clearly delineated, and the extent of motion is tracked with reasonable accuracy.

V.6.2: Results

V.6.2.1: Characteristics of head motion

Head motion was described using the extended distance metric, $D_{ext}(t)$, described in Chapter IV, in order to capture rotation as well as translation. For motion cases, head motion across the datasets varied both in timing, and in extent, as shown in Figure V.7.

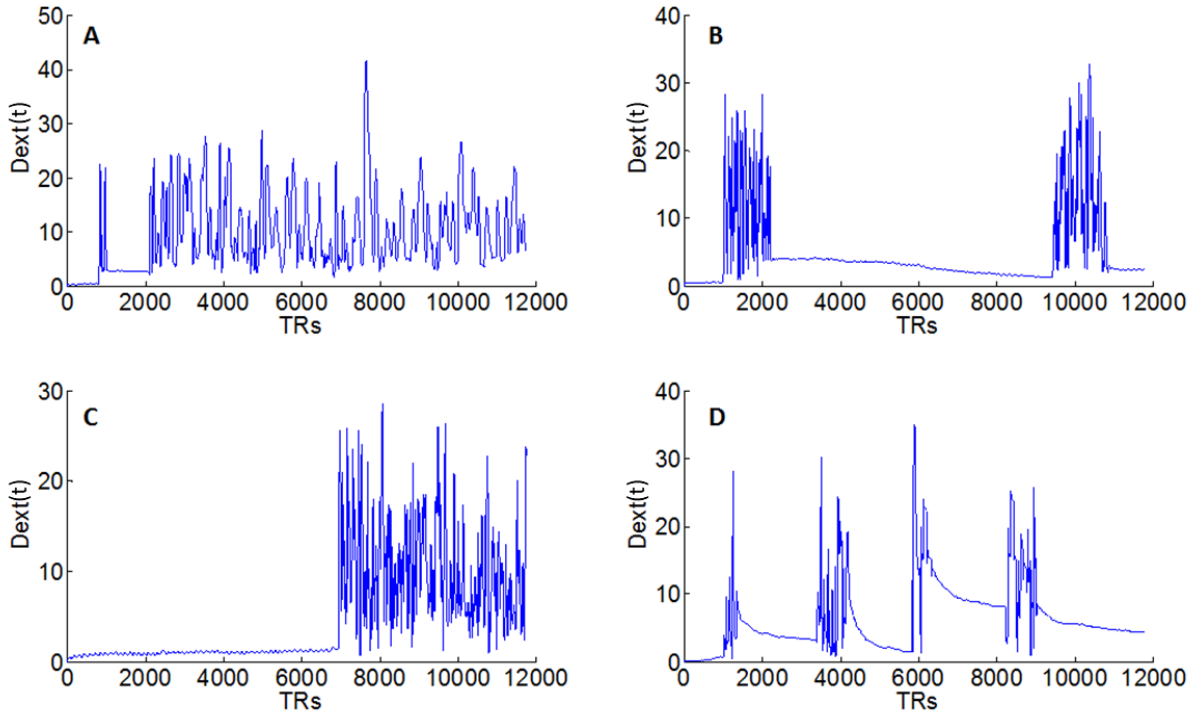

Figure V.7: Head motion for the four motion datasets (derived from position log data without mean-centring), described by the summary distance measure of $D_{ext}(t)$, as defined in Chapter IV. Datasets 1 through 3 (A through C in the figure) were acquired on the volunteer previously described as volunteer 2, while dataset 4 (D in figure) was acquired on volunteer 4. Note the difference in timing and amplitude between the datasets.

V.6.2.2: Optimal filter width-regularisation parameter pairs

The selection process for finding the optimal filter width for given values of λ is illustrated below, using dataset 3, and a model type where position log data is not mean-centred.

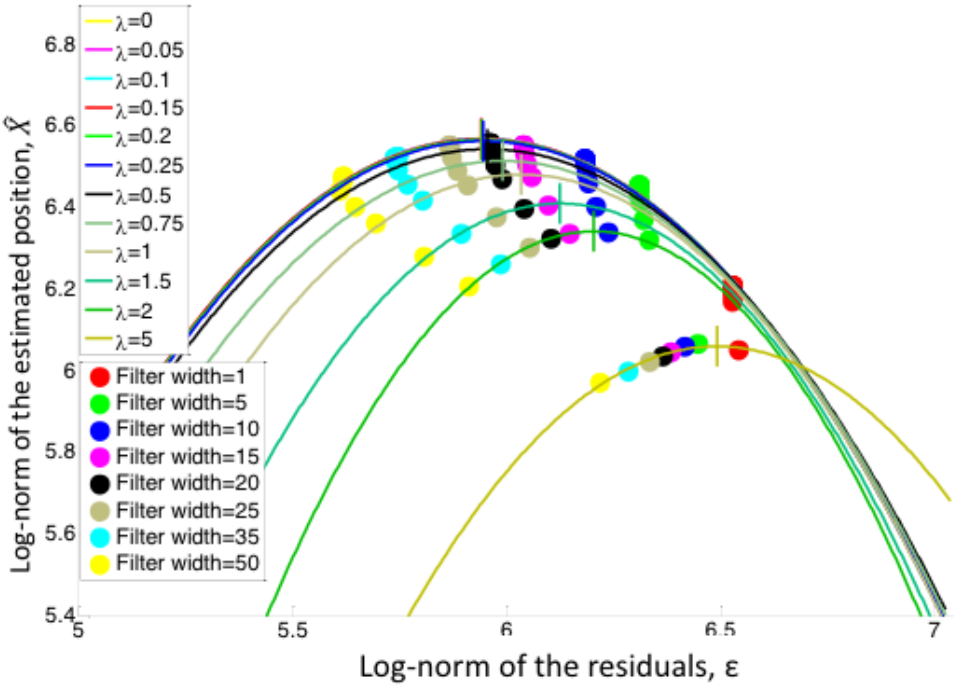

Figure V.8: λ and filter width pairs for dataset 3, using the model without mean-centring position long data. The inverted parabolas fitted for each values of λ are shown, and their inflection point is indicated by a crossing line.

The optimal pairs of λ and filter width for the four datasets are summarized in Table V.9. For all datasets, both models fulfilled the selection criteria.

Dataset	Using position log data without mean-centring		Using position log data with mean-centring	
	Optimal λ	Optimal filter width	Optimal λ	Optimal filter width
1	1	20	1	20
2	1	20	1	20
3	1.5	15	1	15
4	1.5	15	1	20

Table V.9: Optimal λ-filter width pairs for the two model types and four motion datasets.

V.6.2.3: The effect of mean-centring position data

Mean-centring position log data resulted in an increase of residuals in only one dataset out of four, as illustrated in Table V.10, thus both models were taken to the next level of analysis.

Dataset	Log-norm of residuals	
	Positon log mean-centered?	
	No	Yes
1	6.19	6.19
2	6.08	6.08
3	5.99	6.09
4	5.87	5.87

Table V.10: Residuals of the four optimal models with or without mean-centring position log data

For both models, $\hat{\beta}$ matrices showed a similar structure, with highest absolute values found for channels 23 and 29, and for translation in the z direction. This structure was consistent across the four motion datasets and their corresponding matrices, thus both models were taken to the next level of analysis.

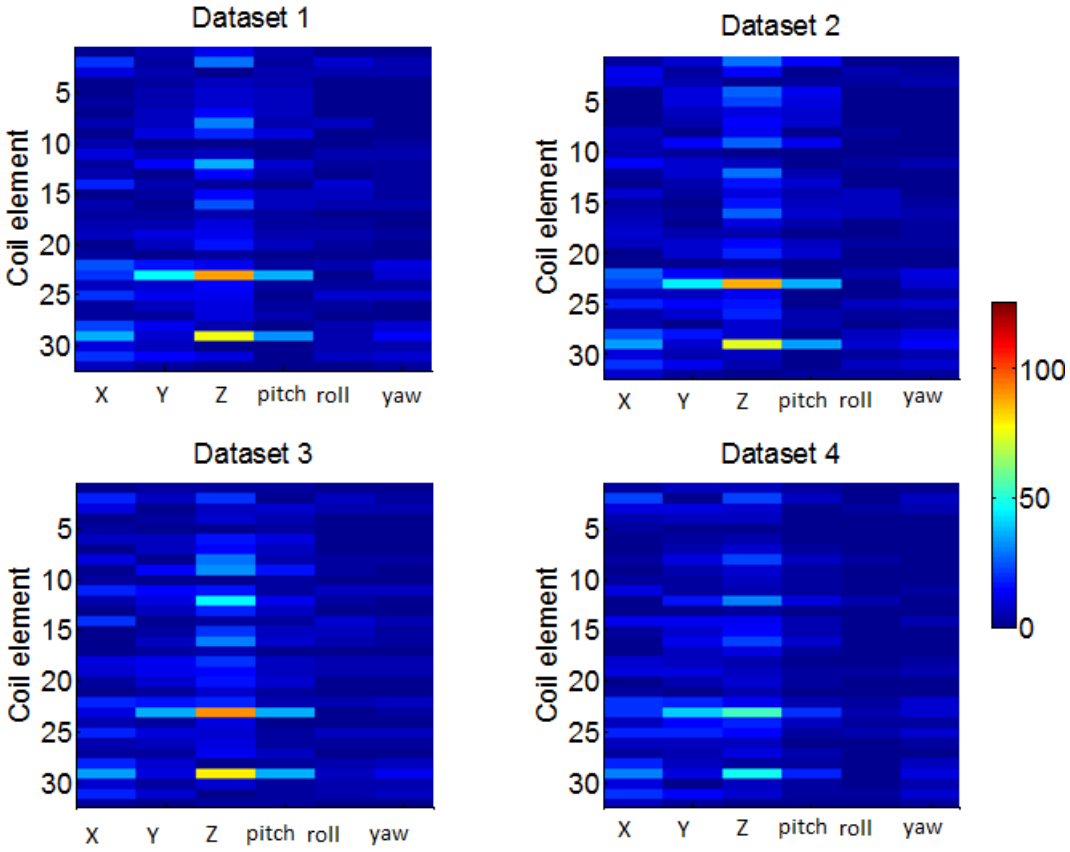

Figure V.9: Absolute values of the four beta-hat matrices for the model without mean-centring position log data.

V.6.2.4: Model performance

An example of applying the mean model is shown in Figure V.10 (without mean-centring) and V.11 (with mean-centring). While the mean model does, for both model types, replicate the trend in the magnitude of motion, the error in the estimation, both for periods of motion, and periods of no motion, is on the order of millimetres and degrees.

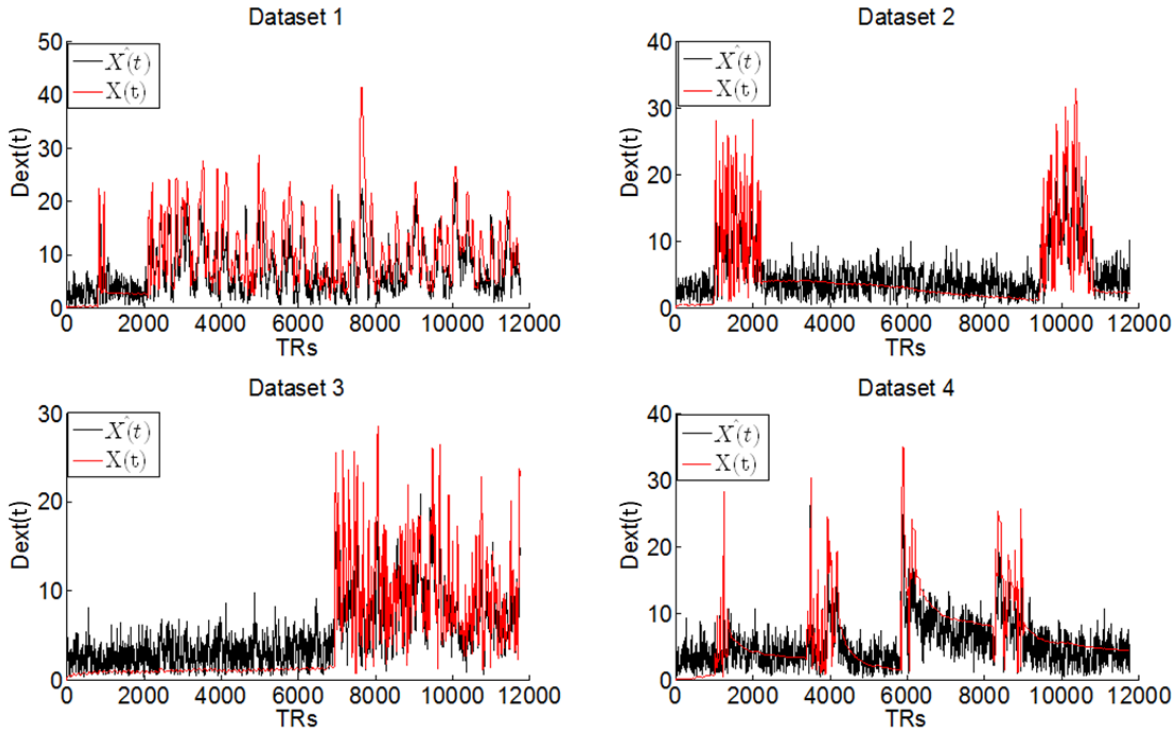

Figure V.10: Summary distance measure of both original motion log data of X(t), and the position estimated by the mean model $\hat{X}(t)$, without mean-centring position log data. Original, measured position information in red, model estimate in black. While the black model estimate does well replicate the trend of the measured positions, in periods of no motion, for example between TRs 2200 and 9000 on Dataset 2 (acquired on volunteer 2, as previously described), the difference between measured and estimated position is on the order of millimetres. Note that the time dependence of X(t) is explicitly noted to highlight the behaviour in period with or without motion.

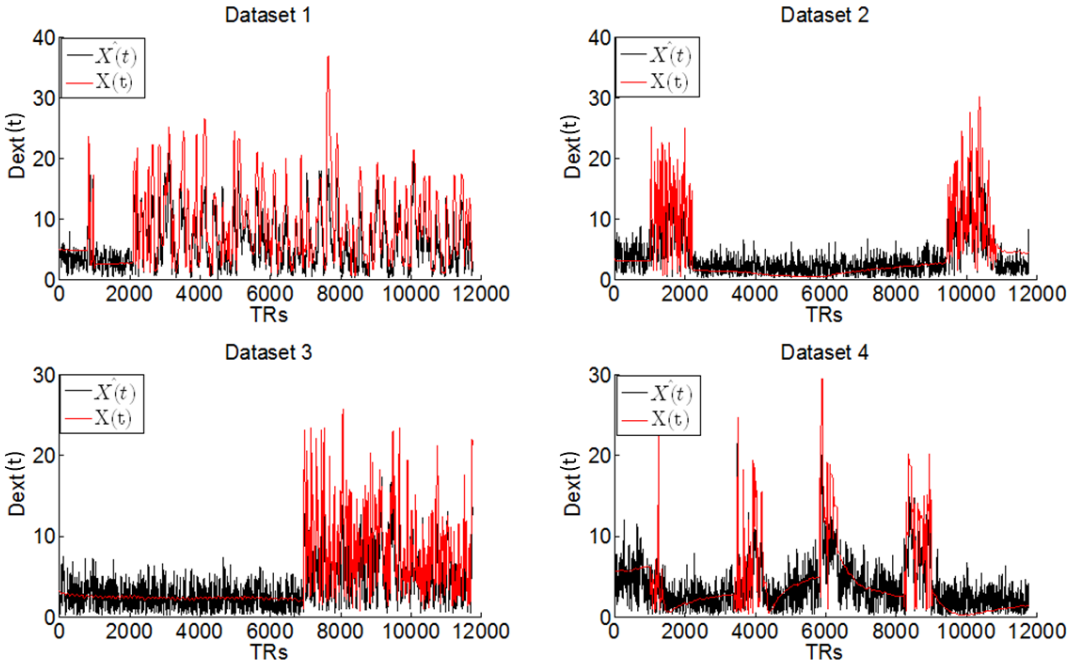

Figure V.11: Summary distance measure of both original motion log data of X(t), and the position estimated by the mean model, $\hat{X}(t)$,, with mean-centring position log data. Original, measured position information in red, model estimate in black. Mean centring position log data does not affect the trend described in the previous Figure, and during periods of no motion, such as the first half of Dataset 3, the error is still on the order of millimetres and degrees. Note that the time dependence of the measured and estimated position is explicitly noted to highlight the behaviour in period with or without motion.

V.6.3: Discussion

During the study presented in this section, I hypothesised that using the 32 receive coils surrounding the head, the navigator signal could be spatially localised with the help of the individual coil sensitivity profiles, and accurate 3D motion information could be derived using a general linear model framework.

Using the navigator information from each coil, a general linear model was constructed in which head position data was estimated from the navigator data. I have found that it was possible to find the parameters of regularisation and average filter width that resulted in the best estimate of position for a given dataset. These individual models could be combined into a mean model. However, head position was predicted with errors on the order of millimetres and degrees, and crucially, this prediction error was also found during periods of no motion. Thus, this approach was not found to be directly applicable for motion correction, i.e., using the motion parameter estimates for registration of images/samples.

Compared to the FID navigator approach, where the navigator signal is similarly localised using the sensitivity profile of individual coils, navigator data is acquired at the end of a TR, during gradient spoiling, thus has a very low signal intensity. In the FID approach, the navigator is acquired at the beginning of each TR, with high signal intensity. This difference may explain why the proposed method did not accurately predict head position, whereas the FID method has been shown to deliver accurate head position information (212,265,266).

In the following section, I describe the subsequent work done using this general linear model framework. The feasibility of using the model estimate as the baseline for outlier rejection was investigated first.

V.7: Outlier rejection based on the general linear model

While head position could not be estimated from the proposed general linear model with sufficient accuracy, I investigated if the model estimation could be used improve the sensitivity and specificity of the classification of individual TRs as affected or unaffected by motion.

V.7.1: Methods

The mean models, both with and without mean-centring position information, presented in the previous section were applied to the no motion datasets of section V.6, in order to determine a classification threshold. The extended distance metric, as described in Chapter IV, of the model estimate $\hat{X}$, $D_{ext}(t)$ was calculated across all no motion cases, and a threshold was defined so that no more than 5% of all TRs for each no motion case had a $D_{ext}(t)$ value exceeding this threshold. This is equivalent to enforcing a false positive rate no higher than 5%, as in section V.4.

This classification threshold was then applied to the motion cases described in section V.6 (and thus, implicitly, to motion cases of volunteer 2, as described in section V.4, as data was taken from those scans), and the sensitivity and specificity of the classification based on this threshold was compared to the gold standard classification based on the optical tracking based position logs, similar to the method described in section V.4.

V.7.2: Results

Both mean models, with and without mean-centring of position data, were applied to the no motion datasets described in section V.6.2, and the mean and standard deviation of the estimated $D_{ext}(t)$ measure were calculated, summarized in Table V.11. Note that no motion datasets 1 and 2 were acquired on volunteer 2, and no motion dataset 3 was acquired on volunteer 4.

No motion dataset	$D_{ext}(t)$ (mean±sd)	
Position logs mean-centred in model?	No	Yes
1	4.25±1.68	1.97±1.07
2	4.21±1.63	1.87±1.03
3	4.20±1.56	1.82±0.99

Table V.11: Means and standard deviations of the estimated extended distance metric for all no motion datasets, and both mean models

A classification threshold was defined using the same approach as in section V.4, defined as: $\overline{D} \pm N * \overline{SD}$, where $\overline{D}$ is the mean of $D_{ext}(t)$, as described in the previous Table, across the three no motion datasets, and $\overline{SD}$ is the mean of the standard deviations of D_{ext} for no motion datasets. For both models, the values of N that resulted in a classification threshold that rejected on average no more than 5% of TRs for no motion datasets was N=2.

The sensitivity and specificity of this classification threshold for detecting motion in motion-corrupted datasets, motion is shown in Table V.12 for both models. Note that the datasets denoted as 1, 2 and 3 in Table V.12 are the datasets denoted as PD scans in Table V.6

Compared with the classification summarized in Table V.6, both models outperformed the previous outlier rejection approach, with and average improvement of sensitivity of 0.21 and 0.04 on average, for the model with and without mean-centring, respectively. The change in sensitivity was -0.02, a slight decrease, for the model with mean-centring, and an increase of 0.09 for the model without mean-centring. Overall, the model with mean-centring showed higher improvements in classification than the model without.

Motion dataset	Sensitivity		Specificity	
Position logs mean-centred in model?	Yes	No	Yes	No
1	0.66	0.45	0.63	0.78
2	0.78	0.65	0.89	0.98
3	0.68	0.49	0.86	0.98
4	0.69	0.54	0.71	0.84

Table V.12: Sensitivity and specificity of outlier rejection based on the two general linear models.

V.7.3: Discussion

I have found that a classification based on applying a general linear model to the collected navigator data, using information from all 32 channels, outperforms the classification based on a collapsed metric, as described in section V.4.

For both models investigated in this section (with and without mean-centring position information), there was an overall increase in classification (the sum of sensitivity and specificity increased). This increase was higher for the model with mean-centring. While this model did result in a slight decrease of specificity, sensitivity was, as in section V.4, rated more important than specificity, thus the general linear model estimated from the mean-centred position logs was chosen for further evaluation as a retrospective motion correction scheme.

This increased performance of this model comes at the cost of acquiring the training datasets used in this section. However, once both camera and navigator training datasets have been acquired, the proposed general linear model approach can be applied to all future acquisitions.

V.8: Application of the general linear model based motion correction method in accelerated imaging

It was demonstrated that, based on navigator data acquired concurrently with gradient spoiling, motion can be detected and classified in an outlier rejection framework, with maximal sensitivity being achieved when this outlier rejection is based on a generalized linear model of the navigator data. In this section, I describe a novel motion correction method, based on re-acquiring data that has been classified as affected by motion, and evaluate its utility in improving image quality.

V.8.1: Methods

V.8.1.1: Implementation of a data re-acquisition technique

The navigator-based outlier rejection was implemented in the image reconstruction framework of the scanner (a Siemens 3T TIM Trio system, running software version VB17). All calculations, and re-acquisition was implemented by modifying the standard ICE online (on the scanner console) reconstruction supplied by Siemens, thus all the modifications described in this section could be easily translated to a clinical scanner. These modifications were carried out with the help of a collaborator at Siemens, Dr. Iulius Dragonu.

An additional computational step was inserted into the online image reconstruction ICE pipeline, in order to directly access raw k-space data. During acquisition, for each TR, for each coil element, the mean of the square of the magnitude of the complex data across the 512 sample points is calculated. A moving average filter of filter width 20 TRs was applied for each coil element. After all imaging data had been acquired, the navigator value was normalized for each coil element by the mean across all TRs. These processing steps were the online implementation of the offline steps described in section V.6.2.

This normalized navigator data were then multiplied by the mean $\bar{\beta}$ matrix corresponding to the general linear model with mean-centred position logs, as described in section V.6. The extended distance metric of the model estimate was calculated for each TR, and TRs were classified as either motion affected or unaffected if the distance metric exceeded, or was below, the threshold as described in section V.7. TRs classified as motion affected were then re-acquired by the scanner in a sequential manner. After the data for all TRs classified as motion affected were reacquired, the images were reconstructed, using the re-acquired data.

Crucially, the GRAPPA reconstruction algorithm implemented on the scanner, did not support the re-acquisition of reference lines. These reference lines were moved to a different data container during acquisition, and once all reference lines have been acquired, this container was sealed. Subsequent to their acquisition, these lines could not be accessed or modified, and any attempt to re-acquire a reference line resulted in the scan stopping without reconstruction. Thus, while the implementation could be used to identify reference lines as motion-corrupted, this information could not be used to improve image quality. Thus, the online implementation of the outlier rejection could only correct for outliers in the acquisitions that were not part of the auto-calibration reference lines.

This version of the sequence and image reconstruction is referred to as the navigator sequence with re-acquisition.

V.8.1.2: Study design

Four volunteers (1 male, age range 27-38) were scanned using the navigator sequence with re-acquisition, under motion and no motion conditions. Volunteers were instructed to perform large and rapid head motions for several periods of over 10 seconds, in the range of several millimetres and degrees, or more, under motion conditions, and to stay as still as possible under no motion conditions. No restriction was placed on the timing of the motion periods, to avoid bias towards k-space points with higher or lower k-space energy. Both PDw and T1w scans were acquired on all volunteers. Volunteer motion was monitored using the camera system. Note that there is no correspondence between the volunteers of this section and the volunteers of previous sections.

V.8.1.3: Image reconstruction

For all scans, raw k-space data was saved. This data included both the original imaging data acquired before any re-acquisition, and the re-acquired data. In the SENSE framework introduced in section V.5, two versions of each scan were reconstructed offline, one with the original data and the other with those data identified as being motion-corrupted having been reacquired.

V.8.1.4: Image processing

For all reconstructed scans, the arithmetic mean of all echoes was calculated, in order to investigate the effect of motion on the data that were used to calculate R1 maps in the MPM approach. For each contrast, images were processed in the following way.

The means of all scans were co-registered to the mean of the scan acquired under a no motion condition without re-acquisition. Tissue probability maps for grey matter, white matter and CSF were derived from the scan acquired under the no motion condition without re-acquisition. A brain mask was created by the conjunction of the grey matter, white matter, and CSF probability maps, each thresholded at 50% probability. This brain mask included both tissues of interest (grey and white matter), and the region into which motion artefacts might displace signal, CSF.

This mask was applied to all co-registered scans. A normalized root mean square error (NRMSE) was calculated for all scans:

$$NRMSE_i = \sqrt{\frac{1}{N}\sum_{j=1}^{N}\left(\frac{I_i(j) - I_{q,1}(j)}{I_{q,1}(j)}\right)^2} \qquad [V.7]$$

Where $NRMSE_i$ is the normalized root mean square error of mean scan i, I_i is the signal intensity of mean scan i at voxel j, $I_1(j)$ is the signal intensity of the mean scan acquired under no motion condition and without re-acquisition at voxel j, and index N sweeps across all nonzero voxels in the brain mask.

V.8.1.5: Quantifying motion artefacts

Motion was independently tracked using the camera system, and TRs were classified, based on the motion logs, as motion corrupted or unaffected by motion, in order to quantify the sensitivity and specificity of navigator-based detection.

Motion during scans was quantified in two ways. The percentage of data points affected by motion was calculated to give an overall measure of the extent of motion, as was done in section V.4.

To characterize not only the extent, but the impact of motion, motion during scans was quantified by the sum of k-space energies for each TR that was identified as motion affected according to the gold standard classification based on motion logs, expressed as a percentage of the total k-space energy of the acquisition. It was hypothesised that a larger ratio of corrupted k-space energy would correspond with lower image quality, as measured by an increase in NRMSE, based on the results presented in Chapter IV.

V.8.1.6: Navigator performance

Sensitivity and specificity of the navigator-based motion detection method was calculated, and compared to the gold standard classification based on the position logs.

V.8.2: Results

V.8.2.1: Motion during scanning

The scans acquired under motion conditions were severely affected by motion, as a large fraction of the total k-space energy was identified as being affected by motion according to the gold standard classification based on the position logs. For all volunteers, motion occurred over more than a fifth of the acquisition, and the ratio of TRs affected by motion was always higher than the ratio of k-space energy affected. This reflects the k-space distribution of an accelerated scan, where some non-central lines are not acquired, as illustrated in Figure IV.9 of Chapter IV.

Volunteer	Corrupted k-space energy		Ratio of TRs affected by motion	
Contrast	PD	T1	PD	T1
1	17.4%	18.2%	20.8%	29.3%
2	27.6%	35.1%	37.9%	46.2%
3	25.8%	26.6%	48.4%	51.0%
4	13.1%	7.9%	23.5%	23.9%

Table V.13: The effect of motion, as characterised by the ratio of motion-affected k-space energy to the total, as well as the ratio of affected TRs.

V.8.2.2: Performance of motion detection

Sensitivity and specificity of the navigator-based classification for the motion cases of the four volunteers is summarized in Table V.14. Both sensitivity and specificity show a wide spread, but for all volunteers and contrasts, motion was detected above chance, as the sum of sensitivity and specificity was, for all volunteers and contrasts, above 1, although only barely for volunteer 4. In the case of volunteer 4, it was hypnotised that due to the relatively small head size, the model failed to adequately capture head motion, as the changes in the navigator measure were not sufficiently large.

Volunteer	Sensitivity		Specificity	
Contrast	PD	T1	PD	T1
1	0.74	0.77	0.79	0.69
2	0.65	0.65	0.52	0.82
3	0.40	0.49	0.83	0.61
4	0.19	0.17	0.84	0.89

Table V.14: Sensitivity and specificity of navigator-based classification for the motion cases of the four volunteers.

V.8.2.3: Image quality

Given the above-chance detection, it was expected that image quality, as quantified by NRMSE, would be improved by data re-acquisition. However, this was not the case, as summarized in Table V.15. It was not possible to re-acquire reference lines, which has a double effect on image quality. First, reference lines are central points in k-space, with very high relative k-space energy. Secondly, reference lines are used to calculate the reconstruction kernel, thus any adverse effect of motion manifests not only in the image information carried by them, but by the effect of a corrupted reconstruction kernel. It was hypothesised that these mechanisms were the reason for the lack of improvement in image quality, despite the reasonable detection of motion.

In the absence of motion, re-acquiring data did not significantly increase NRMSE as expected from section V.5.

Contrast	No motion, re-acquisition	Motion, no re-acquisition	Motion, re-acquisition
PD	0.5±0.1	12.4±1.2	12.0±1.0
T1	0.8±0.3	15.7±4.8	14.6±4.0

Table V.15: Mean and standard deviation (across the group) of NRMSE for the motion cases.

Re-acquiring data falsely identified as motion affected did not introduce visible changes in image quality in a no motion condition, as shown in Figure V.12.

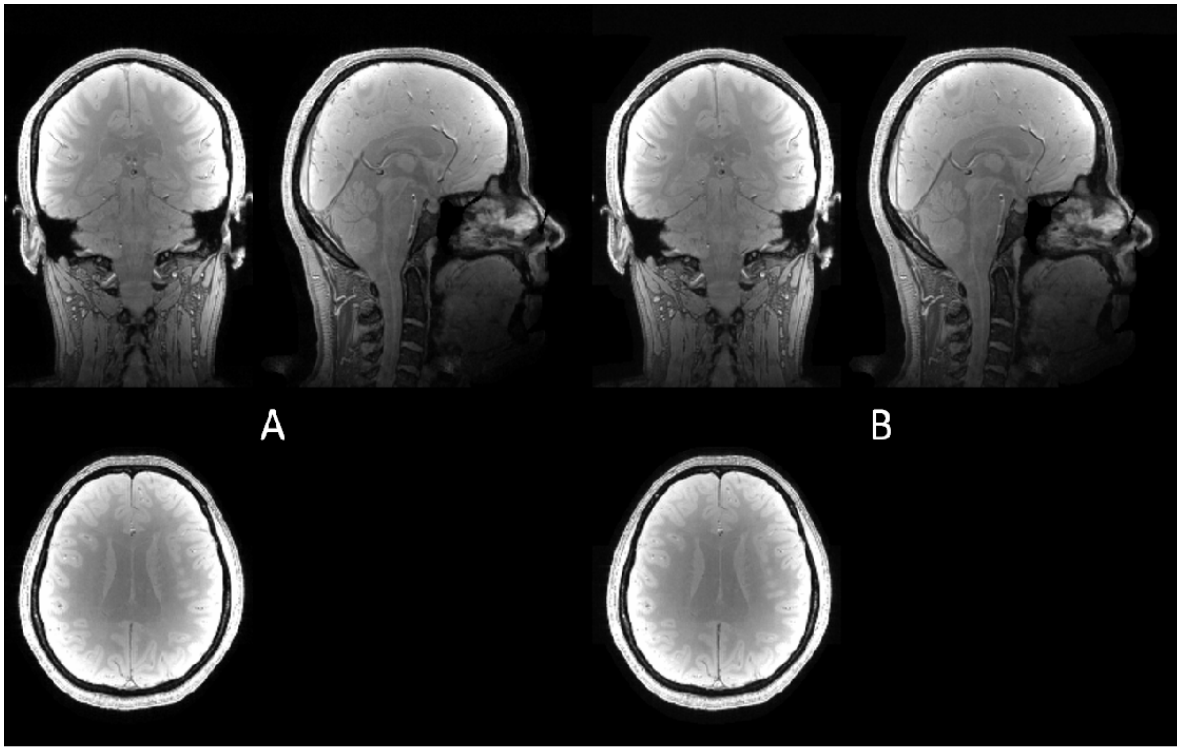

Figure V.12: Image quality of PDw scans acquired on volunteer 2 under no motion conditions, without (A) and with re-acquiring data identified as affected by motion. No overt changes in image quality are visible.

No visible changes were detected under motion condition, as shown in Figure V.13. This may be due to the inability of the navigator implementation to re-acquire autocalibration reference lines.

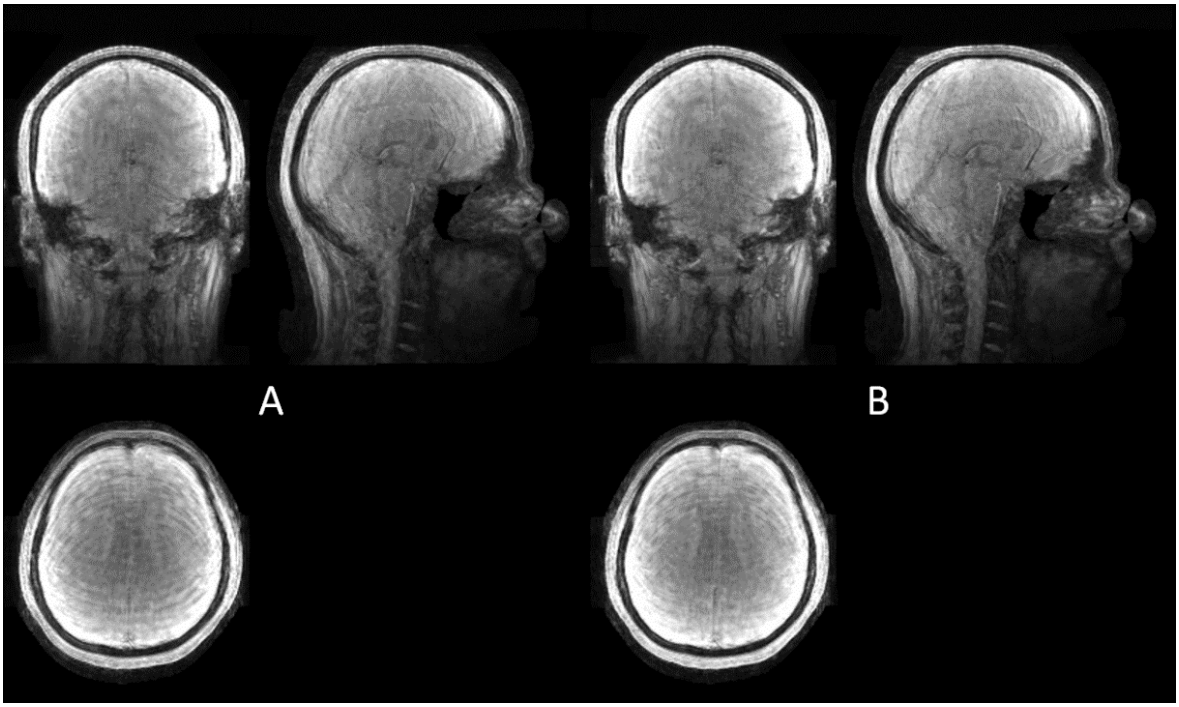

Figure V.13 Image quality of PDw scans acquired on volunteer 2 under motion conditions, without (A) and with re-acquiring data identified as affected by motion. Note the severe motion artefacts for both scans.

V.8.3: Discussion

I have evaluated the performance of the navigator technique, both for detecting and correcting for motion, in an in vivo study. Motion was detected by applying the general linear model described in section V.7 with an outlier rejection formalism, and corrected for by re-acquiring data in a retrospective fashion. Due to restrictions in the image reconstruction framework in which data re-acquisition was implemented, it was not possible to re-acquire reference lines used in parallel imaging. Thus, these central k-space points with high energy could not be re-acquired. These points also form the basis for the calculation of the image reconstruction kernel. The inability to re-acquire this data res resulted in a lack of appreciable improvements in image quality, both visually, and quantified in terms of NRMSE.

The navigator detected motion with above chance probability in all motion cases, for all volunteers and contrasts. However, as not all TRs correctly identified as motion affected could be re-acquired, this was not reflected in the image quality metric of NRMSE. Under no motion conditions, re-acquiring data falsely identified as being motion-corrupted did not significantly increase NRMSE, as compared to a no motion, no reacquisition case, in accordance with the goals of this study.

In this study, it was not possible to re-acquire reference data points. However, it was also not possible, within the confines of this study, carried out using parallel imaging, to differentiate whether the lack of improvement was due to the inability to re-acquire low spatial frequency data alone, or due to the effects on the parallel imaging reconstruction framework, or if the implemented re-acquisition approach is fundamentally not feasible for motion conditions. A new study was thus designed, without the use of parallel imaging, in order to demonstrate the feasibility of the navigator approach.

Results from this section were used to improve the new study. Motion instructions would be shown on a video screen, in order to restrict the duration of motion periods. Due to the relatively high level of motion corruption found in this section, both in terms of affected TRs and affected k-space energy, the motion instructions would be re-designed to focus on short periods of extensive motion. The general linear models of volunteers 1, 2, and 3 were incorporated, along with the models described in section V.6, into a new mean model, to take advantage of the data acquired.

V.9: Application of the general linear model-based motion correction method in non-accelerated imaging

While in the previous section, the ability of the navigator technique to detect motion was demonstrated, the successful detection of motion did not lead to improvements in image quality, as it was not possible to correct for motion that occurred during the acquisition of reference lines. Additionally, it was found that volunteer motion was excessive, when quantified in terms of corrupted k-space energy.

A new proof of principle study was designed to account for both issues. Scans used in this study were acquired without parallel imaging. Scan time was minimised by partial Fourier acquisition, elliptical k-space coverage, and adjusting the FoV on a per-volunteer basis. Explicit motion instructions were given, based on results from clinical literature (192,240,262).

V.9.1: Methods

V.9.1.1: Study design

Two volunteers were scanned in this study. FoV in the second phase-encoded dimension was tailored to the extent of each volunteer's head, in order to minimise acquisition time. Volunteer 1 (32 years, male) was scanned with the T1w version of the sequence, with the following parameters: FoV = 256 x 224 x 160 mm^3, partial Fourier factor in both phase encoded directions: 7/8, elliptical k-space coverage, for an acquisition time of approximately 10 minutes per scan. The volunteer was instructed to perform head motions of no more than 2 cm, according to a randomly chosen timing. Volunteer 2 (38 years, male) was scanned with the PDw version of the sequence, with the following parameters: FoV = 256 x 224 x 176 mm^3, partial Fourier factor in both phase encoded directions: 7/8, elliptical k-space coverage, for an acquisition time of approximately 11 minutes per scan. The volunteer was instructed to perform head motions of no more than 2 cm, according to randomly chosen timing. This scan was repeated with the same motion instructions.

For both volunteers, motion instructions were delivered using a screen positioned at the end of the bore of the scanner, which was visible for the volunteers through a mirror. The timing was determined by a bespoke algorithm implemented in MATLAB. Timings were set such that on average, a period of motion would last 3 ± 2 seconds, and that, on average, 60 ± 10 seconds passed between two motion periods for the first, and 30 ± 5 seconds for the second volunteer. During periods of no motion, and for no motion condition scans, a fixation cross

was shown, in order minimize inadvertent head movement. During periods of motion, the word “move” was shown on the screen.

The data for both volunteers was evaluated using the same methods as described in section V.8.

V.9.1.2: Image reconstruction and processing

Raw k-space data was reconstructed offline in a MATLAB environment. To avoid Gibbs ringing artefacts arising from partial Fourier coverage, a square cosine filter, with a fall-off of 20 data points, was applied to the raw k-space data, before zero-padding.

V.9.2: Results

V.9.2.1: Motion during scanning

The scans acquired in this study were less severely affected by motion, as can be seen by the relatively low percentage of k-space energy that was corrupted by motion, compared to the results of the previous section. The ratio of TRs affected by motion was likewise lower, compared to the previous section. However, the ratio of corrupted k-space energy was again found to be lower than the ratio of affected TRs. This indicates that the central portion of k-space was less affected by motion, due to the random timing.

Volunteer	Corrupted k-space energy	Ratio of TRs affected by motion
1	2.6%	4.1%
2	9.7%	13.5%
2, repeat scan	8.8%	8.7%

Table V.16: The effect of motion, as characterised by the ratio of motion-affected k-space energy to the total, as well as the ratio of affected TRs

V.9.2.2: Performance of motion detection

Sensitivity and specificity of the navigator-based classification for the motion cases of the two volunteers is summarized in Table V.13. Sensitivity for the first volunteer was low, compared to the second volunteer and previous applications of the navigator. This may be reflective of the low level of motion present in the scans of the same volunteer.

Volunteer	Sensitivity	Specificity
1	0.39	0.89
2	0.83	0.75
2, repeat scan	0.76	0.79

Table V.17: Sensitivity and specificity of navigator

V.9.2.3: Image quality

NRMSE for the three motion cases are summarized below. In the absence of motion, the increase of NRMSE was below 2% (note that there was only one no motion condition scan for volunteer 2), and in all motion cases, NRMSE was decreased due to the re-acquisition of motion corrupted data points.

Volunteer	No motion, re-acquisition	Motion, no re-acquisition	Motion, re-acquisition
1	1.8	6.9	5.8
2	1.8	6.7	5.7
2, rescan		6.1	5.2

Table V.18: NRMSE for the motion cases.

Re-acquiring data falsely identified as motion affected did not introduce visible changes in image quality in a no motion condition, as shown in Figure V.14.

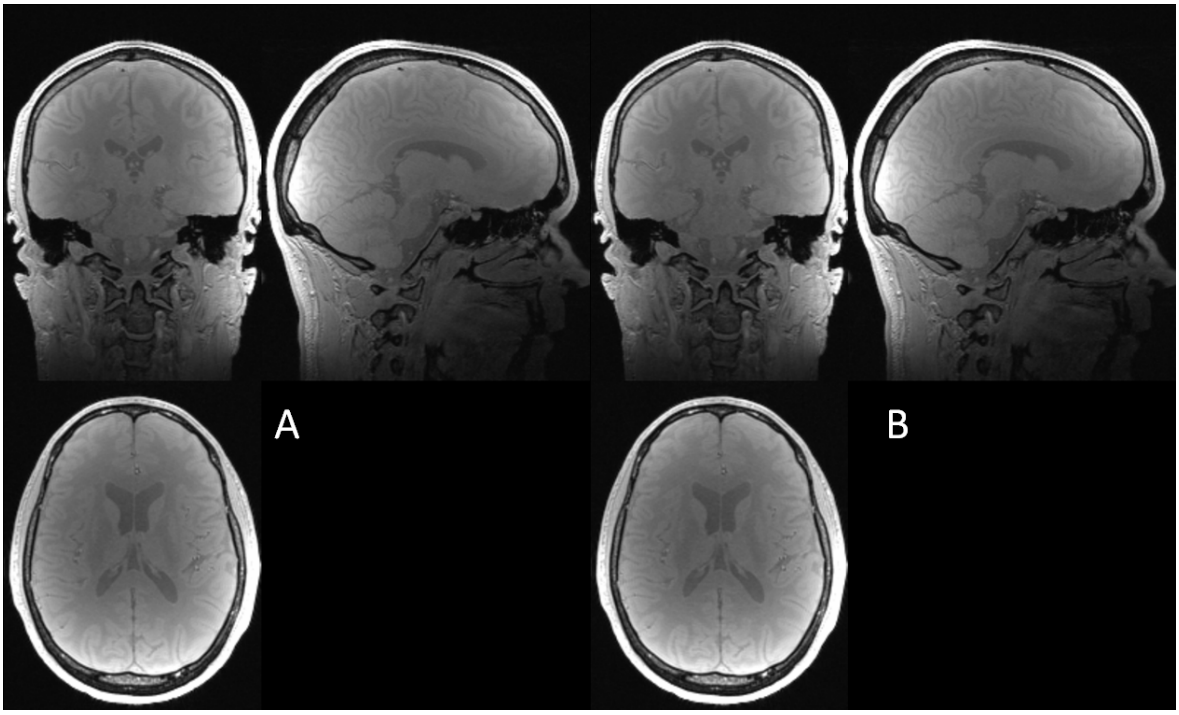

Figure V.14: Image quality of PDw scans acquired on volunteer 2 under no motion conditions, without (A) and with re-acquiring data identified as affected by motion.

Under motion conditions, visual image quality was improved for all scans. Due to the low inherent level of motion artefacts, this improvement was less apparent for volunteer 1, however, a slight decrease in ringing artefacts could be observed, indicated by a blue arrow in Figure V.15.

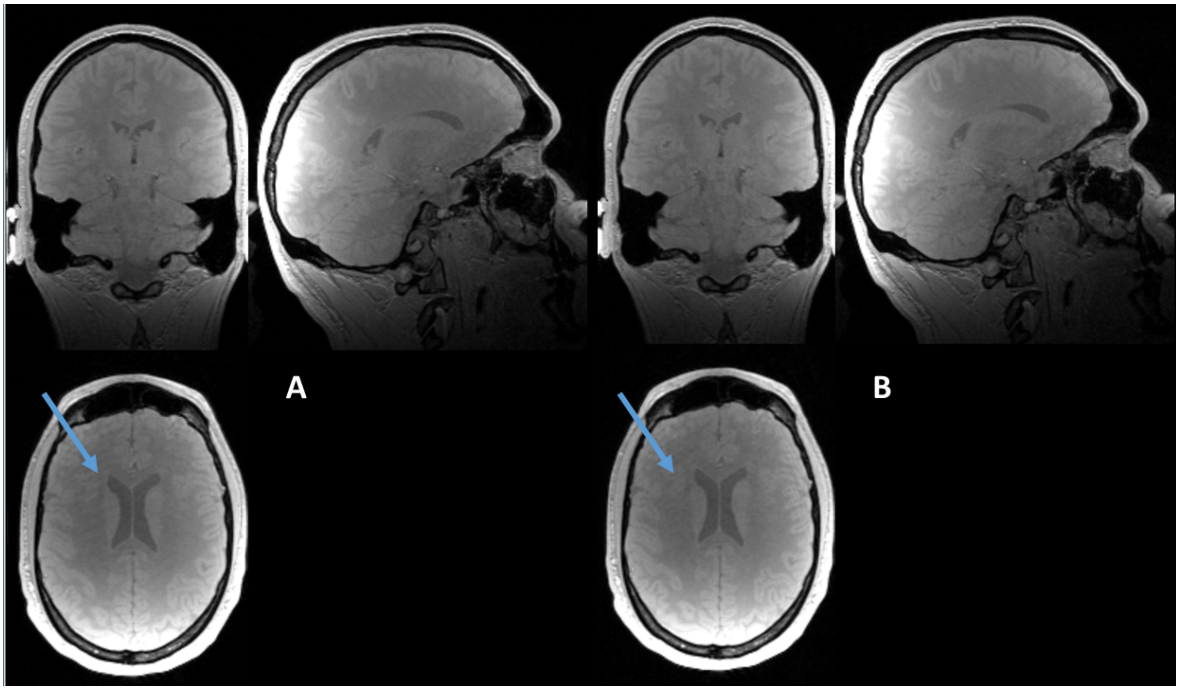

Figure V.15 Image quality of PDw scans acquired on volunteer 1 under motion conditions, without (A) and with re-acquiring data (B) identified as affected by motion. Due the low inherent level of motion, the degradation in image quality is not pronounced. However, re-acquisition of data did result in a decrease of the characteristic ringing artefacts, indicated by a blue arrow, which are more pronounced in the image reconstructed from data without re-acquisition.

For volunteer 2, re-acquiring motion corrupted data improved visual image quality in both scans. In the first scan, there was a marked decrease in artefact levels outside the brain (yellow arrow on Fig V.16 A and B), as well as a decrease in the prevalence of ringing artefacts (red and blue arrows). The outline of the ventricles in the posterior of the brain is better delineated in the image reconstructed using re-acquired data, compared to the case without motion correction. For the second scan, while no decrease in the artefact level outside the brain was observed, the motion correction method decreased the level of ringing artefacts and blurring, indicated by red and blue arrows in Figure V.16 C and D.

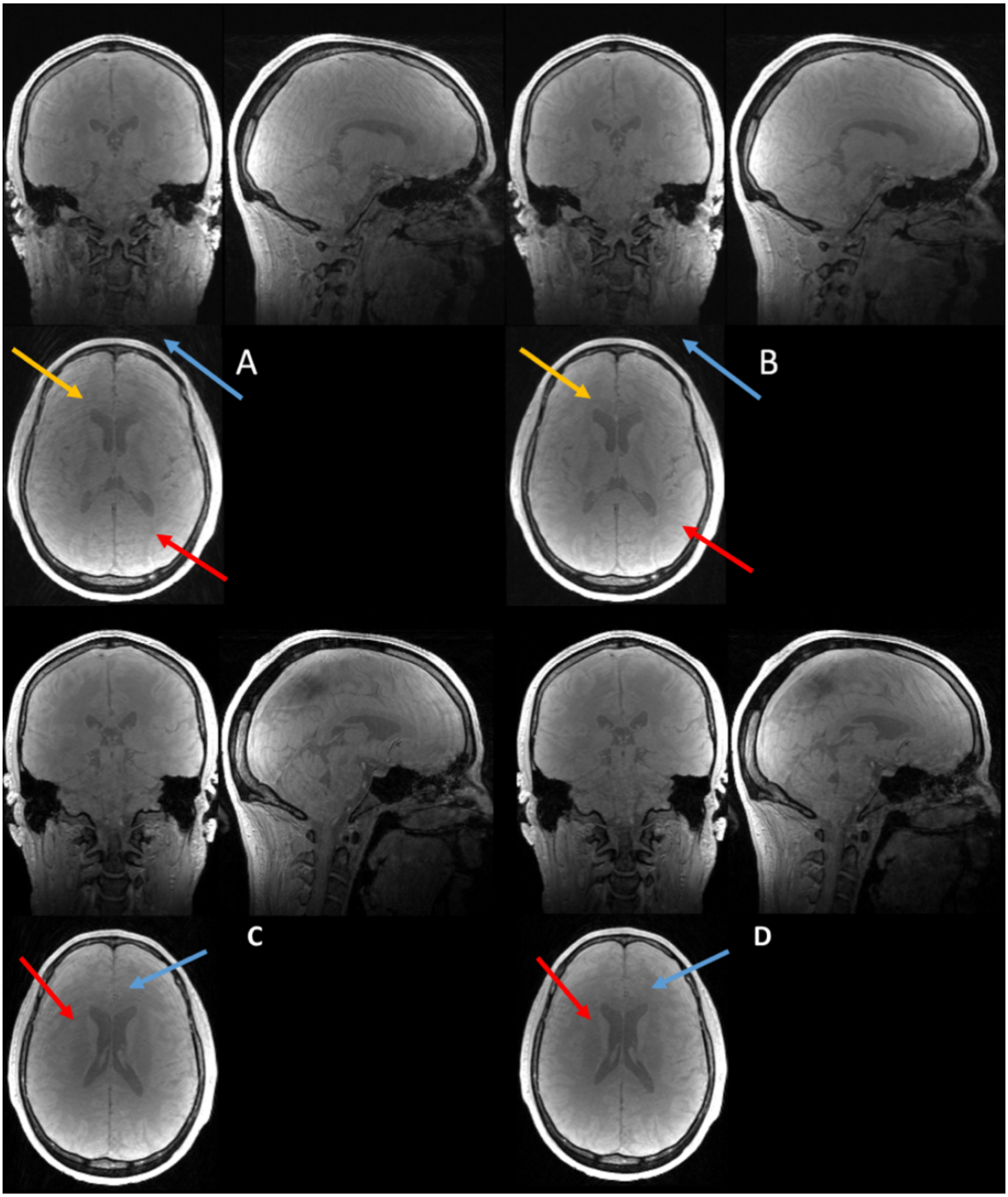

Figure V.16 Image quality of PDw scans acquired on volunteer 2 under motion conditions. A and B show the first scan with and without re-acquiring data, respectively, while C and D show the second scan with and without re-acquiring data, respectively. Areas of decreased image artefact in the case of re-acquisition are indicated by arrows. For A and B, the blue arrow indicates the decrease in image artefacts outside the head, while the yellow and red arrows indicate the decrease in ringing artefacts. For C and D, the red arrow indicate the decrease in ringing artefacts, and the blue arrow indicates a decrease in blur.

V.9.3: Discussion

I have successfully demonstrated that if all data identified by the navigator approach as motion corrupted could be re-acquired, image quality could be improved, both as quantified by NRMSE, and in terms of visual image quality.

Visual image quality was improved by reducing the amount of blurring and ringing present in the images. Image quality was quantified in terms of NRMSE, and re-acquisition decreased NRMSE, compared to a motion, no re-acquisition case, by one percentage point on average. In the absence of motion, the re-acquisition of data points falsely identified as being motion corrupted did not degrade visual image quality in a noticeable way, in line with the stated goals of the project.

For both volunteers, the increase in visual image quality appears to be greater than the increase in quality indicated by the changes in NRMSE. This is likely an observer effect, where only sufficiently large image artefacts are registered visually, while the NRMSE metric is sensitive to any and all changes in image quality.

As the image quality was not degraded by the application of the method in the absence of motion, while in the presence of motion, image quality was improved, I concluded that, based on the proof-of-principle studies detailed in this section, the navigator method presented in this Chapter is viable for the detection and correction of motion.

Due to the low sensitivity and specificity when compared to other navigator methods, such as FID navigators (212) or the fat-based FATNAV approach (205), the method did not detect and correct for all motion-corrupted data, resulting in visible and quantifiable motion artefacts even after re-acquisition. Further improvements in the method, for example a refining of the general linear model, and the classification based upon it, could result in better specificity and sensitivity, increasing the viability of the approach presented in this Chapter.

V.10: Conclusion

The goal of the work described in this Chapter was to evaluate whether a novel motion detection technique could be used to improve image quality in the presence of motion, while not affecting image quality, or scan time, in the absence of motion. If all the data points identified by said technique can be addressed (such as in the form of re-acquiring them), application of this novel technique can indeed result in better image quality. In the absence of motion, the proposed method did not induce appreciable changes in image quality, and parameters of the method were chosen such that scan times were not increased, in the absence of motion, by more than 5%.

In this Chapter, I have demonstrated that, due to the timing of the re-winding and spoiling gradients of the 3D FLASH sequence used in the MPM protocol, data acquired concurrently with gradient spoiling is sensitive to head motion. The changes introduced by motion were sufficiently large, such that an outlier rejection method could be developed, separating the TRs of a given scan into those affected by, or not affected by, motion. An outlier rejection threshold could be chosen such that in the absence of motion, the false positive rate, and thus the increase in scan time, was below 5%. For this outlier rejection threshold, sensitivity was approximately 0.5.

The sensitivity and specificity of this outlier rejection approach was improved by describing the relation of the head position and the navigator signal in a general linear model framework, and applying this model to new navigator data. Applying this approach to data acquired without parallel imaging, image quality was improved.

Compared to other navigator techniques, the required sequence modifications are small, as only a single readout needs to be inserted into the sequence. No additional scan time is sacrificed to acquire the navigator echo, only to re-acquire motion corrupted data, and the data points falsely identified as motion-corrupted. Other methods rely on dead time, during which no data encoding or acquisition takes place, or on the insertion of a navigator block, lengthening scan time. Such navigator blocks are used in the spherical navigator approach (210,218), and it's derivatives, volumetric (208) navigators, which have been proposed for motion correction of FLASH scans, at a scan time cost of a minute for a resolution and TR comparable to that of the scans used during this PhD project (209). Such separate navigator blocks may also disturb the steady-state signal, which is preserved in the proposed method.

While this issue is addressed by the introduction of navigators based on fat, rather than water signal (205,267), this technique also requires either dead time, or an increase of scan time (268). In addition, while the fat images used by the technique can be acquired at very high acceleration factors (267), a calibration period is necessary at the beginning of every scan session. For the navigator approach most comparable to the one proposed in this

chapter, FID navigators (212), both calibration, based on external tracking data (265), which has to be performed on a per-subject level, and additional scan time are necessary. The technique presented in this chapter could be easily adapter to imaging sequences with similar k-space traversal characteristics, at no extra scan time cost, and, while calibration is necessary, it does not have to be performed on a per-subject level, offering advantages over current methods. While this calibration requires the acquisition of independent motion information, which may not be possible in a clinical setting, once the calibration has been performed, the resulting model can be applied to all future scans, and no camera is necessary.

However, the proposed method cannot be used to correct for all instances of motion corrupted data. Both sensitivity and specificity are lower compared to published methods of motion detection (202,203,212,269), both for the originally proposed outlier rejection method without a motion mode, and the improved method, which incorporates a model of head motion.

This low inherent sensitivity can be explained by the timing of the navigator echo. In the navigator approach most similar to the one proposed, FID navigators, navigator data is collected immediately after excitation, at a high signal intensity. Accordingly, FID navigators have been shown to estimate motion in an accurate and precise fashion (212,265,266,270). Conversely, in the proposed method, navigator data is acquired at the end of each TR, and during gradient spoiling. The signal is inherently lower intensity compared to the start of the TR, due to T2* decay, and is furthermore heavily spoiled. Thus, the acquired navigator data may be more heavily influenced by coil characteristics (259–261), rather than the MRI signal, resulting in the poor performance seen in this chapter. This low sensitivity may be improved if the spoiling gradient shown in Figure V.1 is reversed. This change would result in navigator data being collected during the crossing of the k-space centre, at the cost of lower gradient spoiling, or the extension of the spoiling gradient to achieve the same spoiling.

The general linear model introduced in section V.7 is ill-conditioned, as indicated by the high condition number. Acquiring higher signal intensity navigators, as proposed above, may help reduce the condition number. The general linear model may be further improved by acquiring additional navigator and motion data on further volunteers, varying the age, gender and head size of the subjects, and the amplitude and frequency of motion. In clinical populations were to be imaged, the rejection threshold could be adjusted to better reflect the modes of motion characteristic of patients.

A limitation of the proposed technique, the inability to re-acquire reference lines, could be overcome by implementing and independent image reconstruction pipeline, such as those used in the Gadgetron framework (271), in order to evaluate the technique on accelerated imaging as well.

Chapter VI: Research-industrial collaboration

VI.1: Introduction

During this PhD project, I took part in two internships with Siemens Healthcare, visiting their development centre in Erlangen, Germany. During the first visit, in 2015, I developed a proof-of-concept post-processing tool for a clinical post-processing environment. During my second visit, in 2016, I implemented changes to a routine clinical sequence, in order to best match the FLASH sequence used in the MPM protocol.

VI.2: Implementation of the MPM post-processing steps in a proprietary clinical image processing environment

The post-processing steps of the MPM protocol approach are performed offline, not on the scanner, in a MATLAB environment, and data is handled in a Neuroimaging Informatics Technology Initiative (NifTI) file format (https://nifti.nimh.nih.gov/). Images are typically stored locally, and visualised on standard desktop monitors.

In a clinical environment, images are stored in DICOM (Digital Imaging and Communications in Medicine, http://dicom.nema.org/) file format, on a central server, and image processing is either done on the scanner, or through a central server. Images are visualised on high-definition monochrome monitors. To facilitate the clinical deployment of the MPM protocol, it was necessary to connect these two data handling methods.

Post-processing steps were implemented in a Siemens proprietary visualisation and analysis software environment, syngo.via (www.healthcare.siemens.co.uk/medical-imaging-it/clinical-imaging-applications/syngovia). The syngo.via environment is commercially available, can be deployed on supported scanner systems, such as the 3T TIM Trio system used in this thesis.

As part of syngo.via, a rapid prototyping environment, Frontier was available (www.healthcare.Siemens.co.uk/computed-tomography/clinical-imaging-solutions/syngo-via-frontier). Prototypes in Frontier could be developed rapidly, by combining and modifying pre-existing image processing and arithmetic modules, such as co-registration or linear regression. Using the Frontier environment, I implemented a proof-of-concept version of the MPM post processing pipeline in a syngo.via system.

The co-registration steps, the estimation of the RF transmit field, and the calculation of R2* and R1 were implemented in a prototype application. Additionally, the inter-scan motion correction technique, detailed in Chapter III, was also implemented. The syngo.via interface, and the calculated R2* map is shown in Figure VI.1, while Figure VI.2 illustrates the visualisation environment.

Figure VI.1: Proof of concept implementation of the R2* estimation in the Frontier environment.

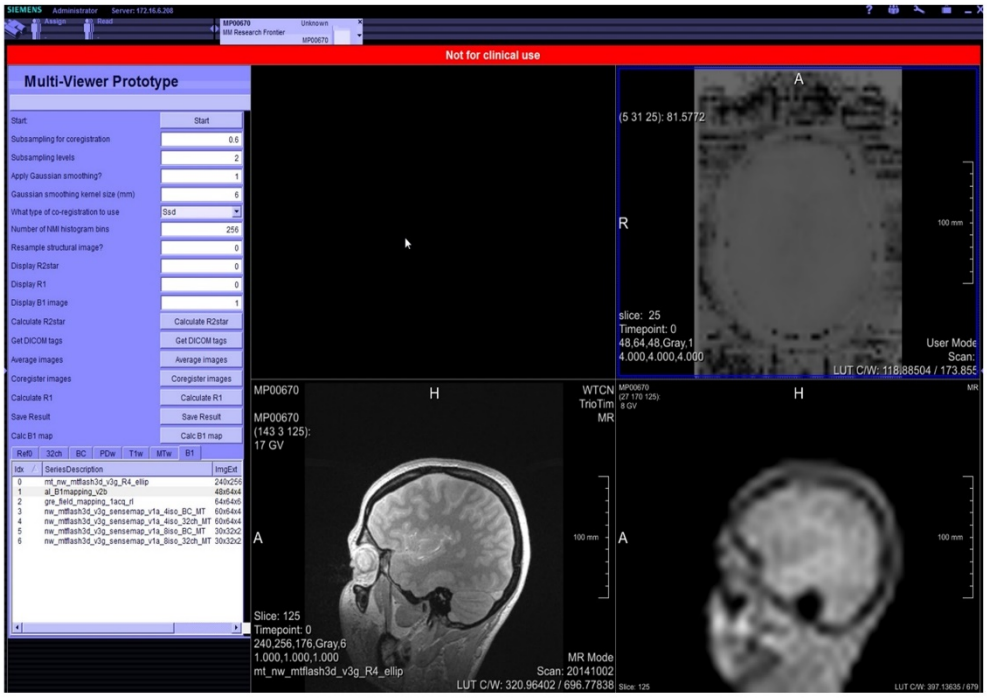

Figure VI.2: The user interface of the prototype implementation, showing an uncorrected B1 map (upper right), a PDw scan (bottom left), and a low-resolution scan used for sensitivity correction.

VI.3: Implementation of MPM sequence characteristics in a routine clinical sequence

To facilitate the acquisition of scans in an MPM protocol, a Siemens proprietary product sequence, a routine clinical gradient echo sequence was modified to match, as well as possible, the acquisition characteristics of the 3D FLASH scans used in this thesis. The excitation and spoiling characteristics were matched, as were the gradient timings. Due to software limitations, it was not possible to adjust the characteristics of the magnetisation transfer saturation pre-pulse. In effect, the T1w and PDw scans used in the MPM protocol can be acquired with this modified sequence, while the MTw scans cannot. A proof-of-principle acquisition, matching the acquisition parameters of the T1w scans of the MPM protocol, is shown in Figure VI.3

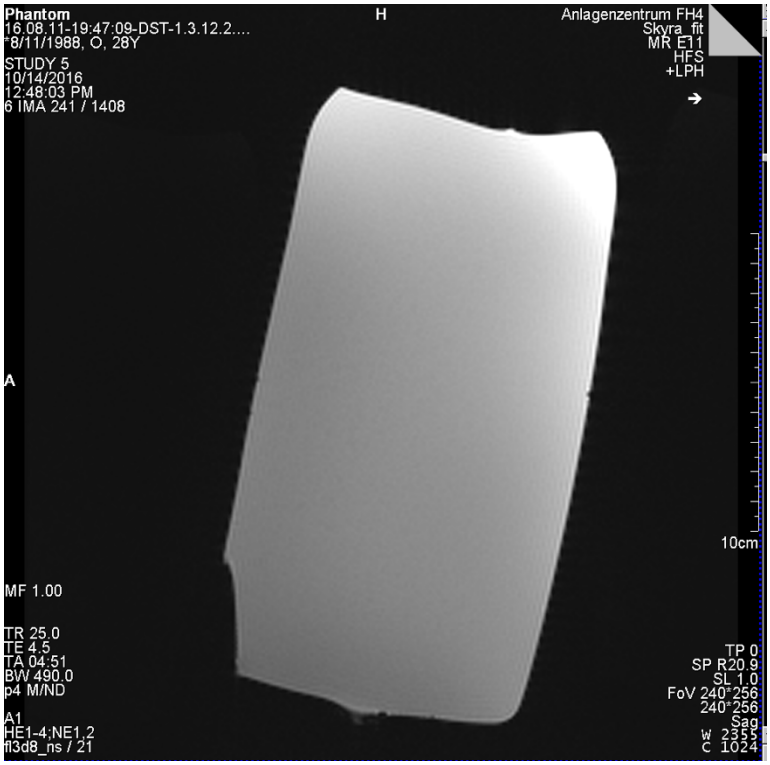

Figure VI.3: T1 weighted scan of a phantom, acquired using the modified Siemens gradient echo product sequence.

Sequence modifications were implemented in the syngo software version VE11C. This software version supported a Frontiers package, and was targeted for long-term support on existing and future MRI scanners. A partial implementation of the MPM protocol in this software version ensured that continued development can stay up to date, and that the protocol, if fully implemented, may be distributed to a wide range of clinical sites.

Chapter VII: Conclusions

VII.1: Summary of findings

The aims of the PhD project summarized in this thesis were: to reduce the acquisition time of the MPM protocol to a duration compatible with clinical scanning, to reduce the motion sensitivity of weighted images acquired in the protocol, and to address motion both between, and within scans.

Motion between scans was found to reduce the accuracy and precision of quantitative maps estimated in the MPM protocol, if data from more than one weighted scan was used in the estimation. This was the result of position-dependent signal intensity modulation by the receive field of the multi-channel head coil. A correction method was developed, in which the relative sensitivity of the receive field is mapped by two short, low-resolution calibration scans, and removed from the weighted scans. This correction method was validated in vivo, and was shown to reduce inter-scan motion related artefact levels to those comparable with scan-rescan variability.

Overall scan time for the protocol was shortened by reducing the acquisition time of weighted scans. By implementing an elliptical k-space coverage scheme, and increasing the parallel imaging acceleration factor, the acquisition time for one weighted scan was reduced to approximately 4 minutes from the original acquisition time of approximately 7 minutes. For the protocol, this reduced scan time from 26:30 to approximately 17 minutes if the RF transmit field map was acquired in addition to the three weighted scans, and to approximately 18 minutes if low-resolution sensitivity maps were acquired as well.

Sensitivity to motion during scanning was reduced by finding the most motion-robust acquisition trajectory, given the field of view alignment used during this PhD project, chosen from a set of trajectories readily available on the scanner.

Motion during scanning was addressed by developing a novel motion detection technique, based on the acquisition of navigator data concurrent with gradient spoiling, at no extra scan time cost. An outlier rejection method for motion correction was developed, and improved by applying a general linear model. Based on this classification, motion-corrupted data were reacquired. This approach did not significantly influence image quality in the absence of motion, and led to a slight improvement in image quality over uncorrected scans in the presence of motion.

VII.2: Avenues for further development

There are potential avenues for further improvements, in scan time reduction, motion correction, and clinical usability.

In the state of the art version of the MPM protocol, the RF field mapping sequences account for more than a quarter of the total scan time. A novel transmit field mapping technique has recently been developed, based on the Bloch-Siegert shift (272), with which the transmit field can be robustly mapped in less than a minute. The feasibility of implementing this technique into the MPM protocol is currently under investigation by Dr. Martina Callaghan.

The navigator based motion correction method may be improved by implementing an offline reconstruction algorithm which allows for the re-acquisition of reference lines, or by improving the classification. The classification could be improved by training the general linear model on additional datasets, if the position of the head is monitored independently.

The full MPM protocol currently consists of five sequential scans if the proposed inter-scan motion correction method is not applied, and eleven sequential scans with the proposed method. This hinders clinical deployment, and makes the protocol susceptible to user errors. Improvements could be achieved if the two low-resolution calibration scans were combined with the corresponding weighted scan. Ideally, all FLASH scans could be combined into one, eliminating the susceptibility to inter-scan motion.

VII.3: Recommendations for best practice

As shown in Chapter III, motion between scans can reduce the accuracy and precision of quantitative maps estimated in the MPM protocol. This may be generalized to all qMRI methods where quantitative information is derived from the combination of two or more scans.

I have shown that Prescan Normalize, the signal intensity flattening technique implemented on Siemens scanners, can partially mitigate this effect. Therefore, I recommend that for all protocols, where data from two or more scans are combined and evaluated in a quantitative fashion, Prescan Normalize is used. I have not investigated the signal intensity flattening techniques provided by other vendors.

To evaluate the utility of these signal intensity flattening techniques in correcting for inter-scan motion, I recommend a phantom study such as the one described in Chapter III.

I recommend that all scans are acquired with the least motion-sensitive acquisition trajectory available on the scanner. While the results of Chapter IV are not readily translatable into practice, for each alignment of the field of view, this trajectory may be found by conducting a short phantom study, such as the one described in section IV.2.

Bibliography

1. OECD: Medical technologies, Health at a Glance 2015: OECD Indicators, OECD Publishing, 2015

2. Europe In Figures: Eurostat Yearbook 2014, Office for Official Publications of the European Communities, 2014

3. NHS Imaging and Radiodiagnostic activity in England. 2013, National Office for Statistics, 2013

4. Gasperini C, Rovaris M, Sormani MP, Bastianello S, Pozzilli C, Comi G, Filippi M. Intra-observer, inter-observer and inter-scanner variations in brain MRI volume measurements in multiple sclerosis. Mult. Scler., 2001;7(1):27-31

5. Filippi M, Horsfield M , Rovaris M, Yousry T, Rocca M a., Baratti C, Bressi S, Comi G. Intraobserver and interobserver variability in schemes for estimating volume of brain lesions on MR images in multiple sclerosis. Am. J. Neuroradiol., 1998;19(2):239-244

6. Van Waesberghe, J. H. T. M., Kamphorst, W., De Groot, C. J. A., Van Walderveen, M. A. A., Castelijns, J. A., Ravid, R., Lycklama à Nijeholt, G. J., Van Der Valk, P., Polman, C. H., Thompson, A. J. and Barkhof, F., Axonal loss in multiple sclerosis lesions: Magnetic resonance imaging insights into substrates of disability. Ann Neurol.,1999 46: 747–754.

7. Tofts P: Quantitative MRI of the Brain: Measuring Changes Caused by Disease, John Wiley and Sons, 2003

8. Rosenkrantz AB, Mendiratta-Lala M, Bartholmai BJ, Ganeshan D, Ambramson RG, Burton KR, Yu JP, Scalzetti EM, Yankeelov TE, Subramaniam RM, Lenchick L; Clinical utility of quantitative imaging; Acad. Radioll 2015; 22(1):33-49

9. Rodionov R, Bartlett PA, He C, Vos SB, Focke NK, Ourselin SG, Duncan JS. : Clinical T2 mapping outperforms normalised FLAIR in identifying hippocampal sclerosis. Neuroimage, 2015;7:788–791.

10. Bartlett PA, Symms MR,Free SL, Duncan JS,. T2 Relaxometry of the Hippocampus at 3T. AJNR 2007(6):1095–1098. d

11. Engblom H, Xue H, Akil S, et al. Fully quantitative cardiovascular magnetic resonance myocardial perfusion ready for clinical use : a comparison between cardiovascular magnetic resonance imaging and positron emission tomography. J Cardiovasc Magn Reson, 2017:19: 78

12. Attili AK, Schuster A, Nagel E, Nagel ASÁE. Quantification in cardiac MRI : advances in image acquisition and processing. Int J Cardiovac Imaging 2010(1):27–40.

13. Eckstein F, Guermazi A, Gold G, Duryea J, Le MH, Wirth W, Miller CG. Imaging of cartilage and bone : promises and pitfalls in clinical trials of osteoarthritis. Osteoarthr. Cartil. 2014;22:1516–1532.

14. Eckstein F, Wirth W. Quantitative Cartilage Imaging in Knee Osteoarthritis. Arthritis 2011;

15. Matzat SJ, Tiel J Van, Gold GE, Oei EHG. Quantitative MRI techniques of cartilage composition. Quant Imaging Med Surg 2013;3:162–174

16. Andre JB, Bresnahan BW, Mossa-Basha M, Hoff MN, Smith CP, Anzai Y, Cohen W a. Towards Quantifying the Prevalence, Severity, and Cost Associated With Patient Motion During Clinical MR Examinations. J. Am. Coll. Radiol. 2015;12:689–695

17. Helms G, Dathe H, Dechent P. Quantitative FLASH MRI at 3T using a rational approximation of

the Ernst equation. Magn. Reson. Med, 2008;59(3):667-672
18. Helms G, Dathe H, Kallenberg K, Dechent P. High-resolution maps of magnetization transfer with inherent correction for RF inhomogeneity and T1 relaxation obtained from 3D FLASH MRI. Magn. Reson. Med., 2008; 60(6):1349-407
19. Weiskopf N, Suckling J, Williams G, Correia MM, Inkster B, Tait R, Ooi C, Bullmore ET, Lutti A. Quantitative multi-parameter mapping of R1, PD(*), MT, and R2(*) at 3T: a multi-center validation. Front. Neurosci., 2013;7:95
20. Whitaker KJ, Vértes PE, Romero-Garcia R, et al. Adolescence is associated with genomically patterned consolidation of the hubs of the human brain connectome. Proc. Natl. Acad. Sci. 2016;113(32):9105-9110
21. Callaghan MF, Freund P, Draganski B, et al. Widespread age-related differences in the human brain microstructure revealed by quantitative magnetic resonance imaging. Neurobiol. Aging,2014; 35(8):1862-72
22. Draganski B, Ashburner J, Hutton C, Kherif F, Frackowiak RSJ, Helms G, Weiskopf N. Regional specificity of MRI contrast parameter changes in normal ageing revealed by voxel-based quantification (VBQ). Neuroimage, 2011; 55(4):1423-34
23. Kullmann S, Callaghan MF, Heni M, Weiskopf N, Scheffler K, Häring HU, Fritsche A, Veit R, Preissl H. Specific white matter tissue microstructure changes associated with obesity. Neuroimage, 2016; 125:36-44
24. Sereno MI, Lutti A, Weiskopf N, Dick F. Mapping the human cortical surface by combining quantitative T1 with retinotopy. Cereb. Cortex, 2013; 23(9):2261-8
25. Lutti A, Dick F, Sereno MI, Weiskopf N. Using high-resolution quantitative mapping of R1 as an index of cortical myelination. Neuroimage 2013; 93:176-88
26. Dick F, Tierney AT, Lutti A, Josephs O, MSereno MI, Weiskopf N. In vivo functional and myeloarchtectonic mapping of human primary auditory areas, J Neurosci., 2012; 32(46):16095-16105
27. Mohammadi S, Carey D, Dick F, Diedrichsen J, Sereno MI, Reisert M, Callaghan MF, Weiskopf N. Whole-brain in-vivo measurements of the axonal G-ratio in a group of 37 healthy volunteers. Front. Neurosci. 2015; 9:441
28. Bloch F. Nucelar Induction, Phys. Rev. 1946; 70:460
29. Rabi II, Zacharian JR, Millman S, Kusch P A new method of measuing nuclear magnetic moment, Phys. Rev 1938: 53:318
30. Gerlach VW. Der experimentelle Nachweis des magnetischen Moments des Silberatoms .Zeitschrift fuer Physik, 1921; 8(1):110-111
31. Purcell EM, Torrey HC, Pound RV. Resonance Absorption by Nuclear Magnetic Moments in a Solid, Phys. Rev, 1946:69:37
32. Ehrenfest, P. Bemerkung über die angenäherte Gültigkeit der klassischen Mechanik innerhalb der Quantenmechanik. Zeitschrift fuer Physik.1927 **45** (7–8): 455–457
33. Bloembergen, E.M. Purcell, R.V. Pound Relaxation Effects in Nuclear Magnetic Resonance Absorption Phyl Rev 1948 73. 7:679-746 24.
34. Brown RW, Ph D, Cheng YN, Ph D, Haacke EM, Ph D. Magnetic Resonance Imaging : Second

Edition, Wiey-Blackwell, 2013
35. Katscher U, Bo P. Parallel RF transmission in MRI. NMR Biomed, 2006; 19(3):393-400
36. Bottomley PA. Spatial Localization in NMR Spectroscopy in Vivo. Ann NY Ac.Sci, 1987;508:333-48
37. Francisco S. An Algorithm for NMR I Based on Multiple RF Receiver Coils. J. Magn. Reson. 1987; 74(2):376-380
38. Hutchinson M, Raff U. Fast MRI Data Acquisition Using Multiple Detectors.Magn. Reson. Med. 1988; 6(1):87-91
39. Haase a., Frahm J, Matthaei D, Hänicke W, Merboldt K-D. FLASH imaging: Rapid NMR imaging using low flip-angle pulses. J. Magn. Reson. 1986; 67(2):258-266
40. Frahm J, Haase A. Rapid NMR Imaging of Dynamic Processes Using the FLASH Technique. Magn. Reson. Med 1986; 3(1):321-327
41. Wright PJ, Mougin OE, Totman JJ, Peters AM, Brookes MJ, Coxon R, Moris PE, Clamence M, Francis ST, Bowtell RW, Gowland PA. Water proton T 1 measurements in brain tissue at 7, 3,and 1.5T using IR-EPI , IR-TSE , and MPRAGE : results and optimization. Mag. Reson. Mater Phy 2008:21:121
42. Ernst RR, Anderson WA. Application of fourier transform spectroscopy to magnetic resonance. Rev. Sci. Instrum. 1966;37:93–102. doi: 10.1063/1.1719961
43. Crawley a P, Wood ML, Henkelman RM. Elimination of transverse coherences in FLASH MRI. Magn. Reson. Med. 1988;8:248–260
44. Zur, Y., Wood, M. L. and Neuringer, L. J. Spoiling of transverse magnetization in steady-state sequences. Magn. Reson. Med 1991., 21: 251–263
45. Preibisch C, Deichmann R. T1 mapping using spoiled FLASH-EPI hybrid sequences and varying flip angles. Magn. Reson. Med. 2009;62:240–246
46. Yarnykh VL. Optimal Radiofrequency and Gradient Spoiling for Improved Accuracy of T1 and B1 Measurements Using Fast Steady-State Techniques. Mag Reson Med 2010;1626:1610–1626
47. Georgiades CS, Itoh R, Golay X, Zijl PCM Van, Melhem ER. MR Imaging of the Human Brain at 1 . 5 T : Regional Variations in Transverse Relaxation Rates in the Cerebral Cortex. Am, J Neuroradiol 2001; 22(9):1732-7
48. Stanisz GJ, Odrobina EE, Pun J, Escaravage M, Graham SJ, Bronskill MJ, Henkelman RM. T1, T2 relaxation and magnetization transfer in tissue at 3T. Magn. Reson. Med. 2005;54(3):507-12
49. Peters AM, Brookes MJ, Hoogenraad FG, Gowland PA, Francis ST, Morris PG, Bowtell R. T2* measurements in human brain at 1 . 5 , 3 and 7 T. Mag. Reson. Imaging 2007;25(6):748-53
50. Finsterbusch J, Matschke J, Lorenzen A, Ding X. Age-Dependent Normal Values of T2* and T2 ¯in Brain Parenchyma. Am J Neuroradiol, 2008;29(5):950-5
51. Kumar R, Delshad S, Woo MA, Macey PM, Harper RM. Age-Related Regional Brain T2-Relaxation Changes in Healthy Adults. J. Mag Reson Imaging 2012;35(2):300-8
52. Wang J, Shaffer ML, Eslinger PJ, Sun X, Weitekamp CW, Patel MM, Dossick D, Gill DJ, Connor JR, Yang QX. Maturational and Aging Effects on Human Brain Apparent Transverse Relaxation. Plos One, 2012;7(2)
53. Steen RG, Gronemeyer SA, Taylor JS. Age-related Changes in Proton T1 Values of Normal Human Brain J Magn. Reson Imaging, 1995; 5(1):43-8

54 Mabray MC, Barajas RF Jr, Cha S. Modern Brain Tumor Imaging. Brain Tumor Res Treat, 2015; 3(1):8-23
55. Cha S. Update on Brain Tumor Imaging, Am J Neuroradiol,: 2006; 27(3):475-87
56. Deshmane A, Gulani V, Griswold MA, Seiberlich N. Parallel MR Imaging.J Magn Reson Imaging 2012; 36(1):55-72
57. Larkman DJ, Nunes RG. Parallel magnetic resonance imaging. Phys. Med. Biol. 2007; 52(7):15-55
58. Blaimer M, Breuer F, Mueller M, Heidemann RM, Griswold MA, Jakob PM. Smash, sense, pils, grappa.Top Magn Reson Imaging, 2004;15(4):223-36
59. Pruessmann KP, Weiger M, Scheidegger MB, Boesiger P. SENSE: sensitivity encoding for fast MRI. Magn. Reson. Med. 1999; 42(5):952-62
60. Griswold M a, Jakob PM, Heidemann RM, Nittka M, Jellus V, Wang J, Kiefer B, Haase A. Generalized autocalibrating partially parallel acquisitions (GRAPPA). Magn. Reson. Med. 2002; 47(6):1202-10
61. Robson PM, Grant AK, Madhuranthakam AJ, Lattanzi R, Sodickson DK, Mckenzie CA. Comprehensive quantification of signal-to-noise ratio and g-factor for image-based and k-space-based parallel imaging reconstructions, Magn Reson Med, 2008; 60(4):895-907
62. Breuer FA, Kannengiesser SAR, Blaimer M, Seiberlich N, Jakob PM, Griswold MA. General formulation for quantitative G-factor calculation in GRAPPA reconstructions. Magn. Reson. Med. 2009;62:739–746
63. Jara H. Theory of quantitative magnetic resonance imaging.World Scientific 20136464. Ramani A, Jensen JH, Helpern JA. Quantitative MR Imaging in Alzheimer disease Radiology. 2006;241(1):26-44
65. Crawley AP, Henkelman RM. A comparison of one-shot and recovery methods in T1 imaging. Magn. Reson. Med. 1988;7:23–34
66. Kay I, Henkelman RM. Practical Implementation and Optimization of One-shot T1 imaging. Magn. Reson. Med. 1991;22:414–424.
67. Pykett IL, Rosen BR, Buonanno FS, Brady TJ. Measurement of spin-lattice relaxation times in nuclear magnetic resonance imaging. Phys. Med. Biol. 1983;28:723–729
68.Look DC. Locker DR. Time saving in measurement of NMR and EPR relaxation times. Rev Sci Instrum 1970; 41:250-1.
69. Henderson E, McKinnon G, Lee TY, Rutt BK, A fast 3D look-locker method for volumetric T1 mapping, Magn Reson Imaging, 199(8):1163-71
70. Marques JP, Kober T, Krueger G, van der Zwaag W, Van de Moortele PF, Gruetter R, MP2RAGE, a self bias-field corrected sequence for improved sgementation and T1-mapping at high field, Neuroimage 2010(2):1271-81
71. Deichmann R, Hahn D, Haase A. Fast T 1 Mapping on a Whole-Body Scanner, Magn Reson Med,. 1999;(42):206–209.
72. Fram EK, Herfkens RJ, Johnson GA, Glover GH, Karis JP, Shimakawa A, Perkins TG, Pelc NJ Rapid calculation of T1 using variable flip angle gradient refocused imaging, Magn Reson Imaging 1987: 5(3):201-8
73. Paus T, Collins DL, Evans AC, Leonard G, Pike B, Zijdenbos A. Maturation of white matter in the

human brain: A review of magnetic resonance studies. Brain Res. Bull. 2001;54:255–266
74. Deoni SCL, Zinkstok JR, Daly E, Ecker C, Williams SCR, Murphy DGM. White-matter relaxation time and myelin water fraction differences in young adults with autism. Psychol. Med. 2014;:1–11
75. Vrenken H, Rombouts SARB, Pouwels PJW, Barkhof F, Voxel-based analysis of quantitative T1 maps demonstrates that multiple sclerosis acts throughout normal-appearing white matter, AJNR, 2006 (27): 867-874
76. Manfredonia F, Ciccarelli O, Khaleeli Z, Tozer DJ, Sastre-garriga J, Miller DH, Thompson AJ. Normal-Appearing Brain T1 Relaxation Time Predicts Disability in Early Primary Progressive Multiple Sclerosis.Arch Neurol, 2007;64:411–415.
77. Bernhardt BC, Fadaie F, Vos R, Wael D, Hong S, Liu M, Guiot C, Rudko DA, Bernasconi A, Bernasconi N. Preferential susceptibility of limbic cortices to microstructural damage in temporal lobe epilepsy : A quantitative T1 mapping study. Neuroimage2017:1–9.
78. Viceic D, Ghika J, Gunten A Von, Clarke S, Meuli R, Frackowiak RS, Knyazeva MG. Demyelination in Mild Cognitive Impairment Suggests Progression Path to Alzheimer ' s Disease. 2013;(8)8.
79. Kubicki M, McCarley RW, Shenton ME, Evidence for white matter abnormalities in schizophrenia, Curr Opin Psychiatry, 2005;18(2):121-134
80. Jellis CL, Kwon DH. Myocardial T1 mapping : modalities and clinical applications. Cardiovasc Diagn Ther, 2014;4:126–137
81. Burt JR, Zimmerman SL, Kamel IR, Halushka M, Bluemke DA. Myocardial T1 Mapping : Techniques. Radiographics, 2014 34(2) 377-385.
82. Broberg CS, Chugh SS, Conklin C, David J, Jerosch-herold M. Quantification of diffuse myocardial fibrosis and its association with myocardial dysfunction in congenital heart disease, Circ Cardiovasc Imaging, 2010 3(6): 727-734
83. Ferreira VM, Piechnik SK, Armellina ED, Karamitsos TD, Francis JM, Choudhury RP, Friedrich MG, Robson MD, Neubauer S. Non-contrast T1-mapping detects acute myocardial edema with high diagnostic accuracy : a comparison to T2-weighted cardiovascular magnetic resonance. J Cardiovasc Magn Reson 2012;14:1
84. Gowland PA, Freeman A, Issa B, Boulby P, Duncan KR, Moore RJ, Baker PN, Bowtell RW, Johnson IR, Worthington BS. In vivo relaxation time measurements in the human placenta using echo planar imaging at 0.5 T. Magn. Reson. Imaging 1998;16:241–247
85. Whittall KP, Mackay AL, Graeb DA, Nugent RA, Li DKB, Paty DW. In vivo measurement ofT2 distributions and water contents in normal human brain. Magn. Reson. Med. 1997;37:34–43
86. Woermann FG, Barker GJ, Birnie KD, Meencke HJ, Duncan JS. Regional changes in hippocampal T2 relaxation and volume: A quantitative magnetic resonance imaging study of hippocampal sclerosis. J. Neurol. Neurosurg. Psychiatry 1998;65:656–664.
87. Brooks DJ, Luthert P, Gadian D, Marsden CD. Does signal-attenuation on high-field T2-weighted MRI of the brain reflect regional cerebral iron deposition Observations on the relationship between regional cerebral water proton T2 values and iron levels. J. Neurol. Neurosurg. Psychiatry 1989;52:108–111

88. Ordidge RJ, Gorell JM, Deniau JC, Knight RA, Helpern JA. Assessment of relative brain iron concentrations using T2-weighted and T2*-weighted MRI at 3 Tesla. Magn. Reson. Med. 1994;32:335–341..
89. Lee J, Shin H, Jung W, Nam Y, Oh S, Lee J. An R 2* model of white matter for fi ber orientation and myelin concentration. Neuroimage 2017;162:269–275.
90. Zhang Y, Gauthier SA, Guota Am Chen W, Comunale J, Chiang GC, Zhou D, Askin G, Zhu W, Pitt D, Wang Y Quantitative Susceptibility Mapping and R2 * Measured Changes during White Matter Lesion Development in Multiple Sclerosis: Myelin Breakdown, Myelin Debris Degradation and Removal , and Iron Accumulation. AJNR, 2016:37(9) 1629–1635.
91. Graham JM, Paley MNJ, Gru RA, Hoggard N, Griffiths PD, Gru CRA. Brain iron deposition in Parkinson ' s disease imaged using the PRIME magnetic resonance sequence. Brain, 2000:2423–2431.
92. Khalil M, Enzinger C, Langkammer C, Tscherner M, Jehna M, Ropele S, Fuchs S, Fazekas F. Quantitative assessment of brain iron by R 2 * relaxometry in patients with clinically isolated syndrome and relapsing – remitting multiple sclerosis.Mult Scler, 2009: 15(9) 1048–1054.
93. Rudko DA, Klassen LM, Chickera SN De, Gati JS, Dekaban GA. Origins of R2* orientation dependence in gray and white matter.PNAS, 2013. E159-E167
94. Neeb H, Zilles K, Shah NJ. A new method for fast quantitative mapping of absolute water content in vivo. Neuroimage 2006;31:1156–1168.
95. Winston GP, Vos SB, Burdett JL, Cardoso MJ, Ourselin S, Duncan JS: Automated T2 relaxometry of the hippocampus in temporal lobe epilepsy, Epilepsia, 2017 58(8) 1645-52
96. Kiefer C, Brockhaus L, Cattapan-Ludewig K, Ballinari P, Burren Y, Schroth G, Wiest R. Multi-parametric classification of Alzheimer's disease and mild cognitive impairment: The impact of quantitative magnetization transfer MR imaging. Neuroimage [2009;48:657–667.
97. Helpern JA, Jensen J, Lee S, Falangola MF. Quantitative MRI Assessment of Alzheimers Disease. J Mol Neurosci, 2004;24:45–48.
98. Townsend TN, Bernasconi N, Pike GB, Bernasconi A. Quantitative analysis of temporal lobe white matter T2 relaxation time in temporal lobe epilepsy.Neuroimage, 2004;23:318–324.
99. Memarian N, Thompson PM, Engel Jm Staba RJ: Quantitative analysis of structural neuroimaging of mesial temporal lobe epilespy, Imaging Med 2013 5(3)
100. Bauer S, Wagner M, Seiler A, Hattingen E, Deichmann R, Nöth U, Singer OC. Quantitative T2 ′ -Mapping in Acute Ischemic Stroke, Stroke. 2014:3280–3286.
101. Hoppe S, Quirbach S, Mamisch TC, Krause FG, Werlen S, Benneker LM. Axial T2 * mapping in intervertebral discs : a new technique for assessment of intervertebral disc degeneration. Eur Radiol, 2012 22(9):2013-9
102. Watanabe A, Benneker LM, Boesch C, et al. Classification of Intervertebral Disk Degeneration with Axial T2 Mapping. AJR, 2007:11–13.
103. Smith SA, Edden RAE, Farrell JAD, Barker PB, Zijl PCM Van.Measurement of T1 and T2 in the cervical spinal cord at 3 Tesla, Magn. Reson Med 2008 60(1):213-19
104. Baum T, Joseph GB, Karampinos DC, Jungmann PM, Link TM, Bauer JS, Cartilage and

meniscal T2 relaxation time as non-invasive biomarker for knww osteoarthritis and cartilage repair procedures, Oestoarthritis Cartilage, 2013 21(10):1474-1484
105. Trattnig S, Quirbach S, Marlovits S, White LM, Welsch GH. Quantitative T2 Mapping of Knee Cartilage : Differentiation of Healthy Control Cartilage and Cartilage Repair Tissue in the Knee with Unloading, Radiology : 2010;254(3):818-826.
106. Echeverría MJ, Castiella A, Emparanza JI. Quantification of iron concentration in the liver by MRI. Insights Imaging 2012:173–180.
107. Hernando D, Levin YS, Sirlin CD, Reeder SB, Quantification of liver iron with MRI: State of the art and remaining challenges, J Magn Reson Imaging, 2014, 40(5):1003-1021
108. Alam MH, Auger D, Mcgill L, et al. Comparison of 3 T and 1 . 5 T for T2 * magnetic resonance of tissue iron. J. Cardiovasc. Magn. Reson. 2016:1–9.
109. Schein A, Enriquez C, Coates TD, Wood JC, Magnetic resonance detection of kidney iron deposition in sickle cell disease: a marker of chronic hemolysis, J Magn Reson Imaging, 2008 28(3): 698-704
110. Pennell DJ. T2 * Magnetic Resonance and Myocardial Iron in Thalassemia. Ann NY Acad Sci, 2005;378:373–378
111. Radunski UK, Lund GK, Stehning C, Schnackenburg B, Bohnen Sm Adam G, Blankenberg S, Muellerleile K: CMR in Patients With Severe Myocarditis: Diagnostic value of Quantitative Tissue Markers Including Extracellular Volume Imaging, JACC Cardiovasc Imaging. 2014;7:667-75.
112. Luetkens JA, Doerner J, Schild H, Naehle CP. Diagnostic Value of Quantitative CMR in Patients Suspected of Having Myocarditis: A;Question of Timing. JACC Cardiovasc. Imaging 2015;8:109–110.
113. Messroghli DR, Moon JC, Ferreira VM, et al. Clinical recommendations for cardiovascular magnetic resonance mapping of T1 , T2 , T2 * and extracellular volume : A consensus statement by the Society for Cardiovascular Magnetic Resonance (SCMR) endorsed by the European Association for Cardiovascular Imaging (EACVI). J Cardiovasc Magn Reson, 2017:19(9)1–24.
114. Lerski R a, Straughan K, Orr JS. Calibration of proton density measurements in nuclear magnetic resonance imaging. Phys. Med. Biol. 1984;29:271–276.
115. Brix G, Schad LR, Lorenz WJ. Evaluation of proton density by magnetic resonance imaging: phantom experiments and analysis of multiple component proton transverse relaxation. Phys. Med. Biol. 1990;35:53–66.
116.. Farace P, Pontalti R, Cristoforetti L, Antolini R, Scarpa M: An automated method for maping human tissue permttivities by MRI in hyperthermia treatment planning, Phys Med Biol, 1997:42
117. Mezer A, Rokem A, Berman S, Hastie T, Wandell BA. Evaluating quantitative proton-density-mapping methods. Hum. Brain Mapp. 2016;37:3623–3635
118. Neeb H, Ermer V, Stocker T, Shah NJ. Fast quantitative mapping of absolute water content with full brain coverage. Neuroimage 2008;42:1094–1109
119. Warntjes JBM, Dahlqvist O, Lundberg P. Novel method for rapid, simultaneous T1, T2*, and proton density quantification. Magn. Reson. Med. 2007;57:528–537
120. Volz S, Nöth U, Deichmann R. Correction of systematic errors in quantitative proton density mapping. Magn. Reson. Med. 2012;68:74–85

121. Weiskopf N, Lutti A, Helms G, Novak M, Ashburner J, Hutton C. Unified segmentation based correction of R1 brain maps for RF transmit field inhomogeneities (UNICORT). Neuroimage2011;54:2116–2124
122. Mezer A, Yeatman JD, Stikov N, et al. Quantifying the local tissue volume and composition in individual brains with magnetic resonance imaging. Nat. Med. 2013;19:1667–72
123. Laule C, Vavasour IM, Moore GRW, Oger J, Li DKB, Paty DW, Mackay AL. Water content and myelin water fraction in multiple sclerosis.J Neurol 2004:284–293. 124. Gracien RM, Reitz SC, Wagner M, et al. Comparison of two quantitative proton density mapping methods in multiple sclerosis. Magn. Reson. Mater. Physics, Biol. Med. 2017;30:75–83.
125. Jurcoane A, Wagner M, Schmidt C, Mayer C, Gracien R, Hirschmann M, Deichmann R, Volz S, Ziemann U, Hattingen E. Within-Lesion Differences in Quantitative MRI Parameters Predict Contrast Enhancement in Multiple Sclerosis. J Magn Reson Imaging, 2013;1461:1454–1461.
126. Yarnykh VL, Krutenkova EP, Aitmagambetova G, Repovic P, Mayadev A, Qian P, Henson LKJ, Gangadharan B, Bowen JD. Iron-Insensitive Quantitative Assessment of Subcortical Gray Matter Demyelination in Multiple Sclerosis Using the Macromolecular Proton Fraction. AJNR 2018 39(4):618-625.
127. Ayata C, Ropper AH. Ischaemic brain oedema. J Clin Neurosci 2002;9:113–124.
128. Shah NJ, Neeb H, Kircheis G, Engels P, Häussinger D, Zilles K. Quantitative cerebral water content mapping in hepatic encephalopathy.Neuroimage 2008;41:706–717.
129. Hori M, Hagiwara A, Fukunaga I, Ueda R, Kamiya K. Application of Quantitative Microstructural MR Imaging with Atlas-based Analysis for the Spinal Cord in Cervical Spondylotic Myelopathy. Sci. Rep. 2018:1–8.
130. Hoffman RA, Forsen S. Transient and Steady-State Overhauser Experiments in Investigation of Relaxation Processes . Analogies between Chemical Exchange and Relaxation. J. Chem. Phys. 1966;45:2049
131. Forsén S, Hoffman R. Study of Moderatly Rapid Chamical Exchange Reactions by Means of 71.
132. Wolff SD, Balaban RS. Magnetization transfer imaging: practical aspects and clinical applications. Radiology 1994;192:593–599
133. Wolff SD, Balaban RS. Magnetization transfer contrast (MTC) and tissue water proton relaxation in vivo. Magn. Reson. Med. 1989;10:135–144
134. Tozer D, Ramani A, Barker GJ, Davies GR, Miller DH, Tofts PS. Quantitative magnetization transfer mapping of bound protons in multiple sclerosis. Magn. Reson. Med. 2003;50:83–91
135. Yarnykh VL. Pulsed Z-spectroscopic imaging of cross-relaxation parameters in tissues for human MRI: Theory and clinical applications. Magn. Reson. Med. 2002;47:929–939
136. Sled JG, Pike GB, Bruce Pike G. Quantitative imaging of magnetization transfer exchange and relaxation properties in vivo using MRI. Magn. Reson. Med. 2001;46:923–931
137. Yarnykh VL, Yuan C. Cross-relaxation imaging reveals detailed anatomy of white matter fiber tracts in the human brain. Neuroimage 2004;23:409–424
138. Graham SJ, Henkelman RM. Understanding pulsed magnetization transfer. J. Magn. Reson. Imaging 1997;7:903–9121

139. Helms G, Dathe H, Hagberg GE. Pulsed saturation of the standard two-pool model for magnetization transfer. Part I: The steady state. Concepts Magn. Reson. 2004;21A:37–49
140. Schmierer K, Scaravilli F, Altmann DR, Barker GJ, Miller DH. Magnetization transfer ratio and myelin in postmortem multiple sclerosis brain. Ann. Neurol. 2004;56:407–415
141. Vavasour IM, Laule C, Li DKB, Traboulsee AL, MacKay AL. Is the magnetization transfer ratio a marker for myelin in multiple sclerosis? J. Magn. Reson. Imaging 2011;33:713–718
142. Levesque IR, Giacomini PS, Narayanan S, Ribeiro LT, Sled JG, Arnold DL, Pike GB. Quantitative Magnetization Transfer and Myelin Water Imaging of the Evolution of Acute Multiple Sclerosis Lesions.Magn Reson Med 2010;640:633–640.
143. Giacomini PS, Levesque IR, Ribeiro L, Narayanan S, Francis SJ, Pike GB, Arnold DL. Measuring demyelination and remyelination in acute multiple sclerosis lesion voxels. Arch Neurol 2009;66:375–81.
144. Mehrabian H, Myrehaug S, Soliman H, Sahgal A. Quantitative Magnetization Transfer in Monitoring Glioblastoma (GBM) Response to Therapy. Sci. Rep. 2018:1–11. doi: 10.1038/s41598-018-20624-6.
145. Tozer DJ, Rees JH, Benton CE, Waldman AD, Ja HR. Quantitative magnetisation transfer imaging in glioma : preliminary results. NMR in Biomed 2011:492–498.
146. Suleiman LI, Weber KA, Rosenthal BD, Bhatt SA, Savage JW, Hsu WK, Patel AA, Parrish TB. High-resolution magnetization transfer MRI in patients with cervical spondylotic myelopathy. J. Clin. Neurosci. 2018;51:57–61.
147. Stroman PW, Wheeler-kingshott C, Bacon M, et al. NeuroImage The current state-of-the-art of spinal cord imaging Neuroimage2014;84:1070–1081.
148. Deoni SCL, Peters TM, Rutt BK. Quantitative Diffusion Imaging With Steady-State Free Precession. Magn. Reson. Med. 2004;51:428–433
149. Deistung A, Schweser F, Reichenbach JR. Overview of quantitative susceptibility mapping. NMR Biomed. 2017;30
150. Wang J, Alsop DC, Li L, Listerud J, Gonzalez-At JB, Schnall MD, Detre JA. Comparison of quantitative perfusion imaging using arterial spin labeling at 1.5 and 4.0 Tesla. Magn. Reson. Med. 2002;48:242–254
151. Gasparovic C, Neeb H, Feis DL, Damaraju E, Chen H, Doty MJ, South DM, Mullins PG, Bockholt HJ, Shah NJ. Quantitative spectroscopic imaging with in situ measurements of tissue water T1, T2, and density. Magn. Reson. Med. 2009;62:583–590
152. Deoni SCL, Peters TM, Rutt BK. High-resolution T1 and T2 mapping of the brain in a clinically acceptable time with DESPOT1 and DESPOT2. Magn. Reson. Med. 2005;53:237–241
153. Deoni SCL, Rutt BK, Arun T, Pierpaoli C, Jones DK. Gleaning multicomponent T1 and T2 information from steady-state imaging data. Magn. Reson. Med. 2008;60:1372–1387. doi:
154. Liu F, Block WF, Kijowski R, Samsonov A, Rapid multi-component relaxometry in steady state with correction of magnetisation transfer effects Magn Reson Med 2016 75(4):1423-33
155. Deoni SCL. Correction of main and transmit magnetic field (B0 and B1) inhomogeneity effects in multicomponent-driven equilibrium single-pulse observation of T1 and T2. Magn. Reson. Med.

2011;65:1021–1035.
156. Cantor-Rivera D, Khan AR, Goubran M, Mirsattari SM, Peters TM. Detection of temporal lobe epilepsy using support vector machines in multi-parametric quantitative MR imaging. Comput. Med. Imaging Graph. 2015;41:14–28.
157. Khan AR, Goubran M, Ribaupierre S De, Hammond RR, Burneo JG, Parrent AG, Peters TM. Quantitative relaxometry and diffusion MRI for lateralization in MTS and non-MTS temporal lobe epilepsy. Epilepsy Res. 2014;108:506–516.
158. Deoni SCL, Mercure E, Blasi A, Gasston D, Thomson A, Johnson M, Williams SCR, Murphy DGM. Mapping Infant Brain Myelination with Magnetic Resonance Imaging. J Neurosci 2011;31:784–791.
159. Warntjes JBM, Dahlqvist Leinhard O, West J, Lundberg P. Rapid magnetic resonance quantification on the brain: Optimization for clinical usage. Magn. Reson. Med. 2008;60:320–329.
160. West J, Warntjes JBM, Lundberg P. Novel whole brain segmentation and volume estimation using quantitative MRI. Eur Radiol 2012;I:998–1007
161. Warntjes JB, Tisell A, Lundberg P. Brain Characterization Using Normalized Quantitative Magnetic Resonance Imaging. Plos One, 2013 8(8)
162. Heule R, Ganter C, Bieri O. Triple echo steady-state (TESS) relaxometry. Magn. Reson. Med. 2014;71:230–237.
163. Stöcker T, Keil F, Vahedipour K, Brenner D, Pracht E, Shah NJ. MR parameter quantification with magnetization-prepared double echo steady-state (MP-DESS). Magn. Reson. Med. 2014;72:103–111.
164. Heule R, Bär P, Mirkes C, Scheffler K, Trattnig S, Bieri O. Triple-echo steady-state T2 relaxometry of the human brain at high to ultra-high fields. NMR Biomed. 2014;27:1037–1045.
165. Juras V, Bohndorf K, Heule R, Kronnerwetter C, Szomolanyi P, Hager B, Bieri O, Zbyn S, Trattnig S. A comparison of multi-echo spin-echo and triple-echo steady-state T2 mapping for in vivo evaluation of articular cartilage. Eur. Radiol. 2016:1905–1912.
166. Metere R, Kober T, Möller HE, Schäfer A. Simultaneous Quantitative MRI Mapping of T1, T2* and Magnetic Susceptibility with Multi-Echo MP2RAGE. PLoS One2017;12:
167. Ma D, Gulani V, Seiberlich N, Liu K, Sunshine JL, Duerk JL, Griswold MA. Magnetic resonance fingerprinting. Nature 2013;495:187–192.
168. Panda A, Mehta BB, Coppo S, Jiang Y, Ma D, Seiberlich N, Griswold MA, Gulani V. ScienceDirect Magnetic resonance fingerprinting – An overview. Curr. Opin. Biomed. Eng. 2017;3:56–66
169. European Society of Radiology: . Magnetic Resonance Fingerprinting - a promising new approach to obtain standardized imaging biomarkers from MRI. Insights Imaging 2015:163–165.
170. Badve C, Yu A, Dastmalchian S, et al. R Fingerprinting of Adult Brain Tumors : Initial Experience. AJNR 2017 38(3):492-99.
171. Su P, Mao D, Liu P, Li Y, Pinho MC, Welch BG, Lu H. Multiparametric Estimation of Brain Hemodynamics With MR Fingerprinting ASL. Magn Reson Med 2017;1823:1812–1823.
172. Badve C, Yu A, Rogers M, Ma D, Liu Y, Schluchter M, Sunshine J, Griswold M, Gulani V.

Simultaneous T 1 and T 2 Brain Relaxometry in Asymptomatic Volunteers Using Magnetic Resonance Fingerprinting.Tomography 2015;1(2) 136-144.
173. Freund P, Weiskopf N, Ashburner J, Wolf K, Sutter R, Altmann DR, Friston K, Thompson A, Curt A. MRI investigation of the sensorimotor cortex and the corticospinal tract after acute spinal cord injury: A prospective longitudinal study. Lancet Neurol. 2013;12:873–881.
174. Grabher P, Callaghan MF, Ashburner J, Thompson AJ, Curt A, Freund P. Tracking sensory system atrophy and outcome prediction in spinal cord injury. Ann Neurol 2015, 78(5) 751-61.
175. Helms G, Draganski B, Frackowiak R, Ashburner J, Weiskopf N. Improved segmentation of deep brain grey matter structures using magnetization transfer (MT) parameter maps. Neuroimage 2009;47:194–198.
176. Lorio S, Lutti a., Kherif F, et al. Disentangling in vivo the effects of iron content and atrophy on the ageing human brain. Neuroimage 2014;103:280–289.
177. Mihara H, Iriguchi N, Ueno S. A method of RF inhomogeneity correction in MR imaging.MAGMA 1998, 7(2)115-120
178. Lutti A, Stadler J, Josephs O, Windischberger C, Speck O, Bernarding J, Hutton C, Weiskopf N. Robust and fast whole brain mapping of the RF transmit field B1 at 7T. PLoS One 2012;7
179. Jiru F, Klose U. Fast 3D radiofrequency field mapping using echo-planar imaging. Magn. Reson. Med. 2006;56:1375–1379
180. Weiskopf N, Callaghan MF, Josephs O, Lutti A, Mohammadi S. Estimating the apparent transverse relaxation time (R2(*)) from images with different contrasts (ESTATICS) reduces motion artifacts. Front. Neurosci 2014;8:278
181. Helms G, Dechent P. Increased SNR and reduced distortions by averaging multiple gradient echo signals in 3D FLASH imaging of the human brain at 3T. J. Magn. Reson. Imaging 2009;29:198–204
182. Ashburner J. A fast diffeomorphic image registration algorithm. Neuroimage 2007;38:95–113
183. Ashburner J, Friston KJ. Unified segmentation. Neuroimage 2005;26:839–851
184. Gringel T, Schulz-Schaeffer W, Elolf E, Frölich A, Dechent P, Helms G. Optimized high-resolution mapping of magnetization transfer (MT) at 3 Tesla for direct visualization of substructures of the human thalamus in clinically feasible measurement time. J. Magn. Reson. Imaging 2009;29:1285–1292
185. Helms G. Correction for residual effects of B1 + inhomogeniety on MT saturation in FLASH-based multi-parameter mapping of the brain. Proc Intl. Soc. Mag. Reson Med. 2015;34:3360
186. Maclaren J, Herbst M, Speck O, Zaitsev M. Prospective motion correction in brain imaging: a review. Magn. Reson. Med.] 2013;69:621–36
187. Zaitsev M, Maclaren J, Herbst M. Motion artifacts in MRI: A complex problem with many partial solutions. J. Magn. Reson. Imaging 2015:42(4) 887-901
188. Godenschweger F, Kägebein U, Stucht D, Yarach U, Sciarra A, Yakupov R, Lüsebrink F, Schulze P, Speck O. Motion correction in MRI of the brain. Phys. Med. Biol. 2016;61:R32–R56
189. Korin HW, Felmlee JP, Riederer SJ, Ehman RL. Spatial-Frequency-Tuned Markers and Adaptive Correction for Rotational Motion. Magn. Reson. Med. 1995;33:663–669
190. Reuter M, Tisdall MD, Qureshi A. Head Motion during MRI Acquisition Reduces Gray Matter Volume and Thickness Estimates.Neuroimage 2015 107:107-15

191. Blumenthal JD, Zijdenbos A, Molloy E, Giedd JN. Motion Artifact in Magnetic Resonance Imaging: Implications for Automated Analysis. Neuroimage 2002;16:89–92
192. Van Dijk KRA, Sabuncu MR, Buckner RL, The influence of head motion on intrinsic functional connectivity MRI, Neuroimage 2012:59:431-43
193. Zaitsev M, Dold C, Sakas G, Hennig J, Speck O. Magnetic resonance imaging of freely moving objects: prospective real-time motion correction using an external optical motion tracking system. Neuroimage 2006;31:1038–1050
194. Qin L, Van Gelderen P, Derbyshire JA, Jin F, Lee J, De Zwart JA, Tao Y, Duyn JH. Prospective head-movement correction for high-resolution MRI using an in-bore optical tracking system. Magn. Reson. Med. 2009;62:924–934
195. Schulz J, Siegert T, Reimer E, Labadie C, Maclaren J, Herbst M, Zaitsev M, Turner R. An embedded optical tracking system for motion-corrected magnetic resonance imaging at 7T. Magn. Reson. Mater. Physics, Biol. Med. 2012;25:443–453
196. Todd N, Josephs O, Callaghan MF, Lutti A, Weiskopf N. Prospective motion correction of 3D echo-planar imaging data for functional MRI using optical tracking. Neuroimage 2015;113:1–12
197. Callaghan MF, Josephs O, Herbst M, Zaitsev M, Todd N, Weiskopf N. An evaluation of prospective motion correction (PMC) for high resolution quantitative MRI. Front. Neurosci. 2015;9:1–9
198. Maclaren J, Armstrong BSR, Barrows RT, et al. Measurement and Correction of Microscopic Head Motion during Magnetic Resonance Imaging of the Brain. PLoS One 2012;7.
199. .Haeberlin M, Kasper L, Barnet C, Dietrich BE, Brunner DO, Gross S, Wilm BJ, Kozerke S, Pruessmann KP Real-time motion correction using gradient tones and head-mounted NMR probes, Mag Reson Med 2015:74(3):647-6
200. Sengupta S, Tadanki S, Gore JC, Brian Welch E. Prospective real-time head motion correction using inductively coupled wireless NMR probes. Magn. Reson. Med. 2014;72:971–985
201. Arnovitch Am Haeberlin M, Gross S, Schmid T, Pruessmann KP: Prospective motion correction with NMR markers using only native sequence elements, Proc Intl Soc Mag Reson Med, 2016:24:0101
202. McConnell M V., Khasgiwala VC, Savord BJ, Chen MH, Chuang ML, Edelman RR, Manning WJ. Prospective adaptive navigator correction for breath-hold MR coronary angiography. Magn. Reson. Med. 1997;37:148–152
203. Bydder M, Atkinson D, Larkman DJ, Hill DLG, Hajnal J V. SMASH navigators. Magn. Reson. Med. 2003;49:493–500
204. Kadah YM, Abaza AA, Fahmy AS, Youssef ABM, Heberlein K, Hu XP. Floating Navigator Echo (FNAV) for In-Plane 2D Translational Motion Estimation. Magn. Reson. Med. 2004;51:403–407
205. Skare S, Hartwig A, Mårtensson M, Avventi E, Engström M. Properties of a 2D fat navigator for prospective image domain correction of nodding motion in brain MRI. Magn. Reson. Med. 2015;73:1110–9
206. Cheng JY, Alley MT, Cunningham CH, Vasanawala SS, Pauly JM, Lustig M. Nonrigid motion correction in 3D using autofocusing with localized linear translations. Magn. Reson. Med. 2012;68:1785–97
207. Gallichan D, Marques JP, Gruetter R. Retrospective correction of involuntary microscopic head

movement using highly accelerated fat image navigators (3D FatNavs) at 7T. Magn. Reson. Med. 2016;75:1030–1039
208. Tisdall MD, Hess AT, Reuter M, Meintjes EM, Fischl B, Kouwe AJW Van Der. Volumetric navigators (vNavs) for prospective motion correction and selective reacquisition in neuroanatomical MRI, Mag Rson Med, 2012:68(2):389-399
209. Tisdall MD. Prospective head motion correction in 3D FLASH using EPI_based volumetric navigators (vNavs). Proc. Intl. Soc. Mag. Reson. Med. 22 2014;22:882
210. Welch EB, Manduca A, Grimm RC, Ward H a, Jack CR. Spherical Navigator Echoes for Full 3D Rigid Body Motion Measurement in MRI. Magn. Reson. Med. 2002;47:32–41
211. van der Kouwe AJW, Benner T, Dale AM. Real-time rigid body motion correction and shimming using cloverleaf navigators. Magn. Reson. Med. 2006;56:1019–32
212. Kober T, Marques JP, Gruetter R, Krueger G. Head motion detection using FID navigators.
Magn.
213. Cheng JY, Zhang T, Ruangwattanapaisarn N, Alley MT, Uecker M, Pauly JM, Lustig M, Vasanawala SS. Free-breathing pediatric MRI with nonrigid motion correction and acceleration. J. Magn. Reson. Imaging 2015;42:407–420.
214. Navest R, Berg C Van Den, Lagendijk J, Andreychenko A. Predictive sensor for real-time respiratory motion monitoring. Proc Intl Soc Mag Reson Med, 2015:23:125
215. Kochunov P, Lancaster JL, Glahn DC, Purdy D, Laird AR, Gao F, Fox P. Retrospective motion correction protocol for high-resolution anatomical MRI. Hum. Brain Mapp. 2006;27:957–62
216. Jenkinson M, Bannister P, Brady M, Smith S. Improved optimization for the robust and accurate linear registration and motion correction of brain images. Neuroimage 2002;17:825–841
217. Kim B, Boes JL, Bland PH, Chenevert TL, Meyer CR. Motion Correction in fMRI via Registration of Individual Slices Into an Anatomical Volume.Mag Reson Med.1999;972:964–972
218. White N, Roddey C, Shankaranarayanan A, Han E, Rettmann D, Santos J, Kuperman J, Dale A. PROMO: Real-time prospective motion correction in MRI using image-based tracking. Magn. Reson. Med. 2010;63:91–105
219. Nehrke K, Barnert P. Prospective correction of affine motion for arbitrary MR sequences on a clinical scanner. Magn. Reson. Med. 2005;54:1130–1138
220. Speck O, Hennig J, Zaitsev M. Prospective real-time slice-by-slice motion correction for fMRI in freely moving subjects. Magn. Reson. Mater. Physics, Biol. Med. 2006;19:55–61
221. Ehman L, Felmlee P. Adaptive technique for high-definition MR imaging of moving structures, Radiology, 1989 {149}. :255–263
222. Atkinson D, Hill DL, Stoyle PN, Summers PE, Keevil SF. Automatic correction of motion artifacts in magnetic resonance images using an entropy focus criterion. IEEE Trans. Med. Imaging 1997;16:903–10
223. Loktyushin A, Nickisch H, Pohmann R, Schölkopf B. Blind retrospective motion correction of MR images. Magn. Reson. Med. 2013;70:1608–18.
224. Christensen R, Linear and Log-Linear Models, Springer, 1990
225. Aschburner J, Friston K, Penny W Human brain function (second edition), Academic Press,2003

226. Tikhonov A, Goncharsky A, Stepanov VV, Yagola AG: N. Numerical methods for the solution of ill-posed problems. 1995
227. Ernst T, Speck O, Itti L, Chang L. Simultaneous correction for interscan patient motion and geometric distortions in echoplanar imaging. Magn. Reson. Med.] 1999;42:201–5
228. Welch EB, Manduca A, Grimm RC, Jack CR. Interscan registration using navigator echoes. Magn. Reson. Med. 2004;52:1448–52
229. Kochunov P, Lancaster JL, Glahn DC, Purdy D, Laird AR, Gao F, Fox P. Retrospective Motion Correction Protocol for High-Resolution Anatomical MRI Hum Brain Mapp. 2006;27(12):957–962
230. Gupta RK. A new look at the method of variable nutation angle for the measurement of spin-lattice relaxation times using fourier transform NMR. J. Magn. Reson. 1977;25:231–235.
231. Wang HZ, Riederer SJ, Lee JN. Optimizing the precision in T1 relaxation estimation using limited flip angles. Magn. Reson. Med. 1987;5:399–416
232. Deoni SCL, Rutt BK, Peters TM. Rapid combined T1 and T2 mapping using gradient recalled acquisition in the steady state. Magn. Reson. Med. 2003;49:515–26
233. Papp D, Callaghan MF, Meyer H, Buckley C, Weiskopf N. Correction of inter-scan motion artifacts in quantitative R1 mapping by accounting for receive coil sensitivity effects. Magn. Reson. Med. 2016;76(5):1478-1485
234. Murakami JW, Hayes CE, Weinberger E. Intensity correction of phased-array surface coil images. Magn. Reson. Med. 1996;35:585–590
235. Wallner BK, Edelman RR, Bajakian RL, Kleefield J, Atkinson DJ, Mattle HP. Signal normalization in surface-coil MR imaging. Am. J. Neuroradiol. 1990;11:1271–1272
236. Axel L, Costantini J, Listerud J. Intensity correction in surface-coil MR imaging. Am. J. Roentgenol. 1987;148:418–420
237. Vovk U, Pernuš F, Likar B. A review of methods for correction of intensity inhomogeneity in MRI. IEEE Trans. Med. Imaging 2007;26:405–421
238. Friedman L, Glover GH. Report on a multicenter fMRI quality assurance protocol. J. Magn. Reson. Imaging 2006;23:827–839
239. Lutti A, Hutton C, Finsterbusch J, Helms G, Weiskopf N. Optimization and validation of methods for mapping of the radiofrequency transmit field at 3T. Magn. Reson. Med. 2010;64:229–238
240. Brown TT, Kuperman JM, Erhart M, White NS, Roddey JC, Shankaranarayanan A, Han ET, Rettmann D, Dale AM. Prospective motion correction of high-resolution magnetic resonance imaging data in children. Neuroimage 2010;53:139–45
241. Aksoy M, Forman C, Straka M, Çukur T, Hornegger J, Bammer R. Hybrid prospective and retrospective head motion correction to mitigate cross-calibration errors. Magn. Reson. Med. 2012;67:1237–51
242. Lutti A, Weiskopf N Optimizing the accuracy of T1 mapping accounting for RF non-linearities and spoiling characteristics in FLASH imaging. Proc. Intl. Soc. Mag. Reson. Med. 21 (2013) 2478
243. Yeatman JD, Wandell BA, Mezer AA. Lifespan maturation and degeneration of human brain white matter. Nat. Commun2014;5:1–12.
244. Ibrahim TS, Baertlein BA, B1 field homogeneity and SAR calculations for the birdcage coil Phys

Med Biol 2001 46(2):609-19.
245. Ibrahim TS, Lee R, Raaijmakers AJE, Klomp DWJ, Jin JM, Analysis of B1 field profiles and SAR values for multi-strut transverse electromagnetic RF coils in high field MRI applications Phys Med Biol 2001 45(2)
246. Dietrich BE, Brunner DO, Wilm BJ, Barmet C, Gross S, Kasper L, Haeberlin M, Schmid T, Vannesjo SJ, Pruessmann KP. A Field Camera for MR Sequence Monitoring and System Analysis Mag Reson Med. 2016;1840:1831–1840
247. Herbst M, MacLaren J, Lovell-Smith C, Sostheim R, Egger K, Harloff A, Korvink J, Hennig J, Zaitsev M. Reproduction of motion artifacts for performance analysis of prospective motion correction in MRI. Magn. Reson. Med. 2014;71:182–190
248. Deichmann R, Schwarzbauer C, Turner R. Optimisation of the 3D MDEFT sequence for anatomical brain imaging : technical implications at 1 . 5 and 3 T. Neuroimage 2004;21:757–767
249. Dijk Van KRA, Sabuncu MR, Buckner RL. The influence of head motion on intrinsic functional connectivity MRI. Neuroimage2012;59:431–438.
250. Ali SH, Modic ME, Mahmoud SY, Jones SE. Reducing Clinical MRI Motion Degradation Using a Prescan Patient Information Pamphlet. AJR 2013:630–634.
251. Gedamu EL, Gedamu A. Subject movement during multislice interleaved MR acquisitions: Prevalence and potential effect on MRI-derived brain pathology measurements and multicenter clinical trials of therapeutics for multiple sclerosis. J. Magn. Reson. Imaging 2012;36:332–343
252. Atkinson D, Hill DL, Stoyle PN, Summers PE, Clare S, Bowtell R, Keevil SF. Automatic compensation of motion artifacts in MRI. Magn. Reson. Med. 1999;41:163–170
253. Atkinson D, Hill DLG, Stoyle PNR, Automatic correction of motion artifacts in magnetic resonance images using an entropy focus criterion. IEEE Trans. Med. Imaging 1997;16:903–10
254. Zhang N, Magland JF, Song HK, Wehrli FW. Registration-based autofocusing technique for automatic correction of motion artifacts in time-series studies of high-resolution bone MRI. J. Magn. Reson. Imaging2015;41:954–963
255. Loktyushin A, Nickisch H, Pohmann R, Schölkopf B. Blind retrospective motion correction of MR images. Magn. Reson. Med. 2013;70:1608–18
256. Filipovic M, Vuissoz P, Codreanu a, Claudon M, Felblinger J. Motion compensated generalized reconstruction for free-breathing dynamic contrast-enhanced MRI. Magn. Reson. Med. 2011;65:812–22
257. Wu HH, Gurney PT, Hu BS, Nishimura DG, McConnell M V. Free-breathing multiphase whole-heart coronary MR angiography using image-based navigators and three-dimensional cones imaging. Magn. Reson. Med. 2013;69:1083–93
258. Maclaren J, Aksoy M, Bammer R Contact-free physiological monitoring using a markerless optical system, Mag reson Med, 2015:74(2):571-577
259. Andreychesko A, Crijns S, Raaijmakers A, Stemkens B, Luijten P, Lagendijk J, van den Berg C, Noise variance of an RF receive array reflects respiratory motion: a novel respiratory motion predicton, Proc. Intl. Soc. Mag. Reson. Med. 2014: 22:3045
260. Tian Q, Gong E, Leuze CWU, Pauly J, McNab J. Effects of Motion on Coupling of Coil Elements

and Parallel Imaging Reconstruction at 3T and 7T. Proc. Intl. Soc. Mag. Reson. Med 2015;23:6702
261. Gong E, Tian Q, MacNab JA, Pauly J Motion estimation from noise intrinsic correlation between RF channels (MECHANICS) Proc. Intl. Soc. Mag. Reson. Med 2015;23:3671
262. Lemieux L, Salek-Haddadi A, Lund TE, Laufs H, Carmichael D. Modelling large motion events in fMRI studies of patients with epilepsy. Magn. Reson. Imaging 2007;25:894–901
258. Med MR. HHS Public Access. 2015;74:571–577. doi: 10.1002/mrm.25781.Contact-free.
263. Castella R, Arn L, , Dupuis E, Callaghan MF, Draganski B, Lutti A. Controlling motion artefact levels in MR images by suspending data acquisition during periods of head motion.Magn Reson Med 2018:1–12.
264. Hansen PC. The L-curve and its use in the numerical treatment of inverse problems, Computational Inverse Problems in Electrocardiology, 2000
265. Wallace TE, Afacan O, Waszak M, Kober T, Warfield SKWarfield SK. Head motion measurement and correction using FID navigators. Magn. Reson Med, 2018
266. Waszak M, Falkovskiy P, Hilbert T, Bonnier G, Meuli R, Gruetter R, Kober T, Krueger G. Prospective Head Motion Correction Using FID-Guided On-Demand Image Navigators. Magn Reson Med 2017;203:193–203.
267. Gallichan D, Marques J, Gruetter R. Overpoof GRAPPA: exploiting the natural sparsity of fat images,Proc. Intl. Soc. Mag. Reson. Med. 2014 (22):4345
268. Federau C, Gallichan D. Motion-Correction Enabled Ultra-High Resolution In-Vivo 7T-MRI of the Brain. Plos One 2016:1–12.
269. Maclaren J, Lee KJ, Luengviriya C, Speck O, Zaitsev M. Combined prospective and retrospective motion correction to relax navigator requirements. Magn. Reson. Med. 2011;65:1724–1732.
270. Babayeva M, Kober T, Herbst M, Hennig J, Seeger M, Gruetter Rm Zaitsev M, Krueger G, Can multi-channel FID navigators quantify head motion?, Proc. Intl. Soc. Mag. Reson. Med 2013 (21) 306.
271. Hansen MS, Sørensen TS. Gadgetron: An open source framework for medical image reconstruction. Magn. Reson. Med. 2013;69:1768–1776
272. Sacolick LI, Wiesinger F, Hancu I, Vogel MW. B1 mapping by Bloch-Siegert shift. Magn. Reson. Med. 2010;63:1315–1322